Computational Models of Endothelial and Nucleotide Function

Andrew Comerford

A thesis presented for the degree of
Doctor of Philosophy
in
Mechanical Engineering
at the
University of Canterbury,
Christchurch, New Zealand.

1 August 2007

Acknowledgements

I would like to thank my supervisor Prof Tim David for giving me this wonderful opportunity. I would not have got this far without his excellent supervision and support. It has been a pleasure working with you and I have learnt a great deal over the past three years

Many thanks to Dr Michael Plank who has been a delight to work with and has provided excellent guidance over the past three years.

I would like to thank my parents for their support and proof reading.

Thanks to everyone in the bio centre for a creating a fun working environment, I have really enjoyed the last three years.

Contents

List of Figures

List of Tables

Nomenclature

List of symbols

$\mathbf{A}$	Face area vector
b	Vector of knowns
C_c	Cytosolic calcium
C_s	Stored calcium
$C_{s,0}$	Resting stored Ca^{2+} concentration
C_{ex}	External Ca^{2+}
D	Diffusion coefficient
f	face
$\mathbf{f}$	body force
$g_{\max}$	Max. WSS-induced eNOS activation
i	Inositol trisphosphate
$\bar{\bar{\mathbf{I}}}$	Identity matrix
$\mathbf{J}$	Mass flux vector
K	Reaction rate
k_{rel}	Calcium release rate
k_{ret}	Calcium resequestration rate
k_{out}	Calcium efflux rate
k_{dis}	eNOS-caveolin disassociation rate
k_{CCE}	Capacitive calcium entry rate
L	Characteristic length
n	Endothelial nitric oxide synthase
$\mathbf{n}$	Normal coordinate vector
N	Number of faces
nb	Neighbour
$q_{\max}$	Max. WSS-induced Calcium influx rate

p	pressure
r	Radial coordinate
R	Radius
S	ATP release rate
$S_{\max}$	Maximum ATP release
S_ϕ	Source term
$\mathbf{T}$	Total traction vector
t	Time
$\mathbf{u}$	Velocity vector
U_∞	Free stream velocity
$[u, v, w]$	Cartesian velocities
V_r	Ratio of cytosol to ER volume
W_0	Shear gating constant
$[x, y, z]$	Cartesian coordinates
α	Zero shear open channel constant
γ	'Slip velocity' or relative strength of the Ca^{2+}-dependent pathway for eNOS activation
Γ	Domain Boundary or incomplete gamma function
δ	Boundary layer thickness or membrane shear modulus
$\bar{\bar{\varepsilon}}$	Rate of rotation tensor
η	Similarity variable
θ	Angle
μ	Dynamic viscosity
μ_1	IP_3 decay rate
μ_2	eNOS-caveolin association rate
ν	Kinematic viscosity
ρ	Fluid density
σ	something
$\bar{\bar{\tau}}$	Stress tensor
τ_w	Wall shear stress
τ_0	Characteristic wall shear stress
ϕ	Arbitrary scalar
ϕ_∞	Bulk ATP concentration
ω	Frequency
Ω	Domain
$\bar{\bar{\omega}}$	rate of deformation tensor
$\forall$	Volume

List of Acronyms

ATP	Adenosine Trisphosphate
ADP	Adenosine Diphosphate
AMP	Adenosine Monophosphate
Ca^{2+}	Calcium ion
CICR	Calcium Induced Calcium Release
CCE	Capacitive Calcium Entry
Cl^{-}	Chlorine ion
eNOS	Endothelial nitric oxide synthase
ECM	Extracellular Matrix
ER	Endoplasmic Reticulum
IP_3	Inositol Trisphosphate
LDL	Low Density Lipoprotien
LHS	Left hand side
NO	Nitric oxide
ODE	Ordinary differential equation
OSI	Oscillatory Shear Index
PDE	Partial differential equation
PKC	Protein Kinase C
PLC	Phospholipase C
RHS	Right hand side
SMC	Smooth Muscle Cells
UDF	User Defined Function
VCAM	Vascular Cell Adhesion Molecule
WSS	Wall shear stress

List of Dimensionless Numbers

Re	Reynolds Number
Sc	Schimdt Number
Da	Damköhler Number
Pe	Peclet Number
Sh	Sherwood Number

Abstract

Atherogenesis is the leading cause of death in the developed world, and is putting considerable monetary pressure on health systems the world over. Although the risk factors are well understood, unfortunately, the initiation and development of this disease still remains relatively poorly understood, but it is becoming increasingly identifiable as a dysfunction of the endothelial cells that line the walls of arteries. The prevailing haemodynamic environment plays an important role in the focal nature of atherosclerosis to very specific regions of the human vasculature. Disturbed haemodynamics lead to very low wall shear stress, and inhibit the transport of important blood borne chemicals.

The present study models, both computationally and mathematically, the transport and hydrolysis of important blood borne adneosine nucleotides in physiologically relevant arterial geometries. In depth analysis into the factors that affect the transport of these low diffusion coefficient species is undertaken.

A mathematical model of the complex underlying endothelial cell dynamics is utilised to model production of key intracellular molecules that have been implicated into the complex initiation processes of atherosclerosis; hence regions of the vasculature can be identified as being 'hot spots' for atherogenesis. This model is linked into CFD software allowing for the assessment of how 3D flow fields and mass transfer affect the underlying cell signalling. Three studies are undertaken to further understand nucleotide variations at the endothelium and to understand factors involved in determining the underlying cell dynamics. The major focus of the first two studies is geometric variations. This is primarily due to the plethora of evidence implicating the geometry of the human vasculature, hence the haemodynamics, as an influential factor in atherosclerosis initiation. The final model looks at a physiologically realistic geometry to provide a more realistic reproduction of the *in vivo* environment.

Chapter 1

The Pathobiology of Cardiovascular Disease

1.1 Introduction

Atherosclerosis is the leading cause of morbidity and mortality in the developed world. It is characterised by the progressive narrowing and hardening of medium and large arteries, which can eventually lead to ischemia of the heart, brain, or extremities, leading to infarction (Ross, 1999). This chapter outlines some of the related biology of the arterial wall, disease formation and cell mechanisms that have been associated with the onset of atherosclerosis. Understanding the cellular responses due to the haemodynamic environment is important for understanding the initiation of atherogenesis.

1.2 The artery wall

The structure of the artery can be broken down into three distinct layers: tunica intima, tunica media and tunica adventitia, see Figure 1.1. The tunica intima is a very thin layer that occupies the innermost region of the artery wall. In direct contact with the flowing blood is a thin layer of endothelial cells which act as an active barrier to the transport of material between the flowing blood and the arterial wall. Below this single layer of endothelial cells exists a layer of connective tissue (fenestrated elastic fibres). The outermost layer of the intima is the internal elastic lamina, consisting of an elastin and collagen fibres' network with a fenestrated appearance. The middle layer, the largest layer, of the artery wall is known as the tunica media. It consists predominately of smooth muscle

cells arranged concentrically, but also contains elastin and collagen fibres; this layer provides the strength and structural integrity of the arterial wall. The composition of media layer is highly dependent on the artery caliber and age. For example, aligning the heart, the left anterior descending coronary artery contains a larger percentage of smooth muscle cells. Finally the outermost layer, the tunica adventitia, consists of connective tissue and some collagen and elastic fibre; this layer is separated from the media by a thin layer of elastic tissue called the external elastic lamina. The adventitia layer also contains vasa vasorum, these are small blood vessels that supply the arterial wall with metabolites and nutrients which are essential for its survival. These vessels may penetrate through into the media layer.

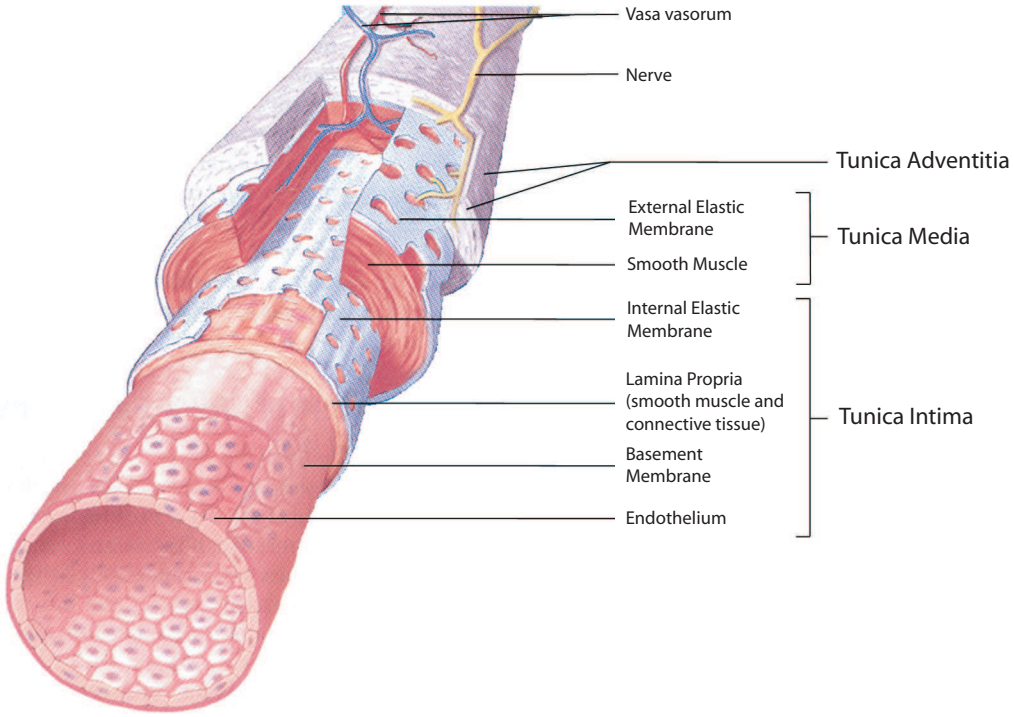

Figure 1.1: Successive layers of the arterial wall. Figure adapted from Seeley et al. (2003).

1.3 Endothelial Biology

A key player in the pathobiology of atherosclerosis is the endothelium. The endothelium is a monolayer of cells that line the inner walls of arteries, hence providing an interface between the flowing flow and the artery wall. Originally

this layer was thought to be a passive barrier between the flowing blood and the artery wall, but subsequently the converse has been identified. This was first demonstrated by Furchgott and Zawadzki (1980), who performed an *in vitro* study on isolated rabbit arteries. They found that arteries with an intact endothelium undergo vasodilation when administered with acetylcholine, but following removal of this layer the vessel constricted under the same conditions. The endothelium responds to both the prevailing haemodynamic and biochemical environment eliciting a number of cellular responses. Additionally, this cell layer has been strongly implicated in the pathobiology of atherosclerosis through its regulatory functionality.

1.3.1 Endothelial cells

The basic architecture of endothelial cells is constructed from membranes, organelles and cytosol. The outer protective coating of the cell is called the plasma membrane; this is a semi permeable lipid bilayer surface coating, that controls the passage of material between the extracellular and intracellular environment. The surface of the membrane contains a variety of integral membrane proteins (or ion channels). These include non-gated ion channels, which control permeability of the plasma membrane, ligand gated ion-channels, which activate in response to ligand binding and flow sensitive ion channels. These respond to the prevailing haemodynamic environment.

The region within the cell is termed the cytoplasm, which is the bulk of the cell volume consisting of cytosol and organelles. The cytosol is the fluid portion of the cytoplasm consisting of ions and molecules, such as proteins. The actual structure of the cell is held together by the cytoskeleton, which is a 3D internal scaffolding network bound within the cytosol and provides mechanical strength to the cell. This network is formed from actin filaments, intermediate filaments and microtubules. Actin filaments are of most interest here as they are involved in force transmission (see section 1.4.2) and reorganisation of actin filaments allows for morphological changes in structure and orientation in the presence of altered environmental conditions.

The rest of the cytosol is made up of organelles which have specific tasks to be carried out for the maintenance of the cell. Some important ones are outlined

below. The endoplasmic reticulum (ER) is a membrane network responsible for the synthesis and modification of proteins and transfer of material throughout the cell and also is a major storage site of intracellular calcium. This extends out from the nucleus of the cell forming a network of sacs and tubules in which the interior space is separated from the cytosol.

The Golgi apparatus is responsible for the distribution of proteins throughout the cell. Proteins from the ER are transported to the Golgi apparatus via small vesicles which are small sacs that break off from the ER and fuse to the membrane of Golgi apparatus. Additionally, the Golgi apparatus releases small vesicles that are transported to the plasma membrane where they fuse to this layer. Here they secrete molecules across the plasma membrane in process called exocytosis.

The mitochondria are a very important organelle in eukaryotic cells providing essential energy to the cell via the production of adenosine trisphosphate (ATP). Within the mitochondria, aerobic metabolism takes place where the conversion of glucose and fatty acids leads to the formation of ATP through a complex series of events that make up the citric acid cycle and electron transport chain. The essence of this process involves the conversion of glucose derived pyruvic acid in a glycolysis reaction to ATP. The indirect importance of this mechanism for ATP will become clear in section 1.4.3.

Finally, the nucleus of the cell is an organelle separated from the cytosol by a double membrane. The nucleus is where DNA is stored and controls the activity of the processes within the cell such as gene expression (important for long term changes occurring in the cell).

1.3.2 Homeostasis

The endothelium by virtue of its unique location is a major controller of vascular homeostasis (Davies, 2000, Gimbrone, 1999). The endothelium responds to external stimuli in an autocrine (signalling effecting the same cell) and paracrine (signalling effecting locally associated cells, such as smooth muscle cells) manner. Major regulatory processes in which the endothelium is involved include: coagulation, growth of underlying smooth muscle cells, leukocyte (white blood cell) uptake and adhesion, lipoprotien uptake and regulation of vascular tone

(Gimbrone, 1999, Traub and Berk, 1998).

Coagulation refers to the process by which blood is able to clot. If coagulation occurs in blood, the healthy endothelium secretes antithrombotic agents. For example, the endothelium expresses proteoglycan molecules which are cofactors for antithrombin. This molecule acts with certain proteins to inhibit thrombin, thus keeping blood in a liquid state (Libby, 2001, Traub and Berk, 1998). The endothelium also actively participates in fibrinolysis (which is the process of breaking down fibrin - the structural component of a clot) through the production of plasminogen activator.

In healthy arteries the endothelium provides a non-adhesive, non-thrombogentic surface, hence leukocytes and other cells such as platelets and red blood cells do not adhere to the endothelium or migrate into the sub endothelial space (Kharbanda and MacAllister, 2005).

The endothelium is a source of various vasoactive substances that regulate the local and systemic vascular tone. Vascular tone refers to the degree of constriction from a basal state. The regulation of tone occurs in response to haemodynamic forces imposed by the flowing blood and also biochemical stimuli. Of particular interest here is the activity of the powerful vasodilator nitric oxide (NO) which exhibits many characteristics that are identified as being atheroprotective including some of the previously mentioned for example, anti-coagulation agents and the limited expression of vascular adhesion molecules, such as vasculature cell adhesion molecule 1 (VCAM-1) (Libby et al., 2002).

The endothelium is also an endogenous source of vasoconstrictors (substances that cause constriction of the vessel and are responsible for the production of cytokines), the most abundant and powerful being endothelin (H.Drexler, 1998). Vasoconstrictors are implicated in the formation of atherosclerosis via smooth muscle cell proliferation and is also released from macrophages. Ultimately, the healthy endothelium is responsible for maintaining many important processes and this balance is critical for a normally functioning cardiovascular system (Gimbrone et al., 2000).

1.3.3 Endothelial Dysfunction

Endothelial dysfunction is the term that refers to a reduced state of homeostatic functionality by the endothelium, hence leading to a number of pathogenic risk factors. The initiation of atherosclerosis was originally thought to be due to an injured endothelium. This was known as the 'response to injury' hypothesis originally posed by Ross and Glomset (1976), but this concept has subsequently been discarded after *in vivo* findings determined that the endothelial cells overlying atherosclerotic lesions were morphologically intact (Davies et al., 1976). From these findings, the concept of endothelial dysfunction has been introduced (Gimbrone et al., 2000).

In the previous section the critical role of the endothelium was to maintain the balance between vasodilators and constrictors. If this balance is disrupted many regulatory processes go astray. Of central importance is the vasodilator NO: a very strong relationship has been identified between reduced activity of NO and endothelial dysfunction, as NO exhibits key atheroprotective characteristics (Barbato and Tzeng, 2004, Naseem, 2005, Shaul, 2003). Whether this is a cause or an effect still remains to be fully established. Following reduced NO availability many characteristics, both *in vivo* and *in vitro*, upregulation of vasoconstrictors such as endothelin and serotonin (Davignon and Ganz, 2004, Drexler and Hornig, 1999); promotion of vascular adhesion molecules (which bind blood leukocytes) and the production of cytokines (signalling molecule); increased permeability to lipoproteins, which can become oxidised within the arterial wall promoting further complications; stimulation of growth factors, which leads to hyperplasia of the underlying smooth muscle cells. As a result the surface of the endothelium undergoes a biochemical change becoming prothrombotic. For example, upregulation of the prothromobotic substance thromboxane (which under normal conditions is balanced by the vasodilator prostacyclin) has been noted in endothelial cells subject to oxidative stress. This increases levels of reactive oxygen species, which are known to damage cell structure (Müller and Griesmacher, 2000).

The cause of endothelial dysfunction is not currently well defined, but is associated with a number of cardiovascular risk factors such as hypercholesterolemia (elevated blood cholesterol levels), smoking and hypertension. Additionally, it is strongly associated with the prevailing haemodynamic environment with the

release of NO controlled by wall shear stress (Cooke, 2003, Gimbrone et al., 2000), which may provide information about predisposed locations for dysfunction. From a clinical perspective, the state of endothelial dysfunction is becoming increasingly recognised as an early marker of sites potentially prone to atherogenesis (Davignon and Ganz, 2004, H.Drexler, 1998).

1.4 Mechanisms of Atherogenesis

This section outlines the processes involved in the formation of atherosclerosis and highlights some of the pathways that are thought to have important roles in the localisation of atherosclerosis to very specific regions of the human vasculature.

1.4.1 Initiation and Development

The precise mechanisms involved in atherosclerosis, especially in its early stages, are still disputed, but it has become evident that atherosclerosis is an inflammatory disease involving a complex manifestation of cellular processes that occur over a considerable number of years (Libby et al., 2002, Ross, 1999). It involves a complex interaction and structural change between the arterial wall, flowing blood and blood borne molecules. The disease is a precursor to well known pathological conditions such as myocardial infarction, stroke and peripheral artery disease. The inflammation is a response by the body's immune system resulting in remodelling of the arterial wall via deposition of lipid laden material in the intima, which eventually encroaches on the arterial lumen, potentially narrowing the vessel and occluding the artery or rupturing.

Atherosclerosis initiates due to a number of well known risk factors, such as hypercholesterolemia (high blood cholesterol levels), hypertension, obesity and more recently infection. Sites of atherosclerosis are also very focal in nature occurring predominately in regions of disturbed flow, where NO production is reduced (Libby et al., 2002). These regions of the endothelial surface are able to over express vascular adhesion molecules, such as VCAM-1, that bind leukocytes and mononuclear cells to the surface. The expression is thought to be caused by the presence of modified LDL in the arterial intima (Steinburg, 1997), and,

as mentioned previously, NO inhibits VCAM expression, hence linking initiation to reduced NO activity. Following attachment to the endothelium, monocytes migrate into the sub-endothelial space via inter-endothelial spaces (a process termed diapedesis) where they differentiate into macrophages (an inflammatory response - that is part of the body's immune response to fight infection). Within the intima the macrophages release monocyte-chemoattractive protein-1 (MCP-1) (Crowther, 2005, Libby et al., 2002), which recruits further luekocytes into the sub-endothelial space. Furthermore, the activated macrophages also secrete cytokines that promote migration and proliferation of smooth muscle cells from the media into the intima. Within the intima LDL undergoes oxidation due to prolonged exposure to reactive oxygen species (related to reduced NO activity). Oxygenated LDL (oxLDL) is very atherogenic, promoting further expression of adhesion molecules, and is very chemotactic for macrophages (Crowther, 2005). Macrophages express scavenger receptors along their outer membrane and these recognise oxLDL. This uptake of the oxLDL by macrophages results in reduced mobilisation and these lipid-laden macrophages are known as 'foam cells' (Libby, 2001). The accumulation of 'foam cells' and leukocytes within the intima leads to the formation of 'fatty streaks', which appear as yellow discolorations on the luminal surface and are now visible to the human eye (Hegele, 1995). The proliferating SMC, from macrophage activation, secrete extracellular matrix (ECM) proteins leading to the formation of a fibrous cap; fibrous plaque is characterised by relatively high mechanical strength and is actually a defense mechanism that prevents further thickening and protruding of the plaque via remodelling of the fatty tissue. After prolonged periods the foam cells may die leaving a necrotic core.

The development of the plaque can vary significantly (Crowther, 2005, Libby et al., 2002). The variation in development is demonstrated in Figure 1.2. In the early stages of atherosclerosis there will be no physical restriction of blood supply through the lumen. This is because the artery will dilate to accommodate the expansion of the intima, until it reaches a maximally dilated state at which point protrusion into the vessel will begin to occur. From this stage it can progress into two forms: a plaque with a thick fibrous cap which is 'reasonably' stable, or a 'vulnerable' plaque with a thin fibrous cap containing within the intima significant amounts of LDL and inflamed cells. It is the latter that is at risk of rupture (Crowther, 2005). Following rupture the thrombus that forms can lead to many acute complications, for example myocardial infarction. The alterative, as

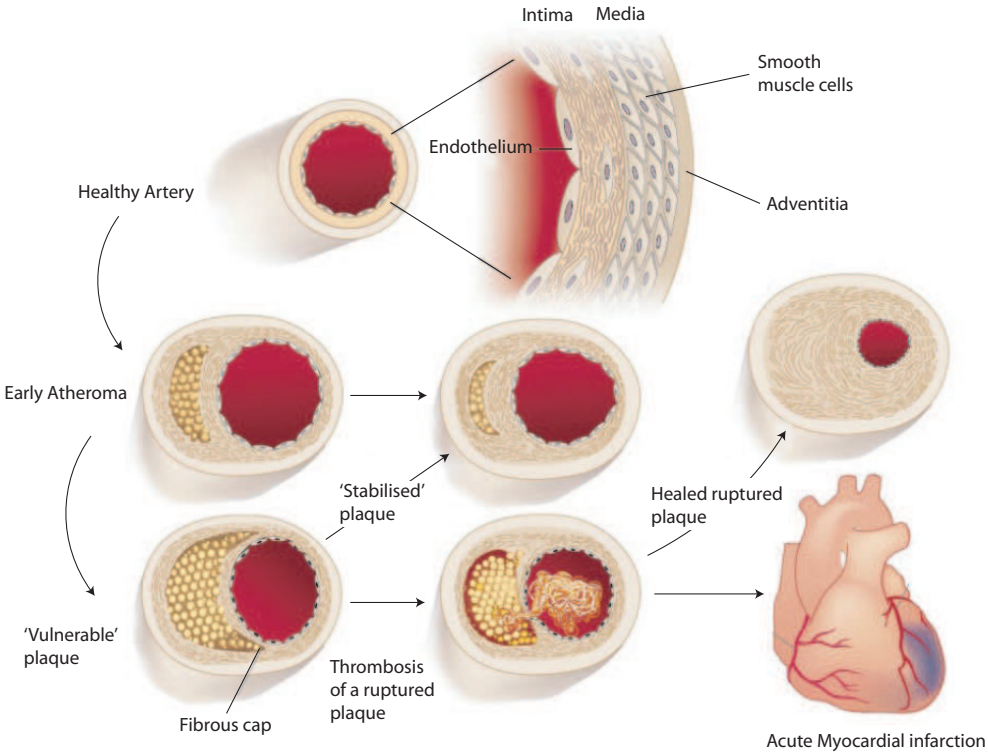

Figure 1.2: The progression of atherosclerosis development, modified from Libby (2002).

illustrated in Figure 1.2, is the initiation of healing process activated by thrombin formation and the platelet derived growth factor can stimulate smooth muscle cell migration and proliferation excreting extracellular matrix thickening. This fibrous cap an expanded intima extends into the lumen, leading to a stenotic vessel which restricts blood supply.

1.4.2 Wall Shear Stress

Wall shear stress and its relationship to atherogenesis has been under intense study for the past 30 years (Asakura and Karino, 1990, Friedman et al., 1981, Zarins et al., 1983). From these studies it has been firmly established that there is a relationship between regions of disturbed flow/low WSS and locations of intimal thickening. Current thinking suggests that WSS exhibits its effects via a number of pathways both directly and indirectly. It is well established that atherosclerosis is not evenly distributed throughout the human vasculature, but tends to be site specific, occurring preferentially on the lateral wall of bifurcations and inner and outer walls of arterial bends (Asakura and Karino, 1990, Fox

et al., 1982, Gimbrone et al., 2000, Zarins et al., 1983). This was identified from experimental studies using arteries excised from humans during autopsy and the similarity between all of these studies was the type of haemodynamic environment. For example, in the study by Zarins et al. (1983), histological sections were taken of the excised arteries and the blood flow was modelled using laser-Doppler anemometry in a scale model. Flow characteristics were then statically correlated to intimal thickness. A major finding was that intimal thickening is associated with low WSS, flow separation and non-axially aligned velocity profiles, whilst areas subjected to moderately high WSS and where the flow is axially aligned were not affected. The natural progression of this study was to implement an unsteady (oscillatory) flow field due to cardiac flow waveform. This was performed by Ku et al. (1985) who studied pulsatile flow in the same scale model of the carotid bifurcation. Their results found a positive correlation between oscillatory WSS and intimal wall thickening and they confirmed a previous observations of WSS inversely correlated with intimal wall thickening. Further studies agreed with the above findings, using arteries exercised from other regions of the body, firmly establishing a relationship between disturbed haemodynamics and atherosclerosis. The above suggests that arterial geometry, hence the haemodynamic environment, is a major factor in the localisation of atherosclerosis, but this cause effect relationship requires establishment at a biological level.

Further to long term responses, such as atherosclerosis, it is known that WSS, both low and oscillatory, is a regulator of many rapid responses, such as vasodilation, hence implicated in disease initiation. WSS being a major stimulus of endothelial structure and biological function has been evidenced by a number of groups (Gimbrone et al., 2000, Malek et al., 1999, Resnick et al., 2003, Traub and Berk, 1998). The biological function characteristics were outlined in the section 1.3.2. In linear sections of the vasculature where WSS is high, the endothelial cells are ellipsoidal in shape, are aligned in an orderly manner with the flow direction and many atheroprotective characteristics are exhibited (as discussed in section 1.3.2); atherosclerosis is rare in these locations. In regions of disturbed/low WSS endothelial cells are poorly aligned and are more susceptible to endothelial dysfunction and potentially have an elevated risk of atherogenesis, for example endothelial permeability and turnover is increased (Davies, 2000, Resnick et al., 2003). These biological changes are from both *in vitro* and *in vivo* experiments as evidenced by a number of groups (see Davies (1995) and references therein). This area remains controversial and therefore remains an area of

intense biological study.

From the above findings, two broad categories, force transmission and force transduction exist, with many pathways implicated in each (Davies, 1995). Force transmission refers to stress distribution via the cell cytoskeleton, whilst force transduction refers to secondary messenger systems, such as a response to biochemical stimuli. Both of these pathways act simultaneously and crossover of the pathways is thought to occur.

As mentioned previously, the cytoskeleton is involved directly in force transmission. The most important component is thought to be actin filaments which are connected to the plasma membrane of the cell at a number of focal adhesion sites (regions of the abluminal cell surface that are attached to the ECM). At focal adhesion sites, the cytoskeleton is connected to an associated protein which is attached to an integrin molecule, a transmembrane protein attached to ECM on the lower surface of the cell (Davies and Tripathi, 1993). Depending on the shear environment actin filaments have been observed to undergo a conformal change via remodelling of focal adhesion sites. In regions of uniform laminar flow the actin filaments are aligned parallel to the flow direction whilst in disturbed regions the filaments are grouped in bundles. This remodelling of actin filaments is thought to be involved with endothelial dysfunction, but mechanisms remain controversial. Another transmission of force is the anchoring to adjacent endothelial cells where the actin filaments are connected to cell-cell adhesion proteins, such as PECAM, thus force transmission occurs between adjacent cells. Other pathways that have been put forward in the literature (Traub and Berk, 1998), including the caveolae (small invaginations in the plasma membrane that are very lipid rich), which are thought to deform less than other regions of the plasma membrane because of high rigidity brought about by high cholesterol content.

Force transduction involves a secondary messenger biochemical response initiated by a mechanoreceptor. Mechanisms of force transduction include, but are not limited to, shear activated ion channels, G-proteins, and phosphorylation of serine residues. The plasma membrane is lined with ion-channels and these are known to be sensitive to the prevailing haemodynamic environment and are thought to act mainly in a secondary messenger response by inducing intracellular Ca^{2+} signalling due to membrane potential (Nilius and Droogmans, 2001). This still remains to be fully characterised. A number of different ion channels exist:

Ca^{2+}, Cl^{-}, and K^{+}, where the former provides a direct entry of Ca^{2+} into the intracellular environment (some examples discussed in section 1.4.4) and the latter two are involved in membrane depolarisation/hyperpolarisation respectively. The latter two are also implicated in Ca^{2+} signalling, for example, K^{+} channels lead to membrane hyperpolarisation (increased polarisation of intracellular environment) which increases the electrochemical gradient in the cell resulting in the influx of Ca^{2+}. The response of these different channels varies markedly exhibiting different time constants to the prevailing conditions, suggesting that ion-channels may be able to sense different types of waveforms, such as coronary versus carotid (Barakat et al., 2006).

The G-protein coupled pathway is an indirect relationship for WSS and is related to the transport of low molecular weight species, which is discussed in the section 1.4.3, but there is some evidence that the receptor may respond directly to WSS (Resnick et al., 2003, Traub and Berk, 1998). The phosphorylation of serine residues by WSS is an important pathway with regard to endothelial nitric oxide synthase (eNOS), which is discussed in detail in section on 1.4.5. Other pathways that are involved include the glycocalyx and integrins. The glycocalyx are plasma membrane molecules that protrude out into the lumen. It is thought that the displacement of these molecules interacts with transmembrane proteins leading to underlying cellular responses (Tarbell and Pahakis, 2006). Integrin molecules are also implicated in force transduction via conversion of a mechanical signal into a biochemical signal (Davies, 1995, Traub and Berk, 1998).

1.4.3 Purinoceptors and Blood Borne Agonists

Blood borne nucleotides, such as adenosine triphosphate (ATP), are widely known to elicit a number of responses by the endothelium (Gordon, 1986). Endothelial cells are lined with purinergic P2 nucleotide receptors (plasma membrane molecules involved in cellular responses). that respond to these agonists (Ralevic and Burnstock, 1998). In this family there are two main classes: the P_{2Y}, and P_{2X}. The P_{2Y} receptor is guanine nucleotide binding protein (G-protein coupled) and is known to be a mediator of many cellular processes on activation of biochemical stimuli, such as ATP and adenosine diphosphate (ADP). G-proteins are transmembrane receptors that transduce the action of ligand binding to a signal within the cell. The P_{2X} are ion channels that open in response to receptor ATP

binding which also leads to many cellular responses.

In more detail, the P_{2Y} G-protein coupled receptor responds to ligand binding initiating a signal-transduction cascade, in which a G-protein activates Phospholipase C (PLC), a key enzyme in phosphatidylinositol (PIP_2) metabolism. PLC hydrolyses the phosphodiester link in PIP_2 forming inositol trisphosphate (IP_3) and diacylglycerol. This respectively leads to intracellular calcium mobilisation and activation of protein kinase C (PKC) and due to the secondary messenger nature of this receptor it is slow acting with a response time of around 300ms.

The P_{2X} receptor is a fast acting receptor with a response time of around 10ms. Following the binding of three ATP molecules (Burnstock, 2004) selectively permeable (K^+, Na^+ and Ca^{2+}) ion channels are opened. This causes the rapid influx of ions into the cytosol of the cell. This leads to depolarisation of the cell membrane and subsequently activates voltage gated ion channels leading to accumulation of calcium in the cytoplasm. Of the P_{2X} family of receptors it has recently been observed by Yamamoto et al. (2006) that the P_{2X4} subtype is the crucial P_{2X} type receptor for modulation of vascular tone. Overall, the above highlights the importance of agonist transport in the blood, and impaired availability to the arterial wall is of great interest when considering affects on underlying cell signalling.

Figure 1.3 shows the important pathways that are currently reported to lead to vasodilation via lumenal nucleotide receptor binding. In the present study, of interest is the transport, and implications for underlying cellular dynamics, of the blood-borne agonist ATP and the dephosphorylation products.

The degradation of blood borne agonists at the endothelial surface is controlled via membrane bound ectoenzymes (5'-nucleotidase). At the surface of the endothelium, ATP undergoes dephosphorylation by the action of three separate ectonucleotidedases (Pearson and Gordon, 1985). The dephosphorylation reaction by ecto-ATPase is as follows:

$$\mathrm{ATP} \rightarrow \mathrm{ADP} + \mathrm{PO}_4^{3-}$$

where ATP is hydrolysed to ADP leading to the release of a free inorganic phosphate group. ADP then undergoes a further dephosphorylation resulting in the

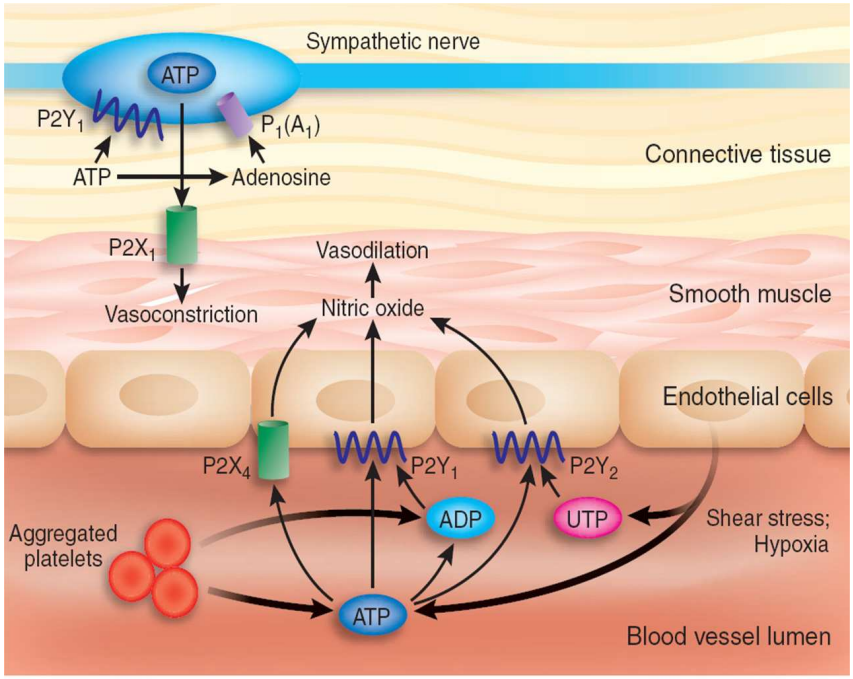

Figure 1.3: Some common pathways and sources of nucleotides that lead to vasodilation in endothelial cells, from Burnstock (2006).

formation of AMP and finally adenosine; these nucleotides are reported to have little to no effect on subsequent cell surface signalling. Therefore, understanding the concentration variation in blood is of utmost importance when considering effects on regulation processes performed by endothelial cells.

ATP is ubiquitous in blood. With many sources of this 'energetic' molecule existing, potentially one of the most important sources of ATP is the endothelium. ATP is synthesised in the mitochondria of the endothelial cell during the citric acid cycle and electron transfer chain: 38 molecules of ATP are produced per breakdown of one molecule of pyruvic acid. The actual mechanisms relating to ATP release into the lumen are still amid much controversy: it has been observed by a number of groups that ATP is released in response to the application of flow (Bodin and Burnstock, 2001, Milner et al., 1990, Yamamoto et al., 2003). The story so far has identified the following: the release is a transient response proportional to the applied wall shear, and is non sustainable on repeated application, indicating that the stores of ATP do not replenish quickly after successive stimulation. There are a number of hypothesised mechanisms around in literature relating to actual release such as: release from vesicles via exocytosis (Bodin and Burnstock, 2001), ATP binding cassette transporters (Larzarowski et al., 2003)

and a not yet identified efflux of ATP via a conductance pathway.

1.4.4 Calcium

The action of extracellular vasoactive agents leads to many intracellular responses. Calcium (Ca^{2+}) is a key intracellular secondary messenger which has a pivotal role in many of the endothelial regulatory processes including vasodilation and cell apoptosis. Calcium is indirectly rather than directly involved in many of these processes. For example an important secondary messenger pathway is the association of Ca^{2+} with calmodulin, which is a ubiquitous cytosolic protein that mediates a myriad of endothelial processes. Raised cytosolic Ca^{2+} levels results in the formation of a Ca^{2+}–calmodulin complex which modulates protein and enzyme activity. One such enzyme is endothelial nitric oxide synthase (eNOS), which will be discussed in the following section.

Calcium can enter the cytoplasm via two different sources: from the internal stores, or across the plasma membrane. The majority of Ca^{2+} in endothelial cells is stored in the ER, accounting for around 75% of total Ca^{2+} stores (Tran et al., 2000). These internal stores are regulated via a number of cell signalling pathways including IP_3. Covering the surface of the ER are IP_3 receptors that caused channels to open following IP_3 attachment. This allows Ca^{2+} to flow naturally down its concentration gradient from the internal stores. This activation eventually plateaus even in the presence of an abundant supply of IP_3. There exist a number of hypotheses for this phenomenon, but potentially it is due to receptor desensitisation.

The release of Ca^{2+} from internal stores activates a number of other Ca^{2+} pathways, such as Ca^{2+} induced Ca^{2+} release (CICR) (Berridge, 1997), and capacitive Ca^{2+} entry (CCE) (Putney et al., 2001).

CICR is a positive feedback mechanism where more Ca^{2+} channels are opened accelerating Ca^{2+} release. Additionally, increased levels of cytosolic Ca^{2+} also increases the rate of IP_3 production, resulting in further depletion of internally stored Ca^{2+}.

Depletion of internally stored Ca^{2+} below basal levels results in CCE. Ca-

pacitive Ca^{2+} entry is a flux of Ca^{2+} across the plasma membrane. The precise mechanisms by which CCE occurs are still amid some controversy with a number of competing theories existing. Theories include: conformational coupling, diffusible secondary messenger, and local Ca^{2+} regulation (Putney et al., 2001, Tran et al., 2000). Conformal coupling is a direct protein-protein interaction and is the most supported idea. This theory states that, following depletion of internal stores, there is a conformal change in the IP_3 protein receptor which interacts directly with proteins in the plasma membrane. Diffusible messenger theory states that a messenger is produced following depletion of stores, this messenger transmits a signal to the plasma membrane. Two alternative hypotheses exist for local Ca^{2+} regulation in the vicinity of the plasma membrane. The first is to do with depletion of an abundant Ca^{2+} pool in the vicinity of an ion channel; this inhibits Ca^{2+} entry initially, but following depletion will allow entry. The second is exocytosis: the depletion of stores causes secretion and fusion of vesicles to the plasma membrane which signals Ca^{2+} entry.

Further to agonist regulated Ca^{2+} mobilisation, WSS directly gates Ca^{2+} influx across the plasma membrane via Ca^{2+} sensitive ion channels as discussed in section 1.4.2.

1.4.5 Nitric Oxide

Nitric oxide is a powerful vasodilator, formerly known as the endothelium-derived relaxing factor (Furchgott and Zawadzki, 1980). It is thought to play a pivotal role in the pathogenesis of atherosclerosis as it is essential for vascular homeostasis countering the effects of vasoconstrictors and has key atheroprotective characteristics as previously discussed. Nitric oxide in endothelial cells in synthesised by endothelial NO synthase (eNOS) and decreased expression of eNOS is thought to play a role in endothelial dysfunction. The activity of eNOS is modulated by two independent but not mutually exclusive pathways (Dudzinski et al., 2006, Shaul, 2002) and see Figure 1.4.

The first of these mechanisms is directly gated via wall shear stress, whilst the second is via a Ca^{2+}-calmodulin pathway (agonist and WSS). The mobilisation of eNOS via WSS has become apparent as the predominant mechanism in the literature (Dimmeler et al., 1999). This mechanism has not been clearly

elucidated yet, but there is reasonable evidence linking the phosphorylation of eNOS at serine residue 1177 by the kinase Akt (a phosphate removing enzyme), which is activated by a shear sensitive phosphatidylinositol-3-OH (PI3K) pathway (Dimmeler et al., 1998). There are also many other pathways implicated, these include many different kinase enzymes, but their relative importance is unclear.

The second mechanism, a Ca^{2+}-calmodulin pathway, works as follows: eNOS in endothelial cells resides in caveolae, which are specific plasma membrane invaginations (micro-domains) high in the protein caveolin-1; this protein binds to eNOS, inhibiting its enzymatic activity (Davignon and Ganz, 2004). Raised levels of Ca^{2+} in the cytosol, from WSS/agonist-activated IP_3 pathways binds with calmodulin which causes eNOS to disassociate from calveolin, activating the production of NO. Hence a reduction in endothelial Ca^{2+} concentration can lead to reduced bioavailability of NO at the artery wall (Lin et al., 2000).

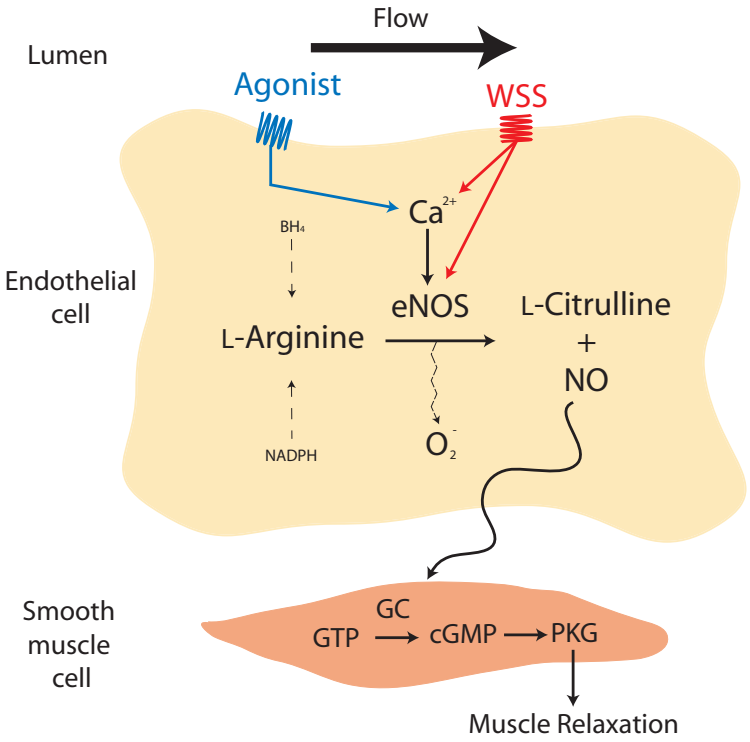

Figure 1.4: Mechanisms involved in nitric oxide generation within an endothelial cell , and the downstream effect on smooth muscle cell relaxation. A potential dysfunction in this mechanism may result in lack of NO at the artery wall, hence a precursor to atherosclerosis. Figure adapted from (Davignon and Ganz, 2004)

Following the activation eNOS (pathways shown in Figure 1.4), this enzyme catalyses the conversion of L-arginine to NO and L-citrulline. For this conversion to take place there are a number of cofactors that must be present, such

as tetrahydrobiopterin (BH_4) and nicotinamide adenine dinucleotide phosphate (NADPH) (Behrendt and Ganz, 2002, Vane et al., 1990). If these molecules are not present the conversion results in the production of a superoxide, hence under deficient BH_4 conditions eNOS may contribute to endothelial dysfunction and susequent complications (Behrendt and Ganz, 2002, Verma and Anderson, 2002). Due to the extremely short half life of NO it can only act in a paracrine manner diffusing into closely associated SMC (Lodish et al., 2004). Here it activates guanylate cyclase (GC), which leads to increased production of cyclic guanosine monophosphate (cGMP) and this in turn activates protein kinase G (PKG) which leads to relaxation of the muscle cell. The vasodilator response of NO is an important mechanism for regulation of blood flow.

1.5 Conclusion

The previous outline of factors involved in atherosclerosis has demonstrated that a very complex array of processes is involved in the initiation and development. Understanding these processes biologically is still amid much controversy, but there are a number of factors that have gained credibility. Low eNOS appears to be a major factor in endothelial dysfunction, hence impaired availability is a potential precursor to the formation of atherosclerosis. Understanding the signalling pathways that lead to the activation of eNOS are very important and currently remains under intense and disputed biological research. These pathways include calcium dependent and independent. The former pathway is signalled via ATP, related dephosphorylation components and WSS, whilst the latter is signalled only via WSS. Once these pathways are fully understood, potentially rapid insight may be gained into eNOS production, or more precisely lack of eNOS production, therefore this could represent a considerable step in understanding the initiation of cardiovascular disease.

Chapter 2

Arterial Modelling Literature Review

2.1 Introduction

Numerical modelling of arterial blood flow presents itself as a powerful and insightful research tool allowing for the identification of numerous haemodynamic parameters, that are impossible to measure *in vivo*. Additionally it allows for the progression (in a mutual sense) of *in vitro* studies by identifying pertinent parameters that require *in vitro* testing; thus allowing the disease initiation to be understood in more detail. This review chapter is subdivided into three sections: computational modelling of haemodynamics, computational modelling of mass transport, and finally fluid/mass transport coupled cell models.

2.2 Computational modelling of haemodynamics and the relationship to atherosclerosis

Over the past twenty years the area of computational modelling of arterial haemodynamics has grown rapidly, having become a powerful tool to identify key parameters that may or may not play a role in the pathology of atherosclerosis. The role of the fluid mechanical environment is sensed through a response by the endothelium (as previously discussed in chapter 1). The results from many of these numerical simulations have identified a casual link between haemodynamic conditions such as flow recirculation and separation and the location of lesions *in vivo*. Early computational models focused more on the flow characteristics, for example, Perktold and Hilbert (1986) developed a finite element numerical

formulation to solve the Navier-Stokes equations in physiologically significant geometry of 2D carotid bifurcations. Their results gave insight into flow conditions that may be associated with the onset of atherosclerosis; these were highlighted as conditions of stagnation an flow reversal, although not explicitly stated in the article related to WSS. Subsequently, the focus has turned towards understanding how the haemodynamic environment effects the artery wall, hence WSS is of great importance.

2.2.1 Wall shear stress

Wall shear stress (and related indices) remains one of the most heavily researched areas in computational arterial modelling primarily due to the strong correlation that has been identified between low WSS and lesion development (Ku et al., 1985, Zarins et al., 1983). Earlier computational models related to WSS were the likes of Perktold and Resch (1990), who modelled the time dependent flow in a 3D arterial T-junction. They concluded that the most physiologically relevant flow variable is WSS, and also how this varies temporally (instantaneous wall shear vector); this result agreed well with previous *in-vitro* research. Over the last decade there have been numerous simulations with regard to WSS in a variety of arterial models, predominantly bends and bifurcations. These models have looked directly at WSS (Myers et al., 2001, Perktold et al., 1998, 1991b), and also characterised WSS related indices such as oscillatory shear index (OSI) (He and Ku, 1996, Taylor et al., 1998), wall shear stress gradient (WSSG), wall shear stress angle gradient (WSSAG) (Hyun et al., 2000, Lei et al., 1995), in an attempt to formulate initiation of underlying characteristics that lead to the onset of atherosclerosis. Unfortunately the latter two suffer greatly from numerical inaccuracy due to the twice differential nature. Although there has been strong correlation between intima thickening and regions of low and oscillatory WSS there is still insufficient detail of the response to these prevailing stimuli at a cellular level.

Obviously WSS is directly effected by the prevailing haemodynamic environment and other factors that have been investigated, such as shear thinning of blood. This effect in large arteries is negligible as essential flow characteristics are captured by Newtonian fluid due to the generally high shear rates (Perktold et al., 1991b). The investigation of geometric variation as a risk factor has seen some

attention (Perktold et al., 1991a), they concluded that large angle bifurcations lead to flow phenomena that are associated with the initiation of atherosclerosis, but further investigation is still required.

2.3 Computational modelling of mass transfer

Recently, CFD studies of mass transfer in realistic artery geometries have become increasingly more accessible. Previous studies in literature have looked at convection-dominated transport and generally the models used a basic form of the arterial wall boundary condition, where a constant concentration or flux was specified. An outline of some of these studies is given below. The significance for the present study, although not directly related, is the transport of low diffusion coefficient species. The studies focused on physiologically significant (with respect to disease development) geometries such as bifurcations and bends.

2.3.1 Bifurcations

One of the first studies on computational mass transfer was performed by Friedman and Ehrlich (1975) using a finite difference scheme. In this study they looked at a simple 2D bifurcation geometry and the transport of oxygen which was subject to a variety of boundary conditions; mass transport variations were observed on the bifurcations outer wall. Ma et al. (1997) studied the convective mass transfer of oxygen in the carotid artery bifurcation for Pe=172000, using the Fluent finite volume code. The simulation geometry is the same as a number of previous studies (Ku et al., 1985, Zarins et al., 1983). From their study, they found impaired mass transfer was observed in the region of flow recirculation (carotid sinus), and this was irrespective of the Schmidt number which they varied three fold. They also concluded that 2D simulations can capture essential dynamics of mass transfer found in the corresponding 3D case; therefore a good first step in understanding the relationship between mass transfer and atherosclerosis. Overall, they predicted low mass transfer on the outer walls of bifurcations, where intimal thickening has been observed *in vivo*; This was done by comparing the results from their carotid bifurcation, with those performed by Ku et al. (1985). Unfortunately due to the similarity between the results for mass transfer, WSS

and intimal thickening, a focus on endothelial response is required to elucidate the mechanisms leading to atherosclerosis. Wada et al. (2000) studied the transport of LDL in a uniform diameter 135^o T junction; their boundary condition included a transmural wall flux given by,

$$V_{\mathrm{w}}C_{\mathrm{w}} - \left.\frac{\partial C}{\partial \mathbf{n}}\right|_{\mathrm{wall}} = KC_{\mathrm{w}} \tag{2.1}$$

Therefore location of previous reported reduced mass transport are now elevated. They reported elevated LDL concentration on the lateral walls of the branch and also at the stagnation point as the vessel branched into the two daughter arteries.

2.3.2 Bends

Rappitsch et al. (1997) studied pulsatile mass transport of oxygen within a 90^o bend; this was to assess local hypoxia in the artery wall. They used a finite-element formulation to discretise the governing equations. For their study, a sinusoidal velocity inlet profile was used, leading to a Peclet number $\mathcal{O}(10^5)$. A number of different boundary conditions were used for the flux at the wall, a standard wall permeability and a simple linear shear dependent condition. The shear dependent boundary is given by

$$\left.\frac{\partial C}{\partial \mathbf{n}}\right|_{\mathrm{wall}} = \beta\|\tau_{\mathrm{w}}\|C. \tag{2.2}$$

They found that impaired mass flux occurred at the inner wall of the bend, and the linear shear dependent boundary condition resulted in greater spatial variation (similar to WSS) in the wall flux, but there is no real experimental evidence to back this finding up. Qiu and Tarbell (1999) studied the transport of oxygen in an idealised curve tube representative of coronary artery dimensions. The model included pulsatile flow and vessel wall compliance. The results demonstrated that oxygen availability to the inner wall was also limited by the fluid phase, but on the outer wall it was not. Unfortunately the accuracy of the species computation was rather limited, due to available computational resources, but

the results still provide a qualitative assessment. Kaazempur-Mofrad and Ethier (2001) modelled mass transfer in a realistic right coronary artery; this was to the author's knowledge the first model of a realistic geometry that includes secondary curvature in the study of mass transfer. The mass transfer was representative of species such as oxygen or ATP, with a Peclet number of 1.5×10^6. The model highlighted the importance of realistic geometries on mass transfer. The Dean like vortices shifted in response to secondary curvature, moving the location of high and low Sherwood number around the artery. In agreement with Qiu and Tarbell (1999), significant differences between the mass transfer to the outer wall compared to the inner wall were observed. Wada and Karino (2002) looked at the transport of LDL in a human right coronary multi bend artery. Their simulations again included a transmural wall flux boundary condition equation (2.1). The study was performed for a variety of Reynolds numbers, where the higher ones induced recirculation at the inner wall of the bend. The results suggested that there is a partial relationship between elevated LDL concentration and locations of low wall shear stress. It was also noted that thin layered peripheral flows, which determine the value of wall shear stress, are important with respect to impaired mass transfer to the arterial wall.

All in all, these studies of curved arterial segments have demonstrated that impaired mass transfer of arbitrary low diffusion coefficient species occurs at the inner walls of bends. Unfortunately, from a disease development perspective the location of impaired mass transfer corresponds closely with wall shear stress; hence it is difficult to separate the two processes, and assess their relative importance. Again the focus on endothelial cell dynamics is required to fully understand the initiation of atherosclerosis.

2.3.3 Stenosis

Although a stenosis represents an already diseased vessel, it is important to consider studies that have been performed in this area as the effects of separated flow on mass transfer can be understood from these investigations. Rappitsch and Perktold (1996) performed an axisymmetric study of mass transfer in a stenosis in order to determine how recirculating flow and WSS affects the concentration at the lumenal surface. They used two boundary conditions at the endothelial surface: a constant wall flux, and a shear dependent wall flux (equation (2.1) in

section 2.3.1). It was found that in the region downstream of a stenosis where recirculation occurs resulted in reduced oxygen concentration that closely follows fluid shear stress; this highlighted geometry as a major controller of arterial mass transport. Wada et al. (2002) performed a fully 3D simulation of LDL transport in an end-to-end anastomosed vessel with and without a mild stenosis at the arterial wall. In the stenosed artery they found that the location of elevated LDL corresponded closely with the location of stagnation in near wall flow patterns. Kaazempur-Mofrad et al. (2005) studied the transport of arbitrary species for Pe=7.5×10^5, which is applicable to the transport of species such as oxygen or ATP. This paper assessed briefly separation characteristics on mass transport by including limiting streamlines, which are the vector valued WSS resolve over the surface of the artery; this provides information about separation conditions. These trajectories correlate strongly with regions of impaired mass transport. Also it was concluded that the effects of pulsatile flow need to be examined.

2.3.4 Modelling ATP concentration at the endothelium

Previous mathematical models have been developed to investigate ATP/ADP concentration at the endothelium, the majority of these providing numerical solutions in a simple parallel plate geometry; they hence lack disturbed flow characteristics observed *in vivo*. Nollert and Mcintire (1992) developed a parallel plate experimental model to determine the effects of flow on the cytosolic calcium levels within the endothelial cells. Their results indicated that endothelial cells responded to a change in flow rate by altering [Ca^{2+}] levels; this flow effect only occurred in the presence of ATP. The concentration of ATP at the endothelium was observed to be a function of the wall shear stress (WSS). They also hypothesised that the mechanism by which endothelial cells detect changes in flow rate was due to the local concentration of ATP at the cell surface.

Shen et al. (1993) developed a mathematical model that included ADP concentration at the surface. The combined decrease of ATP and ADP was small, which led to the conclusion that transport of ATP to the surface and degradation at the surface, could not solely account for the strong dependence of the endothelial cells on shear stress. A drawback of this study and potentially incorrect conclusion, was the *in vivo* significance as impaired receptor mediated signalling likely results in regions of disturbed flow.

John and Barakat (2001) extended on previous mathematical models to include the more physiologically accurate model of pulsatile flow, and shear stress-induced ATP release from the endothelial cells, using both a linear and sigmoidal function of wall shear stress. The inclusion of ATP release was motivated by the research of Milner et al. (1990), in which the results demonstrated that cultured human umbilical vein endothelial cells release ATP when exposed to Kreb's solution; this release was shown to be a function of the blood flow rate. John and Barakat (2001) results showed, not surprisingly, that ATP release had a profound effect on the nucleotide concentration at the endothelial surface. The research also concluded that pulsatile flow provides little change to the surface concentration and that the response is determined by the time-averaged WSS. Again, a limitation of these studies was that they only considered a non-spatially varying wall shear stress by investigating a parallel flow chamber.

David (2003) developed an analytical model of ATP/ADP concentration at the endothelial surface for generic 2D and axisymmetical wall shear stress functions; this was the first model that allowed for spatially varying WSS to be investigated. The geometries modelled were the commonly used experimental ones of a backwards facing step and stagnation flow. This model allowed the concentration profiles at the endothelium of any *reasonable* wall shear function to be investigated. This characteristic is important as a major controller of physiological kinetics is geometry. Excellent agreement was obtained from these models when compared to previous numerical solutions for the constant wall shear stress parallel plate model. It was also demonstrated using the analytical model that ATP concentration at the endothelium increased with shear stress for a variety of Sherwood numbers. This agreed with similar results that Nollert and Mcintire (1992) and John and Barakat (2001) had obtained for numerical models. Plank et al. (2006a) gave a rigorous mathematical analysis and discussion on the validity and application of the similarity solution, and introduced a detailed analysis of ATP/ADP concentration in a 2D backwards facing step geometry for a range of Reynolds numbers. One of the very interesting results was the maximum ATP concentration was determined by the curvature of WSS in the region of stagnation.

2.4 Modelling of Endothelial Cell dynamics

A number of cell models have been developed over the years looking at a variety of different cell mechanisms. Most of these models were not investigating endothelial cells, rather they were interested in excitable cells such as, smooth muscle and nerve cells, but due to the mechanisms involved they provide a basis for future modelling in other cell types. Additionally, they also shared common ground in the understanding and modelling of Ca^{2+} transients that occur in many different cell types.

Meyer and Stryer (1988) developed a cell model of Ca^{2+} spiking in vascular smooth muscle cells. The model accounted for the production of IP_3 due to receptor-ligand binding and subsequent affects on ER Ca^{2+} and cytosolic Ca^{2+} concentrations. The mechanisms relating to IP_3 binding on the ER is a useful result that is applicable to many different cell types. Goldbeter et al. (1990) looked at Ca^{2+} oscillations in neurons. The model included both an IP_3 dependent and independent mechanism for Ca^{2+} signalling. Mahama and Linderman (1994) developed an experimental and mathematical model of Ca^{2+} transients related to smooth muscle cells. They presented a detailed model of IP_3 formation due to receptor binding including the intermediate steps of the signal transduction cascade.

Wiesner et al. (1996) developed a model of endothelial cell dynamics in response to external stimuli; this model included many different cellular processes and was the most complete to date, bringing together a variety of cell models (not necessarily related to endothelial cell dynamics) including the aforementioned. Due to a considerable number of unknown quantities, mechanisms were assessed parametrically and rate constants determined by fitting to known experimental data; this allowed for a physiologically realistic model (or more precisely a realistic reproduction of an *in vitro* response) to be developed. For each of the processes modelled, the effects of altering rate constants was determined. From this study, it was found that extracellular agonist concentration was an important modulator of Ca^{2+} transients; hence intracellular Ca^{2+} dynamics.

Wiesner et al. (1997) furthered the previous model to include WSS related signalling; this was done via flow affecting mass transfer and also through shear gated pathways. For the shear gated pathways the activation was via a wall shear

stress dependent strain energy density function that was related to the proportion of open channels. Their relationship for the strain energy density encompassed both force transmission and transduction components dependent on the applied WSS. From their model, they found that the combined stimulus of WSS and agonist elicited a greater Ca^{2+} transient than either alone.

Following on from the previous model of Wiesner et al. (1996,1997), Plank et al. (2006b) simplified this model and investigated the response in the spatially varying haemodynamic environment of a backwards facing step; this provided an essential understanding on how environmental stimuli effect the underlying endothelial cell dynamics. The details of this model are presented in Chapter 5.

2.5 Conclusion

From the previous discussion, the understanding of haemodynamics is extensively documented in literature, particularly the cause effect relationship between atherosclerosis and low/oscillatory WSS. Mass transport has become more common over the past decade, but there is still a myriad of work to be carried out in this area. More specifically, endothelial agonists, such as ATP and ADP, in physiologically relevant arterial geometries and the responses that these agonists elicit may play an important role in focal initiation of atherosclerosis. The present study models the important signalling molecule ATP and its dephosphorylation counterparts in both simplified 2D environments, aimed at determining essential mass transport characteristics, and complex 3D geometries, aimed at determining responses *in vivo*. Geometric variation is a major area of focus.

One of the most important steps in the progression of understanding is to provide a clear and precise link between arterial haemodynamics, mass transport and endothelial biology. This requires not only extensive mathematical and numerical modelling, but also experimental work to assess how the endothelial cells respond in different environments, and what regulatory responses alter, such as Ca^{2+} an eNOS, and trying to elicit the important pathways. The present work aims to provide some perspective on this via modelling of cell signalling coupled to the blood flow in physiological arterial environments, thus information on the spatial variation and importance of 3D geometries will be evidenced.

Chapter 3

Fluid Mechanics and Blood Flow Modelling

3.1 Introduction

Blood flow in arteries is of considerable interest due to its crucial role in the pathology of atherosclerosis. In order to gain insight into the haemodynamic factors that are involved in the pathogenesis of atherosclerosis a sound understanding of fluid kinematics and dynamics is required. This chapter provides information about major assumptions made when modelling blood flow. A brief overview of the governing equations and the extension of these equations to numerical solutions using the finite volume CFD solver Fluent is given, where the full mathematical and numerical discretisation can be found in Appendix A and B. Finally, a discussion on wall shear stress calculation and an important time dependent index will be introduced.

3.2 Arterial modelling considerations

In order to model a complex fluid such as blood a number of considerations and assumptions need to be made. Blood is a suspension of cells in plasma and its primary function is the transport of nutrients and waste. The suspended particles account for about 45% by volume and includes red blood cells, white blood cells and platelets. Blood Plasma accounts for around 55% by volume and consists of around 92% water, with the other 8% being plasma proteins such as albumin and fibrinogen. Therefore to model this complex liquid, a number of assumptions need to be made in order to achieve physically plausible results in a finite time,

with given computer facilities and analytical complexity.

Blood is assumed to be homogeneous and incompressible. The assumption of a homogeneous fluid treats blood as a piecewise continuous smooth medium in space and time. Strictly speaking, as mentioned above, blood is a suspension of particles in plasma, but in large and medium sized arteries a macroscopic view of blood can be taken as the vessels of interest are between 2-11mm, whereas the largest particles suspended within the plasma are 7.5μm. This provides for at least three orders of magnitude difference, meaning the blood can be treated as homogeneous. The incompressibility assumption is valid for all liquids where pressure variations are relatively small.

Within the cardiovascular system generally, the blood flow is laminar throughout. However in a diseased artery, fatty material accumulates in the arterial wall leading to encroachment into the arterial lumen, creating a stenosis. The downstream region of severe stenoses are known to have turbulent instabilities in the flow and the critical Reynolds number is 300 (Ku, 1997), however this critical value will also depend on the severity of the stenosis and the Womersley number of the flow. In the present study the focus is on non-diseased arterial geometries, hence turbulence is not considered as the flow is well within the threshold of laminar transition (Re=2000) for flow in axi-symmetric tubes.

An interesting characteristic of blood is that it exhibits shear thinning non-Newtonian rheology, meaning the relationship between stress and strain within the fluid is not a simple linear relationship (ie. Newtonian). However, for the present study this is neglected. Neglecting non-Newtonian rheology is common practice in arterial modelling for a number of reasons. In large and medium sized arteries shear rates are generally high and it is well known that for large shear rates ($>100s^{-1}$), blood exhibits approximately Newtonian rheology (Pedley, 1980). In contrast, in small arteries this is not the case and the non-Newtonian effects are significant. Additionally, a previous study by Perktold et al. (1991a) investigated the effects of Newtonian versus non-Newtonian blood rheology in a human carotid artery model. Flow features between the two models exhibited very similar characteristics, furthermore the difference in WSS magnitude between the two rheologies was only around 10%. A quick validation can be obtained if we consider simple Poiseuille flow and it can be shown that the shear rate ($\dot{\gamma}$) is given by the following

$$\dot{\gamma} = \frac{4Q}{\pi r^3} \tag{3.1}$$

where Q represents the flow rate, and r the radius of the artery. Now considering some numbers that are relevant to models presented in later chapters, assuming a Reynolds number of 200, a blood viscosity of 4×10^{-3} Pa·s and a diameter of 3mm the flow rate, Q is approximately 1.9×10^{-6}, the shear rate is calculated as $711s^{-1}$, which is greater than the given threshold.

For Chapters 6 and 7 the viscosity of blood will be assumed to be 4×10^{-3} Pa·s as this is a commonly accepted viscosity value (Ku, 1997). In Chapter 8 a slight variation of the viscosity, for reasons of consistency with a previous study, will be given as 3.465×10^{-3} Pa·s. Throughout it will be assumed that blood is homogeneous and of Newtonian rheology, apart from a small investigation into non-Newtonian effects in chapter 8.

It is well known that *in vivo* arteries are not rigid, rather they are distensible, which means the wall moves in response to pressure induced by the flowing blood. In the present study the effects of a distensible wall are neglected. This is for a number of reasons. Previous studies, such as Perktold and Rappitsch (1995), modelled a distensible wall carotid bifurcation using a simplified shell model, which is suitable for large non-linear deformation models. The results determined that between rigid wall and distensible wall models global flow features and stress field are relatively unchanged. However this does not preclude that arterial distensibility does not have an affect, or more specifically play a role in atherosclerosis. Another reason for neglecting is due to mass transfer considerations. As outlined in chapter 4, numerical mass transfer is computationally expensive for steady and time varying models with rigid walls and as yet still remains to be fully characterised. For pulsatile simulations the wall distensibility is partial taken into account due to the inclusion of a realistic pulse waveform, whose shape is governed by upstream wall movement. The issue of a full FSI distensible wall should be addressed in future models.

3.3 Governing Equations

The governing equations that dictate arterial blood flow are given in this section; for an in depth discussion and full derivation see Appendix A.

3.3.1 Continuity

The continuity equation, or divergence free condition, is a statement of mass conservation throughout the fluid domain. Here it is given in integral form and on the assumption of incompressibility as

$$\int_{CV} \nabla \cdot \mathbf{u} d\forall = 0 \tag{3.2}$$

where CV represents the control volume, $d\forall$ an infinitesimal volume, $\mathbf{u}$ the velocity vector.

3.3.2 Momentum

Application of Newton's second law, assessment of deformation of an infinitesimal fluid element due to applied surface forces and introduction of a well known constitutive relation, leads to the following equation. This is known as the momentum equation, given here in integral form as

$$\frac{\partial}{\partial t}\int_{CV} \rho \mathbf{u} d\forall + \int_{CS} \rho \mathbf{u}\mathbf{u} \cdot d\mathbf{A} = -\int_{CV} \nabla p d\forall + \int_{CS} \mu \nabla \mathbf{u} \cdot d\mathbf{A} \tag{3.3}$$

where terms are defined as before, with additional terms CS representing the control surface, CV the control volume, $\mathbf{A}$ the face area vector p the pressure, ρ the density and μ the dynamic viscosity. Writing the momentum equation as above in integral form is convenient for introduction and discretisation for the computational method introduced in the next section.

3.4 Important Dimensionless Number

Womersley Number

The Womersley number is an important dimensional number associated with pulsatile flow, hence is reported widely in arterial modelling literature as a measure of flow unsteadiness. It expresses the pulse frequency relative to viscous effects and is defined by:

$$Wo = R\left(\frac{\omega}{\nu}\right)^{1/2}$$

where $\omega = 2\pi f$ and f is the frequency.

3.5 Computational fluid mechanics

Due to their mathematical complexities, the previous equations are very difficult to solve analytically, in fact analytical solutions only exist for a handful of cases. For this reason, and because of the complex geometries under consideration, a computational fluid dynamics (CFD) approach is required. This is achieved using the well validated commercially available finite volume CFD code Fluent. For the finite volume method, the fluid domain under consideration is divided up into a finite number of volumes on which the governing equations (3.3) and (3.2) are discretised, meaning the mathematical equations are replaced with discrete equations for pressure and velocity. The equations are then linearised to form a discrete set of equations (matrix), which is then solved iteratively. The full discretisation method is given in Appendix B, and a brief outline is given below.

For equation (3.3) following discretisation for a given volume the governing equations are written in semi-discrete form as

$$\frac{\partial \phi}{\partial t} + \sum_{f}^{N} (\rho \mathbf{u})_f \phi_f \cdot \mathbf{A}_f = \sum_{f}^{N} \Gamma_f (\nabla \phi)_f \cdot \mathbf{A}_f + S_\phi \forall \tag{3.4}$$

where f represents the faces of the enclosed volume and N the number of faces. This is a general discretised equation where depending on the choice of ϕ different transport processes are considered. The discretised equation represents momentum if $\phi = \mathbf{u}$, but can be also used to represent the transport of an arbitrary scalar, for example mass transport. For momentum the source term includes the pressure gradient.

Considering the momentum equation, this can be written conveniently in a linearised form as

$$a_{c0}\mathbf{u}_{c0} = \sum_{nb} a_{nb}\mathbf{u}_{nb} + \nabla p \forall + b \tag{3.5}$$

Here a_{c0} incorporates convective and diffusive discretisation terms for the cell $c0$ (which is the volume under consideration), a_{nb} includes discretisation terms for neighbouring volumes (nb) and b includes source and secondary terms. When this procedure is applied over the entire fluid domain, a system of equations of the following form is produced

$$A\mathbf{u} = \mathbf{b} \tag{3.6}$$

where A is the coefficient matrix (which is sparse), $\mathbf{u}$ the unknown quantities and $\mathbf{b}$ the vector of known quantities. Fluent uses a point Gauss-Seidel method with Algebraic multigrid algorithm to accelerate convergence to solve equation 3.6.

The discritised momentum equation exhibits both a linear dependence on pressure and velocity, for this reason it is required that the dependency between the velocity and pressure is handled correctly. The pressure in equation (3.5) is not known *a priori*, however a family of algorithms (SIMPLE, SIMPLEC and PISO) exist that transforms the continuity equation into an equation for pressure. This method is very common in CFD and is known as the pressure velocity coupling. This also produces a system of the form 3.6 and is solved in a similar manner to the momentum equation.

3.5.1 User defined functions

One of the major draw cards of the Fluent CFD package is it allows models external to the solver to be programmed in the C programming language and then linked into the solver using a compiled user defined function (UDF). There are additionally a number of C programming macros that are included with the Fluent package allowing easy access to essential variables of interest, such as the WSS vector. This modelling approach was used extensively in the present study, predominantly for implementing complex boundary conditions.

Due to the computationally intensive nature of the models in the present study the parallel version of Fluent was utilised. This is generally fairly easily implemented, however considerations in the design of the UDF is required. This is because the parallel setup is broken down into a host and a number of compute nodes. No computation is done on the host process, however input and output must be executed on the host process; hence when files are read into the UDF the information had to be collected and then passed to the compute nodes where it can be used for processing. This was achieved by a number of different methods via compiler directives and MPI message passing; the reason for the two different methods was due to certain Fluent macros not supporting MPI. The computational resources used in this thesis were: A 10 compute-node (20 processor) Beowulf cluster running Rocks Linux with a total of 20Gb of RAM, generally on this computer up to 4 compute nodes were utilised before network latency had a detrimental impact on the performance (details given in chapter 7; A 16 node (128 processor) IBM Power5-575 HPC with 512Gb of RAM running AIX 5.3, on this machine a maximum of 16 processors were used.

3.5.2 Meshing

For the arterial models used in the present study a number of different meshing schemes and programs were utilised. The bifurcation and bend models presented in Chapter 6 and 7 respectively, were meshed using Fluents preprocessor meshing program Gambit. This program includes a number of useful features including the attachment of 3D boundary layers to the surface of the models which lead to well aligned grids in the vicinity of the wall, this is important for WSS calculation

(see section 3.7), but more importantly the transport of low diffusion coefficient species (see Chapter 4). For the bulk fluid part of the domain, away from the walls, a number of different schemes were utilised the Cooper meshing scheme and T-grid. The former creates a mesh using hexahedral volumes (or quadrilaterals in 2D), and the latter creates a mesh of tetrahedral and wedge volumes (or triangles in 2D). In all cases the bulk of the domain consisted of hexahedral elements this had the advantage of reducing the overall size of the mesh, thus memory requirements. The accuracy of the results are also regarded as superior using hexahedral volumes as gradient reconstruction is superior as opposed to tetrahedral and wedge shaped volumes.

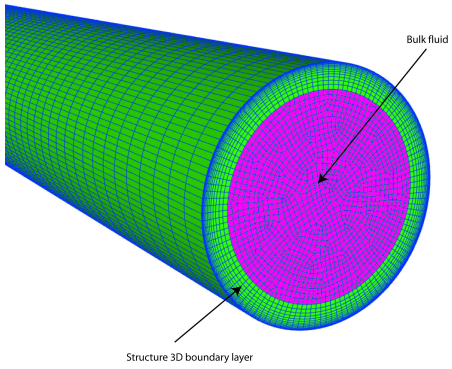

Figure 3.1: Example gambit mesh demonstrating the difference between the mesh within the boundary layer and the bulk fluid.

For the physiologically realistic geometry considered in Chapter 8 the commercially available preprocessor Harpoon was utilised. This meshing program uses an adaptive cartesian meshing method. This type of method leads to a mesh of predominantly hexahedral cells with some prisms and wedges existing in the boundary layer to adapt to the geometry; more wedge and prism type volumes existed in areas of complex curvature. Additional considerations when meshing realistic arterial geometries must taken into account. It is important that the final mesh is sufficiently refined to reproduced the geometric complexity (Prakash and Ethier, 2001), as demonstrated in Figure 3.2

Finally, for all meshing methods considered it is important that the final mesh has a good balance between resolution ie. all essential details of the fluid and mass transport fields are being captured coupled with efficient convergence speed. For this reason mesh dependency tests must be undertaken to determine whether the correct solution has been obtained to a given level of tolerance. Full

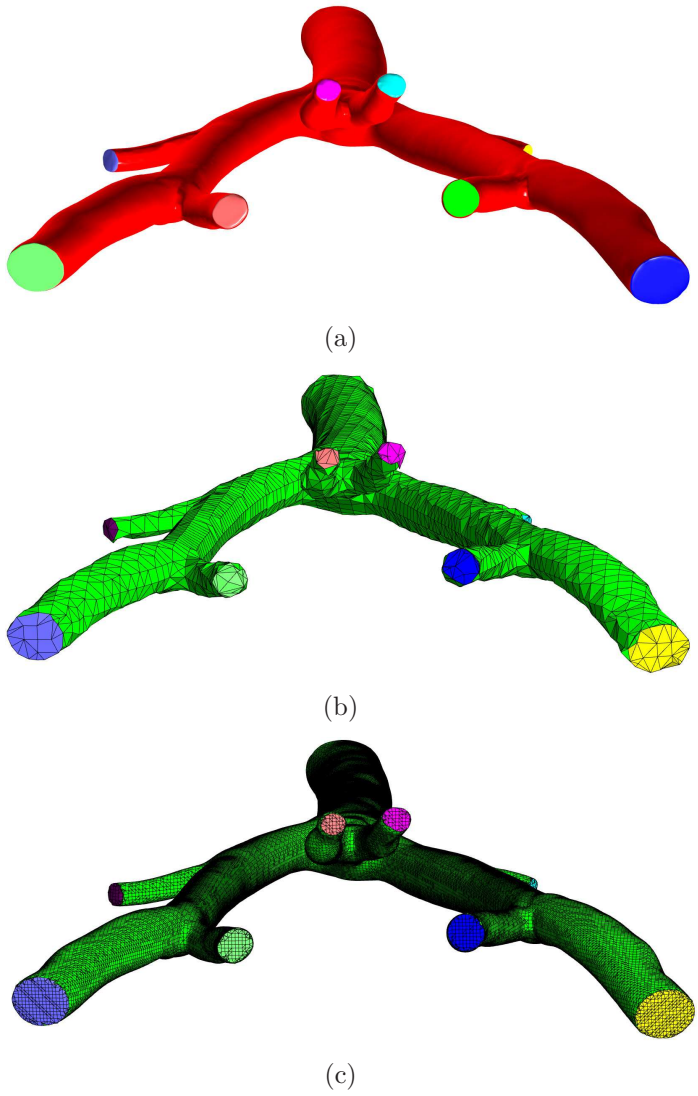

(a)

(b)

(c)

Figure 3.2: Demonstration of mesh refinement required under adaptive cartesian meshing schemes in order to reproduce realistic geometry (a) Geometry (b) Mesh not reproducing geometric complexity (c) Refined mesh.

details of the respective meshes and mesh dependence studies are given in the result chapters of each study.

3.6 Boundary Conditions

Solving partial differential equations requires the use of boundary conditions. The boundary conditions used in the computational models are presented in this section.

At the inlet to the computational domain an inflow condition was used for all simulations, both steady and unsteady. This conditions is a Dirichlet condition where a prescribed velocity is set at the inlet, for the present study this velocity was derived from the Reynolds number.

$$\mathbf{u} = \mathbf{u}_{\text{in}} \tag{3.7}$$

For this condition to be implemented computationally Fluent specifies the mass flow rate at the inlet of the domain, and is represent as follows

$$\rho \mathbf{u}_f \cdot \mathbf{A}_f = \rho u A_f \tag{3.8}$$

Where f represents a given face of the inlet and $\mathbf{A}_f$ represents the face area normal vector pointing into the domain at the inlet. So the velocity at the inlet condition requires the value of u at each face. For the steady state simulations a fully developed Poiseuille profile was defined via a compiled UDF. Using this type of inlet profile is acceptable as previous work by Myers et al. (2001) validated using different inlet profiles, parabolic, 'blunt' or Dean, have little effect on the results downstream, but is dependent on the Reynolds number. Furthermore a study recently by Moyle et al. (2006) concluded that simplification to fully developed flow can be made without penalty. The question arises as to why this profile is used. This is because the length of the computational domain is reduced as the fully developed velocity profile does not need to form, but is still required to be sufficiently upstream away from any disturbances. The UDF was designed to loop over the inlet of the computational domain calculating the radius of the centroid of a given face from the centre of the inlet and prescribing the inlet velocity at that location using the following formula

$$u = U_{\max}(1 - \left(\frac{z}{R}\right)^2) \tag{3.9}$$

here z is the radial coordinate direction, R the radius of the inlet to the vessel, and $U_{\max}$ the maximum velocity across the inlet, which for Poiseuille flow is twice the mean velocity.

For the unsteady flow simulations, the oscillatory component was obtained by Fourier decomposition of a cardiac waveform, such as that shown in Figure 3.3.

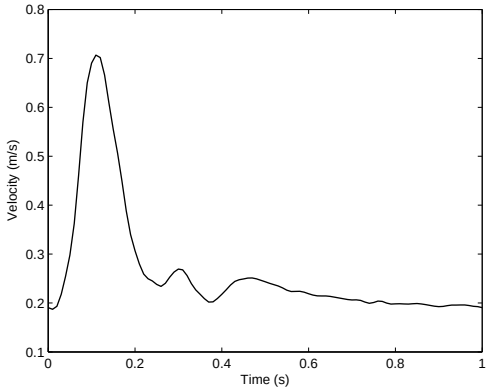

Figure 3.3: Typical carotid artery waveform, from Ku et al. (1985).

The cardiac waveform was first sampled at discrete locations throughout the cycle to produce a discrete waveform. The UDF then calculated the fourier coefficients, these were then used to define the unsteady component ($u(t)$) of the inlet waveform at a given time, t, throughout the cardiac cycle as follows

$$u(t) = \frac{A_0}{2} + \sum_{n}^{N} A_n \cos\left(\frac{2\pi nt}{T}\right) + B_n \sin\left(\frac{2\pi nt}{T}\right), \tag{3.10}$$

here n represents the fourier mode, N the max mode determined by the number of sampling points of the original waveform, and A_n and B_n the Fourier coefficients. Finally, once the unsteady component of the waveform is found, the inlet profile is obtained by superimposing the steady and oscillatory components (Code details given in Appendix E.3). The spatial profile used for the unsteady simulations was in all cases identical to the steady state simulations. This has previously been deemed suitable by Myers et al. (2001), who reported that the changes between inlet profile did not lead to significant changes in WSS distribution. Furthermore, for the trifurcation simulations the inlet profile was flat in order to allow for future comparisons with the previous simulations of Himburg et al. (2004). However this is not to say that there is not an error associated with this simplification, but this was not the focus of the present work. In future, fully developed Womersley solutions could be incorporated or even better

medical imaged *in vivo* measured velocity profiles.

A variety of boundary conditions for the outlet of flow field were utilised: a zero diffusive flux condition (natural), and a pressure outlet condition. For the diffusive condition the following equation was imposed on the outlets of the domain under consideration.

$$\nabla \mathbf{u} \cdot \mathbf{n} = 0 \tag{3.11}$$

where the normal direction on the domain outlet is defined in Figure 3.4. The numerical equivalent of this condition is the diffusive term in equation (B.6) given the value of zero for the cell immediately adjacent to the boundary

$$\Gamma_f (\nabla \mathbf{u})_f \cdot \mathbf{A}_f = 0 \tag{3.12}$$

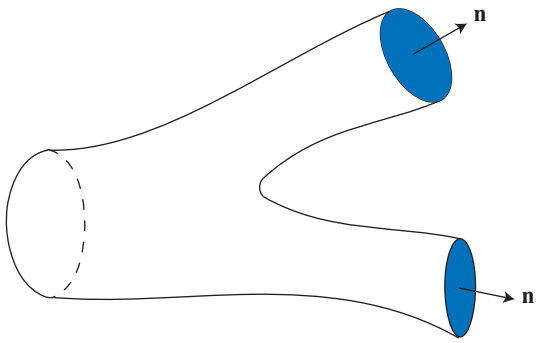

Figure 3.4: Schematic of arterial geometry with the normal coordinate defined in equation (3.11) shown on the outlets.

The placement of an outflow condition is extremely important, as from equation (3.11) the condition assumes that there are no gradients in the streamwise direction. For this reason the boundary condition was placed sufficiently downstream of any flow disturbances to ensure the flow had become fully developed. This boundary condition was utilised in the numerical models presented in Chapters 6 and 7.

The pressure boundary condition was prescribed for simulations in Chapter 8 where the outlet mass flowrates were known. For this condition the pressure at the outlets of the domain under consideration was actually unknown, and a target

mass flow rate was specified. To achieve the desired target, at every iteration the pressure on the boundary is adjusted up or down until the desired flowrate is obtained (For code details see Appendix E.4). The relationship between pressure and mass flow was achieved via Bernoulli's equation

$$dp = \frac{\rho}{2}\frac{\left(\dot{m}^2 - \dot{m_{req}}^2\right)}{(\rho A)^2} \tag{3.13}$$

This provides a known flux that can be directly substituted into the discretised continuity equation.

3.7 Wall Shear stress

Wall shear stress is very important quantity in arterial modelling, due to the cause effect relationship between WSS and atherosclerosis, as mentioned in Chapter 1. Full details of the stress tensor and the derivation of WSS is given in Appendix A, a brief outlined is given below.

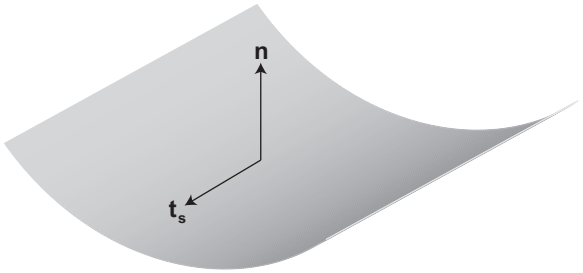

Figure 3.5: Surface element with the traction vector ($\mathbf{t_s}$) and the normal ($\mathbf{n}$) defined.

The tangential vector ($\mathbf{t_s}$) which acts on the surface of the artery wall is defined by the following expression

$$\mathbf{t_s} = \mathbf{T} - (\mathbf{T} \cdot \mathbf{n})\mathbf{n} \tag{3.14}$$

Where $\mathbf{T}$ represents the net traction vector and $\mathbf{n}$ the normal direction. The magnitude of this vector is the WSS magnitude, which from here on in will be denoted τ_w. Due to the nature of the present study being strongly based on WSS

and related phenomena (as is generally true when studying haemodynamics), from a computational prospective accurate representation of WSS is required, numerical differentiation is inherently prone to error and hence it needs to be taken into consideration when designing the computational mesh in the vicinity of the arterial wall.

Oscillatory shear index

An important time dependent WSS index is the oscillatory shear index (OSI). This quantity provides fundamental information about the oscillatory nature of the prevailing haemodynamics. Originally proposed by Ku et al. (1985), and reformulated later more conveniently for 3D geometries by He and Ku (1996). It assesses the variational nature of the WSS vector compared with the time averaged WSS using the following equation

$$\mathrm{OSI} = \frac{1}{2}\left(1 - \frac{\tau_{\mathrm{mean}}}{\tau_{\mathrm{mag}}}\right) \tag{3.15}$$

where the following definitions apply for τ_{mean} and τ_{mag}

$$\begin{aligned} \tau_{\mathrm{mean}} &= \left| \frac{1}{T} \int_0^T \mathbf{t}_s dt \right| \\ \tau_{\mathrm{mag}} &= \frac{1}{T} \int_0^T \tau_w dt \end{aligned} \tag{3.16}$$

From the above definitions, the OSI can vary between 0 and 0.5; where 0 represents unidirectional flow and 0.5 indicating purely oscillatory. There are a number of issues associated with OSI particularly the insensitivity to WSS magnitude.

3.8 Experimental validation of CFD method

Experimental validation of the computational method is relatively difficult and currently is only possible by referring to previous observations in literature. The different geometries investigated in this study include arterial bifurcations and bends. There are a number of experimental bifurcation studies reported in literature (Friedman et al., 1993, Ku et al., 1985, Zarins et al., 1983), mostly concerned with carotid bifurcations. In the paper by Zarins et al. (1983) skewing of the velocity profiles was found to be towards the innerwall and regions of low momentum fluid were associated with the outerwall. This skewing (although a different geometry - symmetric bifurcation rather than carotid type geometry) and region of low momentum fluid was also observed here.

For the bend geometry an experimental study has been performed by Asakura and Karino (1990). They reported the deflection of the fluid towards the outer wall of the bends, the development of secondary peripheral flows and a stand recirculation zone. The previous observations agrees well with flow structures found in this thesis.

Validation of the trifurcation geometry (see Chapter 8) presents a number of difficulties, however it is essentially a combination of bifurcation and bend geometries, so the agreement in more simplified geometries should extend towards this more complex geometry. Furthermore, Perktold et al. (1998) studied numerically with experimental validation a coronary bifurcation with out of plane curvature. They reported vortex rotation, but the division of the artery remain the dominant factor, again this is in agreement with observations reported in this thesis.

Chapter 4

Arterial Mass Transfer Theory and Computation

4.1 Introduction

This chapters outlines the fundamentals of mass transfer, in particular low diffusion coefficient species transport, which are important with respect to arterial mass transport. Firstly the governing theory of mass transfer will be outlined. This will be followed by a mathematical model for the transport of low diffusion coefficient species and in the present case ATP will be developed. Finally a discussion on numerical modelling and complications of the the governing equations for convection dominated mass transport.

4.2 Background

Arterial mass transfer over the past 30 years has been the focus of intense mathematical and more recently computational modelling. Mass transport in arteries was first given attention by Caro et al. (1971), who proposed a relationship between shear dependent mass transfer and atherosclerosis. Their analysis was using the boundary layer equations in unseparated flow regions, leading to the conclusion that minimum mass transfer occurs in regions of low WSS. Further research over the years has also highlighted regions of impaired mass transfer occurring in locations of flow recirculation, which occur commonly in the vascular system at the outer walls of bifurcations and in arterial bends, all of which are subject to low WSS. The precise mechanisms still remain to be fully elucidated

hence arterial mass transfer is an area of intense research.

In the arterial system there are two independent processes which transport material to the arterial wall: convection, and diffusion. Convection (commonly referred to as advection) is transport due to bulk fluid motion, whilst diffusion refers to transport due to random molecular motion that results in a net transport in the direction of negative concentration gradient (the driving potential).

Generally in the human vasculature, the species of interest with regard to the onset of atherogenesis and interaction with the endothelium are of low diffusion coefficient. The transport of low diffusion coefficient species is brought to the artery wall via these convective and diffusive processes described above. In linear sections of the vasculature mass transfer is driven by diffusion ie. process being governed by concentration gradients at the wall, whilst in other sections, such as the outer wall of bifurcations where flow disturbances occur, both convective and diffusive mass transfer is present. These processes above have significant implications, particularly for low molecular weight species such as ATP, when considering availability to the arterial wall (as discussed in Chapter 1). Fully understanding mass transfer processes and characteristics is an essential step to understanding the relationship between haemodynamics and atherogenesis.

4.2.1 Mass transfer Equation

The governing equation mass transfer which describes mathematically the processes mentioned above, commonly referred to as the convection-diffusion equation, is given by the following PDE in differential form (which is convenient for the discussions of this chapter),

$$\frac{\partial \phi}{\partial t} + \mathbf{u} \cdot \nabla \phi = D \nabla^2 \phi \tag{4.1}$$

The first term on the LHS accounts for unsteady mass transfer, the second accounts for convective mass transfer and the RHS represents diffusive mass transfer. For full details regarding the derivation see Appendix C.

4.2.2 Mass transfer Boundary layer

Just like in fluid flow where the 'no slip condition' leads to the formation of a velocity boundary layer, an analogous concentration boundary layer occurs due to concentration differences between a surface and a fluid. The wall normal length scale of the boundary layer varies in the streamwise direction as a result of the prevailing haemodynamic conditions.

Mass transfer processes and atherosclerosis are governed by the form of this concentration boundary layer. Growth of this boundary layer can result in impaired flux of important species that are required by the endothelium. When this occurs the delivery becomes 'fluid phase' limited. A major component of understanding factors involved in atherosclerosis is understanding what affects boundary layer growth as the final surface concentration governed by the relative rates of advection, diffusion and hydrolysis. To fully understand the importance of this and the concentration boundary layer, a discussion of dimensionless numbers is required, which is in the following section.

4.2.3 Important dimensionless numbers in mass transfer

Below some important dimensionless numbers and their implication for the present analysis of ATP transport is considered.

Schmidt Number

The Schmidt number determines the relative thickness of the momentum boundary layer to the mass transfer boundary layer, and is defined as:

$$Sc = \frac{\nu}{D}$$

In arterial mass transfer the species of interest with respect to the pathobiology of the arterial wall are generally of very low diffusion coefficient $\sim 10^{-10}$ m^2/s or smaller. Furthermore, the viscosity of blood is around $3\text{-}4\times10^{-6}$ m^2/s,

hence Sc of $\sim 10^4$. This means the species boundary layer is confined to a very small region immediately above the arterial wall, significantly smaller than the momentum boundary layer.

Peclet

A number closely related to the Schmidt number is the Peclet number, given by

$$Pe = ReSc = \frac{UL}{\nu}\frac{\nu}{D} = \frac{UL}{D}$$

This dimensionless number determines the ratio of convective to diffusive mass transport. For physiological Reynolds numbers (100-1200), the Peclet number is $\sim 10^6$, indicating a very convective dominated transport. Because of this there are a number of numerical considerations that become important in order to obtain a physical solution. These will be discussed in section 4.4.

Damköhler number

The Damköhler number (Da) represents the the ratio of fluid transit time by diffusion to the chemical reaction time (David et al., 2001), and is given by,

$$Da = \frac{kL}{D}$$

where k represents the surface reaction rate. In the present study, the focus is on large arteries (2-11mm) and the transport of ATP, which leads to Da ranging between 14-77; hence the time scale of fluid transport is greater than reaction.

Sherwood number

The Sherwood number (Sh) represents the dimensionless mass transfer coefficient, and is defined as

$$Sh = \frac{hL}{D}$$

where h represents the mass transfer coefficient [m/s].

The ratio of Sh to Da is important in order to understand what is governing final wall concentration (Tarbell, 2003). If Da << Sh then the surface concentration is reaction limited meaning there is sufficient delivery to the arterial wall and the limiting factor is the kinetics of uptake. If Da >> Sh then the surface concentration is depleted due to insufficient delivery to the surface hence the final concentration is fluid phase limited. In the present study, when the flow is fully developed (such as a uniform pipe) the final ATP concentration at the surface is wall limited by hydrolysis kinetics, but in regions of disturbed flow the Sh drops below the Da and hence fluid mechanics plays a central role; these phenomena tend to be in regions that have been implicated in the onset of atherosclerosis.

4.3 Mathematical model of nucleotide concentration at the endothelium

The model presented here outlines a pseudo similarity solution for the steady state concentration of blood borne agonists in 2D geometries. This is done in a similar manner to David (2003) and Plank et al. (2006a). The solution is termed a pseudo similarity solution as it is only an approximation of the true numerical solution, because the upper boundary condition far away from the endothelial surface is not fully satisfied (see Plank et al. (2006a) for full details). This solution allows essential features of mass transport to be studied, such as, convective mass transport over a backwards facing step or a 2D bifurcation. Additionally, the solution has the advantage of being able to compute quickly and effectively the transport of low diffusion coefficient species, without numerically intensive computation. Consider the conservation of species equation (4.1), with the velocity vector $\mathbf{u}=[\tilde{u}, \tilde{v}]$ (where terms with tilde above represent dimensional quantities), and the following choice of non-dimensionless variables and constants:

$$x = \frac{\tilde{x}}{\tilde{L}}, \quad y = \frac{\tilde{y}}{\tilde{L}}, \quad u = \frac{\tilde{u}}{\tilde{U}}, \quad v = \frac{\tilde{v}}{\tilde{U}}, \quad \phi = \frac{\tilde{\phi}}{\tilde{\phi}_\infty},$$
$$\text{Re} = \frac{\tilde{U}\tilde{L}}{\upsilon}, \quad \text{Pe} = \frac{\tilde{U}\tilde{L}}{\tilde{D}} \quad Da = \frac{\tilde{K}\tilde{L}}{\tilde{D}} \tag{4.2}$$

Here L represents the characteristic length scale, U the characteristic velocity, ϕ the concentration of a low diffusion coefficient species, ϕ_∞ the bulk concentration and ρ and υ the density and kinematic viscosity respectively. The following equation is obtained,

$$u\phi_x + v\phi_y = \frac{1}{\text{Pe}}(\phi_{xx} + \phi_{yy}) \tag{4.3}$$

An order of magnitude analysis reveals that $\phi_{xx} << \phi_{yy}$, hence equation (4.3) becomes

$$u\phi_x + v\phi_y = \frac{1}{\text{Pe}}\phi_{yy} \tag{4.4}$$

Here the diffusion coefficients of the species is assumed to be low, so the Peclet number, Pe is correspondingly high. For physiological Reynolds numbers this leads to the mass transfer layer being much smaller than the momentum boundary layer. So the velocity distribution in the normal direction can be assumed to be linear inside the mass transfer layer.

It can be shown with the use of appropriate stream functions (David et al., 2001), that a pseudo similarity solution exists (David, 2003, Plank et al., 2006a). Following on from Figure 4.1, the wall shear stress can be defined by a linear function

$$\tilde{\tau}_w = \mu\frac{\tilde{u}}{\tilde{y}} \tag{4.5}$$

In David et al. (2001), a 'friction' velocity ($\tilde{\gamma}$) was defined by

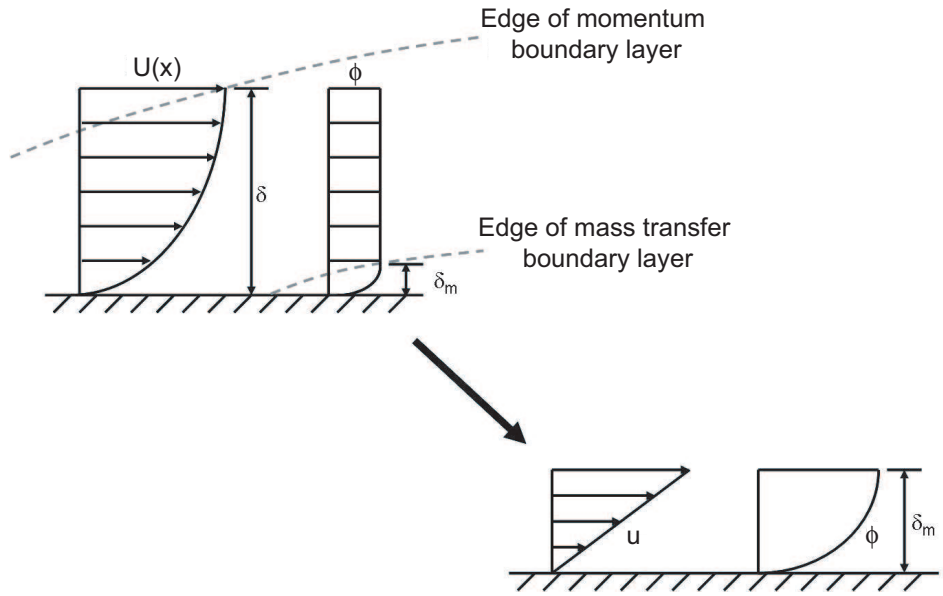

Figure 4.1: Relative thickness of momentum and mass transfer boundary layers for large Peclet number, leading to the velocity distribution being linear in the mass transfer layer.

$$\tilde{\gamma} = \left(\frac{\tilde{\tau}_w}{\rho}\right)^{1/2} \tag{4.6}$$

where the wall shear stress function is known *a priori*. Introducing the following stream function

$$\tilde{\psi} = \frac{1}{2}\frac{\tilde{\gamma}^2}{\nu}\tilde{y}^2 \tag{4.7}$$

following non-dimensionalisation of the wall shear stress by ρU_∞^2 the velocity components can be written as

$$\begin{aligned} u &= \psi_y = \gamma^2 y Re \\ v &= -\psi_x = -\frac{y^2}{2\nu}\frac{d\gamma^2}{dx} Re \end{aligned} \tag{4.8}$$

Substituting this into equation (4.4), we obtain

$$\gamma^2 yRe\phi_x + -\frac{y^2}{2\nu}\frac{\gamma^2}{dx}Re\phi_y = \frac{1}{\mathrm{Pe}}\phi_{yy} \tag{4.9}$$

Now using a von Mises transformation (Schlichting and Gersten, 1999), with new variables defined by

$$\xi = x \qquad \zeta = \gamma yRe \tag{4.10}$$

each partial derivative in equation (4.9) is therefore

$$\begin{aligned} \phi_x &= \phi_\xi \xi_x + \phi_\zeta \zeta_x = \phi_\xi + \phi_\zeta \gamma_x yRe \\ \phi_y &= \phi_\xi \xi_y + \phi_\zeta \zeta_y = \phi_\zeta \gamma Re \\ \phi_{yy} &= \phi_{y\zeta}\zeta_y = \phi_{\zeta\zeta}\gamma^2 Re^2 \end{aligned} \tag{4.11}$$

On substitution of these terms, the following is obtained

$$\frac{\zeta}{\gamma}\phi_\xi = \frac{Re^2}{Pe}\phi_{\zeta\zeta} \tag{4.12}$$

Now we introduce the following transformations

$$\begin{aligned} \sigma &= \zeta\left(\frac{Pe}{Re^2}\right)^{1/3} \\ \chi &= \int_{\xi_0}^{\xi} \gamma d\xi \end{aligned} \tag{4.13}$$

The former is chosen to eliminate the Re^2/Pe term in equation (4.12) and

this leads to the following PDE

$$\sigma\phi_{\chi} = \phi_{\sigma\sigma} \tag{4.14}$$

Now the following similarity variable is defined

$$\eta = \frac{\sigma}{(9\chi)^{1/3}} \tag{4.15}$$

This reduces the partial differential equation (4.14) to an ordinary differential equation (ODE) via the following method

$$\phi_{\chi} = \phi_{\eta}\eta_{\xi} = -\phi_{\eta}\frac{\eta}{3\chi} \tag{4.16}$$

and

$$\phi_{\sigma} = \phi_{\eta}\eta_{\sigma} = \phi_{\eta\eta}\frac{1}{(9\chi)^{2/3}} \tag{4.17}$$

Substituting these previous two expressions into equation (4.14), the following ODE is obtained

$$\lambda\frac{\mathrm{d}^2\phi}{\mathrm{d}\eta^2} + 3\eta^2\frac{\mathrm{d}\phi}{\mathrm{d}\eta} = 0, \tag{4.18}$$

with the η defined in terms of the initial variables as

$$\eta = \frac{(\mathrm{RePe})^{1/3}|\tau(\mathrm{x})|^{1/2}}{(9\int_{\mathrm{o}}^{\mathrm{x}}|\tau(\gamma)|^{1/2})^{1/3}}\mathrm{y} = \beta(\mathrm{x})\mathrm{y} \tag{4.19}$$

This fully characterises the concentration of nucleotide at the endothelium on the wall shear stress. The wall shear stress may be chosen to be any 'well behaved' continuous function, such as for plane flow; hence providing key understanding into the parameters that control transport of dilute chemical species to the arterial wall.

At this point the derivation is for arbitrary low diffusion coefficient species and for ATP we introduce some physiological boundary conditions. At y=0 a reactive boundary condition is imposed to model surface hydrolysis and production

$$\tilde{D}\frac{\partial\tilde{\phi}}{\partial\tilde{y}}\bigg|_{y=0} = \tilde{K}\tilde{\phi} - \tilde{S}. \tag{4.20}$$

This boundary condition represents a conservation of mass statement, where the flux of ATP by diffusion ($\tilde{y}$ representing the surface normal coordinate) to the endothelium is balanced by ATP hydrolysis and release. The hydrolysis of ATP at the endothelial surface takes place via Michaelis–Menten kinetics, but previous studies (David, 2003, John and Barakat, 2001) have shown that rate saturation effects only occur at high ATP concentration (> 100 μM), so the first-order term used in equation (4.23), where K_{ATP} represents the dimensionless rate of uptake of ATP, is a very accurate approximation. The release of ATP has been observed by a number of groups experimentally (Bodin and Burnstock, 2001, Yamamoto et al., 2003). Previous work (John and Barakat, 2001), modelled ATP release using a sigmoidal function for the rate (S) of ATP release. A similar model is utilised here, given by,

$$\tilde{S}_{\mathrm{ATP}} = S_{\max}\left[1 - \exp\left(\frac{-\tau_w(x)}{\tau_0}\right)\right]^3. \tag{4.21}$$

Here τ_0 represents the characteristic WSS and governs how the maximum ATP release rate is obtained. Two different release rates were considered in order to simulate the conditions of both slow and rapid release. $S_{\max}$, represents the maximum ATP release rate and has a value of 10^{-6} μMms^{-1}.

Following introduction of the dimensionless variables

$$K_{\mathrm{ATP}} = \frac{\tilde{K}_{\mathrm{ATP}}\tilde{L}}{\tilde{D}_{\mathrm{ATP}}} \quad \text{and} \quad S_{\mathrm{ATP}} = \frac{\tilde{S}_{\mathrm{ATP}}\tilde{L}}{\tilde{\phi_\infty}\tilde{D}_{\mathrm{ATP}}} \tag{4.22}$$

for the hydrolysis of ATP (ϕ_{ATP}) to ADP (ϕ_{ADP}) and production the following

dimensionless condition is obtained at the artery wall:

$$\left.\frac{\partial \phi_{\mathrm{ATP}}}{\partial y}\right|_{y=0} = K_{\mathrm{ATP}}\phi_{\mathrm{ATP}} - S_{\mathrm{ATP}}. \tag{4.23}$$

Similarly for ADP, the uptake term represents hydrolysis of ADP to AMP and the production term that accounts ATP derived ADP, given by,

$$\tilde{S}_{\mathrm{ADP}} = \tilde{K}_{\mathrm{ATP}}\tilde{\phi}_{\mathrm{ATP}}$$

Again, introducing dimensionless variables

$$K_{\mathrm{ADP}} = \frac{\tilde{K}_{\mathrm{ADP}}\tilde{L}}{\lambda \tilde{D}_{\mathrm{ATP}}}, \quad S_{\mathrm{ADP}} = \frac{\tilde{S}_{\mathrm{ADP}}\tilde{L}}{\tilde{\phi_{\infty}}\lambda \tilde{D}_{\mathrm{ATP}}} \quad \text{and} \quad \lambda = \frac{\tilde{D}_{\mathrm{ADP}}}{\tilde{D}_{\mathrm{ATP}}} \tag{4.24}$$

the boundary condition becomes

$$\left.\frac{\partial \phi_{\mathrm{ADP}}}{\partial y}\right|_{y=0} = K_{\mathrm{ADP}}\phi_{\mathrm{ADP}} - \frac{K_{\mathrm{ATP}}\phi_{\mathrm{ATP}}}{\lambda}, \tag{4.25}$$

Far away from the endothelial surface, providing sufficiently large Pe, the upper and lower boundary conditions do not interact, hence the concentration can be assumed to be that of the bulk fluid species concentration:

$$\mathrm{y} \to \infty; \quad \phi(\mathrm{y}) \to 1; \tag{4.26}$$

The solution of this ODE (4.18) satisfies

$$\phi(\eta) = A \int_0^{\eta} e^{-\gamma^3} d\gamma + \phi(x, 0) \tag{4.27}$$

with the boundary condition (4.23) at the endothelium ($\eta = 0$) meaning

$$A = \frac{1}{\beta(x)} \left(K_{\mathrm{ATP}} \phi_{\mathrm{ATP}}(x,0) - S \right) \tag{4.28}$$

If we impose the far away boundary condition (4.26), the following is obtained

$$\text{as} \quad \eta \to \infty; \quad \int_0^{\eta} e^{-\gamma^3} d\gamma = \int_0^{\infty} e^{-t} t^{-2/3} dt = \frac{\Gamma}{3},$$

which is an incomplete gamma function (Abramowitz and Stegun, 1965), thus the endothelial concentration is evaluated as

$$\phi_{\mathrm{ATP}}(x,0) = \frac{\beta(x) + IS}{\beta(x) + IK_{\mathrm{ATP}}} \tag{4.29}$$

where I is the incomplete gamma function I= $\Gamma/3$. Similarly for ADP, using boundary condition (4.25) and equation (4.27) leads to,

$$A_2 = \frac{1}{\beta(x)} \left(k_{ADP} \phi_{ADP} - \frac{K_{ATP} \phi_{ATP}}{\lambda} \right) \tag{4.30}$$

which on substitution into equation (4.27) and assuming that far away from the endothelium the concentration of ADP is zero leads to,

$$\phi_{\mathrm{ADP}}(x,0) = \frac{IK_{\mathrm{ATP}} \phi_{\mathrm{ATP}}}{\lambda(\beta(x) + IK_{\mathrm{ADP}})} \tag{4.31}$$

and finally substitution of equation (4.29) in the above results in

$$\phi_{\mathrm{ADP}}(x,0) = \frac{IK_{\mathrm{ATP}}(\beta(x) + IS)}{\lambda(\beta(x) + IK_{\mathrm{ADP}})(\beta(x) + IK_{\mathrm{ATP}})} \tag{4.32}$$

4.4 Computational convective dominated mass transfer

The numerical solution of the species convection-diffusion (equation (4.1)) is outlined in Appendix B, where the finite volume method is derived for the transport of arbitrary scalar ϕ. In the present study ϕ represents ATP.

4.4.1 Numerical issues

Modelling low diffusion coefficient species numerically presents a number of difficulties due to the convective dominant nature of the transport. The convection-diffusion equation by nature is mathematically challenging to solve due to the hyperbolic-parabolic nature of the equation. Referring back to equation (4.1), by assuming steady state and introducing the following set of dimensionless variables

$$\mathbf{x} = \frac{\tilde{\mathbf{x}}}{\tilde{L}}, \quad \mathbf{u} = \frac{\tilde{\mathbf{u}}}{\tilde{U}}, \quad \phi = \frac{\tilde{\phi}}{\tilde{\phi}_\infty}, \quad \mathrm{Pe} = \frac{\tilde{U}\tilde{L}}{\tilde{D}}$$

equation (4.1) becomes

$$\mathbf{u} \cdot \nabla\phi - \frac{1}{\mathrm{Pe}}\nabla^2\phi = 0 \tag{4.33}$$

Due to the large Peclet number, the hyperbolic (convective) term ($\mathbf{u} \cdot \nabla\phi$) dominates equation (4.33), leading to some numerical difficulties. Upwinding schemes inherently add numerical diffusion to the flow field (Versteeg and Malalasekera, 1995), which scales with order of the scheme ie. the first order schemes has error term $\mathcal{O}(\Delta x)$. The first order schemes are a highly tempting option numerically due to their highly stable nature, but this stability is actually brought about by the introduction of a second order diffusive term (particularly in flows that are not aligned with the grid); this leads to the 'smearing' of the final solution. In highly convective transport, this phenomenon affects the entire solution domain with numerical inaccuracies, bringing about a non-physical solution. Furthermore, the solution is likely to be over diffusive, meaning more mass is trans-

ported to the surface than would actually occur in the physical process; this has been demonstrated extensively in previous literature (Versteeg and Malalasekera, 1995)

One way to reduce the effects of numerical diffusion is to introduce a higher order scheme for the convective term and in the present study second and third order (MUSCL) convective schemes were utilised. The MUSCL scheme limits the effects of spatial oscillations (due to the possibility of negative coefficients in the descritised equations) observed in higher order schemes by limiting cell gradients, therefore ensuring monotonicity. The accuracy of schemes were verified by computing the steady convection of an arbitrary scalar ϕ with velocity field known *a priori*, and given by $\mathbf{u} = u\mathbf{i} + v\mathbf{j}$ where $u = v$. The example grid and associated boundary conditions for scalar ϕ is demonstrated in Figure 4.2.

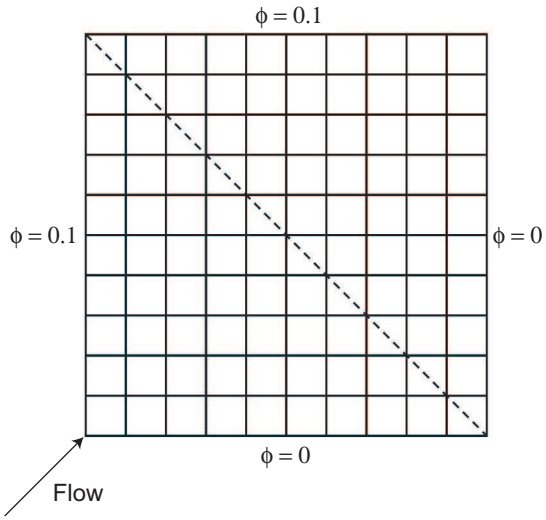

Figure 4.2: Computational domain for assessment of mass transport convection schemes.

To assess the differences between the schemes, the final solution was plotted along the dashed diagonal line in Figure 4.2. In Figure 4.3 the differences between the first and third order schemes is evident; the first order scheme remains over diffusive even in the advent of spatial mesh refinement, whereas the third order scheme becomes very accurate after mesh refinement differing by only 1.6% at the extremities. To a certain degree extremely fine grids will abate the effects of numerical diffusion, due to the truncation error of the discretisation scheme scaling with the spatial mesh resolution, but ultimately higher order schemes are required.

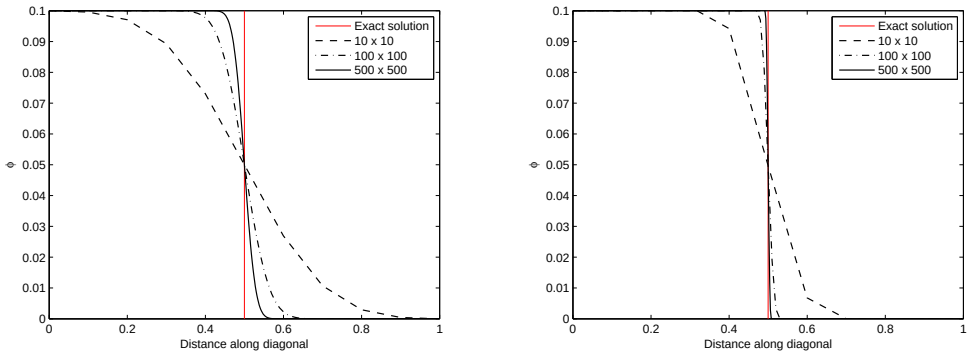

(a) (b)

Figure 4.3: Upwinding scheme assessment over a range of mesh refinement levels (a) first order upwinding (b) MUSCL third order upwinding. Clearly the third order scheme coupled with appropriate spatial mesh resolution is a good approximation to the exact.

The large Peclet number means the mass transfer boundary layer is confined to a very small layer in the immediate vicinity of the wall. Hence very refined meshes in the immediate vicinity of the wall (generally around 1-5μm immediate off wall grid spacing) are also required to fully capture steep mass transfer gradients. This leads to very high aspect ratio cells required to keep the mesh within practical limits from a computational prospective. These type of cells are expected to fully capture the solution due to gradients in the streamwise direction being considerably smaller. Figure 4.4 demonstrates a typical mesh cross section and zoomed in boundary layer section (with off wall grid spacing) that is required to fully capture the steep concentration gradients mentioned above.

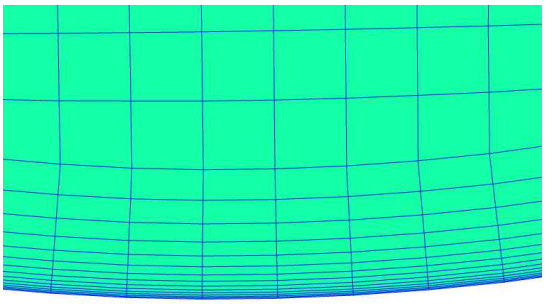

Figure 4.4: Slice of a typical computational mesh, zoomed in on the region of fine off wall grid spacing required to capture steep species gradients.

In time dependent (pulsatile) simulations, transients in species computation persist for multiple cardiac cycles, therefore it is important that the simulation is checked for cycle independent. Cycle independence was obtained in around four

cycles for 2D simulations and eight cycles for 3D. The latter coupled with the large mesh sizes required to capture steep species gradients means the computation is intensive, hence the requirement of parallel model implementation mentioned in Chapter 3.

4.4.2 Boundary Conditions

Consider the domain (Ω) illustrated in Figure 4.5, where Γ_1 and Γ_2 are respectively the upstream and downstream section in which flow enters and leaves Ω. Γ_w represents the boundary walls of the vessel.

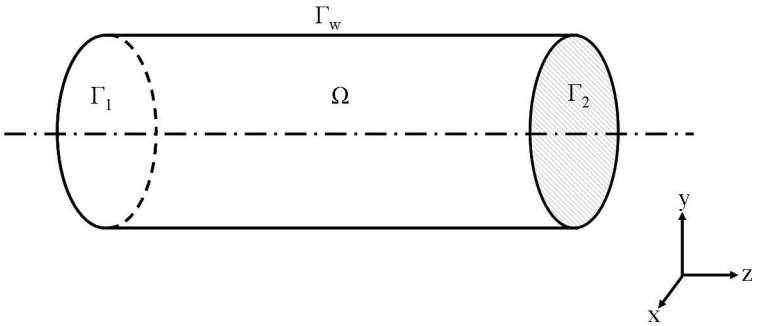

Figure 4.5: Schematic of domain Ω with associated boundary surfaces.

For the solution of the concentration field there are three conditions to be prescribed on boundary surfaces, Γ_1, Γ_2, and Γ_w.

Inlet

At the inlet to the domain a uniform concentration (Dirichlet condition) is prescribed across the entire cross section.

$$\phi = \phi_0 \quad \text{on} \quad \Gamma_1$$

The domain of the geometry always extended significantly up stream from the areas of interest, such as bifurcating arteries, in order to allow for the natural development of the mass transfer boundary layer. This currently is the most

physiological inlet condition for mass transfer, as the profile is unknown *in vivo* and currently is impossible to measure (Ethier, 2002). The numerical implementation of this condition is equivalent to that described for velocity in Chapter 3.

Outlet

A zero diffusion flux boundary condition (Neumann) is prescribed at the outlet,

$$\nabla\phi \cdot \mathbf{n} = 0 \quad \text{on} \quad \Gamma_2$$

This boundary condition is particularly well suited to low diffusion coefficient species transport and has no effect on the upstream solution (Fluent user manual, 2005).

Endothelium

The reactive surface conditions in the CFD model (equations (4.23) and (2.2)) were implemented numerically through a UDF (code details given in Appendix E.2). The reaction condition requires that the flux to the surface is balanced by production consumption at the surface, and is given in the following form,

$$D\nabla\phi \cdot \mathbf{n} = K\phi \quad \text{on} \quad \Gamma_w \tag{4.34}$$

where K defines the surface reaction rate for hydrolysis of reactant (A) to product (B).

$$A \xrightarrow{K} B$$

For the present study, if we consider as an example ADP, there are two equations that govern surface concentration; production from ATP and hydrolysis

to AMP. Production is defined by

$$\text{ATP} \xrightarrow{K_{ATP}} \text{ADP}$$

and the UDF implementation is

$$D\nabla\phi_{ATP} \cdot \mathbf{n} = K_{ATP}\phi_{ATP} \tag{4.35}$$

The hydrolysis reaction is defined by

$$\text{ADP} \xrightarrow{K_{ADP}} \text{AMP}$$

$$D\nabla\phi_{ADP} \cdot \mathbf{n} = K_{ADP}\phi_{ADP} \tag{4.36}$$

4.4.3 Validation of Numerical code

In order to validate using the Fluent code for advection dominated transport, a comparison test was conducted with the well known Graetz-Nusselt (for large Schmidt number) solution for developing mass transfer boundary layer in an axisymmetric pipe (Bird et al., 1960). This is an important step as few reports in literature use the Fluent code for this type of transport. Figure 4.6 shows a schematic of this problem with associated boundary conditions.

This solution reduces the governing PDE (equation (4.1)), on the assumption of axisymmetric, steady state and fully developed flow with linear velocity distribution within the mass transfer boundary layer, to an ODE via a similarity solution. The Sherwood number derived from this solution is given by

$$Sh(z) = 2\frac{\partial\phi}{\partial y} = 2\frac{(Pe\ d/z)^{\frac{1}{3}}}{9^{\frac{1}{3}}\Gamma(4/3)} \tag{4.37}$$

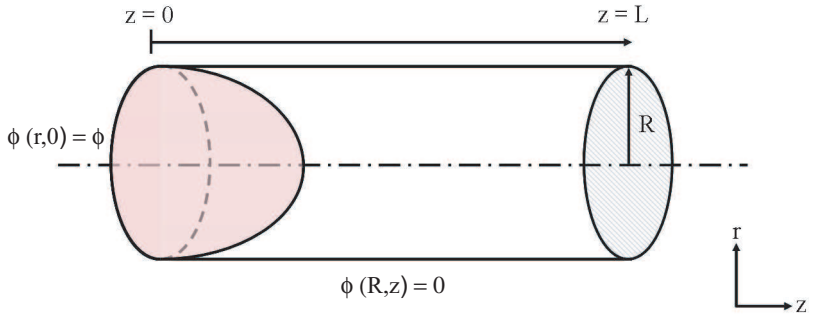

Figure 4.6: Schematic of axisymmetric tube and associated boundary conditions for species (ϕ).

where d is the tube diameter and Γ is and incomplete gamma function. The above analytical expression can then be compared with the numerical solution for the equivalent Peclet number (validation Peclet number is 8.3×10^6). For the numerical model the inlet diameter (d) was 3mm and the domain extended 17D in the streamwise direction. The boundary layer consisted of an off wall spacing of 2.5 μm progressively growing over 15 layers to a total depth of 180 μm. For the numerical scheme the Sherwood number is defined as

$$Sh = 2\nabla\phi \cdot \mathbf{n} \tag{4.38}$$

where $\nabla\phi$ represents the dimensionless concentration gradient and $\mathbf{n}$ the unit normal vector pointing into the domain.

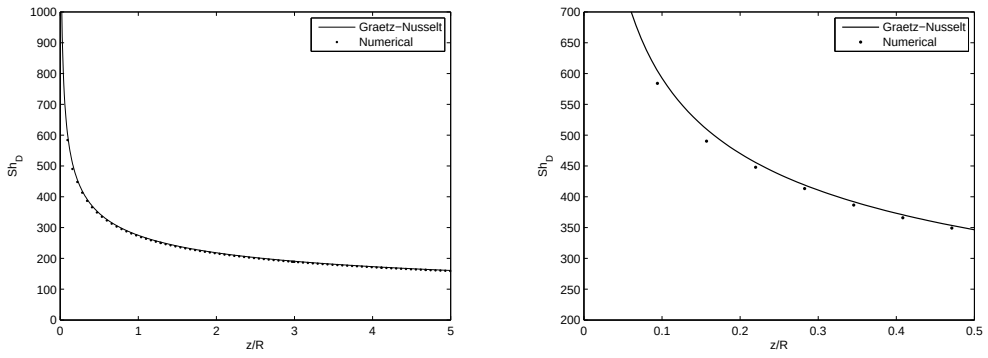

(a) (b)

Figure 4.7: (a) Comparison of numerical developing mass transfer in a pipe with the well known Graetz-Nusselt solution. (b) Comparison in close proximity of the inlet to the domain, where the gradients become very large due to the reduced boundary layer thickness.

It is evident from Figure 4.7(a) that the numerical code is fully capable of capturing steep species gradients adjacent to the wall. The importance of streamwise spacing is evidenced by zooming into the the inlet region (Figure 4.7(b)), where gradients become very large due to the singularity condition when $z/R \rightarrow 0$.

4.4.4 Steady State Assumption

A major simplifying assumption for a fair proportion of the work considered in this study involved simulations under steady state conditions, hence neglecting the effects of flow pulsatility on mass transfer. Previous work by Rappitsch and Perktold (1995) investigated pulsatile flow for low diffusion coefficient species and it was found that the difference between the time averaged concentrations was only moderate, but essential features were captured by the steady state. Another study by Qiu and Tarbell (1999) also found reasonably similar characteristics between time averaged and steady. For ATP, the effects of flow pulsatility have been observed under a basic sinusoidal waveform and little difference was found between the steady and time averaged. However, due to the reports being in more simplified geometries, a study into the effects of flow pulsatility on arterial mass transfer is considered in all result Chapters (6, 7 and 8). One of the major motivations for steady state is it is computationally more efficient and the time scale of the underlying cell dynamics in response to agonist binding is significantly greater than the cardiac cycle (see Chapter 5).

Chapter 5

Mathematical Model of Endothelial Cell Signalling: An integrated fluid mechanics cell model

5.1 Introduction

This chapter outlines a mathematical model of Ca^{2+} and eNOS cell dynamics within endothelial cells that is linked to the prevailing haemodynamic and mass transfer environment. It is based around a set of ordinary differential equations. Also discussed is the procedure for implementing this mathematical model numerically into the CFD code, thus providing a link between underlying cellular dynamics and the prevailing haemodynamics/mass transfer in complex arterial geometries. The results from this model linked to physiologically realistic geometries will be presented in Chapters 7 and 8.

5.2 Cell Processes

The model presented in this section is a mathematical model developed by Plank et al. (2006b) and was adapted from the original models of Wiesner et al (1996, 1997). The model provides a link between the haemodynamic environment, arterial mass transfer and underlying cell dynamics. The key processes incorporated into the model are represented in Figure 5.1. A summary of key processes are as follows:

1. ATP is transported to the surface of the endothelium by the flowing blood

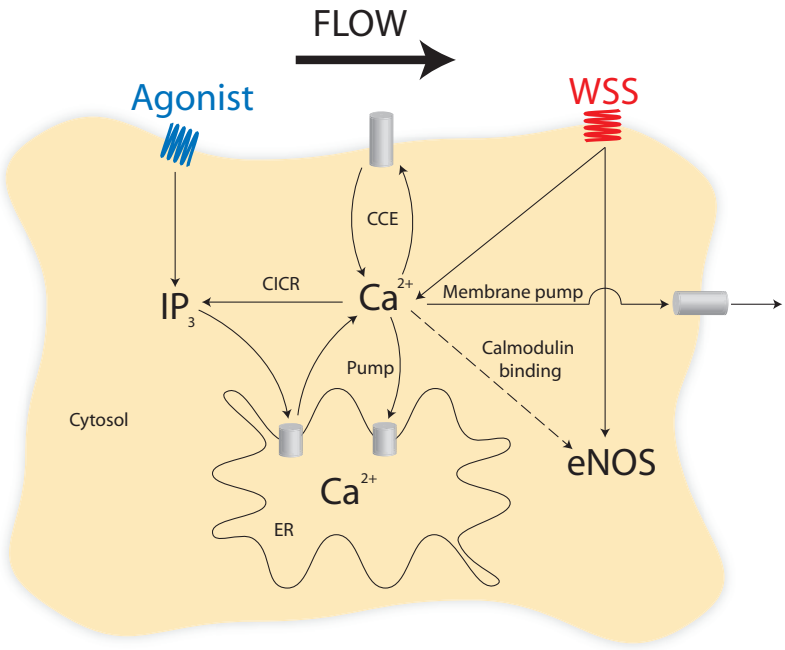

Figure 5.1: Summary of processes included in the endothelial cell model. ATP and WSS provide an external stimulus that initiates responses within the cell leading to the production of the dependent variables, IP_3, Ca^{2+} and eNOS.

undergoing a dephosphorylation at the endothelium to form ADP (as discussed in chapter 1); these agonists then bind to P_{2Y} G-protein coupled receptors that line the surface of the artery wall. The binding of this ligand to the cell surface receptor initiates a signal transduction cascade, which is a series of sequential events resulting in the formation of IP_3 within the cytosol of the cell.

2. Once IP_3 is formed within the cytosol it binds to specific receptors on the endoplasmic reticulum (ER). This binding activates Ca^{2+} release channels leading to an ionic flux of Ca^{2+} out of the ER into the cytosol.

3. Raising cytosolic Ca^{2+} levels initiates a number of different mechanisms, as discussed in Chapter 1. The processes that this model accounts for include: Ca^{2+} induced Ca^{2+} release (CICR), which is the positive feedback mechanism between Ca^{2+} and IP_3 production; capacitive Ca^{2+} entry (CCE), which is influx of Ca^{2+} into the intracellular environment due to depleted ER Ca^{2+} levels.

4. WSS from the prevailing haemodynamic environment directly signals underlying Ca^{2+} responses via shear gated ion channels.

5. The plasma membrane and the ER express a number of transmembrane AT-

Pase, including Ca^{2+}-ATPase, which is responsible for transporting Ca^{2+} from the cytosol back into the ER and across the plasma membrane. The plasma membrane also expresses Ca^{2+}/Na^{+}-ATPase which also transports Ca^{2+} out of the cell.

6. eNOS concentration comes about from two independent, but not mutually exclusive mechanisms. First there is a pathway related to the above mentioned Ca^{2+} cell processes, where free Ca^{2+} in the cytosol binds with Calmodulin (a Ca^{2+} binding protein). This results in the dissociation of eNOS from calveolin in the caveolae thus activating the enzyme (Davignon and Ganz, 2004). Secondly, there is a reported Ca^{2+} independent mechanism where WSS directly gates the activity of eNOS via phosphorylation Akt dependent pathways. This is becoming increasingly identifiable as the prominent pathway.

5.3 Cell dynamics Model

The intracellular Ca^{2+} and eNOS dynamics of endothelial cells were modelled using a set of ordinary differential equations outlined below. The model describes the rate of change of four dependent variables: IP_3 (i), cytosolic free Ca^{2+} (C_c), stored Ca^{2+} (C_s) and activated eNOS (n). The dynamics of these quantities are affected by the local surface values of the shear stress (τ_w) and ATP +ADP concentration (ϕ). The meaning of the symbols and their values are given in Table 5.1.

For the binding of an agonist, a ligand receptor reaction mechanism is used. Agonist (A) reversibly binds to an unoccupied cell surface receptor (R) forming a ligand receptor complex (AR). This then decomposes into modified receptor, R' (which is subsequently recycled back to the surface to form an unoccupied receptor) and n molecules of IP_3, I (the formation of IP_3 represents a multi step process known as a signal transduction cascade). Previously there have been models that explicitly model the dynamics of this G-protein signal transduction cascade (Mahama and Linderman, 1994), but this is simplified here, by including a multi step approximation, in order to reduce complexities.

$$A + R \underset{k_s}{\overset{k_r}{\rightleftharpoons}} AR \xrightarrow{k_d} R' + nI$$

This reaction can be represented via Michaelis-Menten kinetics

$$\frac{\mathrm{d}}{\mathrm{d}t}[I](t) = \frac{k_1[A](t)}{K_c + [A](t)} \tag{5.1}$$

For IP_3 we use an equation describing production and natural decay (μ_1). It is assumed that the production rate (k_1) is an increasing function of the cytosolic Ca^{2+} level and the combined the combined ATP+ADP (ϕ) concentration, hence the following ODE for IP_3 production is thus obtained.

$$\frac{\mathrm{d}i}{\mathrm{d}t} = k_1 \frac{\phi}{K_c + \phi} \frac{C_c}{K_1 + C_c} - \mu_1 i \tag{5.2}$$

Equations (5.3) represents the cellular ionic flux between the cytosol, ER and across the plasma membrane. The transfer of Ca^{2+} is governed by four fluxes representing: Ca^{2+} release from internal stores into the cytosol (q_{rel}); Ca^{2+} resequestration by the internal stores (q_{res}); Ca^{2+} influx (q_{in}); Ca^{2+} efflux (q_{out}).

$$\frac{\mathrm{d}C_c}{\mathrm{d}t} = q_{\mathrm{rel}} - q_{\mathrm{res}} + q_{\mathrm{in}} - q_{\mathrm{out}} \tag{5.3}$$

Equation (5.4) mirrors the relevant terms in equation (5.3) for Ca^{2+} exchange between the cytosol and the ER. V_r represents the volume ratio between the ER and the cytosol, in order to enforce conservation of mass,

$$\frac{\mathrm{d}C_s}{\mathrm{d}t} = -V_r(q_{\mathrm{rel}} - q_{\mathrm{res}}) \tag{5.4}$$

Following the model developed by Meyer and Stryer (1988) the release of Ca^{2+} from the endoplasmic reticulum is saturably dependent on IP_3 with a cubic exponent, where the cubic comes about because of three IP_3 molecules required to bind to the ER surface receptor (determined by experiment in rat basophilic

leukemia), and this opens the ion channel allowing the natural exchange of Ca^{2+}. It is also linearly dependent on C_s.

$$q_{\text{rel}} = k_{\text{rel}} \left(\frac{i}{K_2 + i} \right)^3 C_s, \tag{5.5}$$

The ER resequesters Ca^{2+} from the cytosol back into the ER. This resequestration model is said to be satuarably dependent on the C_c level with a squared relationship reflecting that two Ca^{2+} ions can be transported into the ER per cycle by Ca^{2+}-ATPase.

$$q_{\text{res}} = k_{\text{res}} \left(\frac{C_c}{K_3 + C_c} \right)^2, \tag{5.6}$$

An influx of extracellular Ca^{2+} occurs directly via CCE and WSS. For CCE, the influx is proportional to depletion of Ca^{2+} in the ER below its resting level ($C_{s,0}$) and also due to the difference between the bulk Ca^{2+} concentration in the blood stream (C_{ex}), which is significantly larger than intracellular levels, therefore is taken to be constant. WSS directly gates cytosolic Ca^{2+} via a strain energy density function.

$$q_{\text{in}} = \frac{k_{\text{CCE}}}{K_4 + n}(C_{s,0} - C_s)(C_{\text{ex}} - C_c) + \gamma q_{\max} F(\tau_w), \tag{5.7}$$

The term $F(\tau_w)$ represents Ca^{2+} influx due to shear stress activated channels (a mechanotransduction mechanism as discussed in Chapter 1). The load induced by the applied WSS is distributed between the membrane and the underlying cellular structure. Membrane deformation by shear stress induces a strain energy density. The proportion of channels in the open state depends upon this strain energy density, and is given by

$$F(\tau_w) = \frac{1}{1 + \alpha \exp(-W(\tau_w))} \tag{5.8}$$

where α represents the probability that an ion channel is in its open state.

Additionally, it is assumed that the shear in the membrane is a uniaxial tension field in the flow direction. From this assumption the following relationship can be derived

$$W(\tau_w) = \frac{f_e(\varepsilon\tau_w l + \sqrt{16\delta^2 + \varepsilon^2\tau_w^2 l^2} - 4\delta)^2}{8kT_e N(\varepsilon\tau_w l + \sqrt{16\delta^2 + \varepsilon^2\tau_w^2 l^2})}. \tag{5.9}$$

where f_e represents the fraction of strain energy stored in the plasma membrane that gates shear sensitive Ca^{2+} channels, δ is the membrane shear modulus, T is the temperature, N is the ion channel density per unit area and k is the Boltzmann constant. A major assumption of the above shear stress related ion channel activation is a steady state stress field, but this is seen as a valid assumption due to the time scale of Ca^{2+} dynamics being considerably greater than a cardiac cycle. For the present model this is simplified down in order to reduce complexity and reproduce essential dynamics to

$$W(\tau_w) = W_0 \frac{(\tau_w + \sqrt{16\delta^2 + \tau_w^2} - 4\delta)^2}{\tau_w + \sqrt{16\delta^2 + \tau_w^2}}. \tag{5.10}$$

For full details of the above simplification see (Plank et al., 2006c).

The efflux of Ca^{2+} out of the plasma membrane occurs via Michaelis-Menten kinetics and is an approximation to the Hill function given by Valant et al. (1992). Here it is given as,

$$q_{\text{out}} = \frac{k_{\text{out}} C_c}{K_5 + C_c}, \tag{5.11}$$

Finally, the activation of eNOS is both Ca^{2+} dependent and Ca^{2+} independent. For the dependent mechanism, the activation of eNOS is saturably dependent on the cytosolic Ca^{2+} level, reflecting binding of Ca^{2+} to calmodulin. The independent mechanism is a new addition to the model of Plank et al. (2006b) and is regarded as a very important pathway. Very little data exists regarding the manner of the response, but the results of an *in vivo* experiment by Cheng et al. (2005) suggest a sigmoidal relationship between WSS and eNOS expres-

sion, therefore for the present model a sigmoidal relationship has been chosen for the activation of eNOS. The basic function form of the sigmoidal relationship is equivalent to that given for Ca^{2+} activation in equation (5.7).

$$\frac{\mathrm{d}n}{\mathrm{d}t} = \frac{k_{\mathrm{dis}} C_c}{K_6 + C_c} - \mu_2 n + (1-\gamma) g_{\max} F(\tau_w). \tag{5.12}$$

The first term on the RHS represents eNOS activation of eNOS by cytosolic Ca^{2+} (formation of Ca^{2+}-calmodulin complex) at a maximum rate (k_{dis}). The second term represents deactivation (due to reassociation with caveolin) at constant rate μ_2. The final term is the activation of eNOS directly via WSS. The relative contribution of the Ca^{2+}-dependent (equation (5.7)) and -independent (equation (5.12)) eNOS activation pathways is governed by the parameter γ. This is taken to be 0.1 for the simulations since evidence suggests that the Ca^{2+}-independent mechanism is dominant (Dimmeler et al., 1999). Simulations with different values of γ yield the same qualitative results, but further experimental data is required to determine the relative importance of the Ca^{2+}-dependent and -independent pathways for eNOS activation, which would potentially allow quantitative results of eNOS activity.

Table 5.1: Parameter values for simulations, taken from Plank et al. (2006b)

Parameter	Value and Units	Denotation
K_{ATP}	1.68×10^{-6} m s^{-1}	ATP uptake rate
K_{ADP}	6.45×10^{-7} m s^{-1}	ADP uptake rate
$S_{\max}$	1×10^{-6} μM s^{-1}	Maximum ATP release
D_{ATP}	2.4×10^{-10} m^{2}s^{-1}	Diffusion coefficient for ATP
D_{ADP}	2.4×10^{-10} m^{2}s^{-1}	Diffusion coefficient for ADP
ρ	1000 kg m^{-3}	Density of blood
μ	4×10^{-3} N s m^{-2}	Dynamic viscosity of blood
ϕ_0	0.1 μM	Inlet ATP concentration
k_1	5.46×10^{-3} μM s^{-1}	IP_3 production rate
μ_1	0.2 s^{-1}	IP_3 decay rate
k_{rel}	6.64 s^{-1}	Ca^{2+} release rate
k_{ret}	5 μM s^{-1}	Ca^{2+} resequestration rate
k_{out}	24.7 μM s^{-1}	Ca^{2+} efflux rate
k_{dis}	0.09 μM s^{-1}	eNOS-caveolin disassociation rate
μ_2	0.0167 s^{-1}	eNOS-caveolin association rate
$q_{\max}$	17.6 μM s^{-1}	Max. WSS-induced Ca^{2+} influx rate
k_{CCE}	5.7×10^{-6} s^{-1}	CCE rate
$C_{s,0}$	2830 μM	Resting stored Ca^{2+} concentration
C_{ex}	1500 μM	External Ca^{2+}
K_c	0.026 μM	Michaelis–Menten constants
K_1	0 μM	
K_2	0.2 μM	
K_3	0.15 μM	
K_4	5 μM	
K_5	0.32 μM	
K_6	0.45 μM	
V_r	3.5	Ratio of cytosol to ER volume
α	2	Zero shear open channel constant
γ	0.1	Relative strength of the Ca^{2+}-dependent pathway for eNOS activation
W_0	1.4 Pa^{-1}	Shear gating constant
$g_{\max}$	0.06 μM s^{-1}	Max. WSS-induced eNOS activation
δ	2.86 Pa	Membrane shear modulus

The problem described above is an initial value problem consisting of equations 5.2, 5.3, 5.4 and 5.12 and initial conditions

$$\begin{aligned} i(0) &= 0 \\ C_c(0) &= C_{c,0} \\ C_s &= C_{s,0} \\ n &= n_0 \end{aligned}$$

these are same conditions used in (Plank et al., 2006b) and (Plank et al., 2006c). The parameter values used in the present study are identical to those used in previous publications (Plank et al., 2006b,c). In Plank et al. (2006b) a bifurcation analysis of the previous equations was performed to determine the stability of the system and effects of parameter variation. The bifurcation analysis used ATP and WSS as bifurcation parameters and revealed a relationship between external stimuli and cell response. In addition, the present study introduces a new parameter (γ) which governs the relative strength of eNOS activation by Ca^{2+} and WSS. If the bias is put towards Ca^{2+} the results are quantitatively different (compared with a WSS bias), however the distribution is qualitatively the same. The aim of the present study is to observe relative differences, hence this quantitative variation is of no significance. Finally, the parameters involved with nucleotide binding remain disputed with reports suggesting the response is dependent on the type of endothelial cells Yamamoto et al. (2003). For this reason, removal of the external nucleotide concentration evidences limited change to the final surface concentration. It is hypothesised that this pathway will have more prominence when these parameters become readily available.

Single cell results (Figure 5.2) for a combined stimulus (step increase) of $\phi = 0.09$ μM and $\tau_w = 0.5$ Pa, demonstrates that there is an initial transient response followed by a decay towards a steady state. The solution method was via an adaptive step Runge-Kutta routine of fifth order accuracy. The system was regarded as having reached a steady state when the gradient of all dependent variables was less than 1×10^{-3}.

Figure 5.2(a) shows the formation of inositol trisphosphate due to ligand receptor binding, which leads to a transient increase in IP_3 production that saturates out due to free receptors at the surface. Following IP_3 formation rapid efflux of Ca^{2+} out of the ER occurs, demonstrated by the increase in cytosolic

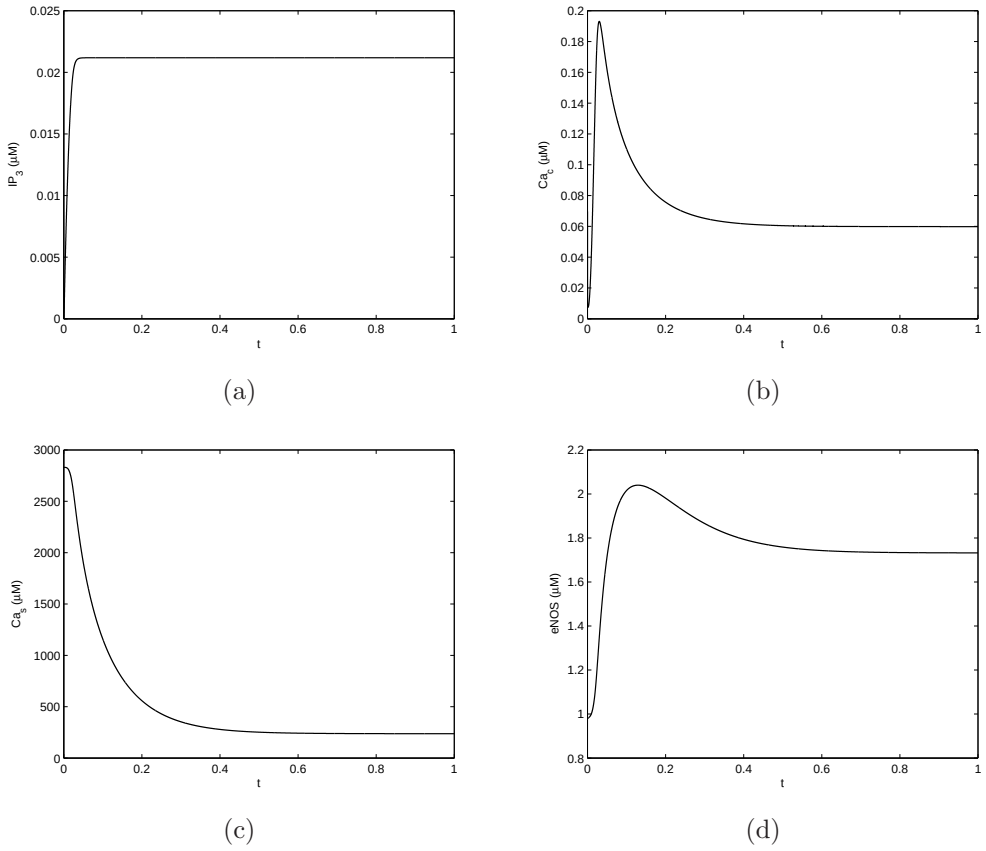

Figure 5.2: Single cell results (a) inositol trisphosphate (b) cytosolic free Ca^{2+} (c) stored Ca^{2+} (d) eNOS. All concentration profiles demonstrate an initial transient dynamic that plateaus over time to a steady state response. Note the time has been non dimensionalised by the characteristic time of 700s.

Ca^{2+} and a corresponding decrease in ER Ca^{2+} (Figure 5.2(b) and 5.2(c) respectively). This transient increase in cytosolic Ca^{2+} is then attenuated due to the pumps that transport Ca^{2+} back into the ER and across the plasma membrane. The initial transient increase in eNOS results from the formation of a Ca^{2+}–calmodulin complex within cytosol which activates eNOS and due to the applied WSS, decaying to a steady state value, resulting from dissociation of the Ca^{2+}–calmodulin complex.

5.4 Numerical implementation

The equations described in section 5.3 were implemented into the Fluent numerical code through a compiled UDF (see Appendix E.1 for code details). The

current model is implemented on steady velocity and mass transfer fields ie. WSS (τ_w) and ATP+ ADP (ϕ) respectively . Hence the coupling here is only a weak coupling as no feedback to the fluid domain occurs. Future models will aim to address this issue. This will most likely be achieved via modification of release of Calcium or NO into the fluid domain. The use of a steady state velocity and mass transfer field is valid because of the significant difference between the timescales of intracellular dynamics (approximately 500s to steady state) compared with the cardiac cycle (around 1Hz). On convergence of the steady state solution the UDF is executed. This solves the above equations via an adaptive step Runge Kutta routine over the entire surface mesh (algorithm demonstrated in Figure 5.3).

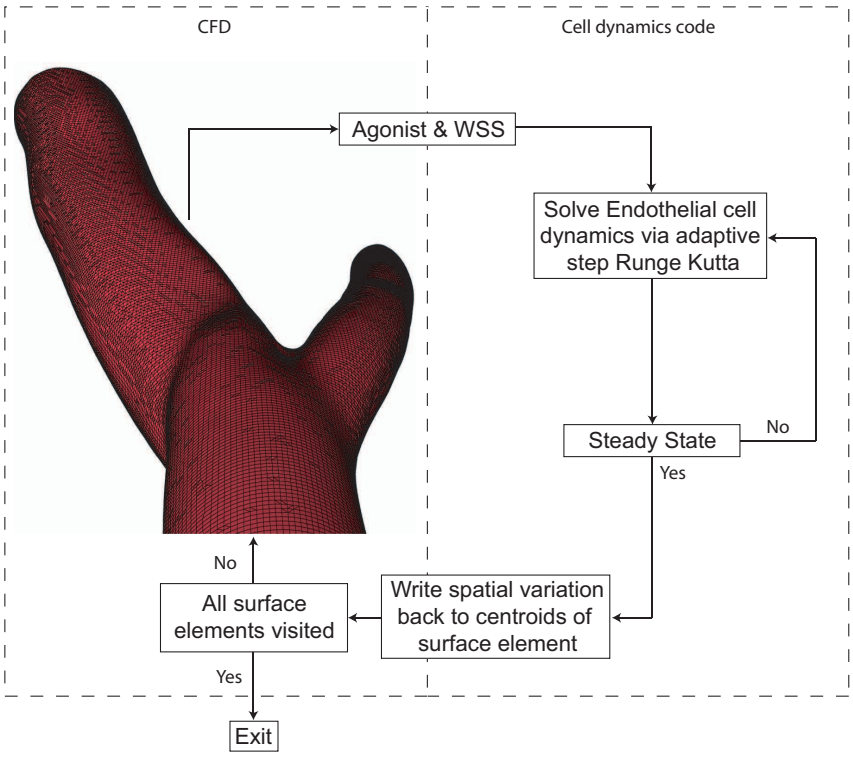

Figure 5.3: The algorithm loops over the surface mesh solving for the dependent variables on each face of the surface mesh. The cell dynamics c-code is linked to the CFD solver via a compiled UDF.

In detail, the UDF identifies the integer ID (stored by the solver) of the boundary mesh surface. This provides access to an array of faces and vertices that make up the mesh. A face loop of this surface mesh is then executed. No data is actually stored on the boundary mesh, rather solution information is stored at the centroid of the adjacent cell within the computational domain. Because of this, at each boundary face (Γ) the cell adjacent to this face requires identification. This is achieved using an in built Fluent macro that identifies

the cell adjacent to the wall within the fluid domain. From here the required information is thus obtained for inputs into the cell dynamics code. For example, the storage of the species scalar ϕ is in the adjacent cell to a given boundary face of interest, therefore the value of ϕ is calculated by returning the value at the cell centroid (see Figure 5.4) and copying onto the boundary surface.

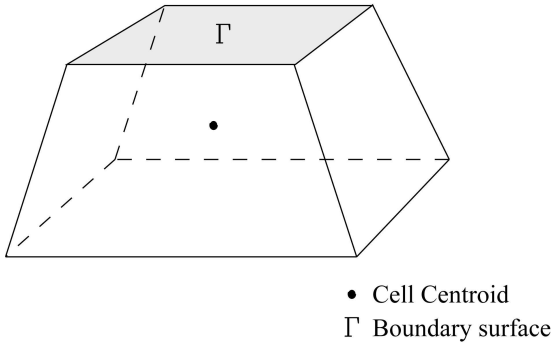

Figure 5.4: Adjacent cell (C0) to boundary surface (Γ), where following convergence of the computational solution, the ATP concentration is resolved from the cell centroid (where scalar variables are stored) to the boundary face.

The WSS is obtained from the storage of the three component shear force traction vector ($\mathbf{S}$) acting on the boundary surface element Γ (see Figure 5.5). Thus the WSS magnitude is calculated by dividing the magnitude of $\mathbf{S}$ by the magnitude of the face area normal vector ($\mathbf{A}$), hence obtaining the magnitude of WSS at the surface.

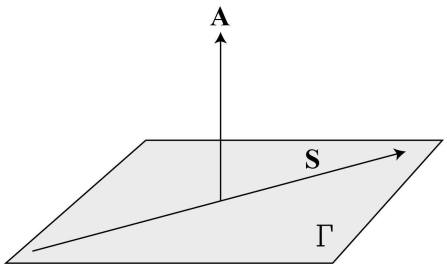

Figure 5.5: Boundary surface element (Γ) where $\mathbf{S}$ represents the shear force traction vector given by $\mathbf{S} = S_x\mathbf{i} + S_y\mathbf{j} + S_z\mathbf{k}$, and $\mathbf{A}$ the face area normal vector.

At each face the above variables provide inputs into the adaptive step Runge-Kutta routine for the solution of equations governing endothelial cell dynamics (5.2, 5.3, 5.4 and 5.12). Following completion of the mesh loop the dependent variables are written back to the surface mesh for post processing.

5.5 Conclusion

Implementation of the mathematical model for endothelial cell dynamics will allow insight into how complex 3D arterial environments affect the underlying cell dynamics. Spatial variations of WSS and ATP+ADP nucleotide will lead to spatial variations of eNOS activity. Thus areas that are subject to reduced eNOS activity will be identified as potential 'hot spots' for the initiation of atherosclerosis by implication of reduced NO production, hence locations prone to endothelial dysfunction. The current model is only weakly coupled and future models will aim to address this issue where feedback via ATP release[1] or eNOS will be coupled back to the fluid domain.

[1]Note ATP release was used in the present simulations for Ca^{2+}/eNOS, but the suggestion here is a mechanism which potentially links ATP release to intracellular Ca^{2+} levels

Chapter 6

Effects of Arterial Bifurcation Geometry of Nucleotide Concentration at the Endothelium

6.1 Introduction

This chapter outlines an analytical solution of ATP/ADP concentration over the surface of a wedge in a potential flow field. This allows for the understanding of how nucleotides respond to spatial variations in WSS in a computationally efficient manner. Additionally, numerical simulations are included to understand how nucleotides respond in the simplified flow scenario of a 2D bifurcation and provides a comparison with the analytical solution.

6.2 Background

The models developed in this chapter are to provide in depth understanding of how ATP/ADP at the inner wall of a 2D bifurcation responds in a spatially varying environment, something which has had little attention previously. The 2D model is a good first study as it provides some essential flow features, without over complicating the characterisation.

The first model examines an analytical solution of ATP/ADP concentration. This geometric variation is derived from the boundary layer equations and allows for a functional form of the WSS to be developed that incorporates geometrical variation; this function changes substantially for the range investigated. Initially a wedge in an unbounded fluid domain is investigated; this provides an excellent

basis for analysis of geometries in which the fluid flow is diverted through an angle (θ). The analysis assumes that the flow is divided into an inviscid core with viscous boundary layers on the walls. Previous analysis of this type has been considered by (Pedley, 1980).

The numerical investigation provides a comparison and extension of the analytical model and has the versatility to be utilised in any arterial geometry. Additionally, the numerical model also incorporates the more physiological pulsatile flow. This was incorporated because there is substantial literature suggesting that oscillatory shear rates and WSS are responsible for cardiovascular remodelling. Furthermore there are few reports of nucleotide variation in pulsatile flow and the reports that are in literature are in non spatially varying environments, which tend to lead to false or inconclusive findings. Generally, it has been fairly computationally expensive due to the fine resolution boundary layers required as mentioned in Chapter 4. In addition, start up transients tend to persist for low diffusion coefficient species for multiple flow cycles before reaching independence. For the present analysis, because the simulations are in a 2D geometry, it is reasonably efficient to obtain these results.

Finally, since ATP release is reported to occur under shear and hypoxia conditions, this effect is modelled using a sigmoidal shear stress-induced ATP release (as many biological phenomena are sigmoidal in manner) have also been included in the numerical model.

The relevance of this section in examining nucleotide concentration is these nucleotides are thought to play an important role in the function of a healthy endothelium, as outlined in Chapter 1.

6.3 ATP/ADP concentration over a wedge

Similar solutions of the boundary layer equations

The variation of the flow due to geometry is introduced using the Falkner-Skan equation for flow past a wedge (Schlichting and Gersten, 1999). In this analysis the fluid outside the boundary layer is frictionless. This is an important

class of solutions in which the 2D incompressible boundary layer equations (a brief description of these equations is given in Appendix D), given by equations (6.1) and (6.2), are reduced to an ordinary differential equation via a similarity transformation. Full details of transforming the boundary layer equations into a general class of differential equation is given in Appendix D. The well known 2D boundary layer equations are given by

$$u\frac{\partial u}{\partial x} + v\frac{\partial u}{\partial y} = U\frac{dU}{dx} + v\frac{\partial u^2}{\partial y^2} \tag{6.1}$$

$$\frac{\partial u}{\partial x} + \frac{\partial v}{\partial y} = 0 \tag{6.2}$$

If the Potential flow velocity is assumed to be of the form

$$\mathrm{U(x)} = \mathrm{u_1 x^m}, \qquad 0 \leq \mathrm{m} \leq 1; \tag{6.3}$$

where the potential flow velocity is proportional to the length of arc, measured downstream from the stagnation point, then a known set of similarity solutions exist. The constraints on m are provided to limit the solution to the range covering flow over a flat plate, m=0 (represented by $\theta = 0$ in Figure 6.1), through to plane stagnation point flow, m=1 ($\theta = \pi$ in Figure 6.1).

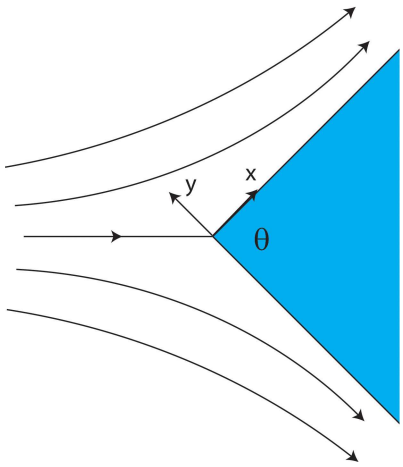

Figure 6.1: Analytical flow domain investigated.

The conformal function

$$z = w^{\frac{2\pi}{2\pi - \theta}} \tag{6.4}$$

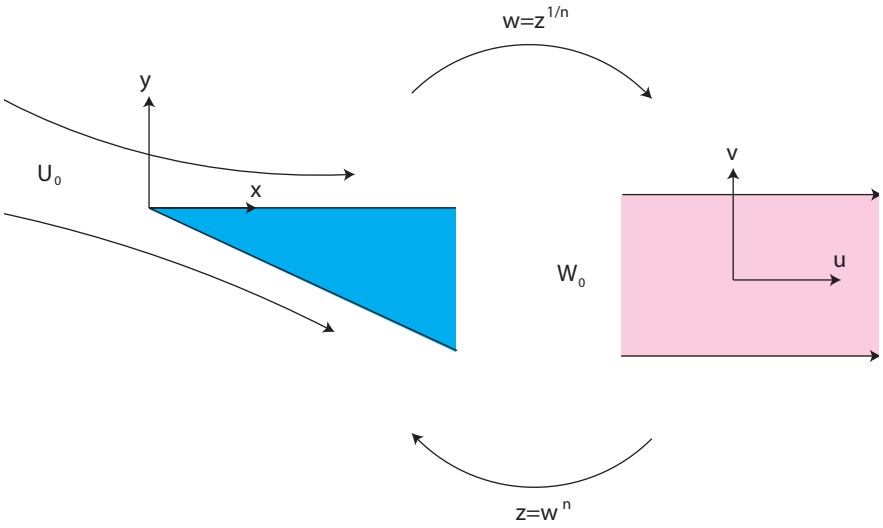

Figure 6.2: Conformal map from the z to the w domain.

maps the complex 2D domain to the z-domain (see Figure 6.2) whose geometry is shown in Figure 6.1. For further information refer to Evans (1968). The parameter u_1 is evaluated from the potential flow solution where

$$\mathrm{u_1} = \frac{2\pi \mathrm{W_0}}{(2\pi - \theta)} \tag{6.5}$$

and W_0 represents uniform flow in the w-domain.

The parameter m is related to the bifurcation angle θ in Figure 6.1 through the following relationship.

$$\theta = \frac{2\mathrm{m}\pi}{\mathrm{m}+1} \tag{6.6}$$

The transformation of the independent variable y, which leads to the boundary layer equations being reduced to an ordinary differential equation (see Appendix D for full details) is defined as

$$\alpha = \mathrm{y}\sqrt{\frac{\mathrm{m}+1}{2}\frac{\mathrm{u_1}}{\nu}}\mathrm{x}^{\frac{\mathrm{m}-1}{2}} \tag{6.7}$$

From (6.3) and (6.7) the streamwise component of velocity can be calculated

$$u = Uf'(\alpha) \tag{6.8}$$

where $f'(\alpha)$ represents the non-dimensional velocity.

From (6.8) the wall shear stress can be evaluated

$$\tilde{\tau}_{\mathrm{w}} = \mu\frac{\partial \mathrm{u}}{\partial \mathrm{y}}\bigg|_{\mathrm{y}=0} = \mu \mathrm{u_1} f''(0)\mathrm{x}^{\frac{3\mathrm{m}-1}{2}}\sqrt{\frac{\mathrm{m}+1}{2}\frac{\mathrm{u_1}}{\nu}} \tag{6.9}$$

which is a function of both geometry and the downstream coordinate. The function $f''(0)$ is outlined for different values of the parameter m in Schlichting and Gersten (1999). The wall shear stress is further non-dimensionalised by

$$\tau_{\mathrm{w}} = \frac{\tilde{\tau}_{\mathrm{w}}}{\rho \mathrm{U}_\infty^2} \tag{6.10}$$

ATP concentration over a wedge

In Chapter 4 it was shown that the similarity variable associated with the analytical solution for concentration of ATP/ADP at the endothelium is given by

$$\eta = \frac{(\mathrm{PeRe})^{\frac{1}{3}}|\tau_{\mathrm{w}}(\mathrm{x})|^{\frac{1}{2}}}{\{9\int_{\mathrm{x_0}}^{\mathrm{x}}|\tau_{\mathrm{w}}(\gamma)|^{\frac{1}{2}}\mathrm{d}\gamma\}^{\frac{1}{3}}} \equiv \mathrm{y}\beta(\mathrm{x}) \tag{6.11}$$

Hence for the present analysis, incorporating geometric variation, the similarity variable becomes

$$\eta = \frac{(PeRe)^{\frac{1}{3}}|\tau_w(x,m)|^{\frac{1}{2}}}{\{9\int_{x_0}^{x}|\tau_w(\gamma,m)|^{\frac{1}{2}}d\gamma\}^{\frac{1}{3}}} \equiv y\beta(x,m) \tag{6.12}$$

On substitution of (6.9) into (6.12) the similarity variable can be rewritten as

$$\beta(x,m) = \left(\frac{RePe\ a(m+1)}{12}\right)^{\frac{1}{3}} x^{\frac{m-1}{2}} \tag{6.13}$$

where

$$a = \frac{\nu u_1 f''(0)\sqrt{\frac{u_1(m+1)}{2\nu}}}{U_\infty^2} \tag{6.14}$$

The above allows an analytical solution of ATP concentration to be sought. This is a powerful tool as it is a quick, effective and insightful means of evaluating surface ATP concentration in response to geometry.

Analytical Wall Shear Stress

The form of the wall shear stress, as described by equation (6.9), immediately after the stagnation point is seen to change dramatically over the range of bifurcation angles. Figure 6.3 demonstrates this phenomenon with the shear stress being very large for angles $\theta < \pi/2$ ($m < 1/3$) and very small for angles $\theta > \pi/2$ ($m > 1/3$); this only applies for small values of $\tilde{x}/h$.

Far downstream the shear stress tends to ∞ for $\theta > \pi/2$ ($m > 1/3$), and to zero value for $\theta < \pi/2$ ($m < 1/3$). This 'far downstream' region is not shown in Figure 6.3 as the WSS has no physiological significance there. Real artery geometries have outer walls, and do not extend infinitely, therefore the region of interest for this investigation is the area immediately downstream of the stagnation point, i.e small x.

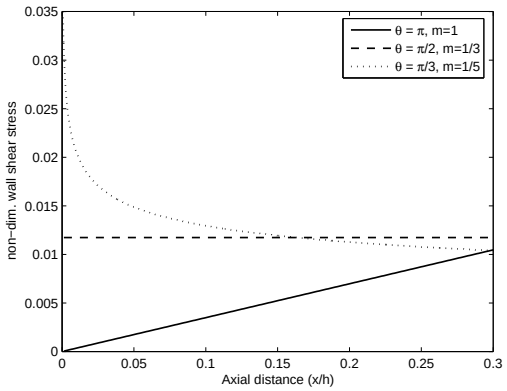

Figure 6.3: Analytical WSS for $\theta = \pi/3$, $\theta = \pi/2$ and $\theta = \pi$.

Equation 6.9 also provides a representation of convection in the boundary layer. When $m = 1/3$ ($\theta = \pi/2$) the shear stress is not spatially varying as

$$x^{\frac{3m-1}{2}} = 1 \quad \text{hence} \quad \tau_w\left(x, \frac{1}{3}\right) = \mu u_1 f''(0)\sqrt{\frac{2u_1}{3\nu}}, \quad \text{a constant.}$$

This is at a constant value due to the boundary layer growing at an equivalent rate to the velocity. For values of $m < 1/3$ ($\theta < \pi/2$) the shear stress in the limit as x tends to zero is infinity since

$$\lim_{x\to 0, m<\frac{1}{3}} (\tau_w(x,m)) = A \lim_{x\to 0} x^n = \infty \quad \text{where} \quad n = \frac{3m-1}{2} < 0$$

with

$$A = \mu u_1 f''(0)\sqrt{\frac{u_1(m+1)}{2\nu}}$$

This is not physiological, but demonstrates that the shear stress tends to a larger value as x tends to zero. In real arterial bifurcation geometries the daughter arteries do not converge to a sharp point, rather the bifurcation looks like a circular cap with a tangential plane at the bifurcation point, hence even for acute bifurcations the WSS would be zero at the stagnation point.

For values of $m > 1/3$ ($\theta > \pi/2$) we have that

$$\lim_{x\to 0, m>\frac{1}{3}} (\tau_w(x,m)) = A \lim_{x\to 0} x^n = 0 \quad \text{where} \quad n = \frac{3m-1}{2} > 0$$

Table 6.1: parameter values used for simulations

Parameter	Value	Units	Denotation
K_{ATP}	1.68×10^{-6}	ms^{-1}	ATP hydrolysis rate
K_{ADP}	6.45×10^{-7}	ms^{-1}	ADP hydrolysis rate
D_{ATP}	2.4×10^{-10}	$\mathrm{m}^2\mathrm{s}^{-1}$	Diffusion coefficient for ATP
D_{ADP}	2.4×10^{-10}	$\mathrm{m}^2\mathrm{s}^{-1}$	Diffusion coefficient for ADP
$\phi_{\mathrm{ATP},\infty}$	0.1	μM	ATP conc. far away from surface
ρ	1000	kgm^{-3}	Density of blood
μ	4×10^{-3}	Nsm^{-2}	Dynamic viscosity of blood
ϕ_0	0.1	μM	Inlet ATP concentration
h	2×10^{-3}	m	Characteristic length
$S_{\max}$	1×10^{-6}	$\mu\mathrm{Mms}^{-1}$	Maximum ATP release rate

Table 6.1 shows the parameter values used for the simulations, which are those used for previous simulations (David, 2003, John and Barakat, 2001). The solutions to the Falkner-Skan equations were evaluated using tabulated data from Schlichting and Gersten (1999) for bifurcation angles ranging from 0 to π radians, a flat plate and stagnation flow solutions respectively. The unlisted solutions were interpolated using cubic splines.

6.4 Numerical Flow and Mass transfer

A numerical model of nucleotide concentration at the endothelium provides a useful comparison of the analytical results. Additionally, certain flow scenarios, such as the 2D arterial bifurcation being investigated here, have wall shear stress functions that are unable to be obtained analytically, so must be obtained from numerical simulations. This can then be substituted back into the analytical model to evaluate nucleotide concentration. Having already obtained analytical WSS this can be compared to the numerically derived WSS and any similarities that exist identified. The model is simulated under steady flow conditions and also the more physiologically realistic pulsatile flow; the pulsatile waveform is non-reversing with non-zero mean flow similar to John and Barakat (2001).

The geometry modelled, shown in Figure 6.4, was developed using the commercially available CAD package Solidworks. The following dimensions for the artery were used: the inlet, diameter 4mm (D_1) dividing evenly into two 2mm daughter (D_2) arteries; this is to represent any generic artery, as the main area of interest here is the diverting of the flow through an angle θ. The variation of the angle was the only change between geometries, with the parent and daughter artery diameters remaining constant.

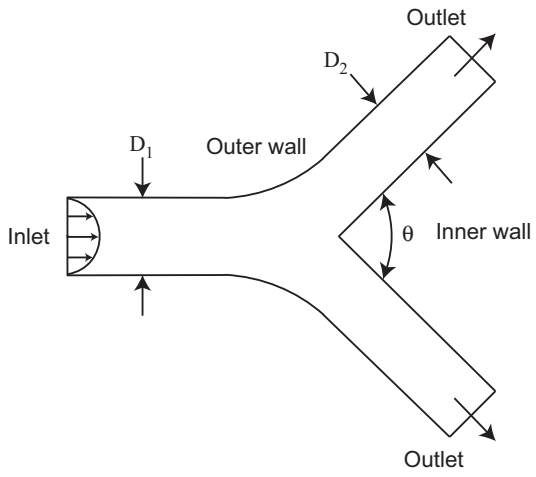

Figure 6.4: Numerical flow domain investigated.

The boundary conditions chosen to model blood flow through the artery bifurcation were inlet velocity conditions coupled with a zero diffusion flux consistent with fully developed flow on the outlets (as outlined in Chapter 3). A fully developed Poiseuille profile was specified at the inlet. The advantage of this method is that it reduces the length of the inlet, hence computation time. Equivalently, for the time-dependent simulations the pulsatile flow was obtained by superimposing a purely sinusoidal flow onto the steady flow solution, Figure 6.5. This is in accordance with previous studies that have used a sine wave to investigate essential features:

$$U_{\max}(1 - \frac{z^2}{r^2})(1 + \sin \omega t) \tag{6.15}$$

where $U_{\max}$ represents the maximum velocity across the lumen, z the normal coordinate, r the radius of the vessel, t the time and $\omega = 2\pi f$ the angular frequency. For the present case ω was taken to be 2π as the frequency, f, was 1 Hz, giving a Womersley number of 2.5. Each cycle was divided into 200 time steps of

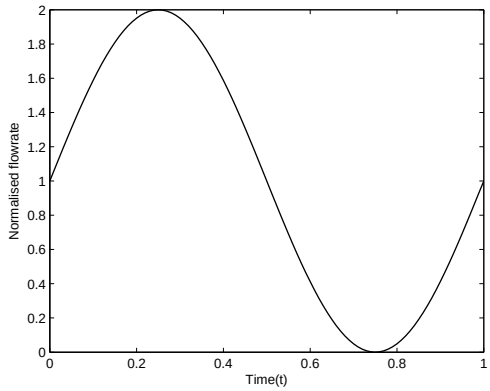

Figure 6.5: Inlet flow waveform for unsteady simulations.

size 0.005s. Data was recorded after four complete cycles in order to eradicate any start up transients; at this point the agreement in ATP concentration between successive cycles differed by $<< 1\%$, and no variation was observed in WSS. Fluent's outflow condition was used for the flow exiting the domain. This condition allows for blood to divide evenly into both daughter arteries and these conditions are located sufficiently downstream (25 artery diameters) of the stagnation point. A uniform ATP concentration of 0.1μM is specified at the inlet to the domain for all simulations; this uniform condition is suitable due to the low mass transfer coefficient, hence large Peclet number. This in turn leads to upstream hydrolysis having a negligible effect on hydrolysis downstream and simulations with upstream hydrolysis (data not shown) have verified this occurrence. A custom reaction rate for the hydrolysis of ATP/ADP was implemented numerically as described by equation (4.23) in Chapter 4. Furthermore it includes the option of shear stress-induced ATP release as described by equation (4.21). Only the inner wall of the arterial bifurcation, as labelled in Figure 6.4, has this reaction. For walls with no reaction occurring at the surface, Fluent prescribes a zero species gradient. Parameters used in the numerical model were also those listed in Table 6.1. Second order upwinding was used for both momentum and mass transfer for the convective terms.

A Hybrid mesh consisting of both quadrilateral and triangular elements was used. Boundary layers were attached to all walls to create a very fine resolution grid varying over 19 layers from $0.0005D_2$ to $0.013D_2$ as this allows for high gradients of species and velocity to be captured accurately in the vicinity of the wall. This is of great importance when dealing with low diffusion coefficients,

as the mass transfer layer is confined to a small region immediately above the wall. Figure 6.6 shows the boundary layer mesh attached to part of the wall downstream of the stagnation point.

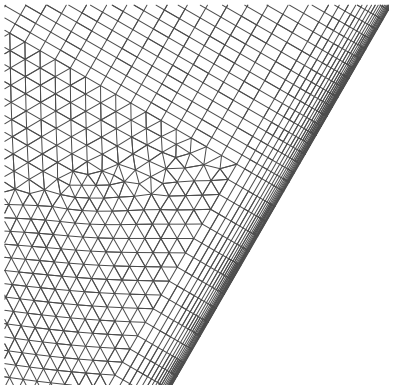

Figure 6.6: Portion of the computational grid demonstrating high resolution boundary layer and hybrid mesh of quadrilateral and triangular elements in the main flow.

Computational meshes contained approximately 130,000 cells. Solutions were also obtained in order to test for mesh convergence on meshes containing approximately 300,000 cells. The majority of the refinement occurred along the reactive wall where the number of nodes along the surface increased from 600 to a 1000. Little or no variation was observed in the flow fields, wall shear stress or wall species concentration Figure (6.7), hence the original mesh was considered grid-independent. The Fluent simulations were considered converged when the scaled residuals dropped below 10^{-6}, at which point no further change in the solution was observed. Numerical simulations where performed on a desktop PC with a clockspeed of 2GHz and 2Gb of Ram. Time for simulation was approximately 6 hours.

The numerical domain varies fundamentally from the analytical model (in which the assumption is made that the domain exists in an unbounded flow field) with the existence of an outer wall. This allows for an extension of the wedge so observations can be made about the effects that an outer wall has on the inner WSS.

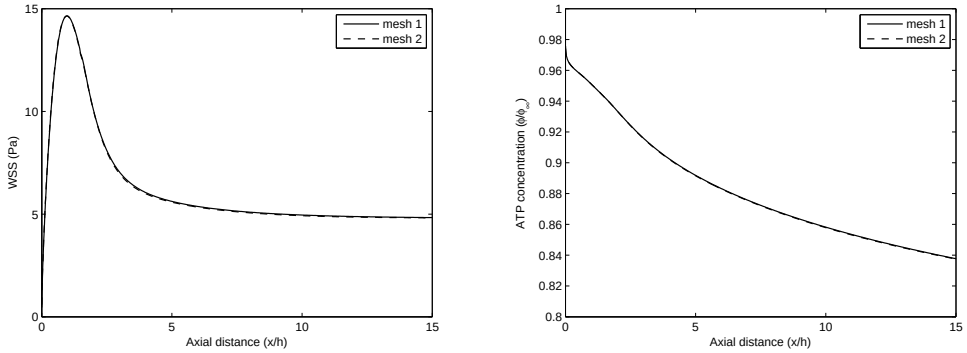

(a) (b)

Figure 6.7: Mesh convergence of the numerical simulations: (a) WSS along inner wall (b) ATP concentration along inner wall. Evidently the two meshes are sensibly identical results.

6.5 Results

6.5.1 Analytical

The case when $\theta = 0$ ($m = 0$) corresponds to the solution for flow over a flat plate. Figure 6.8 shows the concentration profiles as functions of the downstream coordinate for both ATP and ADP when $\theta = 0, \pi/2, 8\pi/9, \pi$ for two distinct Reynolds numbers, 20 and 200.

Over the range of bifurcation angles investigated there is a marked change in the variation of nucleotides along the surface of the endothelium. For bifurcation angles less than $\pi/2$ ($m = 1/3$), there is a relatively large monotonic decrease in the ATP concentration relative to the free stream reference concentration, that decays towards zero further downstream. ADP in this range substantially increases, exhibiting some interesting characteristics depending on the bifurcation angle and Reynolds number. In the lower end of the investigated angles, close to the stagnation point, the ATP concentration drops below ADP, which rises to a maximum concentration and reduces in the streamwise direction thereafter (see Figure 6.8(a)). As the bifurcation angle increases, the point of crossover moves downstream until eventually there is no crossover point due to larger WSS existing downstream (indicating considerable convection into the boundary layer). This is demonstrated in Figure 6.8(c) where ATP never drops below ADP in the investigated domain. Additionally this is is also observed to be a function of the

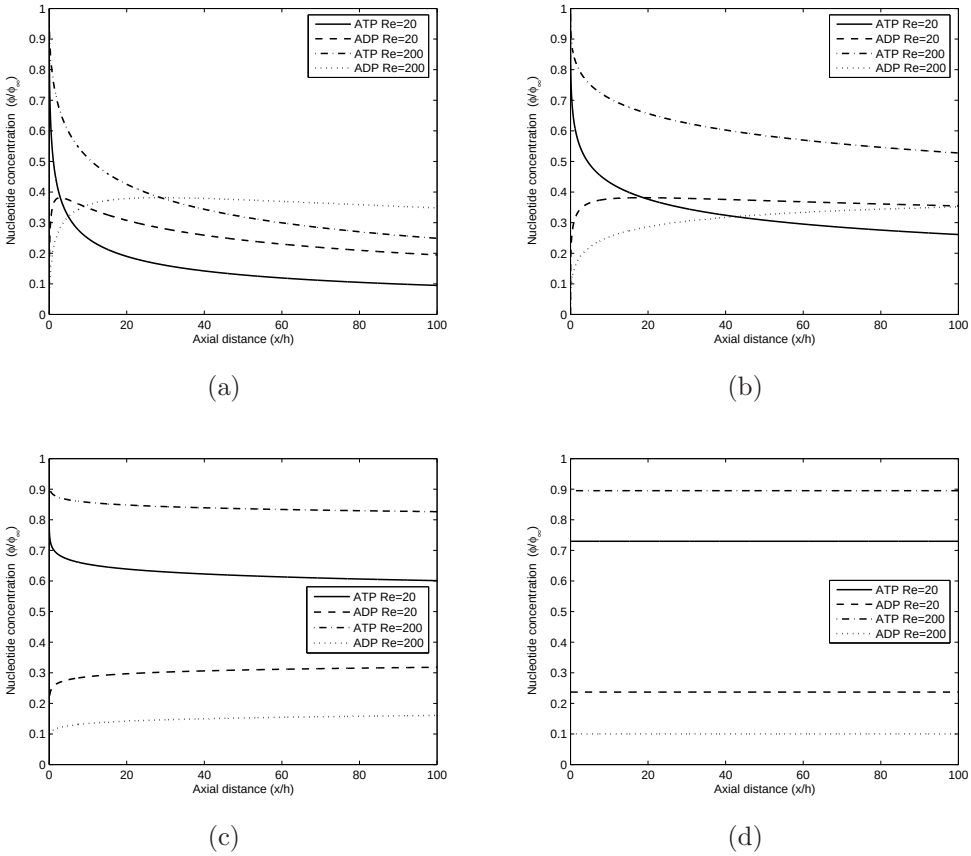

Figure 6.8: Nucleotide concentration at the endothelium calculated using the analytical solution: (a) $\theta = 0$ (m = 0); (b) $\theta = \pi/2$ (m = 1/3); (c) $\theta = 8\pi/9$ (m = 0.8); (d) $\theta = \pi$ (m = 1).

Reynolds number where the crossover point is in closer proximity to the stagnation point for lower Reynolds number, at an equivalent angle. The maximum value in the ADP concentration shown in Figures 6.8(a) and 6.8(b) is expected, as it can be shown using equation (4.32) that ADP concentration exhibits a maximum when $\beta(x) = \sqrt{k_1 k_2}$ (see Plank et al. (2006a) for full details) where k_1 and k_2 represent the Sherwood numbers of the system. This maximum is more pronounced at Re=20 and is only observed for Re=200 at very small angles. The maximum highlights that geometry is extremely important for the concentration of nucleotides at the endothelium and will therefore have a significant effect on endothelial cell signalling and the associated regulation of vascular tone. When $\theta = \pi/2$ ($m = 1/3$) the wall shear stress is not spatially varying and via a simple transformation the governing equation for wedge flow corresponds to axisymmetric stagnation point flow (see Schlichting and Gersten (1999) for details). This

would be the appropriate model for a physiological bifurcation within a small neighborhood of the resulting stagnation point.

Additionally, Reynolds number has a considerable effect on nucleotide hydrolysis at the endothelium where the drop in ATP concentration is significantly greater for the lower Reynolds number which is attributed to the lower WSS. Further downstream for $\theta > \pi/2$ ($m > 1/3$) the nucleotide concentration plateaus due to the large resulting WSS. The convectional delivery of ATP is essentially balanced by the degradation at the surface of the endothelium, although in the limit as $x \to \infty, \quad \phi_{ATP} \to 0$ for $\theta < \pi$ ($m < 1$) due to the growth of the boundary layer. An important point to note about the WSS further downstream for this particular model is that it is non-physiological as mentioned in section 6.3.

When $\theta = \pi$ ($m = 1$) the velocity distribution in the potential flow becomes that corresponding to plane stagnation point flow. The WSS is a linear function of x; therefore β is independent of the downstream coordinate and the concentration of both species is constant throughout the entire domain length. This constant concentration profile indicates that the delivery of ATP to the endothelium is in equilibrium with hydrolysis at the surface. Figure 6.8(d) demonstrates the constant concentration profile.

For small bifurcation angles, initially WSS is very large and decreases monotonically in the streamwise direction; this in turn leads to decreased rates of reduction in ATP concentration near the stagnation point, as convectional delivery overcomes hydrolysis. For $\theta < \pi/2$ ($m < 1/3$) there is a continual decay of the ATP concentration towards zero. The more acute the bifurcation angle, the shorter the distance required for the concentration to reach a negligible level. Further downstream the WSS undergoes a continual decrease towards zero, but at a much reduced rate; this is due to the growth of the boundary layer coupled with low convection into the boundary layer.

6.5.2 Numerical

This section outlines the results of the numerical simulations. A fundamental difference that exists between the analytical and numerical is the form of the outer flow $U(x)$. For the wedge in an unbounded domain the outer flow is assumed to

be potential, whilst in the numerical case with outer walls this is not the case. Two different methods of evaluating ATP/ADP concentration are used in sections 6.10 and 6.5.2: the similarity solution with numerical WSS (semi-analytical) and a full numerical in which the transport of species (equation (4.1)) is solved using the CFD method outlined in Chapters (3) and (4). The numerical section also includes two additional effects: pulsatile flow, in which simulations were carried out over a range of maximum Reynolds numbers from 100 to 800 and steady-state flow-induced ATP release as discussed earlier.

Numerical WSS

The wall shear stress profiles obtained from the numerical simulations exhibit a very similar form to that of the analytical, but this is restricted to the domain located immediately downstream of the stagnation point, before fully developed arterial flow has formed. This domain in the neighbourhood of the stagnation point, like the analytical, is governed by a power law. Figure 6.9 details the the WSS profiles for Re=20 and 200. The ranges of x vary for visual purposes, as the region of interest is where the WSS is spatially varying. The most notable difference between the Reynolds numbers is the reduced WSS gradients observed for the lower Reynolds number and, as expected, the shorter downstream distance required for fully developed flow to form. Other angles in the investigated range exhibited similar characteristics and fitted in between the extremities of the angles shown in Figure 6.9.

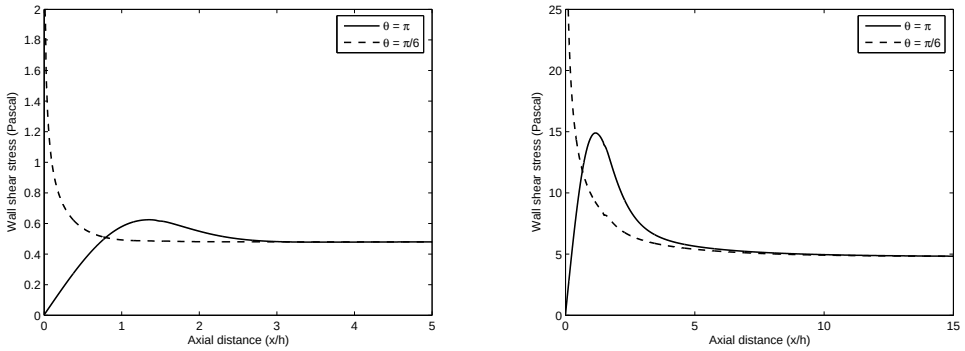

(a) (b)

Figure 6.9: Wall shear stress calculated using the numerical simulations: (a) Re = 20; (b) Re = 200.

Numerical ATP/ADP concentration

The numerical solution of ATP/ADP concentration at the endothelium exhibits some interesting characteristics. Again there is considerable variation in the results over the range of bifurcation angles investigated. Figure 6.10 details the resulting nucleotide concentration from the numerical simulations, for Re=200. In addition to a full numerical solution of equation (4.1), it is possible to substitute the WSS obtained from the Fluent simulations directly into the analytical solution via equation (6.12), providing a semi-analytical means of evaluating nucleotide concentration, using equations (4.29) and (4.32) and enabling a full comparison of the two models to be made. Figure 6.10 also details the resulting ATP/ADP concentration for the semi-analytical (with numerical WSS). Similar profiles occur at Re=20 (data not shown), but the overall drop in ATP is larger due to lower WSS magnitude.

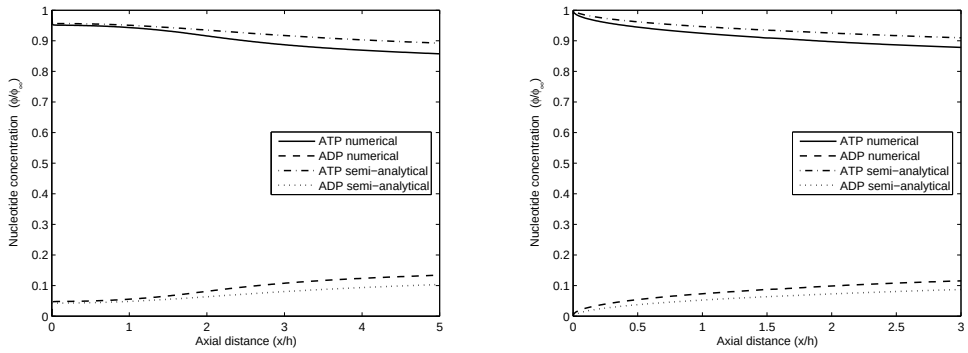

(a) (b)

Figure 6.10: Nucleotide concentration at the endothelium: (a) Re = 200, $\theta = \pi$; (b) Re = 200, $\theta = \pi/6$. The numerical profiles show the numerical solution of the mass transport equation using Fluent. The semi-analytical profiles show the similarity solution using numerical data for the WSS.

The main variation of concentration occurs again in the vicinity of the stagnation point in which there is considerable change in WSS, as discussed previously. Further downstream the profiles become generic to parallel plate solutions as the WSS ceases to be spatially varying. Figure 6.10(a), where the flow is of a 2D stagnation point, for Re=200, demonstrates that there is a small region of almost constant ATP concentration where convectional delivery is in equilibrium with hydrolysis at the surface. However the concentration then begins to drop off as the fully developed arterial flow is established, similarly ADP is initially constant

then increases in the streamwise direction. An analogous occurrence has also been demonstrated in the analytical model. For Re=20, $\theta = \pi/6$: the drop in ATP and corresponding increase in ADP is more profound This is attributed to the considerably lower WSS magnitude, meaning that transport of ATP to the surface is greatly reduced, hence a more substantial drop is observed at the endothelium. The phenomenon was equivalently observed in the analytical model as previously discussed. Additionally the profiles for $\theta > \pi/2$ plateau slightly, due to the increasing WSS, but then continue to drop as the fully developed arterial flow forms. This phenomenon is more pronounced at Re=200 as the boundary layer growth is slower than for the lower Reynolds number flow.

Figure 6.10(b) shows the drop in ATP concentration in the immediate vicinity of the stagnation point is substantially reduced compared with larger angles which can be attributed to the large initial WSS. This WSS decreases rapidly in the streamwise direction, thus ATP concentration reduces and fully developed arterial flow is established, about $x = 1$, where the concentration continues to decay, but at a reduced rate. The two extremities of the investigation show strong indication that the initial concentration drop relative to the free stream concentration is greater as the bifurcation angles increases. This is due to the low WSS, which leads to greater rates of hydrolysis at the endothelium, eventually reaching a state of balance for plane stagnation point flow.

The profiles produced by the semi-analytical model demonstrate very similar characteristics but tend to predict a slightly lower ATP concentration, and hence slightly greater ADP concentration. At a physiological level the difference observed is negligible. The strength of this numerical analysis is that it has provided insight into the dominant parameters associated with this bifurcation geometry that modulate the concentration of nucleotides at the endothelium.

Figure 6.11 highlights the region in close proximity to the stagnation point, in which there is significant variation in ATP concentration. At $\theta = \pi$ there is an abrupt drop in ATP concentration at the stagnation point followed by a small region of balance as already discussed. The concentration drop becomes more gradual as theta decreases. This is a direct result of the WSS gradient in the bifurcating region, which increases as θ decreases. Also this region shows the concentration profile plateau disappearing as the bifurcation angle reduces.

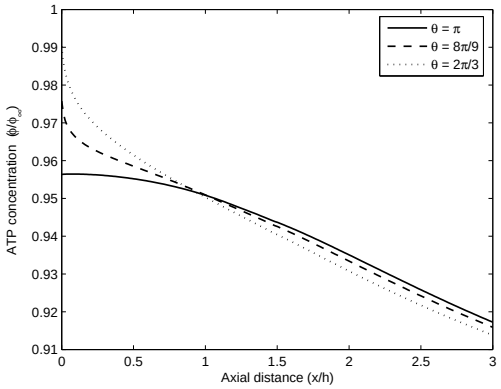

Figure 6.11: Numerical ATP concentration in close proximity of the stagnation point, for three angles, at Re=200.

Flow-induced ATP release

Flow-induced ATP release was simulated under the effects of slow and rapid release, which respectively had characteristic $\tau_0 = 1$ and 5 Pa. This characteristic WSS governs how the maximum release rate of 10^{-6} μMms^{-1} is obtained. Simulations were carried out for two Reynolds numbers of 20 and 200. As expected from the results, the larger the characteristic WSS, hence slower release, the closer the ATP concentration is to the results carried out under no release conditions. Figure 6.12 shows the release obtained for $Re = 200$

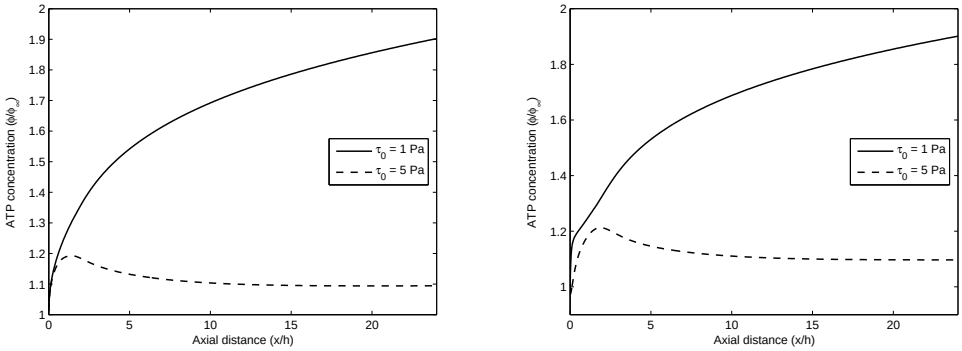

(a) (b)

Figure 6.12: Nucleotide concentration under the conditions of flow induced ATP release: (a) $\theta = \pi/3$ (b) $\theta = 8\pi/9$, at the endothelium with the effects of shear stress-induced ATP release included.

As is evident from Figures 6.12(a) and 6.12(b), the rapid ATP release shows a significant increase in ATP concentration relative to the bulk concentration.

This means that the contribution of ATP release outweighs hydrolysis at the surface. The large increase in surface concentration has many implications for the modulation of cellular processes. The difference in profiles between the two angles is very small, mainly affecting the shape of the profile at small x. For the slower release there is an initial increase, due to the increasing WSS, but the concentration then reduces to a state of equilibrium between endothelial uptake and production. The results for $Re = 20$ (data not shown) demonstrate that, as expected, the surface concentration of ATP is lower than for Re=200 due to lower rates of WSS-induced ATP release. Figure 6.13 shows a comparison between the two different solution methods, profiles are very similar, but the semi-analytical is slightly over sensitive to the effects of ATP release.

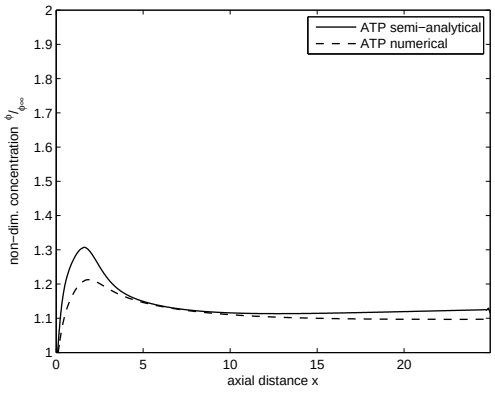

Figure 6.13: Comparison of semi-analytical and numerical solution under slow release conditions, the semi-analytical appears to be over sensitive to the effects of release, but overall profile shapes are similar.

Pulsatile numerical ATP/ADP concentration

Temporal gradients in WSS have been linked with the onset of atherosclerosis (Gimbrone, 1999, White et al., 2001). Therefore, simulations were run with a pulsatile flow cycle to examine the effects of time-dependent flow. The simulations were carried out over a range of maximum Reynolds numbers varying between 100 and 800. As previously described in section 6.4, the inlet waveform is purely sinusoidal in nature and is non-reversing with net positive flow.

The time-dependent flow pulsatility leads to significant gradients in wall shear stress, both spatial and temporal. Throughout the cycle the general form of the WSS did not alter significantly, but the maximum and gradients did. High spatial

gradients exist in the early parts of the cycle, but in the later part this gradient has reduced substantially and the WSS is low with little variation.

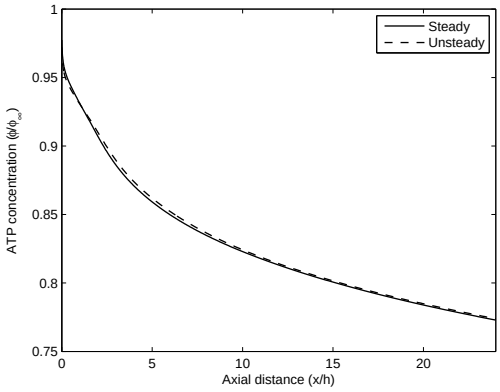

Figure 6.14: Comparison between time averaged and steady state ATP concentration, for Re=200, evidently the steady is very closely matched with the mean of the unsteady.

Figure 6.14 represents a the time averaged ATP distribution at the inner wall compared with the steady state solution, $\theta = 7\pi/9$. The dashed line, representing the steady state ATP concentration, is the approximate mean of the pulsatile flow ATP concentration. The concentration deviates slightly from the mean further downstream, but the differences are negligible. Thus it can be concluded that flow pulsatility has little effect on the surface ATP concentration and the concentration at the inner wall is determined by the mean WSS. This result was replicated irrespective of the bifurcation angle and Reynolds number. For ADP similar characteristics are observed with the the time varying mean and the steady state concentration coinciding. The observations here are in agreement with the findings of John and Barakat (2001) who also concluded that the effects of pulsatile flow were negligible. However, the concentration of ATP needs to be assessed in geometries where flow reversals occur, in order to fully understand the effects of pulsatile flow on nucleotide concentration.

6.6 Discussion

A mathematical model of ATP/ADP concentration at the endothelial surface for varying geometric conditions related to two-dimensional arterial bifurcations has been presented. The model has been studied analytically and numerically and

has shown that both the shear stress and the concentration of ATP/ADP at the endothelium are directly affected by the geometry of an arterial bifurcation. This has extremely important implications for endothelial cell physiology and potential dysfunction as discussed in Chapter 1, where these cells are sensitive to shear stress (via mechanosensitive ion channels and receptors) and external nucleotide concentration (via G-protein-coupled receptors) (Dull and Davies, 1991, Traub and Berk, 1998). Previously, it has been shown that regions where biochemical stimuli and WSS are low lead to deficient endothelial calcium concentration (Plank et al., 2006b). Since calcium is an important activator of endothelial nitric oxide (eNOS) synthase, this can lead to reduced bioavailability of NO at the artery wall (Lin et al., 2000). Lack of NO is associated with endothelial dysfunction, impaired vasodilation and increased platelet aggregation, which have adverse consequences for the onset of cardiovascular disease (Naseem, 2005).

The analytical model is based on a similarity solution of the mass transport equation for nucleotide concentration and uses a power law expression for the shear stress on the inner wall of the bifurcation, where the power depends on the bifurcation angle. The power law is only valid within the neigbourhood of the flow stagnation point (where the size of the region of the validity depends on the Reynolds number). Within this region, the analytical and numerical results show excellent agreement. Outside this region, the effects of the outer wall dominate and the wall shear stress tends to a steady value, consistent with the establishment of fully developed flow.

The importance of the above analysis is that it has provided considerable insight into the important parameters that govern nucleotide concentration at the endothelium. In particular, the effects of different bifurcation angles on the distributions of wall shear stress and ATP/ADP at the endothelium have been investigated. For large bifurcation angles (greater than 90^o), the bifurcation is characterised by a stagnation point, surrounded by a region of low wall shear stress. Convection is low in this area and the mass transfer processes in the nucleotide boundary layer are dominated by the reaction at the endothelial surface. This leads to a substantial drop in ATP relative to the free stream concentration and a corresponding increase in the ADP concentration. Further downstream, the wall shear stress attains a steady value as the flow becomes fully developed, leading to a sustained gradual decline in ATP concentration.

In contrast, acute arterial bifurcations (bifurcation angle less than 90^o) exhibit a region of very high wall shear stress. The enhanced convection at the bifurcation means that the initial drop in ATP relative to the free stream is less pronounced. However, the onset of fully developed arterial flow again leads to a sustained decline in ATP concentration in the downstream direction.

Physiologically, arterial bifurcations do not exist as a salient point experiencing very high wall shear stress. The larger bifurcation angles therefore represent the more biologically realistic model.

The effects of flow-induced ATP release were also investigated. This was shown to have a significant impact on nucleotide concentration at the endothelium, leading to increases relative to the bulk concentration under conditions of rapid release. Currently, there is limited research about how relevant this effect is physiologically and the parameters that control it. Simulations were therefore carried out for a range of parameter values and Reynolds numbers. Under conditions of slow release, the increase in ATP concentration relative to the no-release case is greatest in regions of high wall shear stress (e.g. near to the stagnation point of an acute bifurcation). However, under conditions of fast release, the release mechanism dominates hydrolysis everywhere in the vessel, causing the surface concentration of ATP to increase steadily in the downstream direction.

There is some evidence that temporal wall shear stress gradients may contribute to the onset of atherosclerosis (White et al., 2001). The effects of pulsatile flow (as compared to steady flow of the same time-averaged Reynolds number) were therefore addressed. Although a pulsatile flow cycle created substantial temporal variations in wall shear stress, the time-averaged nucleotide concentration profiles exhibited very little difference compared to the steady case. This is due primarily to the fast time scale for the cardiac cycle compared to the slower time scale for nucleotide convection, diffusion and hydrolysis. This does not preclude the possibility that temporal variations in wall shear stress affect the physiological state of the artery wall, but does suggest that any such link is via some mechanism other than the modulation of chemical concentrations at the endothelial surface. Moreover, there is the possibility of different cardiac waveforms affecting the surface nucleotide concentration differently, which will be an interesting path to pursue.

Some very interesting characteristics of ATP/ADP concentration, brought about by arterial geometry variation, have been observed in this chapter. Ultimately, the combined nucleotide concentration at the inner wall did not alter significantly. Further chapters will address this issue by studying nucleotide concentration in complex spatially varying environments.

Chapter 7

Endothelial Nitric Oxide Synthase and Calcium Production in Arterial bifurcations and Bends

7.1 Introduction

This chapter presents the development of the physiologically relevant 3D geometries of bifurcations and bends, the results for mass transfer and the cell dynamics model. It thus provides insight into linking the prevailing haemodynamcs to important underlying cell dynamics and potential pathological implications.

7.2 Background

The mathematical model of cellular dynamics presented in chapter 5 has been incorporated into various physiologically important 3D bifurcations and arterial bend geometries. This is to provide insight into the cellular dynamics specific to these geometries, therefore leading to understanding of the spatial relationship between flow, reduced Ca^{2+} and eNOS signalling. This will evidence factors directly affecting the pathphysiology of the artery wall, in particular reduced NO activity. Previously, cell models have been limited to 2D geometries, without any evidence whether a 2D environment can infer the complex 3D nature of flow *in vivo*. The present computational analysis aims to shed some light on this topic.

The bifurcation geometries are varied through multiple bifurcation angles and this is predominantly motivated by observations that bifurcation angle has been implicated in the formation, severity and extent of atherosclerosis (Friedman

et al., 1993, Sharp et al., 1982). The models here will be able to determine regions of the vasculature subject to reduced eNOS as a function of this angle.

The results obtained for the mass transfer field in this study could apply to any blood borne species of low diffusivity, for example LDL. Low diffusion coefficient species exhibit a mass transfer boundary layer that is confined to a small region adjacent to the cell surface. Given that the endothelial cells are sensitive to the mechanical wall shear stress and to the surface ATP concentration, and that both these physiological signals are spatially varying, cellular behaviour will vary according to the position within the arterial geometry.

Finally, an in depth look at the effects of different flow waveforms on nucleotide concentration in arterial geometries is undertaken. Previously, this has been studied for WSS alone by Myers et al. (2001). They reported that the time average distribution between a sinusoidal and physiological coronary waveform were very similar, however the temporal evolution was significantly different (distribution follows form of inlet profile). Furthermore the consideration of pulsatile mass transfer in complex haemodynamic environments has had little attention. The interest here is whether the same is true for the transport of low diffusion coefficient species, such as ATP.

7.3 Model Development

7.3.1 Geometries

The arterial geometries were developed in SolidWorks (SolidWorks, Concord, Massachusetts, USA). Three arterial bifurcation angles were investigated $\theta = 37.5°$, $75°$ and $135°$; this was in order to provide insight into how differing bifurcation angles affect the transport of nucleotides, the distribution of wall shear stress and the subsequent intracellular dynamics. The dimensions of the bifurcation were a 3 mm (D_1) inlet diameter that bifurcates into two 2.38 mm (D_2) daughter arteries in accordance with 'Murray's law' (Zamir, 2000). These dimensions are representative of medium-sized arteries, in which atherosclerosis is known to occur. In all bifurcations the branching plane is the plane of symmetry.

The procedure for developing these models is outlined below.

An initial 2D sketch with the basic geometry was created on a plane surface, with the required branching angles being specified. Onto the ends of the 2D line sketch, orthogonal planar surfaces were attached, with the normal direction defining the axial direction of the artery, see Figure (7.1(a)).

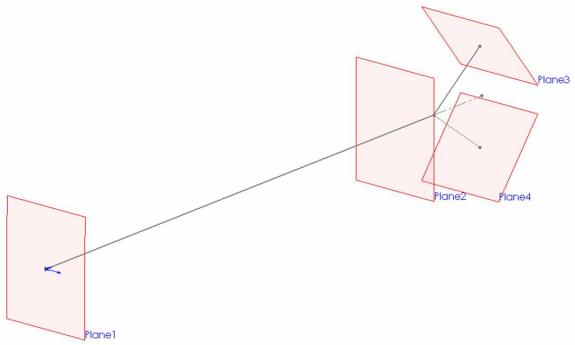

(a)

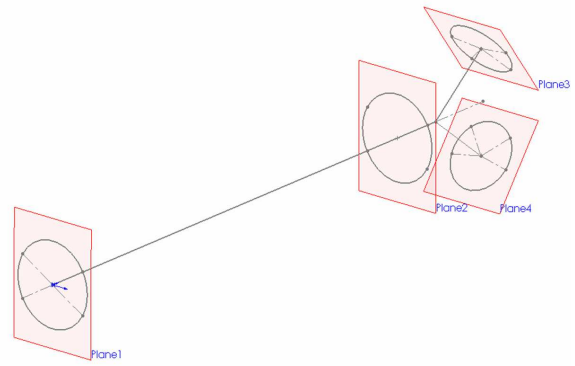

(b)

Figure 7.1: Geometry set up for the bifurcation model: (a) sketch of underlying geometry with planes inserted (b) sketches inserted on planes representing artery diameter.

Onto each planar surface a circle was drawn (Figure 7.1(b), in which the diameter was the diameter of the vessel in that location. The sketches on each plane are then lofted (B-spline interpolation) to its corresponding sketch on other planes to form a hollow surface of the artery as demonstrated in Figure (7.2(a)). The arrows indicate the direction of the lofted segment and the tangency to the adjoining face.

Finally, the leftover hollow sections on the upper and lower surface of the artery

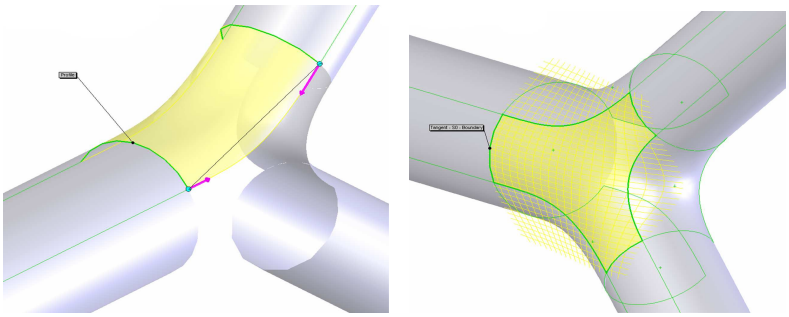

(a) (b)

Figure 7.2: Development of 3D surface: (a) lofting outer walls of bifurcation (b) filling of surface with tangent conditions at each edge on upper and lower wall.

were filled using a tangent fill condition. This applies surface tangency at each adjoining face, indicated by the mesh overlain in Figure 7.2(b), leading to the final smooth idealised artery model. This model was then solidified to create a geometry suitable for meshing. Figure 7.3(a) shows an example bifurcation geometry with mesh overlain.

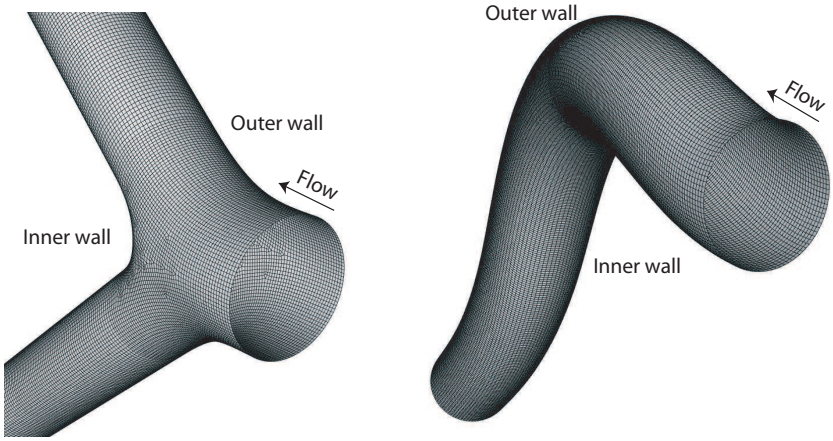

(a) (b)

Figure 7.3: Computational geometries used in simulations (a) bifurcation (b) bend. Inlet and outlet extensions have been removed.

Arterial bends are another region of the human vasculature known to be prone to atherogenesis. One arterial bend geometry was developed. Similar methods were utilised to develop the bend. An initial sketch of the underlying curvature of the model was created and a circle representing the arterial diameter was inserted onto the end points of the sketch. These sketches were then lofted and solidified to form the final model for meshing. The bend had a constant diameter of 3 mm (D_3) throughout. The geometry with mesh overlain is shown in Figure 7.3(b). This is similar to the bend Wada and Karino (2002) used in their computational

study of LDL transport. The bend consists of a mild curve in the entrance region, followed by a substantial curve in the opposite direction, and a mild curve on exit aligned the same as the inlet curve.

7.3.2 Mesh details

The mesh for the geometries contained 1.5 million volumes for the bifurcations, and 1.2 million for the bend. A hybrid mesh was created in the Fluent preprocessor Gambit. Both meshes consisted of a majority of hexahedral volumes. This is in part due to the high aspect ratio cells required to keep the mesh in practical limits which, with tetrahedral meshing, will lead to a mesh of poor quality. Due to the extremely low diffusion coefficient of ATP (large Peclet number), the species transport is convection-dominated. Therefore, it was important to divide the geometry in the immediate vicinity of the wall into sufficient elements to fully capture steep species gradients and prevent non-physical solution oscillations, as explained in Chapter 4. This region contained a structured boundary layer comprising of hexahedral elements that progressed from approximately $0.0021D_2$ (5 μm) to a total thickness of $0.064D_2$ (152 μm) over 14 layers. In the streamwise direction the minimum element size was approximately $0.025D_2$ (in the region of flow divider), progressing to a maximum of $0.34D_2$ at the flow exits. In the circumferential direction the daughter artery contained 90 elements for all geometries, whilst the inlet contained 120 elements. Similarly for the bend, the circumferential direction was divided into 100 elements and in the streamwise direction the minimum element was $0.013D_3$. Figure 7.4 shows a slice through the bend's computational mesh, demonstrating the fine resolution elements near the wall.

Mesh sensitivity tests were carried out to determine whether the solution of ATP concentration was sufficiently converged at two different Peclet numbers (5×10^6 and 8.3×10^6). Figure 7.5(a) and 7.5(b) respectively show the results at two different off wall mesh spacings. There is some mesh dependence exhibited, but from a computational perspective the 5 μm off wall mesh spacing is deemed suitable. Overall, the final mesh used provided for a very refined velocity field and a good balance between computational efficiency and accuracy for the mass transfer field.

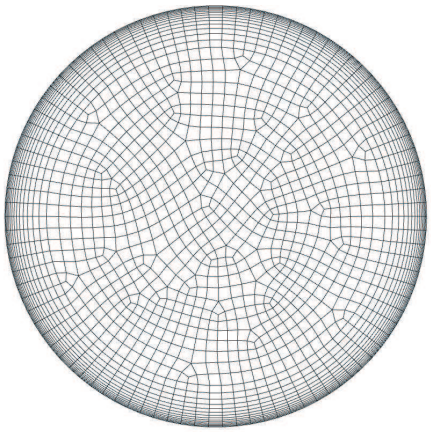

Figure 7.4: Slice of computational mesh, showing the very refined mesh in the vicinity of the arterial wall.

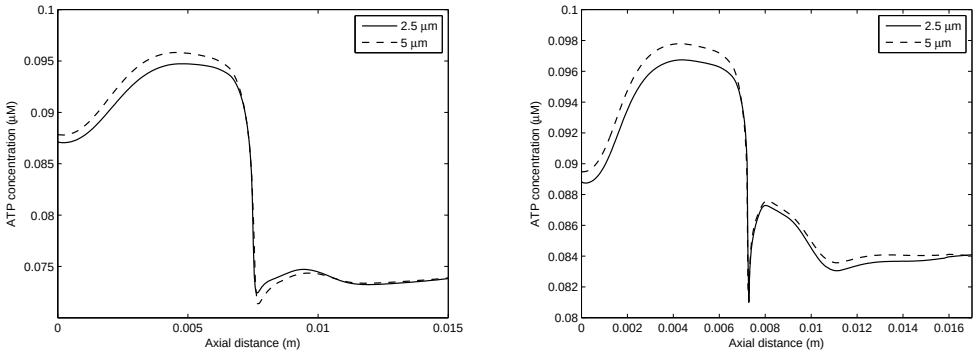

(a) (b)

Figure 7.5: Convergence tests for the solution of ATP concentration for two different off wall spacings(2.5μm and 5μm): (a) Pe=5×10^6 (b) Pe = 8.3×10^6. There is a some mesh dependency exhibited, but essential features exist for 5 μm off wall spacing.

Variations in circumferential element spacing was investigated to capture changes in flow feature related measures. The WSS shown in Figure 7.6 shows little difference between the two spacings and this refinement had no effect on the final ATP solution.

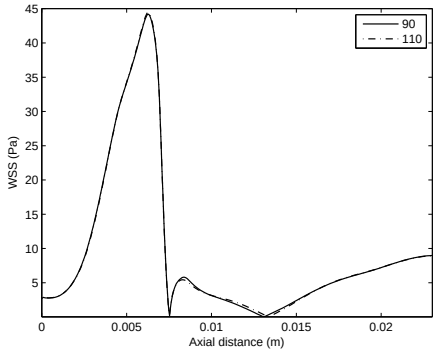

Figure 7.6: Variations of circumferential spacing, visibly WSS changes only slightly between 90 and 120 elements.

7.3.3 Flow and Mass transport

The simulations were carried out using Finite volume CFD solver Fluent. Information regarding boundary conditions is provided in Chapter 3 for the flow field and Chapter 4 for the mass transfer field. Simulations were carried out at Reynolds numbers of 200 and 500 (based on the inlet diameter) for the arterial bifurcations, and 300 and 500 for the arterial bend. This was to provide an understanding on how different flows, such as the larger recirculations expected at higher Reynolds numbers, affect the transport of ATP to the surface and the resultant endothelial signalling. The elevated Reynolds number is expected to be representative of peak diastole conditions or during a period of mild exercise.

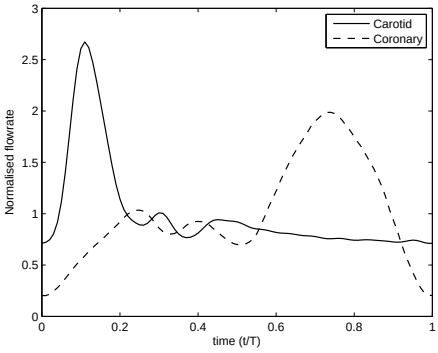

Figure 7.7: Pulsatile inlet waveforms, Carotid waveform given by Ku et al. (1985), and coronary waveform given by Matsuo et al. (1988). The profiles have been scaled to a mean Reynolds number of 200 and 300 for the bifurcation and bend respectively.

Although it has been reported that the time-averaged nucleotide concentration during pulsatile flow differs little from the concentration during steady flow

(John and Barakat, 2001), this has yet to be validated in regions where the flow has characteristics such as flow separation and recirculation. The 2D bifurcation in Chapter 6 did not exhibit these characteristics. This is not expected to occur on the outer wall, due to the advent of flow recirculation, but will potentially provide some interesting effects on the final luminal concentration. Two different pulsatile waveforms, as shown in Figure 7.7, were considered: a carotid waveform given by Ku et al. (1985) and a coronary given by Matsuo et al. (1988). Simulations for the carotid waveform were carried out on the bifurcation geometry, whilst the coronary waveform was applied to both geometries under consideration. The mean Reynolds number was 200 and 300 respectively for the bifurcation and bend. All waveforms were divided into 100 time steps. The Womersley number of the flow was 2.1. Data was recorded after eight complete cycles in order to eradicate any start up transients; this is particularly important for low diffusion coefficient species in which transients persist for many cycles. After eight cycles the agreement in ATP concentration between successive cardiac periods differed by less than 1% and no variation was observed in WSS. The numerical solution algorithms are outlined in Chapter 3.

Solutions were considered converged when the scale residuals dropped below 1×10^{-5}, at which point no further change in the surface WSS was observed. Steady state simulations took approximately three hours on a single node (2 processors) of the Beowulf cluster mentioned in Chapter 3. Solution of the Ca^{2+} and eNOS model took approximately 20 minutes. For transient simulations, due to the computationally intensive nature, a balance had to be determined between number of compute nodes and network latency. Solution tests were carried out over 100 iterations to determine the time per iteration versus number of processors (Figure 7.8). A good balance between resource usage and convergence time was obtained using eight processors (four compute nodes).

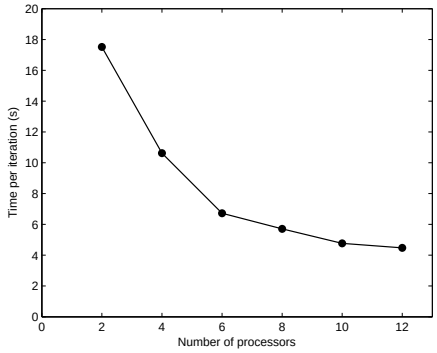

Figure 7.8: Time versus number of processors for an iteration of the transient ATP simulations. Each dot represents one additional compute node.

7.4 Results

7.4.1 Arterial bifurcation

Flow characteristics

The flow features of the bifurcation are similar to previous studies, with the finite curvature and branching between the parent and daughter artery causing the flow to assume a helicoidal trajectory rotating about the streamwise axis. In detail, the curvature of the outer wall induces a radial pressure gradient (or centripetal acceleration) towards the inner wall. Thus high inertia fluid is 'thrust' towards the inner wall of the bifurcation (7.9). To satisfy the continuity condition, flow is then diverted around the peripheral of the artery towards the outer wall. The pressure gradient, induced by the curvature, leads to the low momentum fluid at the outer wall flowing towards the inner wall, hence setting up secondary flows. Figure 7.10 details streamlines showing helicoidal nature of flow and low velocity region near the outer wall.

Secondary flow is highly dependent on the bifurcation angle, with the symmetric counter-rotating helicoidal flows each side of the mid plane strengthening with increasing bifurcation angle θ. This is demonstrated in Figure 7.11. This is to be expected, because as the radius of curvature through which the flow is diverted decreases (bifurcation angle increase) centripetal acceleration increases. This is further evidenced by considering velocity contours (Figure 7.12), where

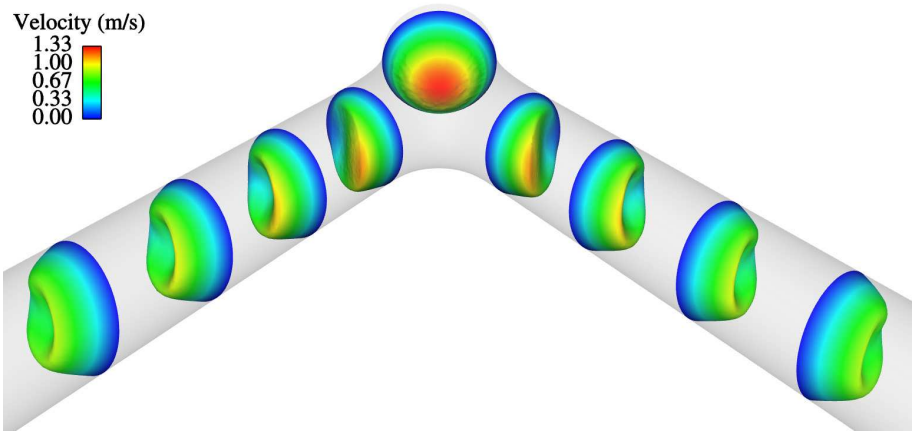

Figure 7.9: Elevated velocity contours in a 75° bifurcation, Re=500. High momentum fluid is thrusted towards the inner wall of the daughter artery due to the curvature of the outer wall.

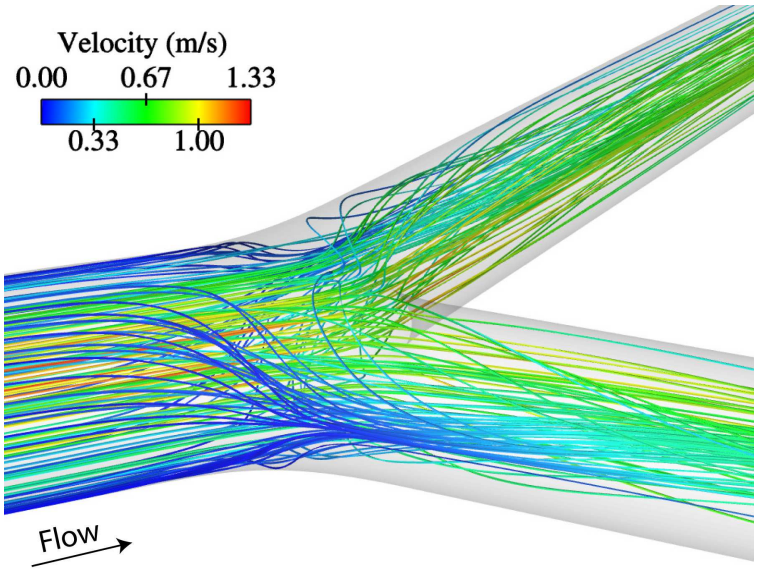

Figure 7.10: Streamlines in a perspective view of the 75^o bifurcation, flow is from left to right. Substantial retarding of the flow occurs on the outer wall.

the small angle bifurcation is characteristic of lower Dean numbers, whereas with increasing θ the effects of circumferential flow are evident and is characteristic of higher Dean number and distortion of the profile in the circumferential direction (Berger et al., 1983).

The stronger secondary flow leads to larger velocity gradients at the artery wall (due to high inertia fluid near the inner wall), which maintains the WSS in a higher range with increasing θ.

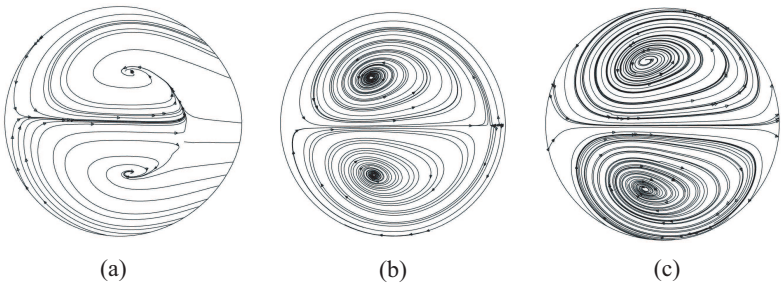

Figure 7.11: Secondary flow streamlines in the daughter artery: (a) 37.5° (b) 75° (c) 135°. The vortices strengthen as θ increases, and move closer to the outer wall (left hand side of each cross section). The slight asymmetric breaking is due to the use of unstructured meshes, hence seeds for particle release (at cell centres) are not symmetric over a given cross section.

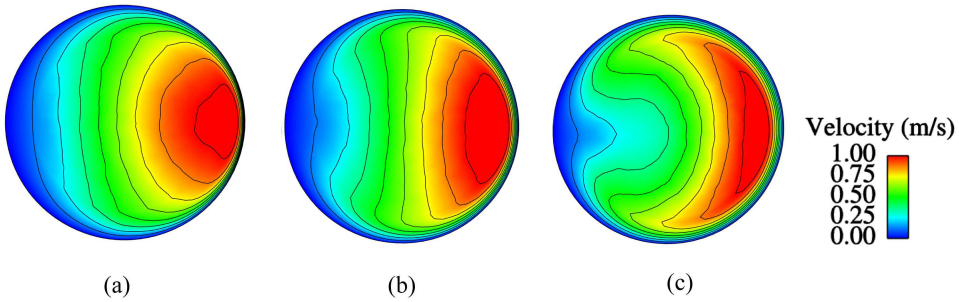

Figure 7.12: Axial velocity contours immediately downstream of the bifurcation (limited to one for visual purposes): (a) 37.5° (b) 75° (c) 135°. For lower angles the profiles are characteristic of low Dean number flow, whilst for larger angles axial distortion is evident.

As of result of counter-rotating flows, following the flow divide, the velocity profile is skewed to the inner wall, leading to high WSS in this zone. On the outer wall a large region of low velocity flow exists, with the central part of the low velocity region extending into the vessel and forming a horseshoe profile; this profile results from the characteristic Dean vortices, brought about by curvature. For smaller angle bifurcations the same skewing of the profile occurs, but the low velocity region spans a wider portion of the outer wall, due to substantially reduced secondary flows and reduced circumferential fluid velocity.

From the numerical simulations, it was found that the regions of low wall shear stress are localised on the outer wall of the bifurcation. This result is irrespective of bifurcation angle and Reynolds number.

At the inner wall of the bifurcation the wall shear stresses observed are high,

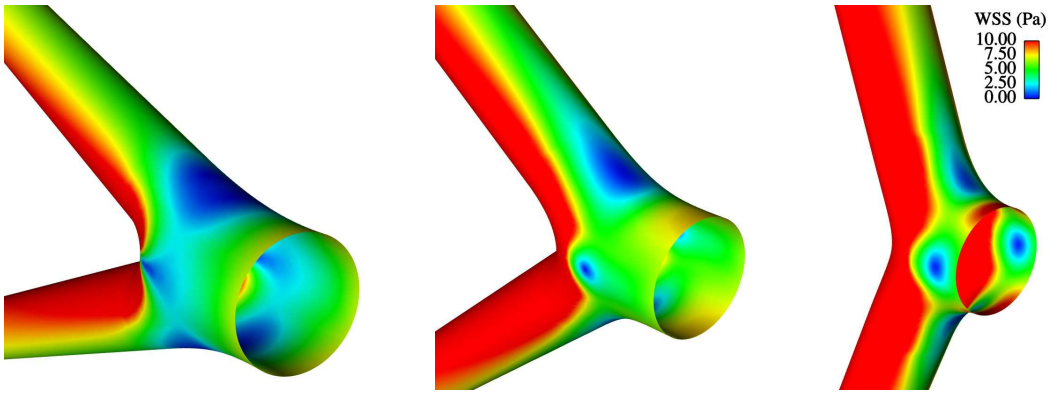

(a) (b) (c)

Figure 7.13: Contours of WSS magnitude, $Re = 500$: (a) $\theta = 37.5°$; (b) $\theta = 75°$; (c) $\theta = 135°$. Regions of reduced WSS increase with decreasing θ. This is consistent with the secondary flows observed.

regardless of the bifurcation angle, so this area is unlikely to be of significance for the onset of cardiovascular disease. Examining WSS in detail along a cut plane through the outer wall (Figure 7.14) reveals a relationship between low WSS and smaller bifurcation angle. Clearly the Reynolds number plays a central role: at $Re = 500$ lower overall wall shear stresses are observed on the outer wall and this is attributed to the stronger secondary flows that lead to a larger low velocity fluid region in the vicinity of the outer wall. However, it is the *spatial* variation in WSS that is of primary interest here. The key observation is that the outer wall of the bifurcation is subjected to relatively low WSS irrespective of the Reynolds number and the region of low WSS is larger for smaller bifurcation angles.

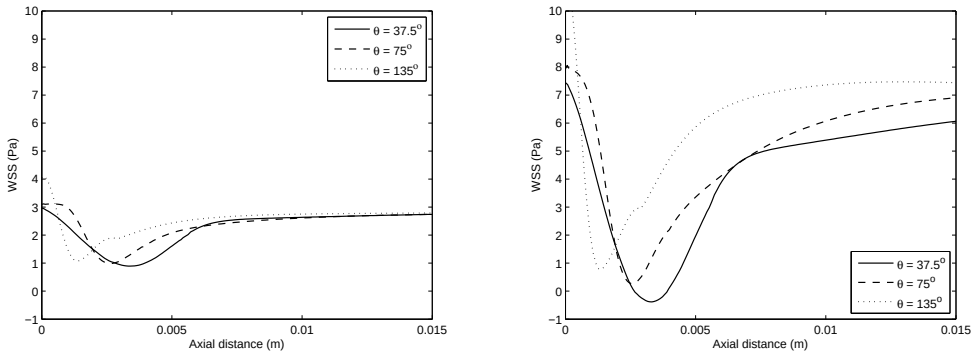

(a) (b)

Figure 7.14: WSS plotted along a cut plane through the outer wall of the bifurcation: (a) $Re = 200$ (b) $Re = 500$. The minimum WSS decreases as θ decreases.

Nucleotide concentration

ATP concentration undergoes an overall decline in the streamwise direction, but increases/ decreases in response to various flow conditions. In Chapter 6 the ATP concentration was assessed at the inner wall of a 2D bifurcation and it was found that ATP responds to the WSS magnitude. Additionally, another study investigated ATP concentration over a 2D backwards facing step and again WSS and Reynolds number was significant (Plank et al., 2006a). While WSS magnitude is 'reasonably' related in 3D, the most important controller is the WSS vector. This is affected by complex flow structures such as secondary vortices. Secondary vortices are responsible for the growth of the mass transport boundary layer in the outer wall regions, which results in substantial depletion of ATP at the surface. This occurs due to the convection of ATP from the outer to the inner wall, hence reduced convection of ATP into the boundary layer (see Figure 7.15).

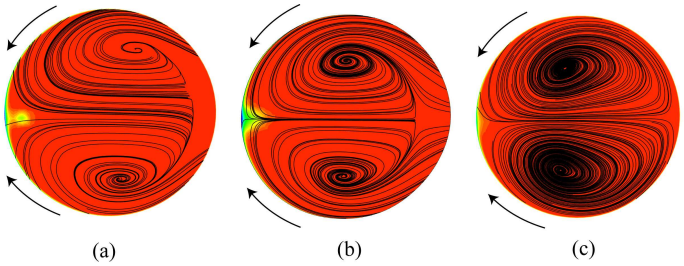

Figure 7.15: The strengthening of the counter rotating vortices results in enhanced delivery of ATP to the surface as θ increases, (a) $\theta = 37.5°$ (b) $\theta = 75°$ (c) $\theta = 135°$, Re=500. The separation of the low concentration region into a region close to the wall and another within the fluid domain at $\theta = 37.5°$ is due to the formation of a recirculation zone.

In simplified 2D geometries secondary flow features do not exist, so essential features are lost in the simplification that can not be inferred by extrapolating the velocity field. Figure 7.16 shows surface ATP concentration contours (under no release conditions) on the outer wall of a 75° bifurcation with stress lines (vector valued WSS trajectories resolved over the surface (Tobak and Peake, 1982)). Evidently, the surface depletion follows these flow patterns very closely and the location of reduced ATP concentration corresponds to the meeting of two Dean vortices. Additionally the variation being strongly dependent on these patterns shows the dependence on secondary flows. The depletion at the surface is greater for smaller bifurcation angles as a result of weakened secondary vortices. Although there is evidence that ADP is also capable of eliciting responses by the

endothelium, it is also important to consider ATP alone to understand the mass transfer processes occurring, because ATP is the sole agonist that activates the P_{2X} receptor (ion channel), which has recently being identified as a vasoactive signalling receptor (Yamamoto et al., 2006).

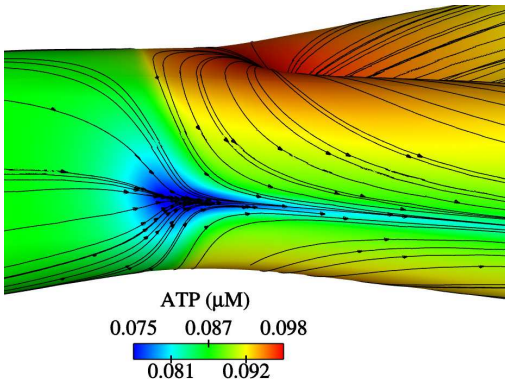

Figure 7.16: ATP contours with stress lines overlain, $\theta = 75°$, $Re = 500$. This is a perspective view looking at the outer wall. Where the streamlines converge on the outer wall corresponds with minimum ATP concentration (hence mass transfer) and as the bifurcation angle is reduced, this region expands undergoing further depletion (data not shown).

The present simulations have also included the effects of flow-induced ATP release. Figure 7.17(a) shows the results for a Reynolds number of 500 and τ_0 = 3.16. Although the surface ATP is elevated with respect to the bulk concentration (0.1 μM), there is a definite reduction of nucleotide concentration in the vicinity of the outer wall. Similar results were obtained throughout the investigated bifurcation angles with lower nucleotide concentration on the outer wall as θ decreased. Reducing the value of the reference WSS τ_0 results in a similar profile, but with higher nucleotide concentrations (Figure 7.17(b)). The reduction that ocurrs at the outer wall is a complex balance between ATP delivery, WSS magnitude and hydrolysis. Where reductions in surface ATP concentration occur is a direct result of low WSS magnitude and boundary layer growth. Low WSS magnitude results in limited release of ATP into the lumen. This coupled with boundary layer growth results in reduced delivery of ATP into the boundary layer, thus the surface nucleotide concentration is depleted.

The current model of ATP release contains a number of limitations. For example, there would be uneven release over the surface of the endothelium and the stores of intracellular ATP would deplete after a certain period of activation,

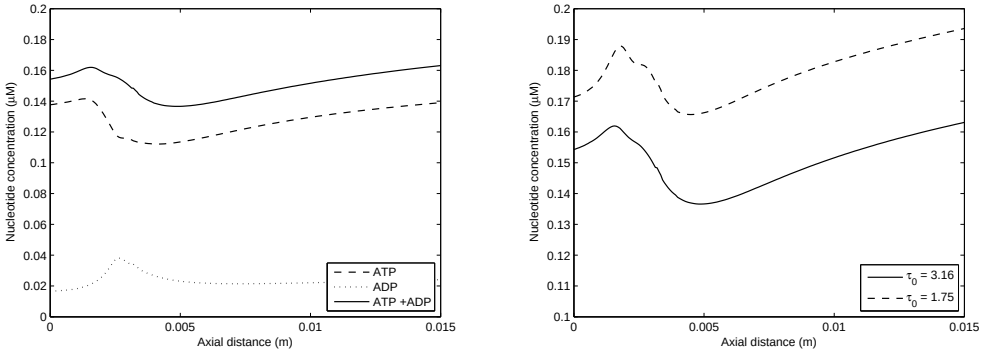

(a) (b)

Figure 7.17: Nucleotide concentration along the outer wall of the 75° bifurcation, $Re = 500$: (a) ATP, ADP and ATP+ADP concentration for τ_0=3.16. (b) ATP+ADP concentration for different ATP release rates. It is clear that the outer wall of the bifurcation is subject to reduced combined nucleotide concentration relative to other regions.

eventually leading to no-release conditions. Therefore, the response would most likely consist of an initial transient release that decays. Future models will attempt to address these issues and include the cell dynamics that lead to ATP release. The present analysis, including both no-release and varying degrees of release, covers the different situations that may be encountered *in vivo*.

Endothelial cell signalling

The surface distributions of shear stress, ATP concentration (under slow release conditions) and ADP described above act as the external factors driving the intracellular signalling of the endothelial cells. At each grid point on the artery wall, the local WSS τ_w and surface concentration $\phi = \phi_1 + \phi_2$ of ATP+ADP are used as the 'inputs' to the model presented in chapter 5 via equations (5.2), (5.3) and (5.12). This enables the steady-state distribution of important intracellular chemicals such as calcium and eNOS to be evaluated. Again following the WSS and ATP+ADP concentration patterns, regions of reduced cytosolic calcium are found predominantly on the outer wall (data not shown). This, and also low WSS directly, leads to reduced activation of eNOS: Figure 7.18 shows the resulting eNOS concentration contours. All bifurcation angles are subjected to a region of low eNOS concentration.

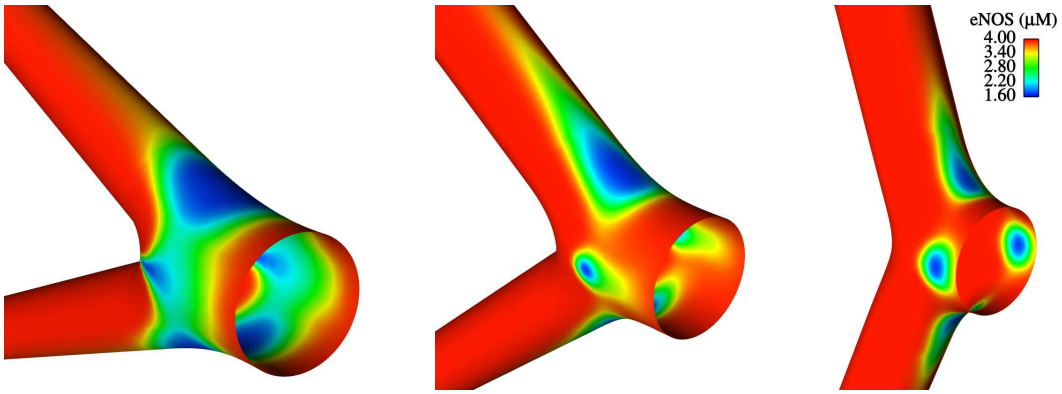

(a) (b) (c)

Figure 7.18: Contours of eNOS concentration, $Re = 500$: (a) $\theta = 37.5°$; (b) $\theta = 75°$; (c) $\theta = 135°$ Regions of impaired eNOS signalling increase with decreasing θ.

Observing a cut plane (Figure 7.19), it is evident that, although the level of depletion does not change considerably for the investigated range, smaller angle bifurcations contribute to sustained low eNOS concentration over a larger portion of the endothelial surface. The extended region of depleted eNOS concentration at a bifurcation angle of $\theta = 37.5^0$ results from flow recirculation. There is a clear relationship between the eNOS concentration and the WSS, but ATP does not show a strong relationship with the resulting distribution.

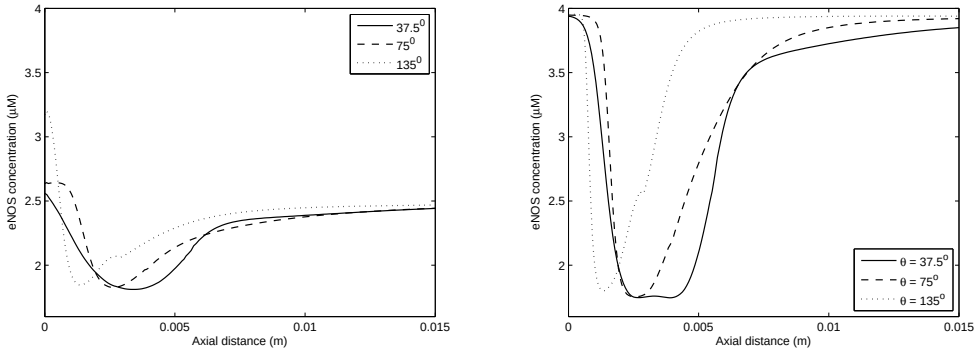

(a) (b)

Figure 7.19: eNOS concentration along a medial cut plane of the bifurcations outer wall: (a) Re=200 (b) Re=500.

The results suggest that the low WSS region found on the outer wall will be more susceptible to endothelial dysfunction at all bifurcation angles, but it is hypothesised that this is more likely to occur on the outer wall of acute angle

bifurcations. In addition to the outer wall depletion, there is a region of low eNOS concentration located on the top and bottom of the bifurcation shown in Figure 7.18. However, the severity and extent of this depletion has been observed to change significantly depending on the curvature of the geometry in this region.

7.4.2 Arterial bend

Arterial bends are also subject to disturbed flow conditions, such as detachment and recirculation, and are prone to atherosclerosis (Asakura and Karino, 1990). Simulations were carried out at Reynolds numbers of 300 and 500. Additionally, unsteady simulations were carried out to investigate the variation of nucleotides under this flow condition.

Flow characteristics

The flow characteristics in the arterial bend are as expected, exhibiting secondary flows (Dean vortices) and skewed velocity profiles towards the outer walls of the bends (Figure 7.20) due to the radial pressure gradient (or centripetal acceleration) induced by the curvature. These flow features are well documented in literature.

A standing recirculation zone forms at the inner wall of the second bend, see figure 7.21(a). The change of curvature between the first mild bend and the second major bend induces peripheral flow to come down from the outer wall encircling the main flow. This flow phenomenon is demonstrated in figure 7.21(b). At the inner wall the peripheral flow slows rapidly as it encounters the recirculation at the inner wall; this flow is then pulled in the upstream direction due to an adverse pressure gradient, before finally being pulled rapidly back into the main flow. The extremities of this range define a point of flow separation and flow reattachment. The flow characteristics for the two Reynolds numbers are very similar, just amplified more at $Re = 500$.

Figure 7.22 shows that, for both Reynolds numbers investigated, the inner and outer walls of the bend both exhibit a region of low WSS. For $Re = 500$, there is a small region of higher WSS within the recirculation zone, but this

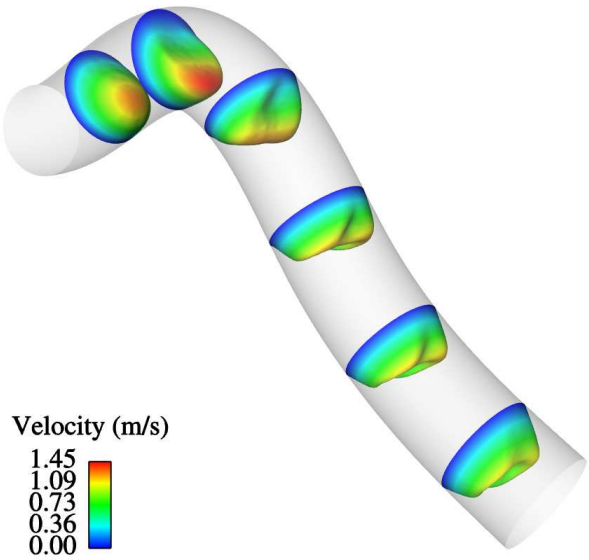

Figure 7.20: Elevated axial velocity contours through the arterial bend, Re=500. The second major bend forms characteristic Dean like velocity contours (horse show profile).

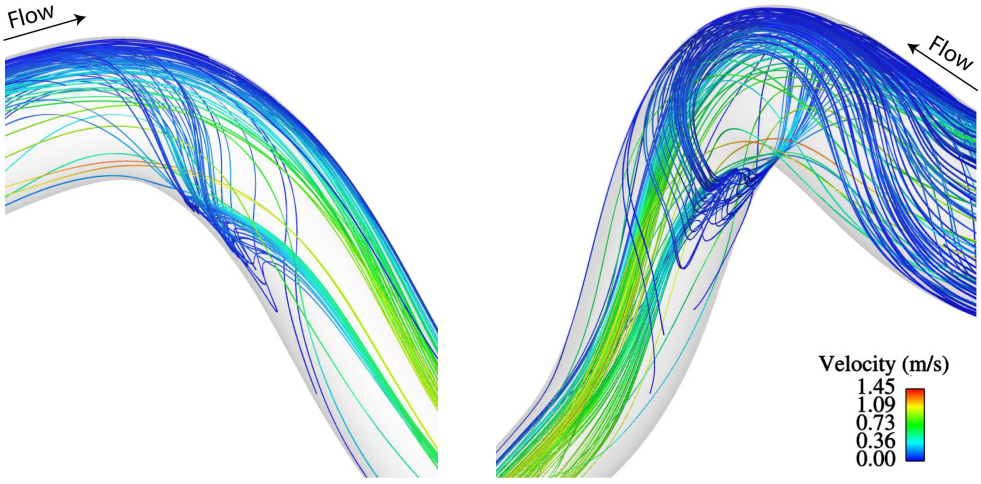

(a) (b)

Figure 7.21: Streamlines in the artery bend, Re=500: (a) side view showing the recirculation zone (b) perspective view demonstrating peripheral flows that come from the outer wall and interact with the recirculation zone.

region is still predominantly a low wall shear region. The recirculation zone is similar for both Reynolds numbers, but occupies a larger region of the inner wall at $Re = 500$.

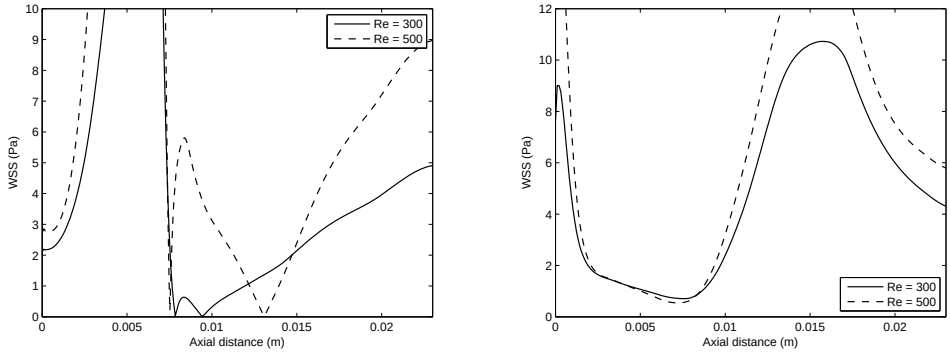

Figure 7.22: WSS plotted along a cut plane through the walls of the bend, $Re = 300$ and 500: (a) inner wall (b) outer wall. Essentially, the elevated Reynolds number provides for amplified responses.

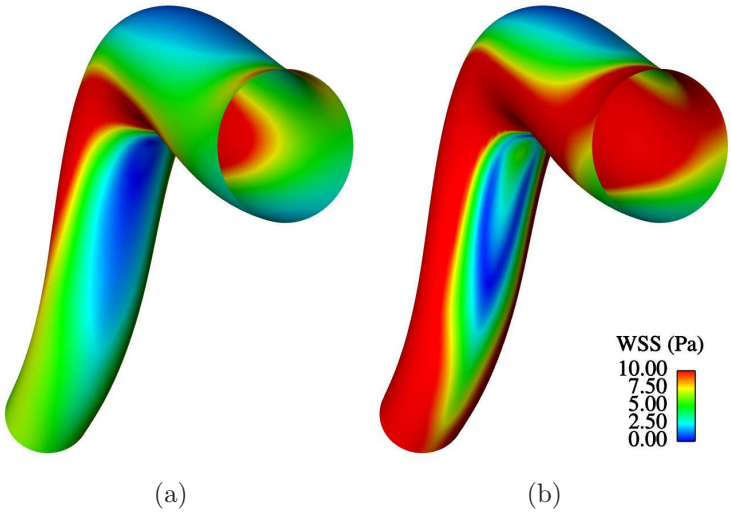

Figure 7.23: Contours of WSS magnitude: (a) Re=300 (b) Re=500.

Nucleotide concentration

The flow characteristics such as flow separation (nodal point) and reattachment (saddle point-which is a necessary condition for flow separation (Tobak and Peake, 1982)) lead to impaired mass transfer, with both locations subject to reduced ATP concentration, again following the limiting flow patterns closely. Figure 7.24 shows the distribution with stress lines for Re=500.

This bend geometry clearly shows that WSS magnitude is not as closely

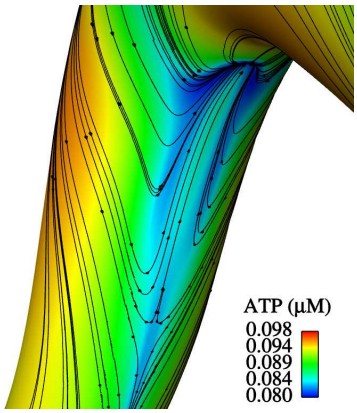

Figure 7.24: ATP contours with stress lines overlain on a perspective view looking at the inner wall, Re=500. The location of minimum ATP concentration is located at the nodal point of separation where all streamlines converge. Furthermore the general influence of these patterns on ATP concentration is notable, for example where peripheral flow changes direction (wall stagnation) impaired mass transfer is observed.

related to surface ATP concentration as was predicted by the wedge 2D analysis. On the side walls of the bend the WSS magnitude is very high (>10Pa), as shown in Figure 7.23, but the ATP concentration is not necessarily high and is even observed to deplete along a band from the outer wall to the inner wall (Figure 7.25).

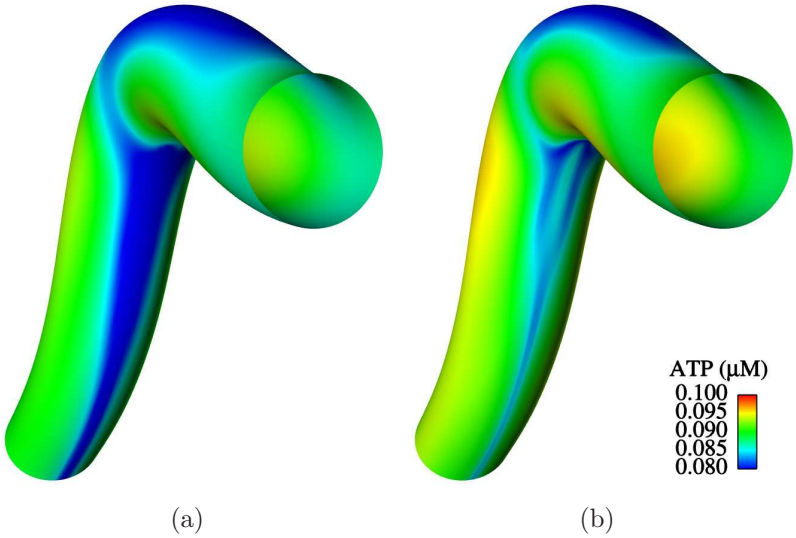

Figure 7.25: Contours of ATP concentration: (a) Re=300 (b) Re=500. No flow induced ATP release.

Due to the flow detachment, a significant growth of the concentration bound-

ary layer is observed at the inner wall. This is 'pulled' into the main flow along the 'boundary' of the separation zone (the jet of fluid that propagates from the inner wall into the main flow in Figure 7.21(a)). Within the recirculation zone, convective transport results in a slight increase in the ATP concentration. At $Re = 500$, the low concentration region moves to either side of the central plane, leaving at the point of flow detachment, extending along each side of the central plane and rejoining at the point of flow reattachment. This is a wall stagnation line where the peripheral flow that comes around from the outer wall (Figure 7.21(b)) meets the reverse flow at the inner wall, creating a region of stagnant fluid. Again, the depletion is related to secondary flow features, where the vortices meet the recirculation zone at the inner wall, which leads to convective transfer away from the wall, hence a zone of depleted ATP. At $Re = 300$, the lower flow velocities and reduced secondary flow allow further depletion of ATP at the artery wall. The minimum in ATP concentration at the reattachment point is an interesting flow phenomenon and further validates the need for 3D flow fields; in 2D geometries the ATP concentration is maximum at the reattachment (Plank et al., 2006a).

Following the addition of ATP release (Figure 7.26), again there is elevated concentration with respect to the bulk, but as has previously been demonstrated in 2D backwards facing step geometries Plank et al. (2006b), the concentration at the stagnation point is minimum. In the present case, there is no stagnation streamline, rather in the limit there is a streamline that defines the location of reattachment; this location corresponds to the minimum in ATP concentration in Figure 7.26. At the location of flow detachment the ATP concentration drops rapidly, but due to the peak in ADP concentration resulting from this there is no rapid drop exhibited by the combined stimulus. Interestingly, the first curvature of the bend results in a depletion of both ATP and ADP. This is due to the combined effects of peripheral flow convecting ATP away and general decrease in wall shear just prior to the first mild bend, hence hydrolysis of ATP counters the effects of ATP release and the strong peripheral flows mean ADP is also depleted.

Endothelial cell signalling

Figure 7.27 shows the spatial variation of eNOS (Again this is using the combined ATP+ADP concentration with slow ATP release). The inner and outer wall are both subjected to reduced eNOS levels (due to the combined effect of

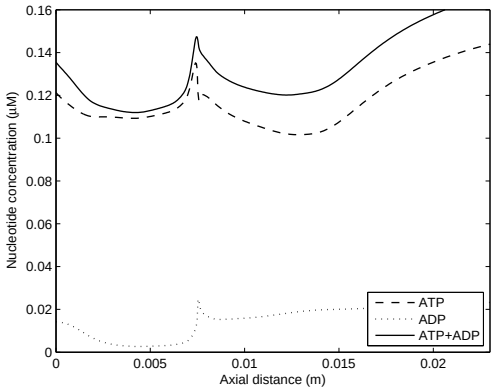

Figure 7.26: Nucleotide concentration under slow release conditions plotted along the inner wall of the arterial bend, Re=500. The location of minimum nucleotide concentration corresponds to the flow reattachment point.

impaired calcium signalling and low WSS). Again these correspond to regions of flow recirculation and, in particular, low WSS. For the higher Reynolds number, the region of impaired signalling is reduced, but the inner and outer walls are still areas of relatively low eNOS activity. The inner wall contains a small portion of high eNOS concentration, as a consequence of the WSS in this region resulting from a strong recirculating flow.

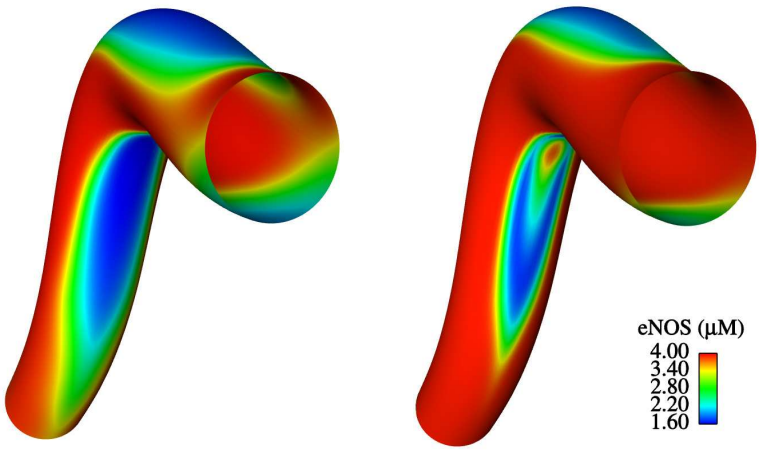

(a) (b)

Figure 7.27: Contours of eNOS concentration: (a) $Re = 300$; (b) $Re = 500$. Reduced eNOS signalling is observed at the inner and outer wall, which will result in reduced production of NO. The regions of reduced signalling are more significant at the lower Reynolds number.

Plotting along the centreline of the bend's walls (Figure 7.28) highlights the key aspects: eNOS concentration is low in regions of low WSS, particularly where the flow detaches or reattaches. The region of constant eNOS concentration, of around 4 μM, prior to the flow detachment on the inner wall is due to the very high WSS in this area, which results in saturation of eNOS activation.

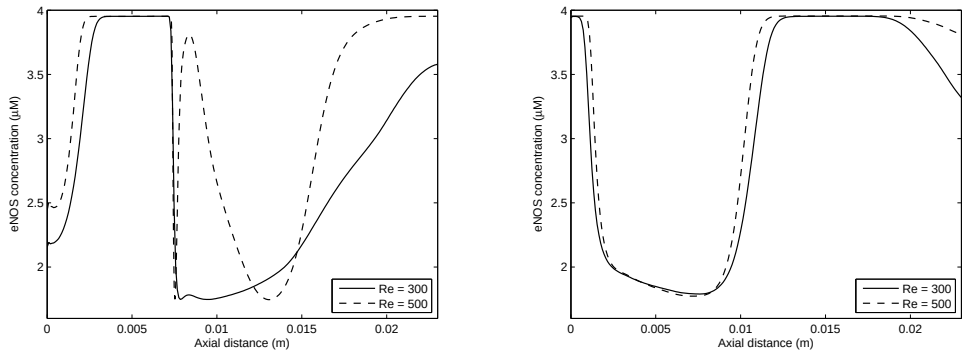

(a) (b)

Figure 7.28: Endothelial NOS concentration plotted along the central axis of the arterial bend walls, $Re = 300$ and 500: (a) inner wall (b) outer wall. Endothelial NOS concentration is low in the regions corresponding to low WSS.

7.4.3 Pulsatile flow

In order to validate the use of steady-state simulations, pulsatile simulations were also performed. Moreover, there is little data available in literature regarding transients under realistic waveforms and how different waveforms affect surface concentration, hence simulations are carried out under waveforms from a carotid and coronary artery.

Time averaged

The time averaged ATP concentration over the course of a cardiac cycle of period T is given by

$$\bar{\phi} = \frac{1}{T}\int_0^T \phi \; dt.$$

This was plotted along the cut plane of the bifurcations outer wall and the inner and outer wall of the bend so comparisons could be made to the steady state concentration. For the bifurcation the time varying concentration is reduced compared with the steady state (Figure 7.29(a)). Evidently the WSS distributions are similar for steady and unsteady (Figure 7.30(a)). To understand the further depletion variation of the instantaneous wall shear vector was investigated by calculating the oscillatory shear index (OSI), this was shown to spike up in the region where the time averaged ATP concentration drops, see Figure 7.30(b). The primary contribution to this OSI was a brief period of flow separation induced by the adverse pressure gradient late systole for the carotid waveform and late diastole for the coronary. This period of separation late systole results in attenuated ATP delivery, hence reduced surface concentration compared with steady state. The effects of different cardiac waveforms provides for very similar depletion at the surface. The inclusion of ATP release results in significantly closer tracking between the steady and unsteady.

For the bend similar characteristics were observed with the time variance exhibiting very similar characteristics to the steady, again the rapid drop in ATP concentration corresponds with a low mean WSS. However in addition WSS is

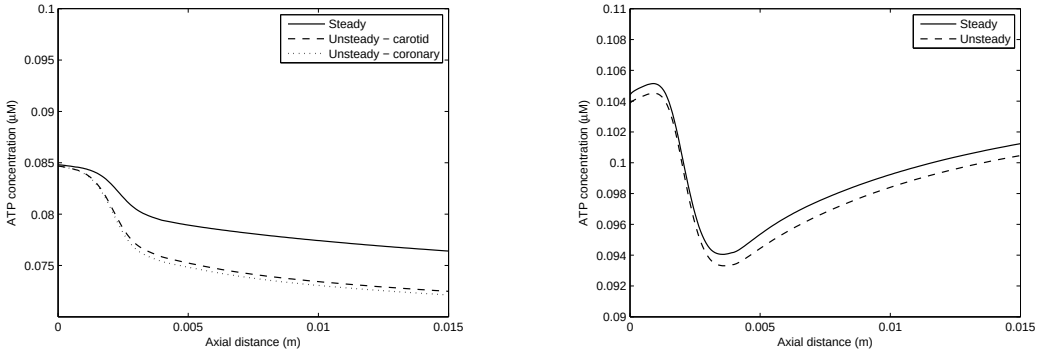

(a) (b)

Figure 7.29: ATP concentration in steady flow and time-averaged concentration in pulsatile flow plotted along medial plane of the outer wall of the bifurcation: (a) No ATP release (b) with ATP release. Evidently the steady state exhibits essential features of the time averaged profile.

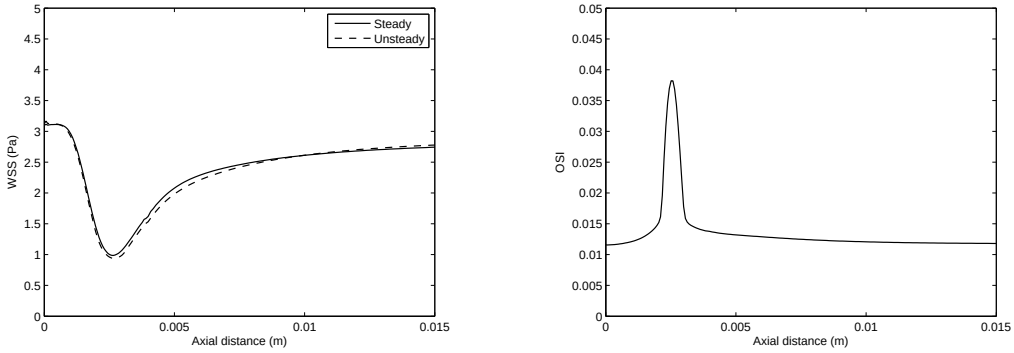

(a) (b)

Figure 7.30: Temporal WSS and related indices: (a) Time averaged WSS compared with the steady state, evidently there is very good tracking between the two profiles. (b) OSI along the outer wall of the bifurcation. WSS is slightly more oscillatory in the the region corresponding with a reduced ATP concentration (for no release and release conditions). Note the OSI scale has been limited to 0.05, hence representing only a small increase.

highly oscillatory in this location, nearly purely (0.48 where 0.5 corresponds to purely oscillatory).

The depletion at the surface being lower under steady conditions is due to the standing recirculation zone that forms (Figure 7.31(a)), whilst in unsteady flow this is non existent during the systolic phase, with the flow being unidirectional. At the outer wall (Figure 7.31(b)) the depletion is greater under unsteady con-

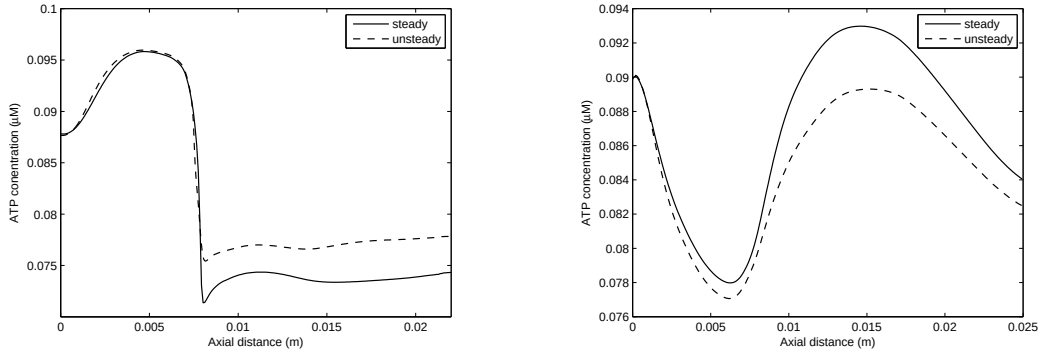

(a) (b)

Figure 7.31: ATP concentration in steady flow and time-averaged concentration in pulsatile flow plotted along the central axis of the arterial bend walls: (a) inner wall (b) outer wall. The pulsatile flow was simulated using the coronary flow waveform given by Matsuo et al. (1988) (Figure 7.7). The two profiles exhibit very similar characteristics, but the surface depletion varies slightly.

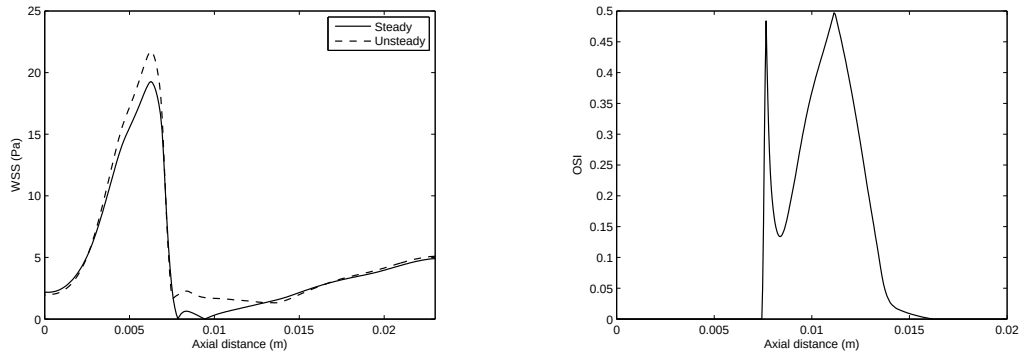

(a) (b)

Figure 7.32: Time varying WSS indices (a) mean WSS (b) OSI.

ditions due to the formation of a recirculation zone. Understanding the effects of OSI on ATP concentration in more detail comparing Figure 7.32(b), with a zoomed in region of low ATP concentration, Figure 7.33, max OSI occurs prior to this region. The location of low ATP concentration is associated with attenuated transport within the recirculation zone and more sustained lower concentration over the cycle is involved with the location of relatively low WSS and intermediate OSI level. The second drop in ATP concentration occurs where the mean WSS is low (due to stagnant flow). In this location the OSI is at an intermediate to low level. Additionally, at flow separation there is also very low mean WSS

(Figure 7.32(b)(a)).

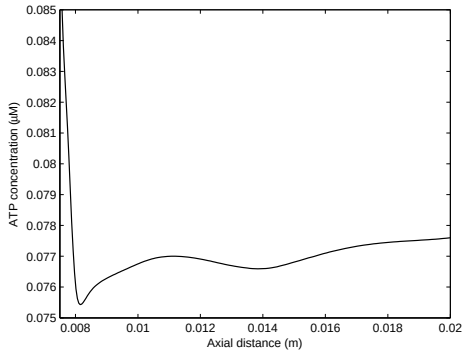

Figure 7.33: Detailed temporal mean ATP concentration along the medial cut plane in the recirculation zone. The minimum ATP concentration corresponds with the location of reasonbly low mean WSS and elevated OSI. The maximum post flow separation corresponds with low WSS coupled with high OSI.

The results suggest that there is a difference in concentration between pulsatile and steady flow. However, this difference is quite small and was within 4% for the arterial bend and 6% for the arterial bifurcation, whereas spatial variation over the entire surface is in the range of 0.075-0.098.

Transients

Previously, little information has been reported on transient effects of low diffusion coefficient species. Both waveforms were considered for the bifurcation, whereas in the bend only a coronary waveform was considered. Figure 7.34, shows the transient effects at a specific spatial locations. Figure 7.34(a) shows the sampling locations for the bifurcation and bend (looking at the inner wall). Locations A, B, and C in the bifurcation are progressing along the outer wall in a low shear region, whilst D is in a region where the WSS follows the inlet waveform pattern. This is in agreement with a previous study by Myers et al. (2001) looking solely at WSS, where temporal characteristics were found to be very waveform specific. In the Bend location 1 corresponds with a higher shear region (again WSS following inlet waveform), whilst locations 2, 3 and 4 progress through the recirculation zone. Sampling in other locations around the artery wall provided for very similar characteristics (data not shown).

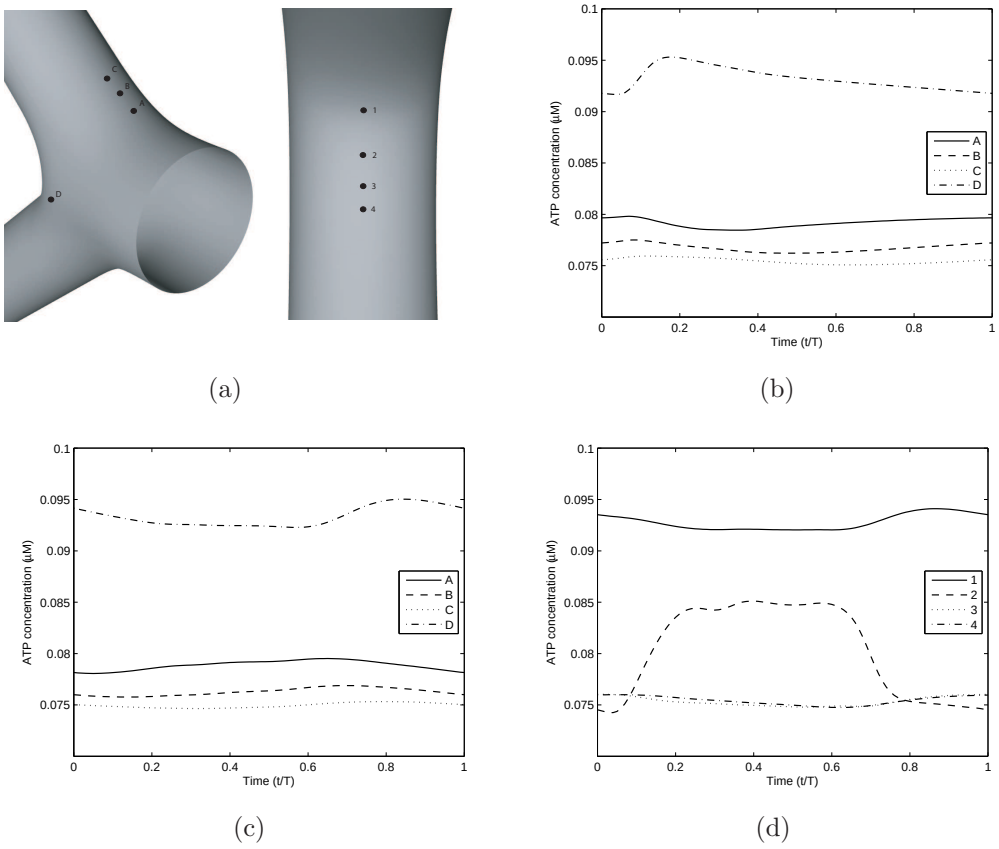

Figure 7.34: Time variations in ATP concentration for different flow waveforms: (a) Sampling locations on the bifurcation and the bend (looking at the inner wall) (b) bifurcation with carotid waveform (c) bifurcation with coronary waveform (d) bend with coronary waveform.

Evidently, the variations are very waveform specific, for example, the bifurcation simulated under a carotid waveform (Figure 7.34(b)) exhibits a small rise in ATP concentration during the systolic phase, whilst under a coronary waveform (Figure 7.34(c)) the rise is during the diastolic phase; both results reflect the characteristics of the specific waveform. The reason for this is due to secondary flow patterns. For a carotid waveform during the systolic phase the Dean vortices strengthen and move towards the outer wall, resulting in enhanced convective delivery of ATP in the circumferential direction, which essentially disperses the low concentration region (Figures 7.35(a) and 7.35(b)). During the systolic deceleration the vortices move closer together and away from the outer wall. This 'drags' the boundary layer out resulting in a slight reduction in endothelial ATP concentration (Figures 7.35(c) and 7.35(d)). This boundary layer growth is due to the formation of a small recirculation zone (because of adverse pressure gradient) at the end of systole. The vortices slowly track towards the outer wall during the diastolic phase until there is relatively little movement. Despite this rapidly changing boundary layer thickness this appears to only affect the outer portions of the boundary layer, thus concentration change at the wall is small. Progressing along the outer wall in the sampling locations, the point of lowest ATP concentration is further out of phase with the waveform and is reflected in the different movement of secondary flow patterns along the vessel. However overall the characteristics of the waveform are dominant.

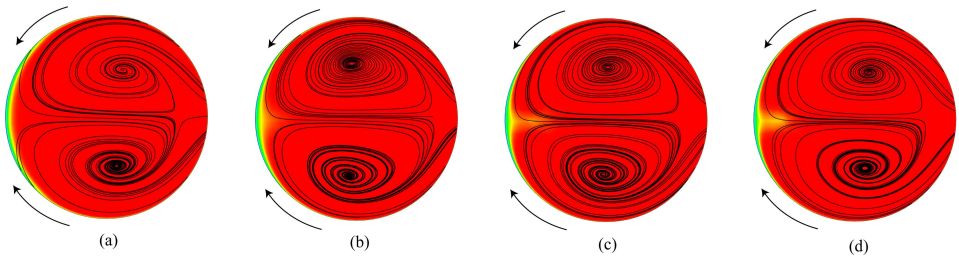

Figure 7.35: Contours of ATP concentration with secondary streamlines overlain on a section of the daughter artery immediately downstream of the bifurcation, sampled during the large forward flow of the carotid waveforms systolic phase. (a) t=0.05s (b) t=0.1s (c) t=0.15s (d) t=0.2s. Later times in the cycle looked similar to t=0.05, as the flow did not change considerably during this period.

Figure 7.36 assesses the resultant surface distribution at specific times throughout the carotid waveform and demonstrates that the variation in the vicinity of the outer wall is small, but there is reasonable growth of the high concentration region near the inner wall. This also reflects the results in Figure 7.34(b)

and (c) where the high temporal variations are greater in the high shear region. Very similar surface distribution was observed for the coronary waveform, but at the different respective times ie. peak systole carotid similar to peak diastole coronary.

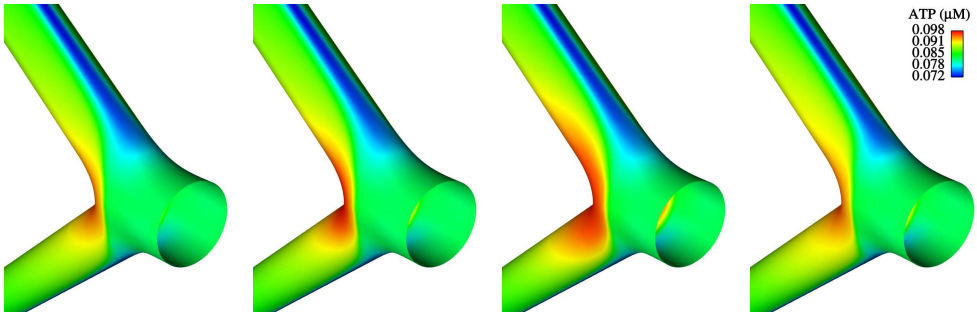

Figure 7.36: Contours of ATP concentration at various times through the cardiac cycle: (a) t=0.05s (b) t=0.1s (c) t=0.2s (d) t=0.7s. Visibly there are no major changes, but there is a slight narrowing of the low concentration region at the end of systole, coupled with a growth of the high concentration region.

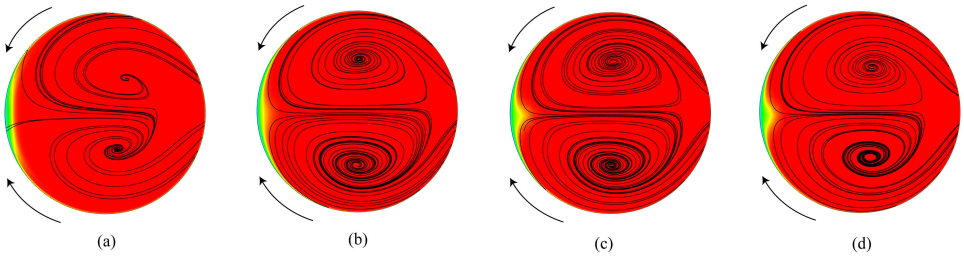

Figure 7.37: Contours of ATP concentration with secondary streamlines overlain on a section of the daughter artery immediately downstream of the bifurcation, sampled during the large forward flow of the coronary arteries diastolic phase. (a) t=0.1s (b) t=0.7s (c) t=0.8s (d) t=0.9s.

For the coronary waveform very similar characteristics are also observed (Figure 7.37), but the final strength of the secondary flows is reduced due to the much lower 'slew' rates compared with the carotid waveform. The effect this has on ATP (identified in Figure 7.37(c) and 7.37(d)), is that during the diastolic phase with the boundary layer not extended as far into the lumen, the actual size of low concentration is enhanced. The boundary layer growth again occurs during deceleration with the boundary layer being pulled away from the wall, but not nearly to the degree that occurs for a carotid waveform. During the systolic phase secondary flows are relatively weak, but the temporal evolution on the outer wall shows a gradual decrease as vortices move away from the surface. This

is followed by increase as the vortices move back towards the outer wall (with some oscillation due to the slewing of the waveform). This was again dependent on the sampling location. Following the addition of ATP release, the transient characteristics are as for the model without release, albeit the transients in the vicinity of the inner wall are larger.

For the bend (Figure 7.34(d)) similar conclusions can be drawn, except for the region in which flow separation occurs, where there are some relatively significant transients. This is because of the variational position of the flow separation point resulting in this region of the artery wall progressing into the recirculation zone, where concentration decreases rapidly due to attenuated transport and boundary layer growth. The WSS for this same sampling location 2 is given in Figure 7.38. The ATP concentration drops rapidly as a result of boundary layer growth induced by flow separation during the acceleration of the diastolic phase.

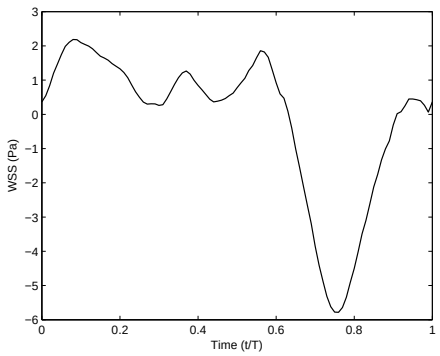

Figure 7.38: Time evolution of axial WSS at the location 2 of Figure 7.34(a). Negative WSS indicates this point been within the recirculation zone.

This is further evidenced by time varying contour plots along the inner wall (Figure 7.39). The most significant transients occur along the boundary of the high and low shear zone. Rapid reduction of ATP concentration occurs during separation of the diastolic phase.

Figure 7.40 details instantaneous ATP concentration at sampling location 4. During the early systolic phase the vortices move closer to the vertical axis of the plane and inner wall resulting in elevated ATP concentration. In the intermediate parts of the phase there is a small rotation of the vortices directed away from the vertical plane and in doing so, it displaces the vortices away from the lower wall resulting in the decrease in ATP concentration. The formation of two weak vortices in the earlier part of diastolic acceleration rotates the vortices further

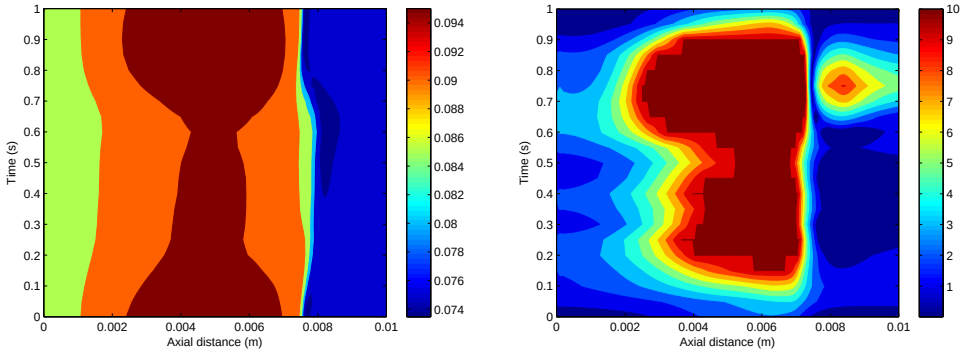

(a) (b)

Figure 7.39: Time variation of over (a) ATP and (b) WSS plotted along the inner wall varying over time. Data record every 5 time steps.

away from the inner wall (Figure 7.40(c)), thus reducing the surface concentration. During the large forward flow of the diastolic phase, the weak vortices at the outer wall strengthen and the ones near the inner wall weaken. However during the final deceleration phase (Figure 7.40(d)) the upper vortices dissipate and the lower vortices strengthen and rotate back towards the vertical axis (and inner wall), but due to this location being well within the recirculation zone convective transport is enhanced. In the high shear region, such as sampling location 1, the skewing of the velocity profile towards the lower wall is the predominant mechanism for ATP delivery. Figure 7.41 details the surface distribution at specific times throughout the cardiac cycle, consistent with the the secondary flow patterns of Figure 7.40. The expansion of the low concentration region late in the diastolic phase is due to decelerating flow.

Overall, the transients in ATP concentration are reasonably negligible, but potentially in regions of the vasculature, such as the carotid sinus, where flow recirculation occurs these transients may be significant. Although ATP concentrations in this particular flow separation zone are significant the Ca^{2+} and thence eNOS may not necessarily follow this, as the time-scales are much longer than the cardiac cycle for Ca^{2+} dynamics.

The results have determined that ATP concentration over the course of the cardiac cycle was found to vary from the mean concentration only by around 10%. Importantly for this model, the distribution of depleted ATP concentration regions is not significantly altered. Therefore, the simplification of the model to

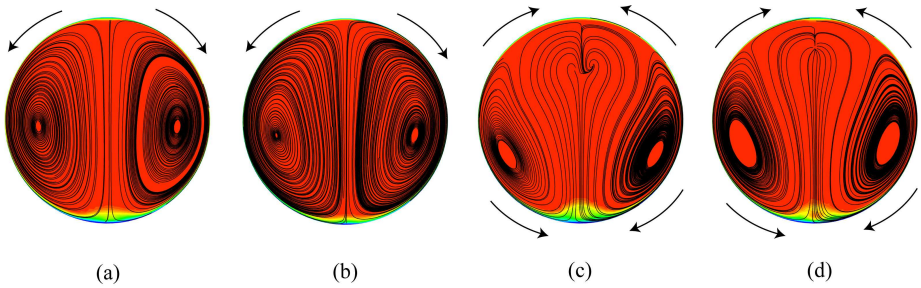

Figure 7.40: ATP concentration with secondary streamlines overlain: (a) t=0 (b) t=0.5 (c) t=0.7 (d) t=0.9. Evidently, rotation of the lower vortices is observed during the the diastolic phase.

steady flow is justified as the spatial location of regions of low eNOS is largely unaffected.

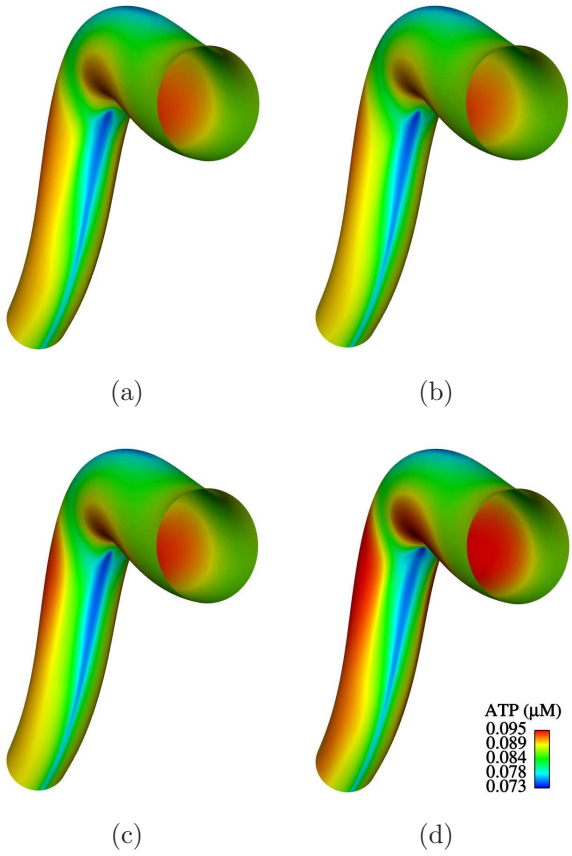

Figure 7.41: Contours of ATP concentration at various times throughout the cardiac cycle: (a) t=0.3 (b) t=0.5 (c) t=0.7 (d) t=0.9. Visibly there are no major differences in the low concentration region, albeit some 'smearing' is observed during the diastolic phase.

7.5 Discussion

There is a significant amount of literature that identifies the outer walls of bifurcations and recirculation zones as regions that are more susceptible to the formation of atherosclerotic plaque (Gimbrone, 1999, Malek et al., 1999). The current model, which incorporates the prevailing haemodynamics, transport of blood borne agonists in bifurcation and bend geometries and underlying endothelial cellular dynamics, shows strong correlation between regions of low WSS and low intracellular eNOS activity. Regions of reduced Ca^{2+} and eNOS signalling imply reduced bioavailability of NO, which has been linked with endothelial dysfunction and the subsequent onset of atherogenesis (Davignon and Ganz, 2004, Naseem, 2005).

Simulations in an idealised arterial bifurcation and bend have identified the areas that are subjected to low WSS and reduced eNOS activity and hence most susceptible to endothelial dysfunction and disease. These are the outer walls of the bifurcation, the proximal outer wall and distal inner wall of the bend. The extent and severity of the pathological conditions vary with the Reynolds number of the flow, but these regions always suffer from low WSS and eNOS *relative* to other parts of the endothelial surface. Hence these regions are identified as 'hot spots' for the initiation of atherosclerotic plaque formation, due to endothelial dysfunction and impaired NO-mediated vasodilation. There is a possibility that the upper and lower walls of the bifurcation may also be prone to disease, as regions of low WSS and hence reduced eNOS exist. However, this phenomenon is highly dependent on the curvature in this region, which will vary markedly in human arterial bifurcations. This observation also implies that an arterial wall of varying topology may be significant for atherosclerosis initiation.

In the present study, the concentration of ATP and ADP at the arterial wall appears to be of less significance for eNOS activation than the WSS. This is particularly true when the effects of flow-induced ATP release are included. This observation suggests that WSS is the dominant factor determining the spatial variation in endothelial function, although this statement should be accompanied by the following caveats. It has been assumed in this model that the EC are sensitive only to the combined surface concentration of ATP+ADP, which does not vary greatly over the region of endothelium studied. There are a number of

other signalling pathways that have not been explicitly included in the present model. For example, the P_{2X} ion channel pathway is only sensitive to ATP. Future work will include the addition of this pathway, which may increase the sensitivity of eNOS activity to ATP concentration. Furthermore, certain rate constants in the cell model are not known, so the sensitivity to ATP may be greater than predicted with the current parameter set.

Although there is always a spatial relationship between the outer wall of the bifurcation and a pathological environment, the bifurcation angle has been found to play an important role in the response. Regions of low WSS are more significant at smaller bifurcation angles, due to weakened secondary flow. There have been some reports (Friedman et al., 1993, Sharp et al., 1982) that acute angle bifurcations are correlated with a larger lateral distribution of low WSS (as observed in the present study) and atherosclerotic plaque. However, the evidence to date is inconclusive and this remains a controversial issue. Other studies have investigated carotid bifurcation geometries (Perktold et al., 1991a) and it was observed that although secondary flows increase with bifurcation (as found here), so did the recirculation zone. This is in contrast to the present study and is due to the different vessels, used symmetric versus asymmetric. This means that other factors, such as parent–daughter artery area ratios and out-of-plane bifurcation effects (Friedman and Ding, 1998, Sitzer et al., 2003) may be important, and a definitive relationship between branching angle, fluid shear stress and disease has yet to be firmly established. Furthermore it may very well depend on the type and location of the bifurcation. The theoretical predictions of this model therefore, call for further experimental study in this area.

The results of this model agree well with *in vitro* research that has identified regions of low time-averaged WSS/disturbed flow, such as those found on the outer wall of bifurcations, with the onset of cardiovascular disease (Asakura and Karino, 1990, Zand et al., 1999). Further experimental research needs to be focused on *in vitro* cellular function (in particular endothelial calcium dynamics and NO production) in order to validate model predictions regarding eNOS activity and the implications for cardiovascular disease. Studies of this nature have been undertaken in parallel plate flow chambers (Shen et al., 1992). However, the cell culture in such a setup is exposed to a uniform flow field. In contrast, there has been relatively little experimental research on cell function in a spatially varying mechanical and biochemical environment, which is key to understanding

the localisation of atherosclerotic lesions *in vivo*.

The assumption that there are no major differences between ATP concentration in steady flow and the time-averaged concentration over a pulsatile cardiac cycle has been validated by performing pulsatile flow simulations. The time-averaged concentration was found to differ from the steady state by no more than 4% for the arterial bend and 6% for the arterial bifurcation. Transients in ATP concentration where found to 'generally' be negligible, but in regions of flow separation this is not the case suggesting further investigation is required in this area to determine transients in complex recirculating environments and realistic arterial geometries in which complex secondary curvatures exist. The unsteady results also provide qualitative information for arbitrary species, such as oxygen. In Ku et al. (1985) OSI was correlated with intimal thickening and elevated OSI was shown here to be elevated in the region of the vasculature subject to impaired mass transfer. However, the primary reason is due to attenuated mass transfer when a recirculation zone forms.

Chapter 8

Flow, mass transfer and atherogenesis, in a realistic porcine aortic trifurcation

8.1 Introduction

This chapter takes on the models developed in previous sections, and applies it to a physiologically realistic geometry. This model has some very interesting geometric complexities that potentially could be more insightful for atherosclerosis prone regions of the human vasculature.

8.2 Background

This chapter implements the previously described numerical models for ATP and endothelial cell signalling into a realistic arterial geometry. The present study will focus predominantly on mass transfer characteristics, as there are very few published studies considering mass transfer in realistic geometries. Furthermore, a number of research groups in the literature have requested a greater focus on physiologically realistic geometries to further understand both flow characteristics and potential atherosclerosis initiation (Myers et al., 2001, Perktold et al., 1998), hence applying the previous developed models may provide some information in this area. Generally previous studies have looked solely at WSS variations and provided very interesting results that were not evident in idealised models, mainly the local variations in geometry leading to local variations in WSS (or more accurately the WSS vector).

A major focus on ATP transport will be whether the non-uniform arterial wall geometry, which includes bifurcations, branches and curving arteries, leads to boundary layer growth and separation. This will potentially inhibit ATP delivery to the endothelium, and may provide additional information that is not observed in simplified geometries. To the author's knowledge, the only previous study that considered mass transfer in a realistic geometry was that performed by Kaazempur-Mofrad and Ethier (2001). This was a model of a human right coronary artery bend and possessed very interesting flow characteristics, providing information about mass transfer differences between inner and outer walls of the bend. However essential flow features, such as flow recirculation and separation that exist more commonly in bifurcating geometries and more importantly are implicated in atherosclerosis, were not present. Therefore the novel aspect of the present study is the complexity of the haemodynamic environment and how this affects mass transfer, which should provide some new insight into this area. The results for the transport of ATP can also be considered qualitatively for other arterial species, for example LDL or oxygen.

In addition to Newtonian fluid flow effects on mass transfer, a non-Newtonian blood rheology is also investigated. This is again motivated by the fact that previous mass transport studies in literature have not considered this effect. Although non-Newtonian effects are generally regarded as small for medium and large arteries, as described in Chapter 3, small variations in viscosity may impart considerable effects on the transport of low diffusion coefficient species.

Further to the mass transfer, it is interesting to see the effects that a complex haemodynamic environment has on endothelial cell signalling. This is motivated primarily by observations made in the idealised model that demonstrated small variations of eNOS concentration on the upper and lower wall of the bifurcation were brought about by the tangent fill condition used to generate the geometries (see section 7.3 of Chapter 7). Hence local irregularities in the wall surface will potentially provide localised variations in intracellular eNOS concentration. Ultimately this model implementation determines whether realistic geometries are required for the study and understanding of haemodynamics, mass transport and endothelial cell signalling in the initiation of atherosclerosis (via endothelial dysfunction).

8.3 Geometry

The arterial geometry is of a realistic porcine aortic trifurcation obtained from a silicone casting followed by laser scanning. Shown in Figure 8.1 (see Himburg et al. (2004) for full details).

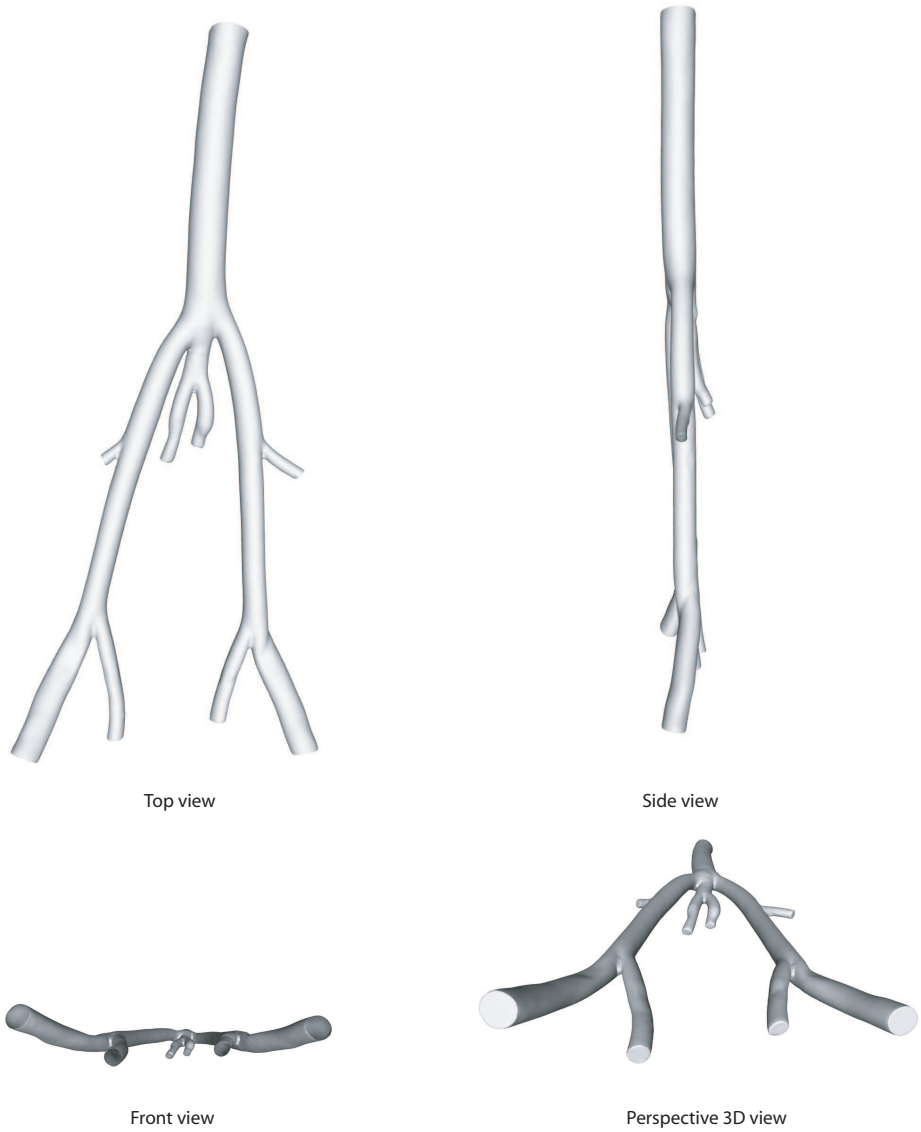

Figure 8.1: Views of the trifurcation model used for computation. The model is physiologically accurate, obtained from silicon cast and has complex curvature and calibre.

The porcine vascular system is a good basis for understanding the progression of atherosclerosis, as it has been previously reported that the pathology of atherosclerosis in pigs is very similar to that of humans (Ratcliffe and Luginbuhl, 1971). The portion of the porcine arterial system the geometry represents

is the major trifurcation from the terminus of the abdominal aorta into the iliac arteries: left, right and common. The left and right iliac arteries include two daughter branches: the circumflex and the deep femoral. Within humans the abdominal aorta and its major branches is a common anatomical site for atherosclerosis(DeBakey et al., 1985).

This geometry exhibits very interesting variations. One such variation is *secondary curvature*, which is curvature that is out of the dorsal plane (also referred to as non-planarity in literature (Caro et al., 1996, Friedman and Ding, 1998)). Areas that exhibit significant secondary curvature are in the femoral bifurcations (as is visible in the side and front view of Figure 8.1). The surface of this model is not smooth, rather it exhibits true *in vivo* characteristics where the wall includes topological variations. These topological variations lead to differences in cross-sectional area along the vessel. One of the main differences that will be interesting to observe is the difference between this model and the idealised, such as the in-plane (see dorsal view of Figure 8.1) curvature of the daughter arteries. It will also be interesting to compare with the previous bifurcation models which consist of straight downstream segments.

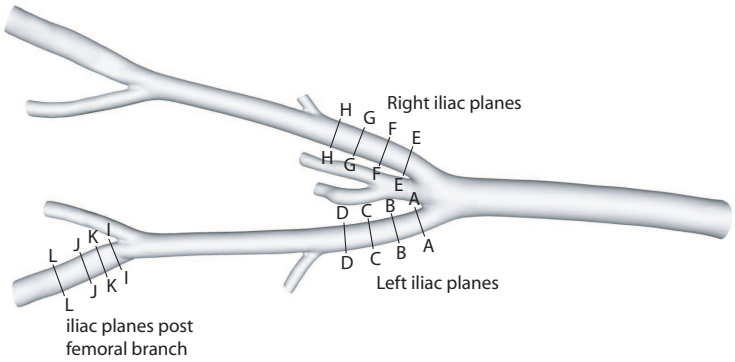

Figure 8.2: Lines along artery wall for observing flow and mass transport characteristics.

Figure 8.2 details planes set up to observe flow and mass transfer features. Planes were observed along the left and right iliac artery between the terminus of the descending aorta and the branch of the circumflex artery. The other locations sampled in the region of the iliac artery distal to the deep femoral branch. The geometry in this region exhibits significant secondary curvature; the planes have been tightly spaced to capture the effects of significant changes in arterial calibre. Also information regarding ATP, WSS and eNOS was detailed along lines on the outer and inner walls of the left illiac, right iliac and the left iliac were the

femoral artery branches. Each of these lines encompasses regions of important information such as recirculation zones. Figure 8.3 shows the location of the different lines with the name that they will be referred to in the main text.

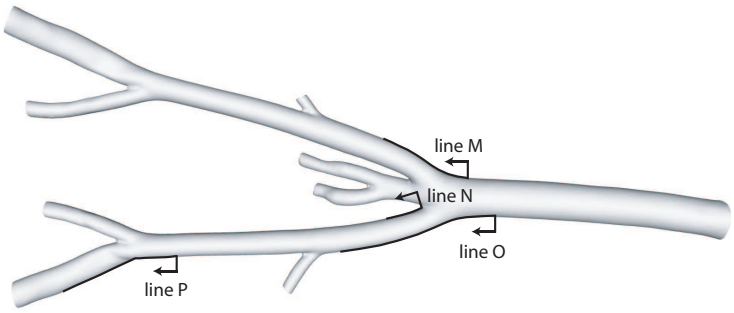

Figure 8.3: Locations of cut planes for observing streamwise variations of flow and mass transfer variables. Arrows indicate plot direction.

8.4 Numerical Formulation

8.4.1 Mesh details

The mesh of the full porcine trifurcation contained 7 million volumes, this is due to a number of factors. Firstly, the geometry represents a significant portion of the arterial tree involving multiple bifurcations. Second, the wall boundary layer was required to be significantly refined to capture steep species gradients that arise at the surface as discussed in Chapter 4. An example portion of the mesh is demonstrated in Figure 8.4.

The geometry was meshed using the commercially available Harpoon meshing software (Sharc software, 2006). This software uses an adaptive cartesian meshing method with hanging nodes (evident in Figure 8.4 on the domain slices). The Fluent CFD solver is validated for dealing with this type of mesh structure. The species boundary layer had a near wall cell spacing of 2.5 μm progressively growing over 13 layers to a total thickness of 150μm. This leads to very high aspect ratio cells required to keep the mesh within practical limits from a computational prospective. In the streamwise direction a mesh spacing of 0.19 mm was deemed sufficiently refined to capture local variations in surface topology, as mentioned in Chapter 3, without the mesh becoming excessively large. In order to check

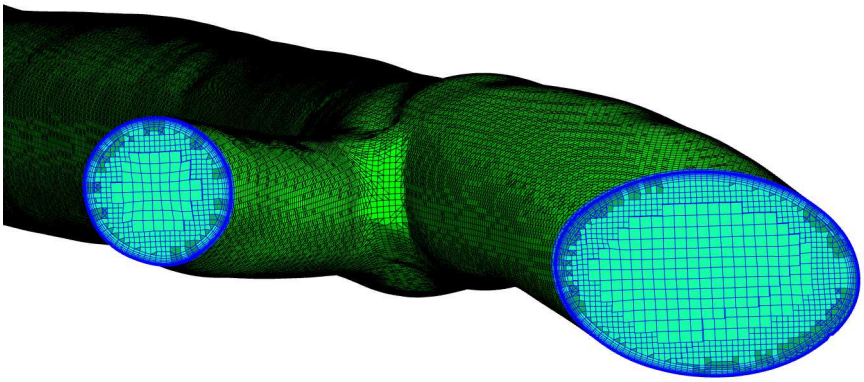

Figure 8.4: Portion of computational mesh showing boundary surface elements and cross sections of the mesh within the fluid domain. The complexities of the surface geometry mesh are also very visible with many topological variations.

for mesh convergence the off wall grid spacing was reduced to 1 μm. This provided little change in the solution for ATP, although a very slight dependence was observed in the aorta to iliac branch. The solution was considered mesh converged for mass transport. A comparison of the solution for the two different mesh spacings is shown in figure 8.5.

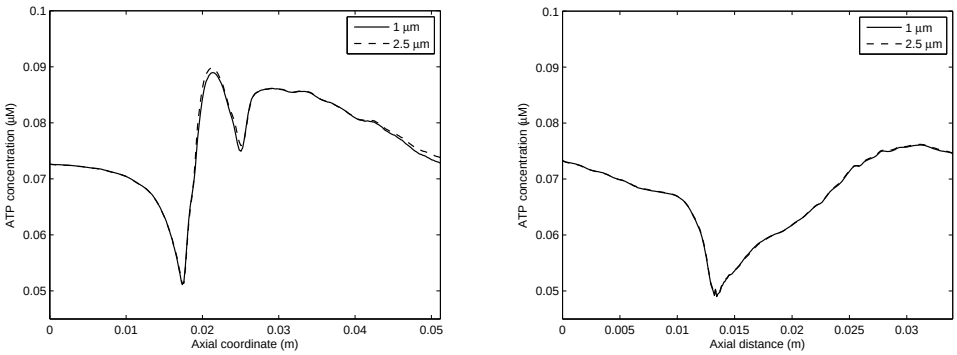

(a) (b)

Figure 8.5: ATP convergence check. (a) plot line M (b) plot line P

The flow field was assessed for convergence via refinement of the bulk flow outside the boundary layer (the largest volumes in Figure 8.4 were subdivided into four sub-volumes). This was the limits of refinement of this geometry, because further reduction of the surface mesh resulted in an excessively large increase in mesh size, which was not deemed suitable for computation. The final mesh size for convergence check contained 9 million volumes. A comparison between WSS on the outer wall of the left iliac is shown in Figure 8.6, some mesh dependency is

exhibited. However this is only very localised and it is deemed that the 7 million volume mesh is considered suitable to achieve a balance between computational efficiency and accuracy. Furthermore the conclusions of the study will unlikely change between these two mesh resolutions.

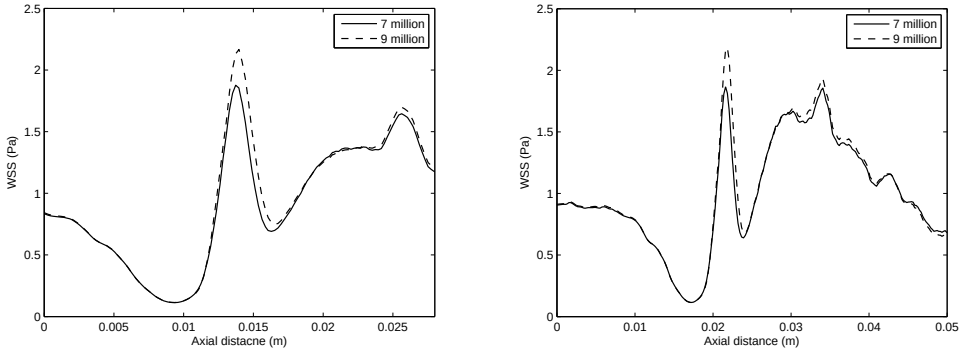

(a) (b)

Figure 8.6: WSS between the seven million volume and the nine million volume mesh where the bulk fluid domain had been subdivided. (a) plot line M (b) plot line O

8.4.2 Flow and Mass transport

The simulations were carried out using the Finite volume CFD solver Fluent. Information regarding boundary conditions is provided in Chapter 3 for the flow field and Chapter 4 for the mass transfer field. Simulations were carried out at Reynolds number of 885 based on the mean of the time varying simulations performed by Himburg et al. (2004). Estimations of outlet flowrate distribution follow from the experiment of Henderson et al. (1999) who conducted an *in vitro* study of haemodynamics in swine. The flow distribution for symmetric variation, as used in this study, is summarised in Table 8.1 given as a proportion of the inlet flowrate (Q_{in}).

Table 8.1: Outlet flowrate distribution

Outlet	Proportion of inlet
Circumflex iliac	$0.033Q_{\text{in}}$
Common iliac	$0.117Q_{\text{in}}$
Deep femoral	$0.183Q_{\text{in}}$
Reference	$0.167Q_{\text{in}}$

The flowrates were obtained using the pressure mass flow update presented in Chapter 3. At the inlet to the computational domain a uniform velocity profile was applied. This develops over the length of the descending aorta into a well developed Dean profile at the terminus of this vessel and was also observed in a previous study by Himburg et al. (2004). In addition, as reported in Chapter 3 previous work by Moyle et al. (2006) found that different inlet profiles have little effect on the downstream WSS distribution in realistic arterial geometries providing sufficient inlet length and the length of the descending aorta, meets this criteria.

As part of the nucleotide study, a non-Newtonian blood rheology using the Carreau-Yasuda model (Cho and Kensey, 1991) is investigated. As discussed in Appendix A for a Newtonian fluid, the stress tensor $\bar{\bar{\tau}}$ is a linear function of $\bar{\bar{\varepsilon}}$ with the relation given by

$$\bar{\bar{\tau}} = 2\mu\bar{\bar{\varepsilon}} \tag{8.1}$$

In a non-Newtonian fluid this is not the case. μ is a function of the shear rate ($\dot{\gamma}$), where the shear rate for generalised 3D flows is obtained from the second invariant (D_{II}) of the rate of strain tensor, given by

$$\dot{\gamma} = \sqrt{2D_{II}} \tag{8.2}$$

The present study employed the Carreau-Yasuda rheological model given by

$$\frac{\mu - \mu_\infty}{\mu_0 - \mu} = [1 + (\lambda\dot{\gamma})^a]^{n-1/a} \tag{8.3}$$

where μ_∞=0.000345, μ_0=0.056, λ=3.3132, a=2, and n=0.3568. This parameter set was used in previous studies by Cho and Kensey (1991) Hence from equation (8.2), the viscosity equation can be expressed as

$$\mu = \frac{\mu_\infty + \mu_0[1 + (\sqrt{2D_{II}})^a]^{n-1/a}}{2 + (\sqrt{2D_{II}})^a]^{n-1/a}} \tag{8.4}$$

Pulsatile flow and the effects on mass transfer was considered to determine whether the results from the idealised models follow through to realistic geometries. The waveform is typical of a abdominal aorta-iliac region of the vasculature, and is shown in Figure 8.7

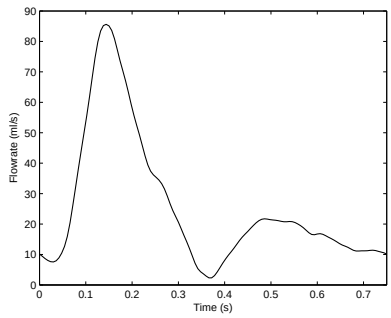

Figure 8.7: Waveform used in pulsatile flow simulations, taken from Himburg et al. (2004).

The waveform was divided into 125 time steps of 0.006 seconds, data was recorded after 8 complete cycles. Due to the heavily computational nature simulations were performed on an IBM Power5-575 HPC, as described in chapter 7,

16 processors were utilised on this system. Time per iteration was an average of 10.6 seconds leading to a total simulation time of 13440 CPU hours.

8.5 Results

8.5.1 Flow characteristics

On observing flow patterns in the region where the trifurcation divides from the abdominal aorta into the iliac arteries there exist some very interesting flow phenomena including helicoidal flows and reverse flows. Helicoidal flows are formed in all of the bifurcating arteries, and is brought about by the curvature between the parent and daughter artery inducing a centripetal acceleration (or radial pressure gradient), forcing the flow towards the inner wall of arteries. Following the movement of high momentum fluid towards the inner wall, in order to satisfy continuity condition the flow is forced to follow a trajectory around the circumference of the vessel towards the outer wall, setting up counter rotating vortices. This flow phenomena has been observed in previous arterial geometries, however the vortices observed in this geometry are unmatched due to the non-symmetric geometry.

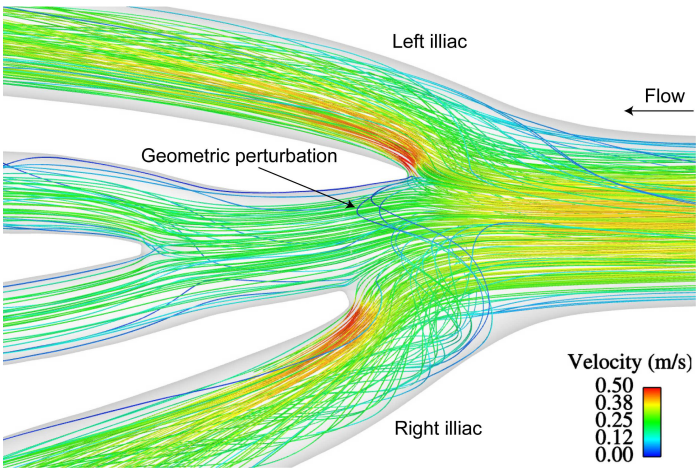

Figure 8.8: Detailed flow patterns in the trifurcating artery looking at lower surface. The flow retrograde that forms on the lower surface, due to a small perturbation of the geometry, is pulled around into the right iliac artery, this sets up a very strong helicoidal flow.

An interesting feature of the trifurcating region is the marked difference be-

tween the left and right iliac flows, as seen in Figure 8.8. In the left iliac artery the flow field is similar to previous models simulating bifurcation models, with the high momentum fluid at the inner wall and low momentum fluid at the outer, but due to the in-plane curvature a very small recirculation zone forms at the inner wall (evidenced by stress lines). In the right iliac artery, due to the formation of recirculating flow on the lower surface of the artery, caused by a small perturbation in the geometry (visible in Figure 8.8), coupled with the branching (which has significant area reduction) the flow in the right iliac artery is very disturbed and exhibits very strong helicoidal characteristics. The retrograde flow being pulled into the right iliac artery is visible in Figure 8.8.

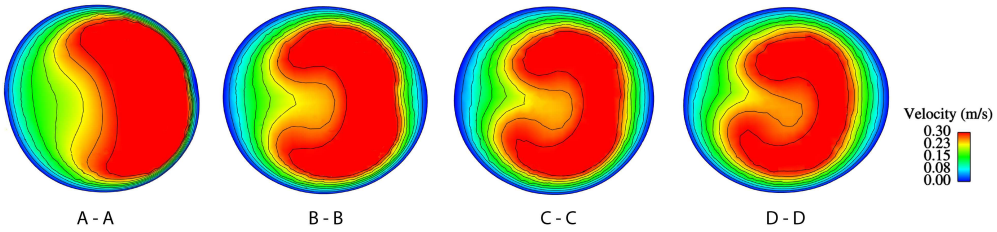

Figure 8.9: Axial velocity contours progressing along the left iliac artery. Right side of planes is the inner wall, left side the outer wall. Interestingly these are remarkably similar to that of an idealised bifurcation, however there is some rotation of the contour due to secondary curvature.

In contrast to the idealised models where the daughter arteries were straight segments, the present model has both in-plane and secondary curvature leading to significantly different flow dynamics. These curvatures set up opposing pressure gradients, to that caused by branching, that displaces high velocity fluid away from the inner wall. Consider Figures 8.9 and 8.10 showing axial velocity contours progressing along the iliac arteries between the main trifurcation and the circumflex branches. In the left iliac artery, the downstream velocity contours exhibit characteristic *horse shoe* profiles (indicating secondary flows exist), the shape of the profile indicates intermediate Dean numbers with axial distortion (azimuthal motion). It is noted that there is a small rotation of this velocity field due to secondary curvature, however secondary curvature is only small in this region. In the right iliac artery the contours are significantly different, and the horse shoe profile is highly disturbed, leading to the region of high momentum fluid being very localised, with the rest of the high velocity region dissipating significantly. Furthermore, at the inner wall of the artery a region of low velocity fluid forms due to the curvature of the vessel in plane (a small recirculation zone exists in this location). These observations were not recorded in more idealised

models, but this potentially could be captured by including secondary curvature into these geometries.

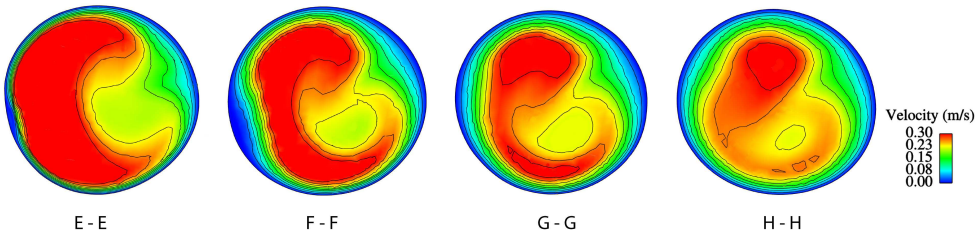

Figure 8.10: Axial velocity contours progressing along the right iliac artery. Left side of planes is the inner wall, right side the outer wall.

Secondary flow streamlines, evidencing vortical structures, in the two iliac arteries highlight the differences (see Figures 8.17 and 8.18 in section 8.5.3). In both iliac arteries rotation of the lower vortex was observed this is due to the secondary curvature, and has previously been observed by others (Moore et al., 1999, Myers et al., 2001). The implications of these flow features on mass transfer is discussed in section 8.5.3. As with previous models secondary velocity weakens down the length of the daughter arteries.

In the left iliac artery the formation of counter rotating vortices is evident and the upper one is initially relatively weak (plane A-A Figure 8.17). Progressing into the daughter artery (plane B-B) the vortices strengthen and are evenly matched. Two smaller vortices form near the inner wall in plane B-B and is most likely induced by the the in-plane curvature of the vessel (see dorsal view Figure 8.1), but possibly due to the small recirculation zone that formed upstream. Rotation of the vortices is observed in plane C-C and a small vortex forms in the upper left side. Plane D-D closest to the left circumflex branch shows substantial vortex dissipation, but also evidences a fairly strong clockwise motion, which agrees with the observed rotation of the velocity profiles.

Coming into the right iliac artery counter rotating flows are strong, as the lumen narrows the flow accelerates and a clockwise movement of the secondary flow occurs (due to secondary curvature). Plane E-E of Figure 8.18 shows the strong counter rotating unmatched vortices compared with the left iliac artery, as expected due to the very evident helicoidal streamlines (Figure 8.8). The strength of the lower vortex is driven by the flow retrograde (leading to a large vertical component of velocity near the outer wall) that comes from the geometric perturbation of the lower surface; this lower vortex dominates inducing a counter-

clockwise motion. This rotation is also driven by secondary curvature of the daughter vessel upwards, thus the resulting vortices are superposition of these two effects and the branching of the artery. Circumferential movement of the upper vortex is observed as the flow progresses along this vessel (planes F-F, G-G and H-H), additionally this vortex rotates counter-clockwise along the streamwise axis. In plane G-G movement of the two vortices away from the upper outer wall is induced primarily by the straightening of the in plane vessel resulting in the formation of small vortices near the outer wall (plane G-G). By plane H-H the two vortices are relatively evenly matched and have nearly rotated a full 90°, this slow rotation is attributed to a very slight secondary curvature in this region of the geometry.

In the artery segment between the circumflex branches and the iliac-deep femoral region, the previously mentioned vortices are observed to dissipate and establishment of near Poiseuille flow results. This occurs in both the left and right iliac artery. Interestingly the circumflex branches have little effect on the downstream flow in the iliac artery.

Some of the most interesting flow phenomena occur in the iliac - femoral branch. Here secondary curvature is significant and coupled with the branching arteries induces flow separation and strong torsional characteristics in the downstream flow. Figure 8.11 demonstrates left and right iliac artery flow characteristics, in the vicinity of the femoral branch. Flow retrogrades exist at the location of divide. Additionally, very strong torsional flow exists in the left iliac propagating from the location of flow separation.

The geometry in this location exhibits a rapid change in curvature at the flow divide. Progressing into this location the artery is descending, but distal to the flow divide the artery is ascending. This leads to interesting haemodynamics. Figure 8.12 shows a large low velocity region on the outer wall (where flow separation occurs). This low velocity region is seen to clearly rotate in the clockwise direction (secondary curvature) and extend into the domain due to the 'branching effect'.

Secondary flow features are very strong in this region (see Figure 8.20 of section 8.5.3), with two unmatched vortices forming. Again, rotation of these structures is observed due to the secondary curvature, but considerably more

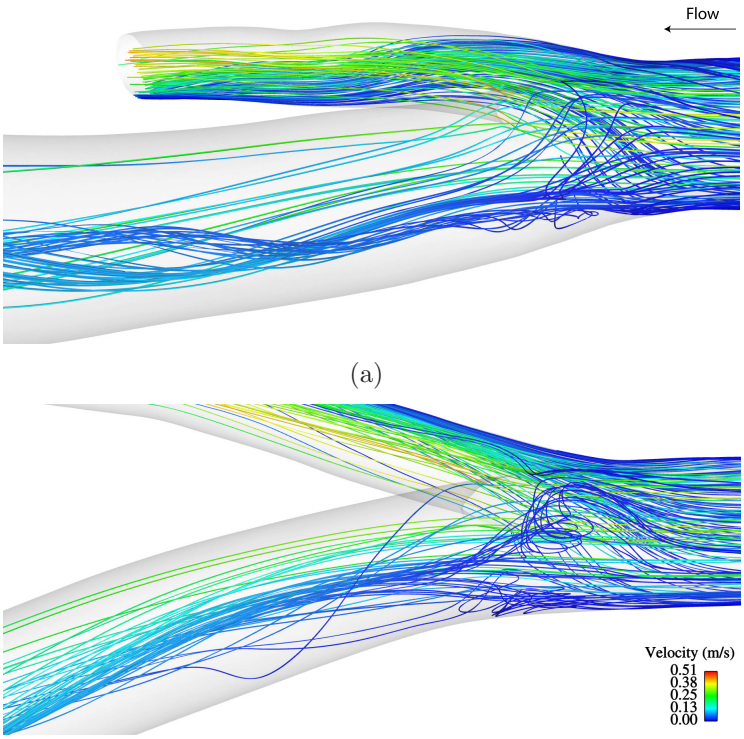

Figure 8.11: Detailed flow patterns in the iliac artery distal to the femoral branch (a) left iliac (b) right iliac. Helicoidal flows are present in the downstream region.

due to the much more appreciable curvature. An interesting flow characteristic observed between planes I-I and J-J is: the upper vortex moves away from the upper inner wall, due to a 'crease' in the artery. This accelerates the flow as the cross sectional area reduces, thus the vortex reduces. Following this the artery curves up and the cross-section expands resulting in displacement of the core away from the inner wall. This coupled with the 'branching effect', 'squashes' the vortex near the inner wall around in the clockwise peripheral direction of the artery. Between planes J-J and K-K this upper vortex rotates 90°, due to secondary curvature domination relative to the branching(vertical in plane velocity increases on outer and inner wall), and continues towards the outer wall (data not shown), thus inhibiting the movement of the vortex noted by the squaring off of the right hand side in plane K-K. Plane L-L sees the dissipation of the inner wall cell with a consequential growth of the outer vortex.

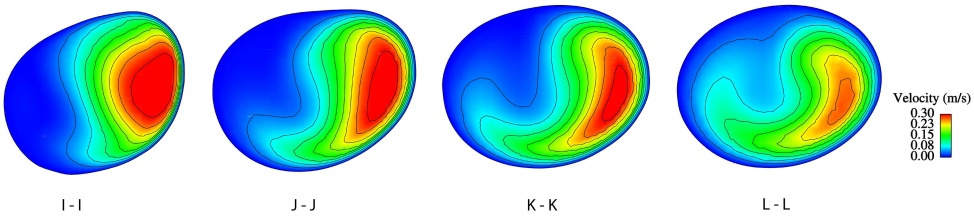

Figure 8.12: Axial velocity contours in the iliac artery distal to the femoral branch. There is a reasonably large region of low velocity fluid which rotates around the vessel due to secondary curvature.

8.5.2 Wall Shear stress

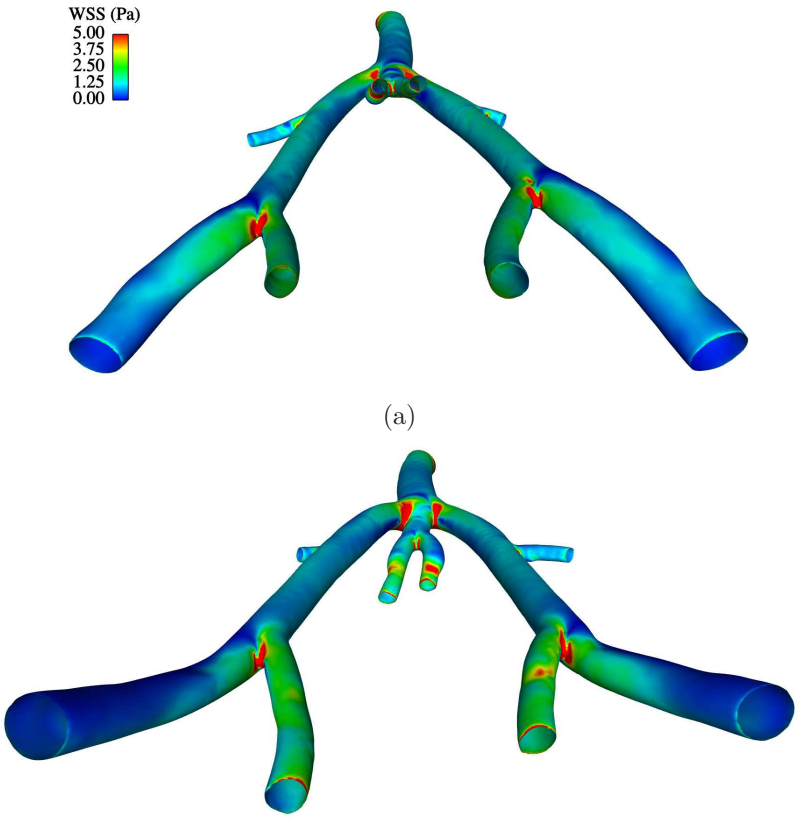

(a)

(b)

Figure 8.13: WSS distribution through the aortic trifurcation (a) ventral and (b) dorsal view.

WSS distribution varies significantly more in this realistic geometry compared to idealised. Regions such as the inner walls downstream of branching arteries are subject to low WSS. This is directly related to the high momentum fluid been displaced away leading to a low shear environment. This was clearly evidenced

in Figure 8.10 where a growth of the low velocity region occurs at the inner wall. The distribution of WSS is fairly inconsistent in comparison with idealised models, this is due to local variations in curvature, creating a wall that is a series of small 'hills and valleys' (this topological variation is clearly observed in the surface mesh of Figure 8.4). Additionally the non-uniform calibre along the vessel leads to local fluid acceleration and deceleration hence altering the WSS. Portions of the artery that protrude into the domain were subjected to elevated WSS, whilst regions where there was a cavity induced low shear environments. The high shear environments are very visible in Figure 8.13 (bright red) in the common iliac bifurcation and the left deep femoral artery. The shear environment in the iliac artery distal to the femoral branch is considerably lower than the deep femoral artery, although this is dependent on flow partition, and is consistent with previous observations by Friedman et al. (1983).

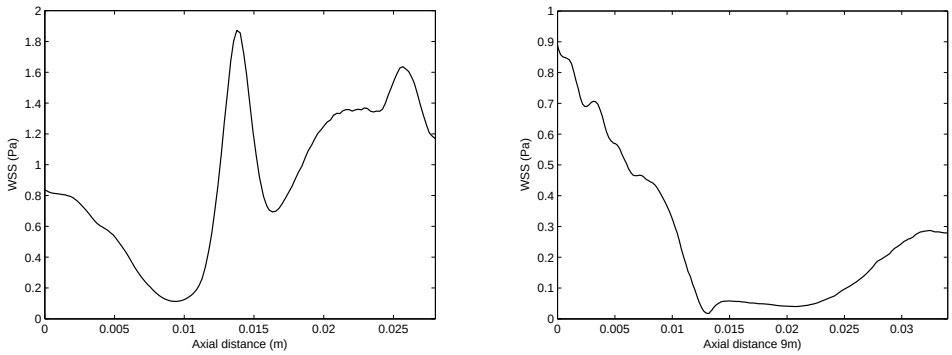

(a) (b)

Figure 8.14: WSS plotted along cut planes (a) plot line M (b) plot line P.

Figure 8.14 demonstrates WSS variations along plot lines M and P, consistent with the flow patterns observed, there are significant variations in WSS magnitude. In the iliac artery the rise in WSS is due to relatively high velocity fluid being diverted into the daughter artery from a combined effect of branching and the flow retrograde on the upper surface, hence leading to a small region of elevated WSS on the outer wall. The reduction in WSS following elevation results from the small perturbation on the upper surface that leads to low velocity fluid being pulled around in the peripheral direction by accelerating flow as the lumen narrows. In Figure 8.14(b) the drop in WSS corresponds with flow separation. Small variations seen in both distributions are due to artery calibre changes.

8.5.3 Nucleotide concentration

In order to understand the mass transfer processes occurring in the trifurcation a discussion on ATP variation alone under no release conditions is pertinent. The realistic geometry provides for very interesting cell surface ATP distribution, which has not been evident in previous models. Despite the variations in WSS observed in the previous section, surprisingly the surface distribution is rather smooth, again as discussed in Chapter 7, this is attributed to the dependence on the WSS vectors rather than the magnitude. Small variations in curvature can effect the WSS vector considerably. Overall, the low concentration fluid generally co-localises with regions of low momentum fluid, which has been evidenced in previous models, predicts location such as outer walls of bifurcations and inner walls of bends; however some variations from this generalised observation occurs.

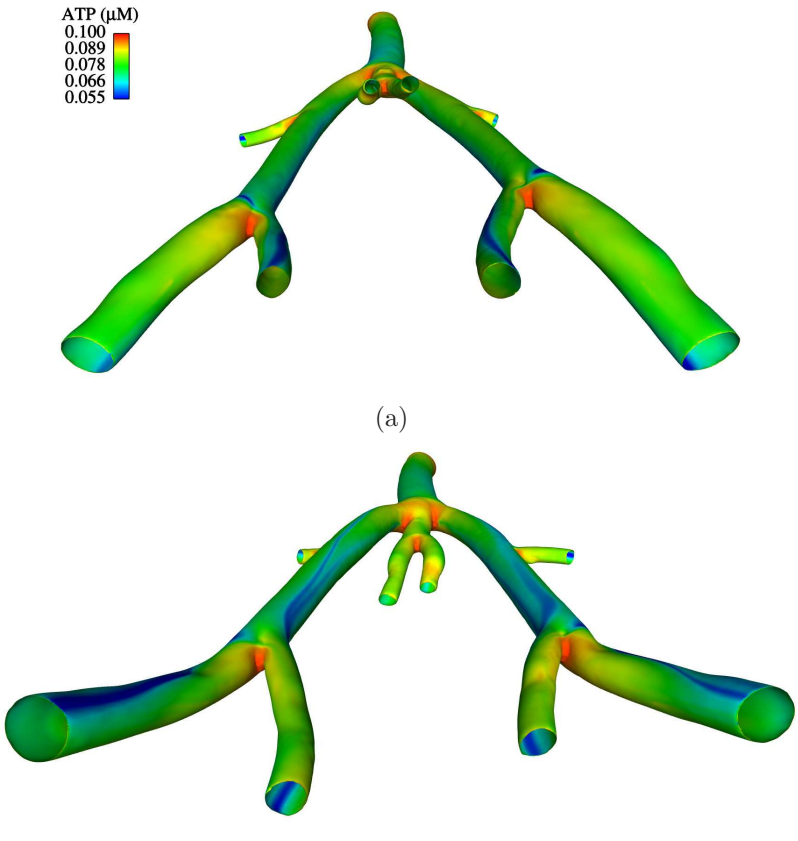

(a)

(b)

Figure 8.15: ATP distribution through the aortic trifurcation (a) ventral and (b) dorsal view.

From the results, the influence of secondary flows is a key aspect in impaired

arterial mass transport. The focal nature of impaired ATP concentration along the surface results from the meeting of two counter rotating vortices (secondary flow separation) in branching and curving arteries. This leads to pockets of depleted ATP extending into the domain (as has previously been identified in Chapter 7). However, clearly from Figure 8.15, unlike in the idealised geometries, the region of depleted ATP concentration does not remain in the outer wall region, rather it moves in a circumferential direction along the axis of the artery. This is attributed to the effects of both secondary curvature and the non-uniform cross-section of the vessel influencing the vortices that induce the movement of depleted concentration fluid in the circumferential direction.

In the left iliac artery, as previously discussed, the flow characteristics are very similar to previous bifurcation models, hence the ATP concentration is solely on the outer wall as demonstrated in Figure 8.16. The low concentration region spans a reasonable portion of the outer wall. This is due to the weak vortical structures initially in the daughter artery (Figure 8.17), hence reduced delivery of ATP into the boundary layer. The low concentration region moves slightly in the circumferential direction due to vortex rotation coupled with a weakening upper vortex. A small growth is seen in the ATP concentration boundary layer because of the movement of the vortices to the outer wall coupled with a second small vortex formation in the upper left corner, most likely due to the combined effect of in plane and secondary curvature.

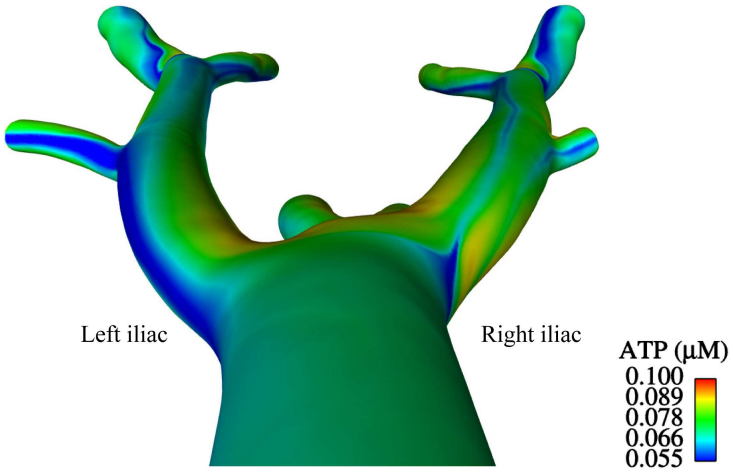

Figure 8.16: ATP concentration looking in the downstream direction. In the right iliac artery the flow characteristics, hence geometry, lead to ATP concentration moving away from the outer wall.

In the right iliac artery the flow is more disturbed and the ATP concentration moves away (circumferentially) from the outer wall with more than one area of significant depletion forming. Again in plane curvature results in low concentration fluid localising on the outer wall. Immediately into the right iliac artery two unmatched vortices form with the stronger vortex nearer the outer wall (Figure 8.18(a)). From here it is evident that the location of the meeting near the inner wall and a small recirculation zone results in a small growth of the boundary layer. Near the outer wall there is greater complexity in the flow. Initially the low ATP corresponds with the meeting of counter rotating vortices. Locations 1 and 2 in Figure 8.18 represent the regions of low concentration fluid. From the secondary flow lines, movement of the flow can be observed in the opposite circumferential directions, as the upper vortex weakens, rotates and moves towards the lower wall along the axis of the artery, the location of low concentration region 1 redistributes in the counter-clockwise direction (due to the formation of weak counter rotating vortices at the outer wall). The vortex near the lower outer wall moves slightly towards the centre of the vessel, which induces convection of ATP in the clockwise direction and a slight relocation of the low concentration region 2, but this is only slightly due to the maintained strength of this vortex. The secondary flows change induced by secondary curvature and the geometric perturbation at the location of branching upstream is the predominant mechanism in ATP distribution in the downstream area which is interesting that it can have such a sustained effect. The location of point 1 moves a greater distance in the streamwise direction because the upper left hand cell is considerably weaker.

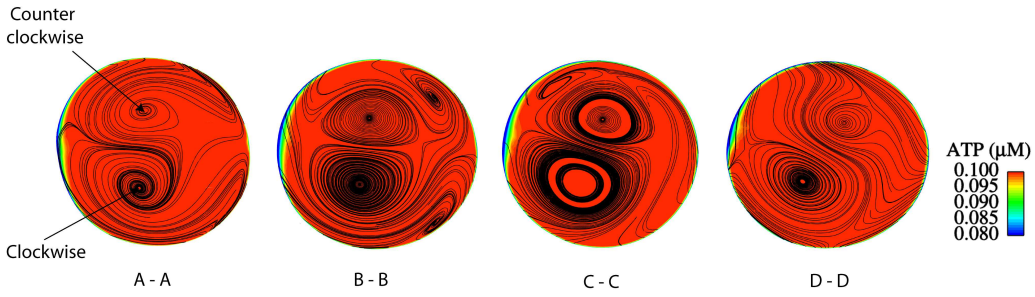

Figure 8.17: ATP concentration looking in the downstream direction left side of planes' outer wall and right side inner wall. Note lower limited on ATP concentration restricted for visual purposes.

Very interesting mass transfer occurs in the iliac artery around the femoral branch. The curvature change leads to significant rotation of the low concentration regions. As before the location between the meeting of these two opposing

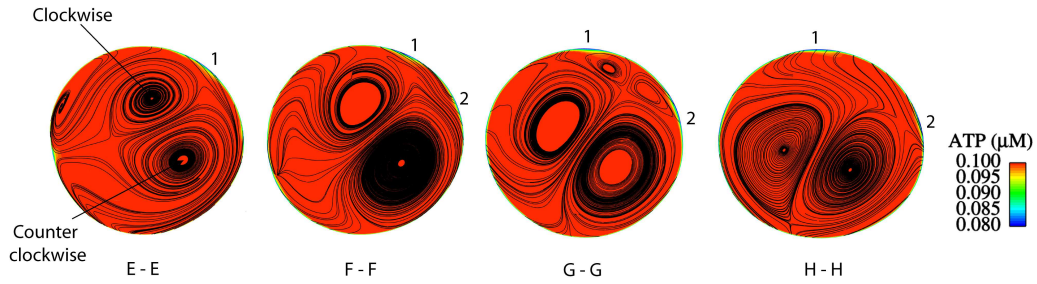

Figure 8.18: ATP concentration looking in the downstream direction left side of plane's inner wall and right side outer wall. In the right iliac artery the flow characteristics, hence geometry, lead to ATP concentration moving away from the outer wall. Locations 1 and 2 track low concentration regions at the wall.

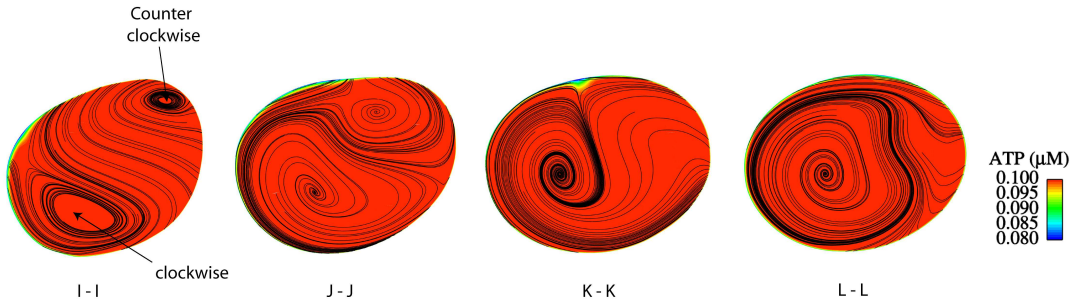

Figure 8.19: ATP concentration contours looking in the downstream direction at the plane locations (Figure 8.2) distal to the femoral branch with secondary flow lines overlain.

secondary flows (secondary flow separation) results in a region of low concentration fluid (Figure 8.19). This in turn convects ATP away from this region, hence the movement of the low concentration fluid away from the outer wall. This boundary layer interaction grows as the vortices move closer together and the growth is also attributed to streamwise hydrolysis with continued insufficient convective delivery of ATP into the boundary layer. The strong vortices in this region of the vasculature show a very clear relationship between flow interaction and low ATP concentration, more so than in any other regions. When the vortex near the inner wall dissipates ATP concentration is dispersed due to the enlarging of the outer wall vortex. Similar characteristic to the above are also observed in the right iliac artery distal to the femoral branch, however the low concentration region spans a greater region of the outer arterial way due to weakened secondary flow characteristics.

To understand the location of depleted ATP concentration stress lines are

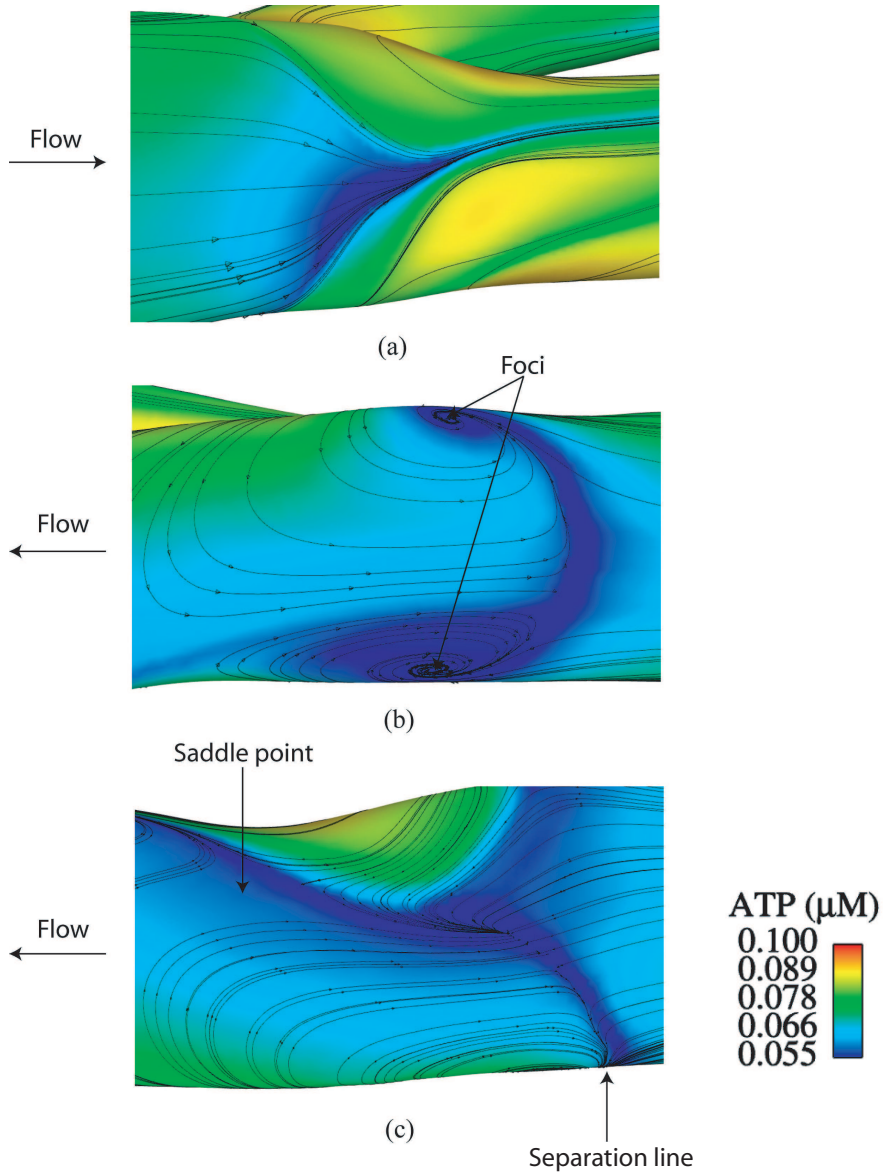

Figure 8.20: ATP distribution in three locations of the trifurcation with stress lines overlain (a) branch into left iliac (b) outer wall of the left iliac femoral branch (c) outer wall of the right iliac femoral branch. Separation characteristics evidenced by nodal and focal points lead to low ATP concentration.

again employed. These firmly establish the role of WSS vectors in the distribution of depleted ATP concentration. Furthermore, the location of separation characteristics is highlighted by stress lines. The nodal points refer to locations where all components of WSS are zero and must conform to a constraint arising from the kinematics of the flow (Ethier et al., 2000). At the outer wall of the right iliac femoral branch, Figure 8.20(b), the depletion of ATP is observed to

run along the line of separation terminating at the foci point; these correspond with heavily depleted (0.055 μM) concentration. In the left iliac femoral branch, Figure 8.20(c), the line of separation (where all streamlines converge) propagates along the outer wall moving in the circumferential direction before termination at the saddle point; this separation line also corresponds with depleted ATP concentration. Significant depletion occurs as a result of the interaction between the flow retrograde and secondary flows. The previous two flow situations seem to provide conditions that impair delivery of ATP to the endothelial surface, hence may represent flow conditions that have implications for impaired signalling and atherosclerosis.

Figure 8.21 investigates a slice into the domain through the line of separation in the right iliac artery. The depletion is brought about by convection of ATP into the domain as the flow separates. The clockwise rotating vortex indicates the recirculation zone.

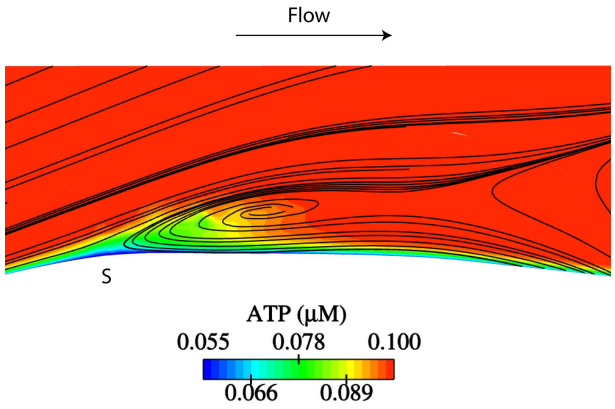

Figure 8.21: Growth of ATP boundary as a result of flow separation. S represents the separation point.

Flow induced ATP release

It is well established that the endothelium is an endogenous source of ATP in response to flow (Bodin and Burnstock, 2001). For this reason and to produce a more physiologically realistic model it is important to include this phenomenon. The models of the previous chapters did not show this significant reduction in ATP concentration under release conditions. The release conditions chosen were

rapid, moderate and slow respectively corresponding to characteristic WSS of 0.4386, 0.877 and 1.75 which puts the sensitivity range of WSS less than 2.5, 5 and 10.

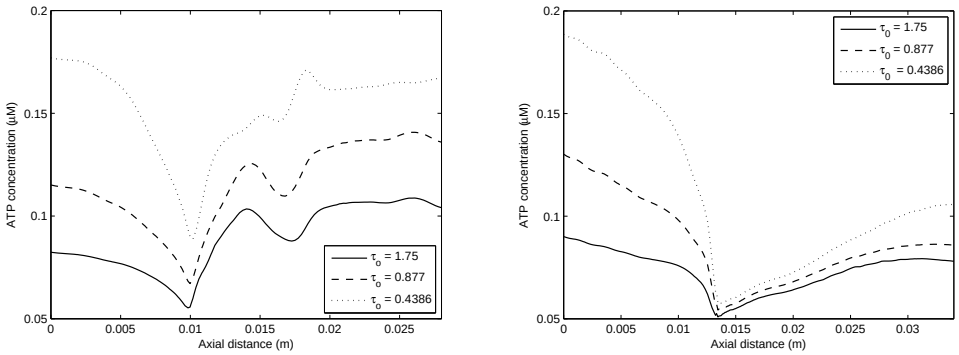

Figure 8.22: ATP concentration in the femoral bifurcation under varying levels of ATP release: (a) plot line M (b) plot line P. The concentration is reduced relative to the bulk in the region of flow separation irrespective of the release rate.

Figure 8.22 demonstrates the surface distribution along wall cut planes at two locations in the vasculature. In Figure 8.22(a), which shows ATP plotted along the outer wall of the right iliac artery, as the release rate increases the concentration at the surface increases and is similar to previous models. However, under the flow conditions in the iliac artery where the femoral artery branches, the surface ATP concentration is substantially depleted with respect to the bulk concentration irrespective of the release rate, as demonstrated in Figure 8.22(b). It appears that secondary curvature induced separation results in depleted ATP concentration. A primary reason for the significant depletion irrespective of the release rate is the *line* of flow separation. This leads to very low WSS, zero at separation, hence from the sigmoidal release there is no addition of ATP into the domain. The small difference in ATP concentration that does occur at the outer wall is primarily due to the different ATP release rates that affect the upstream ATP concentration. For example, under high release conditions, the ATP concentration is elevated upstream, whilst for lower rates the domain is not saturated to the same extent. This results in the slightly different levels of surface ATP concentration observed in the vicinity of the bifurcations outer wall. What is interesting is that the differences along the separation lines are very small, hence the strong growth of the mass transfer boundary layer appears to be the dominant factor. From the above, it is hypothesised that the availability of ATP to the P_{2X} receptor is reduced, hence the possibility of impaired vasodilation.

This also implies that potentially out of plane bifurcations are at a greater risk factor for atherogenesis or more specifically the separated flow.

If the combined ATP+ADP concentration is considered at the surface, an important factor for signalling of the P_{2y} pathway in the eNOS model, the depletion is generally very similar to the lumenal ATP concentration (Figure 8.23), with a slight tendency to be more elevated (Figure 8.23(b)). However, in the iliac-femoral branch region, the combined concentration is still reduced slightly compared with the bulk concentration, as shown in Figure 8.23(b).

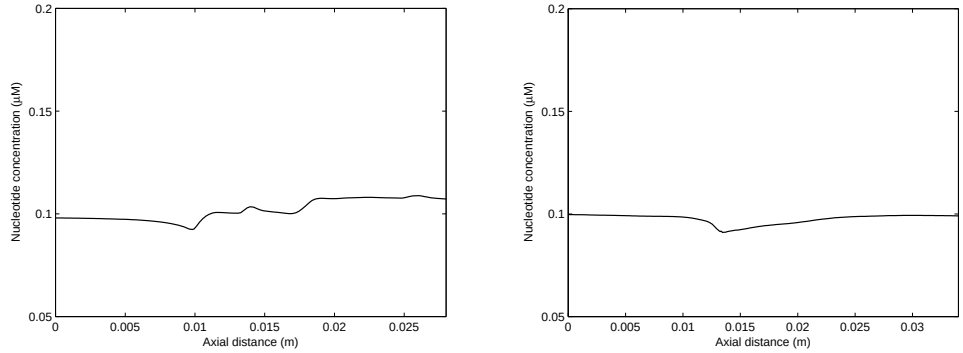

(a) (b)

Figure 8.23: Combined ATP+ADP nucleotide concentration at the endothelium: (a) plot line M (b) plot line P. The combined nucleotide concentration varies significantly less.

Non-Newtonian blood rheology

There have been limited studies into the effects of non-Newtonian blood rheology on mass transport and although this may be valid in the more idealised models, there is potential for some variation in shear rate through the porcine geometry. Evidently in Figure 8.24 there are some differences exhibited, however essential features are captured by the Newtonian model and the differences exhibited are generally negligible at a physiological level. The one location where there is a significant difference is the outer wall of the iliac artery at the location of the femoral branch. This is primarily due to weakened secondary flows under non-Newtonian blood rheology. The surface distribution is very similar to the Newtonian blood rheology, but the low concentration regions tend to span a greater region due to reduced secondary flow, hence reduced convection of ATP to

the endothelial surface. Overall, this effect appears to be insignificant compared with geometric induced changes.

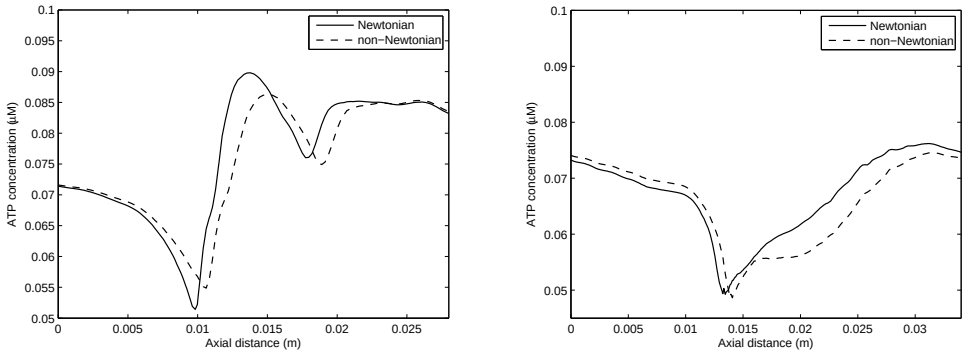

(a) (b)

Figure 8.24: Comparison of blood rheology effects on mass-transport (a) plot line M (b) plot line P. The two profiles tract very closely.

8.5.4 Endothelial cell signalling

As inputs to the Ca^{2+}-eNOS model, presented in Chapter 5, the combined ATP+ADP concentration under slow release conditions and WSS magnitude were used. As assumed with the previous model the sites of low eNOS concentration relative to other regions represent 'hot spots' for atherosclerosis formation, via implication of reduced NO formation and endothelial dysfunction. The model is only qualitative in nature because only essential dynamics that govern eNOS activity were considered.

The surface of this geometry consisting of many 'hills and valleys' is evident in the variations of surface eNOS concentration (Figure 8.25, with regions in relatively linear sections being subject to cycling between elevated eNOS concentration and depleted eNOS levels. Clearly in Figure 8.26, the locations of minimum eNOS concentration localise in regions of low WSS, as a result of disturbed arterial haemodynamics. Figure 8.26 also highlights that the inner regions of daughter arteries can be subject to reduced eNOS activity (due to the curvature of the artery). Many computational studies do not observe this characteristic but it is definitely a location observed *in vivo* (Asakura and Karino, 1990). As with the idealised bifurcation models in Chapter 7 the upper surface of the region prior to

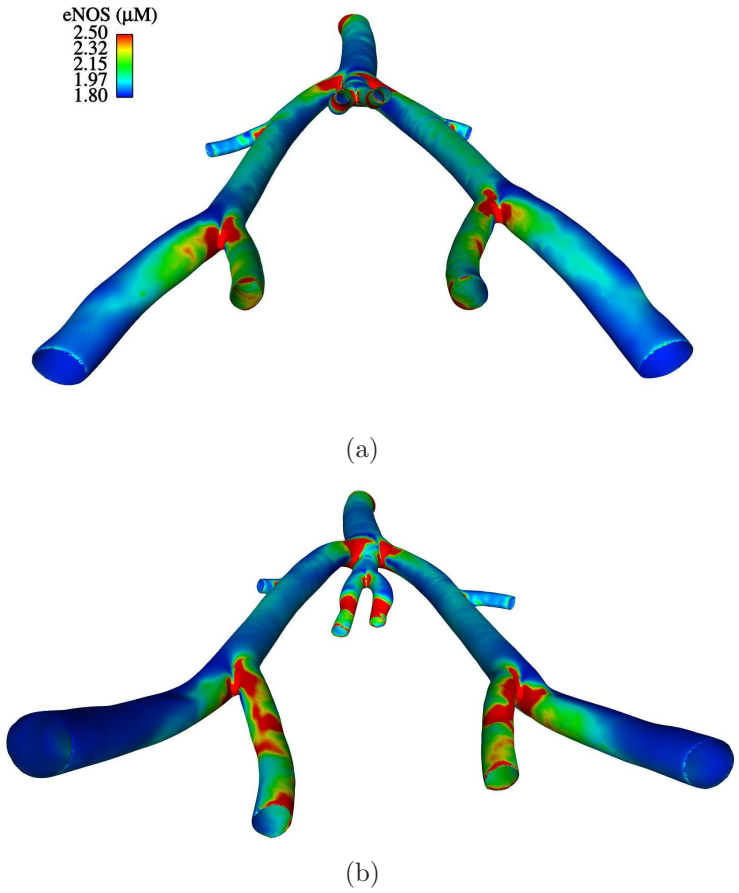

Figure 8.25: eNOS distribution through the aortic trifurcation (a) ventral and (b) dorsal view.

the flow divide can be subject to reduced eNOS concentration, as occurred in the common iliac bifurcation. Here this is furthered and demonstrates that relatively small perturbations in geometry may represent sites prone to atherosclerosis formation, however these perturbations are generally associated with bifurcations and branches.

Figure 8.27 provides information about the eNOS variation along plot lines on the outer wall of the right iliac artery and the left iliac artery at the location of femoral branch. This backs up the previously stated observations that reduced eNOS activity collocates in regions of low WSS (see Figure 8.14) and also demonstrates that the haemodynamic environment in the iliac artery distal to the femoral branch leads to sustained low eNOS activity (Figure 8.27 (b)).

Due to the some controversy surrounding the activation of signalling path-

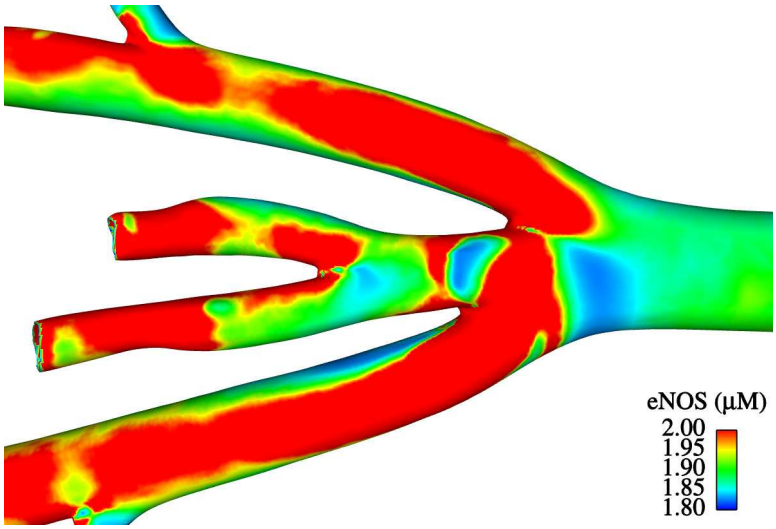

(a)

Figure 8.26: eNOS distribution zoomed in the the central trifurcation region. Note the upper limit on eNOS has been altered to fully demonstrate regions where impaired signalling occurs. These regions are predominantly where the flow is disturbed.

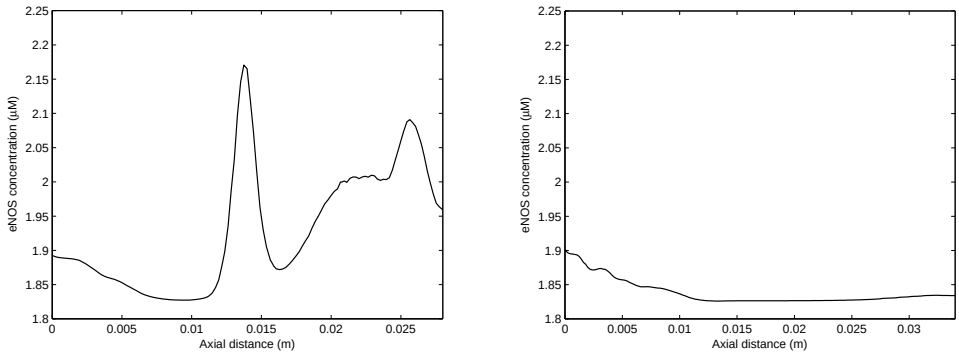

(a) (b)

Figure 8.27: eNOS concentration variation: (a) plot line M (b) plot line P

ways, a variation of the model was investigated. This is one of the major advantages of numerical models is they are easily varied to test potential mechanisms and assess the effects. In the present case, the pathways for eNOS activation were reversed so the calcium dependent pathway is dominant (90% activation via the formation of calcium-calmodulin complex). This resulted in quantitatively different but qualitatively the same distribution of eNOS at the surface, due to different rate constants of the calcium dependent pathway.

8.6 Pulsatile flow

The results presented in this section are only a preliminary analysis (the unexpected results were deemed important enough to get a mention) and, for this reason, some conclusions need further verification. Pulsatile flow and the effects on mass transfer indicate significant differences in the surface distribution, albeit the locations of depleted ATP concentration are generally similar to the steady state mass transfer. Furthermore, the distribution is elevated considerably under pulsatile conditions. Figure 8.28 demonstrates the difference between the unsteady and steady. Generally under steady conditions the depletion at the surface is greater (maximum 33% in the iliac artery distal to the femoral branch). However, locations of reduced ATP concentration do exhibit some similarity.

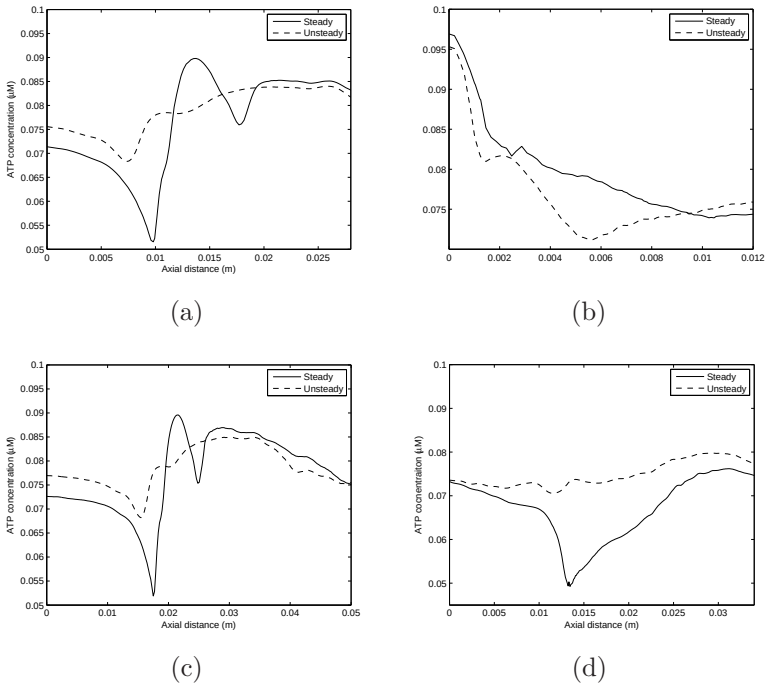

Figure 8.28: Comparison of steady and unsteady ATP along cut planes: (a) line M (b) line N (c) line O (d) line P.

Figure 8.29 observes the difference in topological ATP variations between the steady state and the time averaged unsteady state. Despite the elevation in ATP concentration there appears to be some consistency in terms of low concentration regions. The lower concentration at the inner wall of the iliac artery (plot line N) is due to substantial recirculation (for a large proportion of the cycle) in this

region (the same is true at the inner wall of the right iliac artery).

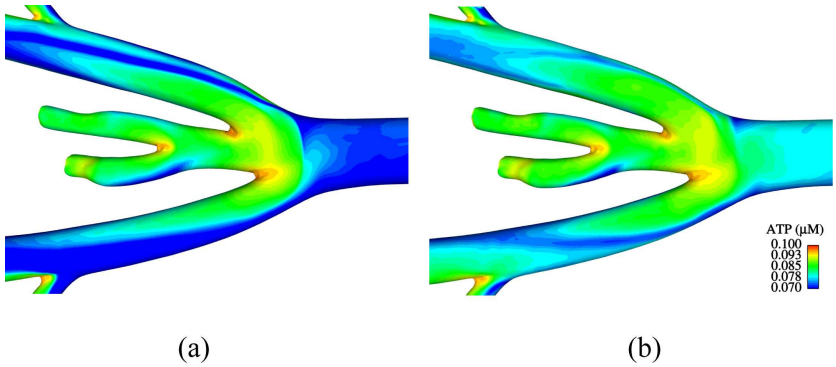

Figure 8.29: Comparison of ATP topology (a) Steady (b) Time averaged. Although the surface concentrations are different to a certain degree there are very similar characteristics.

There are a number of possible reasons for the difference. The secondary flow features, which vary throughout the pulse cycle, enhance convective mixing, thus increasing the effective diffusivity of ATP. This allows increased rates of delivery, which overcome hydrolysis (to a certain degree) leading to elevated surface concentration with respect to the steady state.

For the pulsatile simulations local separation occurs at the inner wall of both the iliac arteries (see figure 8.30), which impacts on the ATP concentration, leading to pockets of depleted ATP concentration at the inner wall. During systolic deceleration the size and extent of the recirculation zone grows (see figures 8.30 and 8.31). These different flow phenomena under pulsatile flow lead to major differences at the surface (specifically the inner walls of the iliac arteries). Furthermore the mean flow field varies significantly from the steady state primarily due to the higher Womersley number.

The lack of response by ATP to changes in haemodynamic conditions is primarily due to the low ATP diffusivity. This is approximately four orders of magnitude smaller than momentum diffusivity (Schimdt number of $\sim$14000), hence it does not respond rapidly to these changes in fluid momentum. Considering the Navier-stokes equation (3.3) and the conservation of species equation (4.1), the unsteady term in both equations scales with the Womersley number squared, but due to the large Schmidt number ATP is relatively unaffected. Therefore variations in ATP concentration do not change in response to different flow conditions. This is evidenced in Figure 8.30 where the haemodynamic conditions

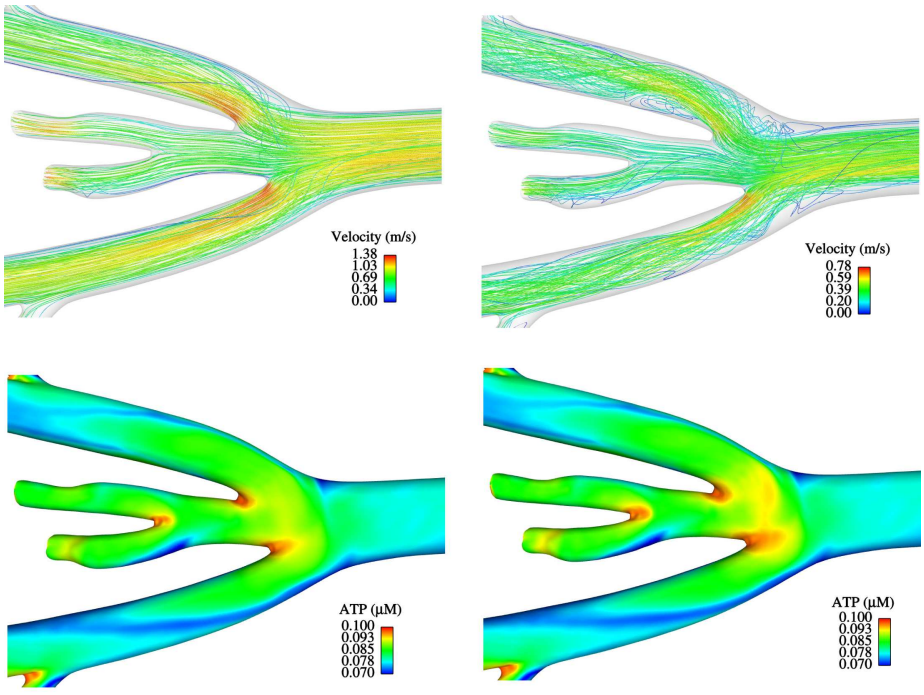

Figure 8.30: Comparison of haemodynamics and resultant ATP distribution (a) t=0.12 (b) t=0.24 The large recirculation zone during systolic deceleration has limited change in the overall surface distribution.

change, but the ATP concentration remains relatively unchanged. As with previous transient models (chapter 7) the size of the elevated ATP concentration region grows during periods of larger forward flow (or more specifically systolic deceleration), where convective delivery is enhanced.

The slight movement in ATP concentration that does occur throughout the cycle is again attributed to secondary flow characteristics. Figures 8.33, 8.34 and 8.35 (planes B-B, E-E and J-J) detail velocity contours at three specific locations throughout the cycle. Evidently the axial velocity contours highlight strong secondary flow characteristics, but this does not have a major impact of the resulting distribution (as already mentioned). For assessment of transient ATP, evolution surface points were sampled in the low concentration and high concentration regions. Furthermore planes B-B, E-E and J-J were sampled over time to determine effects of secondary flow on boundary layer growth. Figure 8.32 shows the sampling times through a cardiac cycle.

Figure 8.33 presents the axial velocity contours at the sampling times given

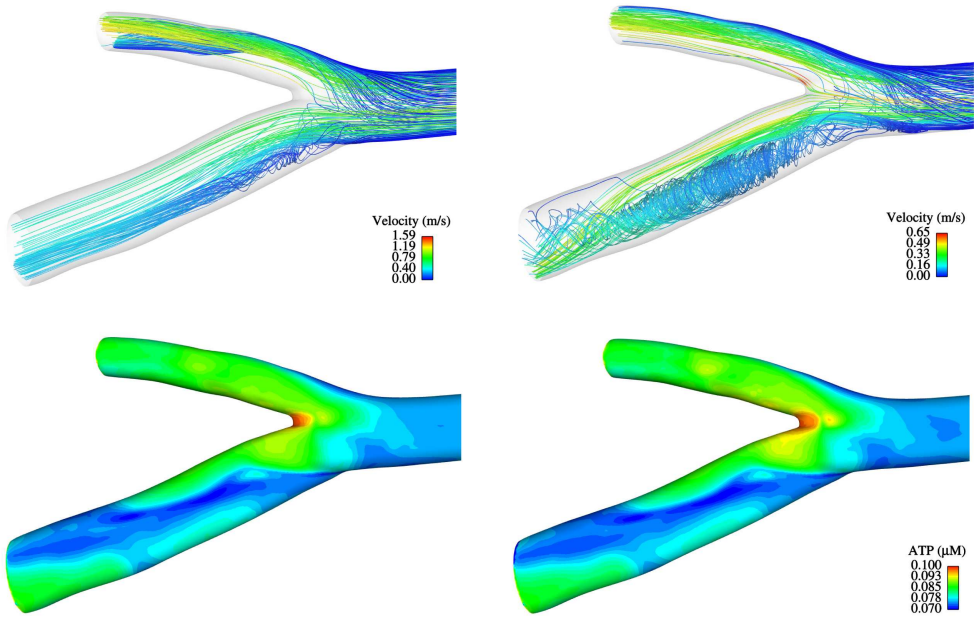

Figure 8.31: Comparison of haemodynamics and resulting ATP distribution in the iliac artery in the region of femoral branch (a) t=0.15 (b) t=0.27. The size and strength of secondary flow is considerably greater during the deceleration phase (t=0.27), however ATP distribution does not change significantly due to the very low diffusivity.

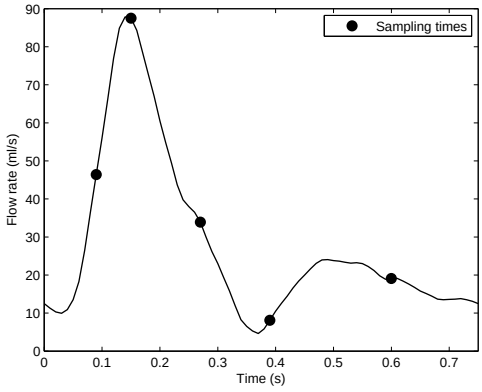

Figure 8.32: Sampling times for transient effects.

in Figure 8.32. The high velocity fluid is always predominantly skewed towards the inner wall. There is some disruption of this profile during the cycle, most notably during systolic phase where the recirculation zone which forms along the inner wall strengthens. This results in a profile that is typical of a branching artery, albeit with a small portion of low velocity fluid at the inner wall (Figures 8.32(a)). This low velocity region grows during the deceleration phase, and per-

sists throughout the diastolic phase. The only disappearance of the recirculation zone (in this plane) is evidenced during the early systolic phase (where the recirculation zone has shrunk and moved upstream). Circumferential movement of the profile is observed throughout the cycle.

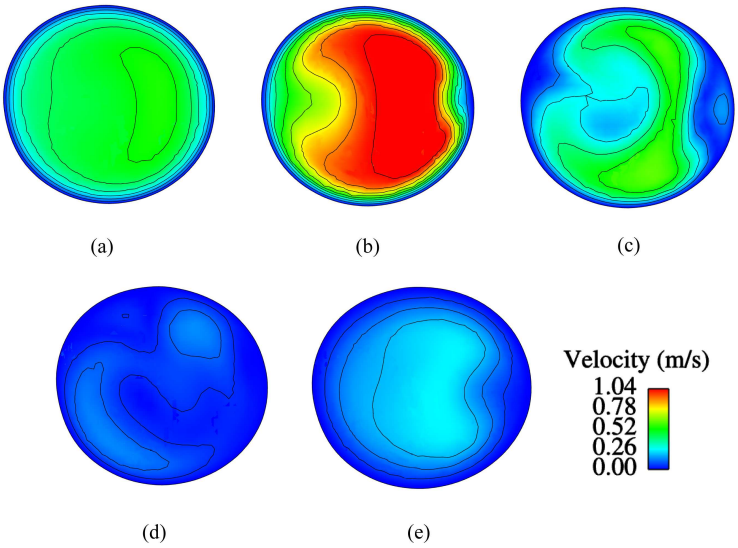

Figure 8.33: Instantaneous axial velocity contours on plane B-B in the left iliac artery (a) t=0.09s (b) t=0.15 (c) t=0.27 (d) t=0.39 (e) t=0.6. The maximum velocity is limited to four times the mean inlet.

Figure 8.34 details velocity contours in the right iliac artery. There is the expected skewing towards the inner wall, which varies in intensity throughout the cycle. There is evidence that the recirculation zone begins at the inner wall resulting in a small skewing away from this surface. This skewing strengthens on downstream planes as the recirculation zone grows (data not shown). In the early diastolic phase axial velocity is almost stagnant which is because of the increase cross flow velocity due to the interaction of two recirculation zones.

Figure 8.35 details velocity contours in the iliac artery distal to the femoral branch. During the systolic phase the growth of the low velocity region is observed. This is also where the strong rotational flow is observed (Figure 8.31). Reduced axial velocity is observed throughout the diastolic phase with the profile skewing remaining towards the inner wall. The previous results overall are consistent with the steady velocity contours found. However the formation of the recirculation zone at the inner wall of the iliac arteries does have a reasonable effect on this profile, which is sustained throughout the cycle.

Figures 8.36, 8.38 and 8.39 detail ATP distribution with in plane secondary

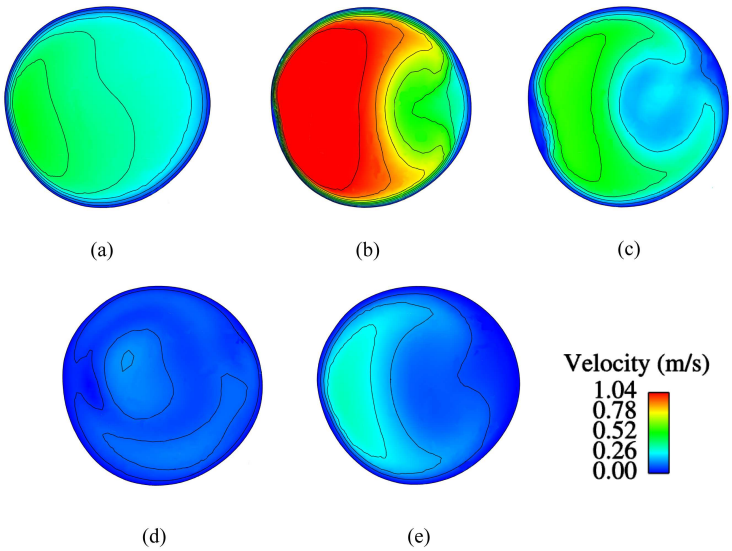

Figure 8.34: Instantaneous axial velocity contours on plane E-E in the right iliac artery (a) t=0.09s (b) t=0.15 (c) t=0.27 (d) t=0.39 (e) t=0.6. The maximum velocity is limited to four times the mean inlet.

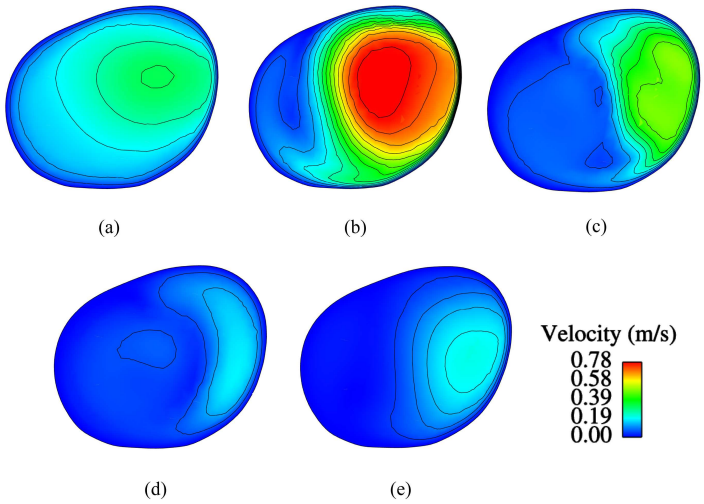

Figure 8.35: Instantaneous axial velocity contours on plane J-J in the left iliac artery in the region of the femoral branch (a) t=0.09s (b) t=0.15 (c) t=0.27 (d) t=0.39 (e) t=0.6. The maximum velocity is limited to three times the mean inlet.

flow lines overlain. The interaction of the vortices shifts pockets of depleted ATP. For the left iliac artery (Figures 8.36) during the systolic phase, the low concentration regions that extend into the domain are 'washed' around in response to the interaction of the vortices. However during the diastolic phase the pocket of fluid is dispersed. This results from the dissipation of the upper vortex and subsequent rotation of the lower vortex around the peripheral dispersing low concentration fluid. This rotation during the small diastolic acceleration results in

the formation of a weak co-rotating vortex (not shown). This previous action pushes the pocket of depleted concentration clockwise. The upper vortex then strengthens resulting in the dispersion of the ATP and leads to a small rise in ATP concentration on the upper surface.

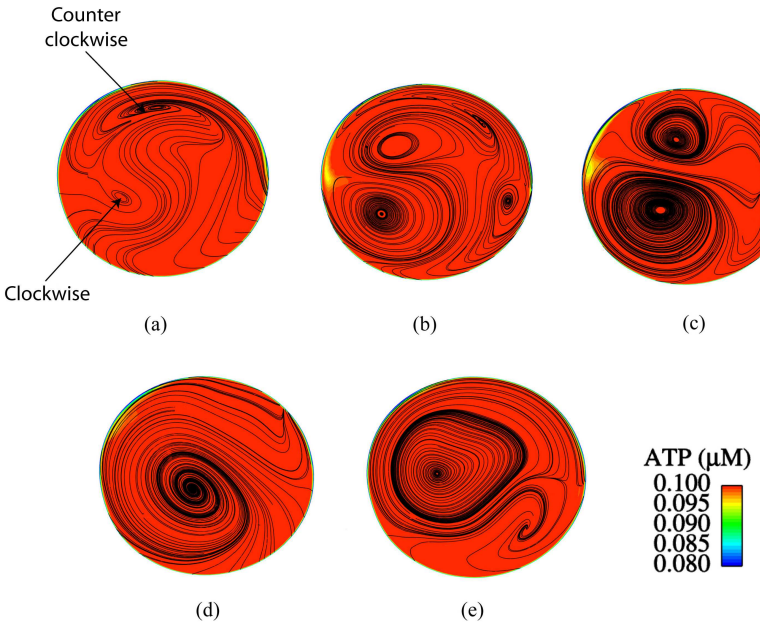

Figure 8.36: Instantaneous ATP contours on plane B-B with secondary flow lines overlain (a) t=0.09s (b) t=0.15 (c) t=0.27 (d) t=0.39 (e) t=0.6. There is considerable extension of depleted ATP into the domain.

In the right iliac artery (Figure 8.38), the low ATP concentration is split into two regions due to the formation of a small vortex at the outer wall (not visible here), which pushes slightly depleted ATP concentration in opposite circumferential directions. However the predominantly low concentration region is essentially unmoved. During the diastolic phase, counter rotating vortices reform and are relatively evenly matched. This process involves the dissipation of the vortex at the inner wall (8.38(d)), the movement of the lower vortex upwards and finally reforming of the counter rotating vortices. During the course of this phase the vortices slowly track towards the outer wall with the lower vortex strengthening resulting in a slight boundary layer growth and associated decrease of ATP concentration at the surface. The vortices at the outer wall are dissipated in the early stages of the diastolic phase due to the interaction of two recirculation zones (see figure 8.37). This interaction results in a strong cross flow characteristic.

Figure 8.39 shows ATP concentration sampled in a location of significant secondary curvature. During the early systolic phase the lower vortex is ill formed.

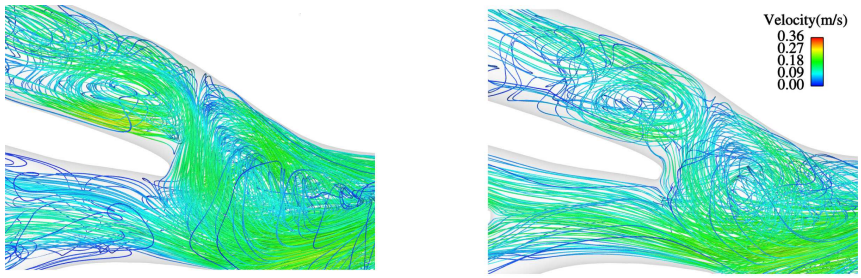

Figure 8.37: The interaction between the two recirculation zones on the outer wall of the branch into the right iliac artery and the inner wall of the right iliac artery at the end deceleration start of diastolic acceleration (a) t=0.36 (b) t=0.39. The interaction of the two recirculation zones results in strong cross flow from inner to outer wall. Flow is from right to left.

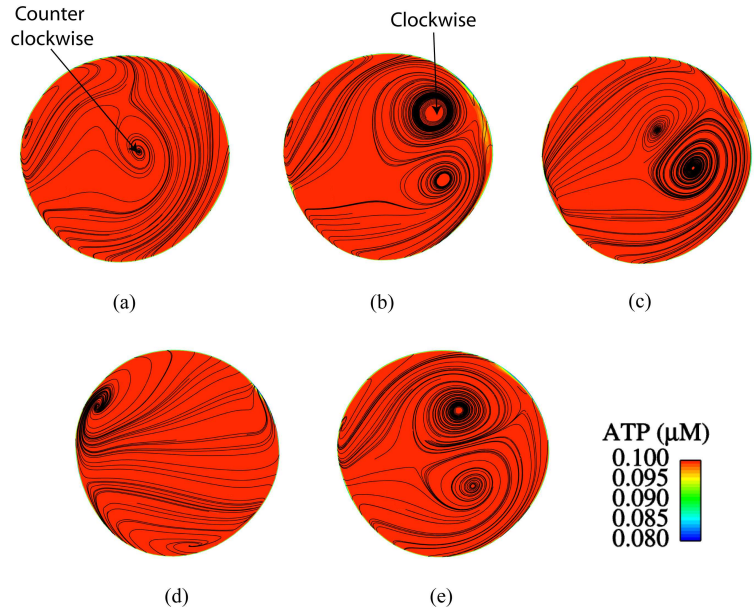

Figure 8.38: Instantaneous ATP contours on plane E-E with secondary flow lines overlain (a) t=0.09s (b) t=0.15 (c) t=0.27 (d) t=0.39 (e) t=0.6.

However it strengthens significantly. The strengthening of the lower vortex results in the pocket of depleted ATP concentration extending into the domain, where the two vortices meet. A movement of this depleted fluid is observed to rotate slightly in a clockwise direction as the lower vortex strengthens during systolic deceleration. During the diastolic phase the upper vortex strengthens resulting in a small shift of depleted ATP concentration in the counter-clockwise direction.

However, it appears only to shift portions that extend into the domain and

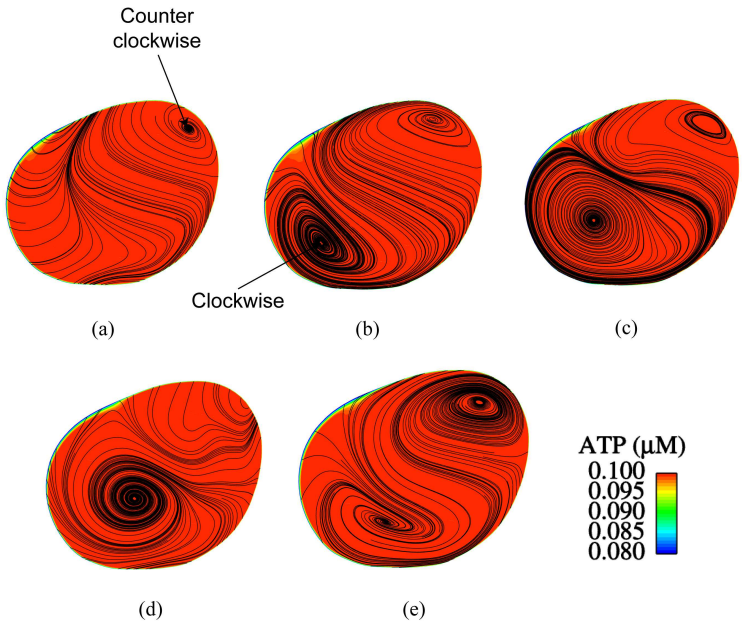

Figure 8.39: Instantaneous ATP distribution on plane J-J with secondary flow lines overlain (a) t=0.09s (b) t=0.15 (c) t=0.27 (d) t=0.39 (e) t=0.6. There is a notable strengthening of the lower vortex during systolic deceleration which moves the low concentration ATP region slightly to the right.

ultimately has little effect on the surface distribution, thence ATP concentration at the endothelium is predominantly geometrically driven, which agrees with previous results of the simplified models of Chapter 7. The changes in the secondary flows observed, due to the curvature of the geometry, may result in further enhancement of convective transport.

Figure 8.40 details some WSS related indices along the inner wall of the left iliac artery and the outer wall of the right iliac artery, plot lines M and N respectively. Both locations represent regions where flow separation occurs at some stage through the pulse cycle. Locations of increased OSI are consistently in location of low mean WSS and these locations correspond reasonably closely with locations of depleted ATP concentration (see Figure 8.28). Overall, OSI infers nothing that cannot be assessed from mean WSS alone, but provides a good assessment of regions in which recirculation occurs

Figure 8.41 details ATP transients at the outer and inner wall of plane B-B, at the location of flow separation at the inner wall of the left iliac artery immediately distal to the trifurcation (plot line N) and at the lower and outer wall of the right iliac artery. As with the models of Chapter 7 the transients that

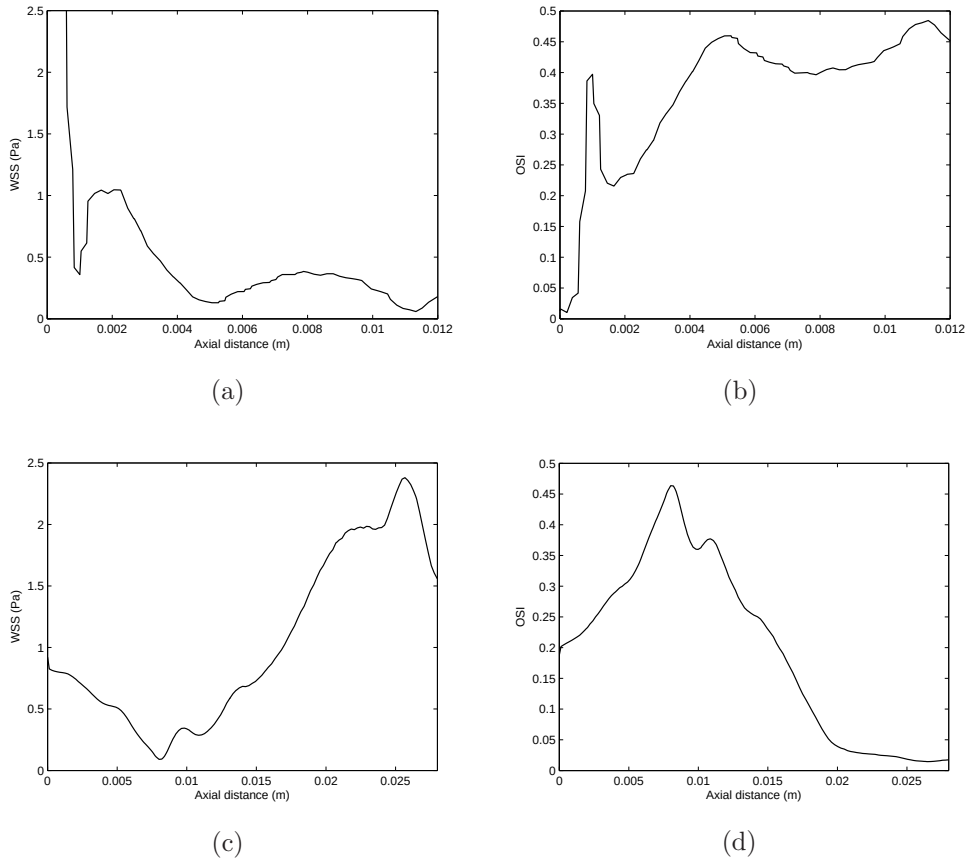

Figure 8.40: Mean WSS magnitude and OSI (a) mean WSS magnitude plot line N (b) OSI plot line N (c) mean WSS magnitude plot line M (d) OSI plot line M.

occur throughout the cycle are very small. Variations near the inner wall of the artery are due to variations of the WSS, however in recirculation regions the variation is due to growing, shrinking and direction changes of the recirculation zone (hence attenuated transport). As with the model of Chapter 7 the most significant transients occur progressing into a recirculation zone in an area preceded by high shear environment (Figure 8.41(b)). This phenomenon only occurred on the inner walls of the two iliac arteries where there was an elevated high shear region followed by separation/attachment. This results in elevated concentration during the large forward flow of the systolic phase which is reduced as the flow separation point moves back towards the bifurcation region during systolic deceleration. Thus the rapid change is governed by the temporal variations in WSS. The locations sampled in Figure 8.41(b) are sampled when mean WSS is low and OSI is elevated.

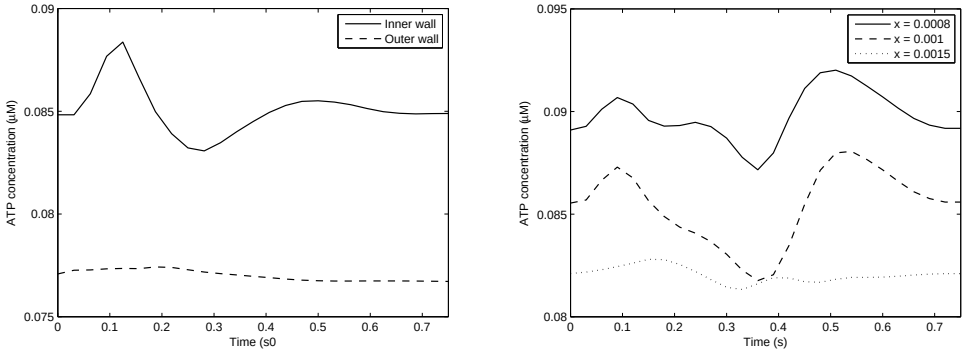

(a)

(b)

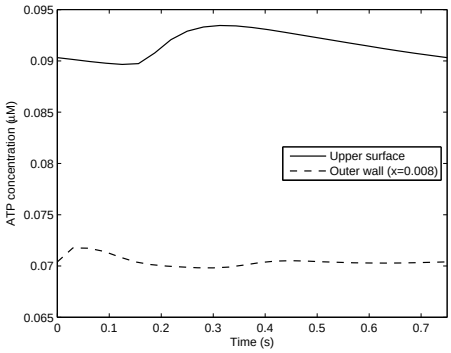

(c)

Figure 8.41: Transient ATP concentration (a) Inner and outer wall of plane E-E (b) Progressing into the recirculation zone along plot line N (x represents the distance from the start of the plot line (c) Sampled on the lower surface and the outer wall where the artery branches into the right iliac (plot line M).

Figure 8.41(c) demonstrates a delayed rise of the upper surface relative to the flow cycle peak. This is because strengthening of the flow across the upper surface during late systole, which enhances convective delivery of ATP to the surface. The locations, such as the outer wall in Figure 8.41(c), observe reduced endothelial concentration due to the movement of the separation line, which results in boundary layer growth. As a region of the vasculature moves into this zone the surface level is seen to decrease. As opposed to the inner wall of the left iliac artery the separation and reverse flow characteristics in this location are even more complicated, but overall the ATP is less variable primarily due to no region of very high wall shear stress. Other locations sampled around the wall (such as the iliac distal to the deep femoral) exhibit similar characteristics to the low concentration region of Figure 8.41(a), with only significant transients occur near branching points in which the ATP concentration is elevated. The

results fully established that transients for low diffusion coefficient species are small. Figure 8.42 investigates the distribution of ATP and axial WSS along plot line N throughout the waveform. Variation of elevated WSS and the separation region lead to larger transient variations in ATP concentration, but this is still considered to be a negligible compared with geometric variations.

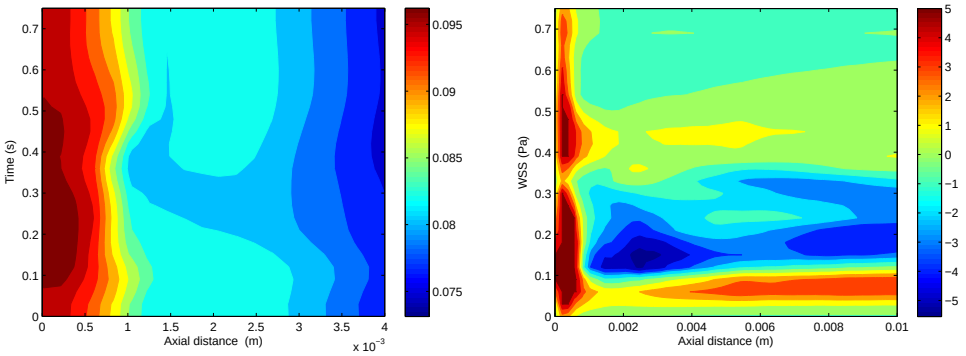

(a) (b)

Figure 8.42: Time variation of (a) ATP and (b) WSS. Distribution plotted along a zoomed in portion of plot line N. Data record every 5 time steps (0.03s)

The results for pulsatile flow and the subsequent effects on mass transfer confirm beyond all doubt that the surface distribution of ATP has limited transient variations. However there are significant differences between the steady and unsteady depletion possibly due to secondary flow induced convective mixing, but also identified are fundamental differences between the underlying flow characteristics. This result is a major finding of the preliminary analysis as these differences were observed to be significant, as much as 33% in regions which are subject to flow recirculation under steady flow conditions. From the above and the previous results provided in this chapter, it is implied that endothelial ATP concentration is more likely to track (hence be depleted in this geometry) the steady state concentration under lower Womersley number flows ie. smaller arteries. This is also backed up by the results of Chapter 7 where the lower Womersley number flow provided for closer tracking between the steady and unsteady.

8.7 Discussion

Application of the models to a realistic geometry has provided for some very interesting and unexpected results. The most significant of these being the flow field and underlying effects on agonist transport and hydrolysis in the iliac-femoral branch. Secondary curvature coupled with a bifurcating artery leads to this location within the vasculature being subjected to depleted surface ATP concentration and occurs even under maximal flow induced ATP release. This condition may very well be important for a number of atherosclerosis related mechanisms. For example, under hypoxia conditions, where reduced oxygen is availability to the arterial wall it has been reported that endothelial cells release ATP to abate these effects and vasodilate the artery (Abbracchio et al., 2006). However this may be of little consequence to this region, as natural delivery of ATP is impaired.

The trifurcation exhibited both in-plane and out of plane curvature; this induces unmatched secondary flows that rotate in the circumferential direction along the axis of the artery. Secondary curvature and implications for atherosclerosis has been considered by a number of groups (Caro et al., 1996, Friedman and Ding, 1998, Myers et al., 2001, Perktold et al., 1998) and in all cases it was shown to have a significant effect on the flow field. Moreover, local curvature (anatomically realistic) variations between different sections of the artery have important effects that can lead to non-uniformity in the WSS distribution. This was also reported in previous publications (Myers et al., 2001, Perktold et al., 1998).

Previously, the only other reported physiologically accurate geometry in which the transport of a low diffusion coefficient species was modelled was performed by Kaazempur-Mofrad and Ethier (2001) in a coronary artery bend. Hence this model is the first of its kind to detail mass transfer in realistic bifurcating arteries. Interesting mass transfer characteristics were exhibited due to the bifurcating geometry (which has not been observed in previous idealised bifurcation models) such as the movement of depleted ATP in the circumferential directions of the vessel because of vessel curvature and variations in cross-sectional area. Another interesting observation is that the distribution of ATP is relatively smooth compared with the variations of WSS. The depleted ATP concentration evidenced here is significant and has implications for impaired signalling. A brief review

by Burnstock (2006) implicated ATP as an important modulator of vasodilation. This has also been reported numerously by others (Gordon, 1986, Kennedy et al., 1985). However, the current model does not find any further reduction in combined ATP+ADP concentration.

In addition the spiral pattern observed in the location of reduced ATP concentration may have some relevance in the distribution of atherosclerosis *in vivo*. A number of studies in literature have reported a spiral pattern in the distribution of atherosclerosis (Caro et al., 1996, Fox et al., 1982, Wensing et al., 1998). Considering the location of reduced mass transfer, these regions may be subject to impaired signalling, hence predisposed to the formation of atherosclerosis via this pathway. From a non signalling perspective these regions of the vasculature may also be more naturally permeable to other species such as LDL.

The implications of separated flow on mass transfer observed are significant, not only for cell signalling. The results represent a qualitative measure of other low diffusion coefficient species, hence the delivery of arbitrary species is impaired. For example if oxygen was considered, then local hypoxia conditions may occur or for LDL, with transmural flux, these regions would be subject to elevated intima LDL levels.

The present implementation of the cell signalling model extends beyond the previous model in the idealised geometry by application to the realistic geometry. Again the emphasis is on 3D cell signalling. The present geometry leads to some very local variations, primarily due to the local variations in WSS. Again, ATP does not show a significant effect, but the same reasons as given in Chapter 7 apply here and resolution to some of these problems are given in Chapter 9. The importance of the cell signalling work presented here is to extend to a cellular level the plethora of work that has established the cause effect relationship between WSS and locations of atherosclerosis. Again, the locations on the outer wall of the bifurcations and inner walls of the curved arteries seem to represent 'hot spots'. The latter area is an interesting observation as it does not imply that the inner wall of bifurcations are risk free, which is commonly reported, as they are generally not straight vessels, similar observations for realistic bifurcations has been reported in (Perktold et al., 1998). This inner wall 'hot spot' is brought about by flow separation/stagnation occurring at the inner wall induced by the curvature. Another interesting observation is along the outer wall of the iliac

artery distal to the femoral branch, substantial flow separation occurs on the outer wall which leads to sustained low eNOS levels. Adjustment of some of the parameters that are not known in vivo was also investigated. When the the calcium dependent mechanism was made the predominant, the resulting surface distribution was qualitatively the same, however the level record in the cells was lower.

As with previous models, separated flow regions in the vasculature are subject to reduced ATP, WSS an eNOS concentration. However the cellular model only identifies with WSS, even with the significantly depleted nucleotide concentrations observed. As previously stated, there is a plethora of evidence that ATP is involved in responses by the endothelium and the results here do not disregard ATP involvement with eNOS production completely. It must be reiterated that the model here only represents a first step towards modelling complex cellular dynamics in 3D environments. The endothelium being a complex ever changing organ means there is still a lot to be understood. Numerical models of this nature presented here can help steer experiments in the appropriate directions to provide information that can extend these models, which are more easily implemented in variations of scenarios than in experiment. This was demonstrated here where variations of the calcium dependent and independent eNOS activation were considered. Potentially, the results disregard the P_{2Y} receptor, but this comes with the same caveats mentioned in Chapter 7. Considering the large variations observed in ATP concentration in this realistic model, pursuing the P_{2X4} pathway reported by Yamamoto et al. (2006) could possibly provide a fundamental link between ATP and the underlying Ca^{2+} response, thus eNOS dynamics, but further experimental and mathematical modelling is required to determine the characteristics of this only recently identified, pathway.

Another problem that comes to light is the lack of knowledge of receptor function and distribution *in vivo*. For example, observations have been reported by Yamamoto et al. (2003) that the response observed when studying human pulmonary artery endothelial cells (HPAECS) is different to that observed in studies using human umbilical vein endothelial cells (HUVECS). Furthermore, a study by Deng et al. (2004) found that gene expression in vein endothelial cells was different to arterial endothelial cells. This potentially implies that responses reported on cultured vein endothelial cells and related back to arterial responses may draw incorrect conclusions about the *in vivo* characteristic. This leads to the question:

Do different regions of the vasculature respond differently? Observations would suggest yes. Considering the initiation of atherosclerosis, the pathobiology of the disease is potentially different in different regions of the vasculature. If this is the case, then receptor distribution may be important and expression levels would need to be determine pharmacologically. Some variations in distribution have been reported and hypothesised in the literature (Ralevic and Burnstock, 1998). In the review paper by Ralevic and Burnstock (1998) it refers to the variations of expression level of P_{2Y1} and P_{2Y2} in hamsters, piglets and lamb arteries, however whether the same is true for humans still remains to be characterised. Variation in expression levels between subtypes could lead to regions of the vasculature becoming insensitive to certain prevailing agonists. Additionally, between the P_{2Y} subtypes it is reported that P_{2Y2} can become desensitised, whereas P_{2Y1} does not (Abbracchio et al., 2006, Ralevic and Burnstock, 1998). This could also lead to variations in the response to local agonist concentrations. Ultimately, the responses being reported in literature with sub-types is conflicting. Finally, due to the large amount of evidence that nucleotides are involved in vasodilation, an important step is to characterise experimentally in full detail the rate constants involved with agonist binding and underlying cell signalling. Only then will a clearer picture become evident.

Although the results for pulsatile flow and effects on mass transfer indicate a reasonable difference between steady and unsteady in this realistic geometry there were still no significant transients observed. Hence none of the prior conclusions made are contradicted. However the actual depletion levels at the surface were significantly reduced and it is hypothesised from this that in lower Womersley number flows greater agreement will be obtained between steady and unsteady concentration profiles. This is primarily due to the greater similarity between steady and time averaged flow fields at low Womersley number. This elevated concentration level under pulsatile conditions is attributed to enhanced convective mixing with the reasonably high Womersley number and this has the effect of increasing axial ATP delivery (Sharp et al., 1990), thus over coming surface hydrolysis. However, the depletion also depends on the extent of flow recirculation occurring throughout the cycle which results in attenuated transport.

The present study has highlighted that non-uniform walls are important for arterial mass transfer, which agrees with a previous study looking at WSS alone in LAD coronary bifurcations (Perktold et al., 1998). Additionally, the major

variations observed in ATP transport were driven by vortex rotation. Secondary curvature and narrowing of the lumen specifically associated with bifurcations appears to be an important geometric feature for atherosclerosis initiation, as evidenced in the iliac-femoral region, where low mass transport and WSS levels were observed. An interesting extension of this model and an increase in realism, would be to introduce arterial wall movement as has been done in idealised geometries (Qiu and Tarbell, 1999). However for the present model there are are number of obstacles in implementation, because of the refinement required to capture arterial variations; some solutions to this problem are presented in Chapter 9.

Chapter 9

Conclusion and Recommendations

9.1 Current Findings

This chapter provides a summary of the important findings from the current study. Furthermore it provides recommendations on future directions that should be pursued to further add a valuable contribution to the field.

9.1.1 Wedge

Chapter 6 investigated the inner wall of a 2D bifurcation to determine how geometry affects nucleotide transport. This was done using a pseudo-similarity solution (David, 2003, Plank et al., 2006a) coupled with a boundary layer solution for flow past a wedge. This allowed geometrical variations to be implemented effectively in order to provide insight into the effects of WSS (geometry) on mass transfer.

The analytical WSS model derived from the boundary layer equations provided a useful first step to understanding geometrical variations on nucleotide concentration. A major assumption made was the flow was potential outside the viscous boundary layer. Although in the immediate vicinity of the inner wall this does not pose a problem, further downstream this was not the case and wall shear stress would increase/decrease infinitely depending on the bifurcation angle, therefore the analysis was only valid for a specific domain in the vicinity of the stagnation point.

Following extension to a CFD model in an idealised 2D geometry (to pro-

vide essential characteristics), the WSS was obtained numerically and was used as input to a semi-analytical model. The difference between this model and the fully-analytical became very evident. In the CFD simulation of the 2D Navier-stokes equation the whole domain was a boundary layer, rather than a 2D region flow of viscous boundary layer and invicid free stream. However there were some marked similarities between the solutions in the immediate vicinity of the bi-furcating artery where both solutions led to similar characteristics in nucleotide distribution. When the model was extended to a full fluid mass transfer CFD simulation of an idealised 2D bifurcation good similarity was obtained between the full numerical and semi-analytical solutions. The semi-analytical method provides for an excellent approximation of the full numerical. Furthermore it has the advantage of being considerably more computationally efficient, as high resolution boundary layers are not required to fully capture steep species gradients. The differences that do exist between the numerical and semi analytical is due to the similarity solution for low diffusion coefficient species not fully satisfying the upper boundary condition, and is termed a pseudo-similarity solution. Full details are provided in Plank et al. (2006a). The results demonstrated a strong relationship between ATP mass transfer, hydrolysis and WSS magnitude.

With the extension to pulsatile flow, the time varying ATP concentration provided little to no difference in endothelial ATP concentration. This was a very important observation, as it suggests that steady state simulations are sufficient to capture detail for secondary messenger responses by the endothelium, which occur over a time scale of minutes, hence mean responses are of interest. However this was in an environment where flow separation and recirculation did not occur and the variation characteristics of the flow, such as the WSS vector, were small.

Finally, with the advent of flow induced ATP release under a variety of release sensitivity conditions an increase was seen in the surface ATP concentration. Under high release conditions, this was a result of a dominating effect of release over surface hydrolysis leading to a continual rise in surface ATP concentration. Under a slightly reduced release rate in the immediate vicinity of the arterial wall ATP release dominated, but further downstream hydrolysis at the surface exhibited a greater effect, before equilibrium between release and degradation was reached. Again, comparison between the semi analytical and numerical showed reasonable agreement, but not to the same level as in the release model. The semi-analytical appears to be slightly oversensitive to the effects of flow induced

release.

9.1.2 Bifurcation and Bend

Previously, ATP transport and cell signalling had not been observed in 3D environments, therefore a study was undertaken to determine the effects of bifurcation angle on mass transfer and underlying eNOS signalling. In addition, it was interesting to determine whether 2D stimulations capture the essential features of a more complex 3D environment. A study of the same models was also undertaken in a multi-bend, which induces flow recirculation at the inner wall.

In contrast to the 2D ATP mass transport, the results of the 3D simulations demonstrated that 2D geometries do lack sufficient flow detail to infer complex 3D mass transfer. The secondary flows that are present in 3D arterial geometries are responsible for regions of the vasculature that are subject to reduced ATP surface delivery. This was evidenced in both the bifurcation and bend geometries, very notable in the bend were regions of very high WSS magnitude that were not subject to raised ATP concentration.

Transients observed in ATP concentration over the course of a cardiac cycle were found to be 'generally' negligible, but this comes with the following caveats. In regions of flow separation, which occurred in the arterial bend, there were reasonably significant transients. Thus this implies that mean concentration levels could be significantly different to steady conditions, however this was not observed here and requires further investigation. Different cardiac waveforms provide very similar overall mass transfer effects, specifically time averaged effects. The transients that do occur come about due to attenuated transport in regions of flow separation/ recirculation. This is also dependent on the waveform under consideration, however reduced surface concentration always occurs during the large forward flow: systolic carotid waveform and diastolic coronary waveform. This was also responsible for the reduced mean ATP levels observed in the bifurcation under pulsatile conditions. For steady flow conditions no recirculation occurs. Similar observations were made in the bend, however the concentration is elevated under pulsatile conditions due to the recirculation zone not being sustained throughout the cycle, whereas under steady conditions a standing recirculation zone exists at the inner wall. Although differences were

exhibited between steady and unsteady these differences were still within a reasonable tolerance band (maximum of 6% difference) and spatial variations seem to be more significant.

Incorporation of the cell signalling in 3D geometries, coupled to the prevailing agonist and haemodynamic environment, identified the outer walls of bifurcations and inner and outer walls of bends as 'hot spots' for impaired eNOS production, hence NO. This progresses to a cellular level the causative-effect relationship with WSS that has previously been identified through numerous arterial modelling studies. Acute angle bifurcations may be a pathogenic risk factor, there is some reports of this in literature, but there are also reports to the contrary, suggesting a myriad of factors such as flow division and area ratio. This may also depend on the types of bifurcations that exist within different locations of the vasculature.

9.1.3 Trifurcation

In order to provide some *in vivo* significance of the present work a similar study was implemented for a realistic arterial geometry. This was primarily motivated as a result of a number of observations made from the results of the bifurcation and bend model and also due to the limited mass transfer studies in realistic geometries. This geometry exhibits some very interesting characteristics that lead to very complex flow structures.

This is the first model of its kind to simulate low diffusion coefficient species in an extensive and realistic arterial geometry with bifurcating arteries. Previously in literature the only other published report was that of a realistic right coronary artery bend. An important and interesting finding was the significance of secondary curvature in bifurcating arteries and implications for mass transfer. This geometric structure led to flow separation and torsional downstream flow characteristics. Furthermore, even under ATP release this region of the vasculature was still subject to depleted surface ATP concentration irrespective of the release rate. This occurred because along the separation line, the WSS magnitude is zero (providing no release of ATP in this region). This coupled with significant mass transfer boundary layer growth led to very little change in this region over the different release rates examined. Therefore it is hypothesised that this type of geometry may be susceptible to atherosclerosis through the implications of

insufficient receptor activation (via the ATP sensitive P_{2X} pathway).

The complexities of this geometry, lead to mass transfer effects that are not observed in idealised geometries. For example the local curvature, such as changing cross-sectional shape, affects the location of vortices, which in turn shifts the region of depleted ATP concentration. Finally, the realistic geometry has firmly established that WSS magnitude is secondary to local curvature changes that influence the WSS vector.

From the endothelial cellular model, the differences from previous models are that the non-uniformity of the arterial wall provides for local surface variations in eNOS levels. However, similar regions of the vasculature were susceptible such as regions of flow separation and recirculation and the outer walls of bifurcations. Additionally a new region that is not highlighted in more idealised models is the inner walls of bifurcations. In the femoral bifurcation the lowest intracellular eNOS levels were recorded in this area. Thus, geometries exhibiting significant secondary curvature throughout the cardiovascular system possibly represent 'hot spots' for the initiation of atherosclerosis. Overall, the model applied to a realistic geometry shows good agreement with locations reported *in vitro* and *in vivo*.

Pulsatile flow simulations evidence that the surface ATP concentration is raised compared with the steady state (around 33% in locations of recirculation). This is a significant difference and occurs due to the appearance and disappearance of flow recirculations throughout the course of the cycle. Furthermore the surface distribution is affected by local surface variations, more so under unsteady conditions, however it is generally similar. As with previous pulsatile models transients occurring throughout the cycle are generally insignificant, as there is a very slight enhancement of the low concentration regions during systolic deceleration. The elevated ATP levels found under pulsatile flow is possibly due to convective mixing induced by the complex secondary flows, which results in effective ATP diffusivity that is higher than the actual.

9.2 Future Work

Future work should aim to progress the current models to even more accurately reproduce the *in vivo* situation. This could be done by implementing models

along the lines given below.

9.2.1 Numerical Arterial Modelling

From a numerical perspective there is a reasonable amount of work that could be implemented over and above what has already been done. Although transient mass transfer effects are fairly negligible, it would be very interesting to study transients with the effects of arterial wall movement (fluid-structure interaction). Although this would present itself as very computationally intensive (cf. the time for unsteady non-compliant artery wall simulations $\sim$ 35days), the local nature of low diffusion coefficient mass transfer suggests this may play a reasonably significant role and possibly highlight some interesting characteristics for cell signalling. For example wall movement will induce recirculation lowering the mean ATP concentration. Implementation of such a model on geometries such as the femoral portion of the trifurcation would provide for very interesting results specifically with out of plane effects. Moreover, with the implementation of a fluid structure interaction model, it would be interesting to use the most accurate boundary conditions. This would be achieved by coupling a 0D or 1D models of the entire cardiovascular system. A mathematical arterial modelling review by Quarteroni (2006) provides information and references on this topic. This would then provide the boundary conditions for the inlets and outlets of the 3D computational domain, hence providing a 0D-3D or 1D-3D coupled model.

A new CFD solver is required for future work. This is for a number of reasons. Due to the increasing complexity and size of the problems being undertaken, Fluent is an expensive option because of a large number of parallel licenses required. A suggestion to remedy this is move to an open source solver such as OpenFoam (OpenCFD, 2007). Furthermore the coupled models mentioned above are not able to be implemented into Fluent in its current form.

9.2.2 Cell Modelling

Future work will involve the addition of NO release to the model and the effects of NO-dependent arterial wall vasomotion. Endothelium-derived NO induces

relaxation of sub-endothelial SMC and consequent vasodilation (Davignon and Ganz, 2004). The altered vessel diameter will in turn modify the fluid flow field, acting as a feedback controller. In addition, this will allow realistic blood waveforms to be coupled to the underlying cellular dynamics. The potentially nonlinear interaction between spatially and temporally varying species, WSS and vasomotion may be significant.

Include the P_{2X} pathway in the cellular model: this is a pathway that is sensitive only to ATP, but experimental work is really required to determine the rate constants. This could then be used alongside experimental observations to determine how different pathways respond.

Models of ATP release that is transient and allows for decay: This could be achieved by coupling to a cell model. The difficulty with pursuing this route is the observations in literature are still rather inconclusive, with mechanisms of release still remaining poorly understood (Yamamoto et al., 2003). The other option in this area is to fit to experimental data and model the process to reproduce essential features.

Finally, there needs to be a real push towards experimental investigations into intracellular signaling; this is a complicated task, but for the furthering of understanding of it is a necessity. This could be implemented initially in a relatively simple environment, such as a backwards facing step, with endothelial cells cultured on the lower surface. Measurements of eNOS activity could be made to determine the response to different stimuli, such as ATP and WSS.

Appendix A

A.1 Perspectives of fluid flow

There are two view points that can be taken to describe fluid motion: Lagrangian and Eulerian. These two different descriptions are represented in Figure A.1. The Lagrangian description considers a closed system that follows an identifiable material volume through the domain, which can be considered as a mapping of the original configuration to the current. In the Eulerian description the interest is what happens at a local (fixed) spatial region and considers a closed system where fluxes in and out are assessed. These two descriptions lead to an important operator in fluid mechanics known as the material (or substantial) derivative, given by

$$\frac{D}{DT} = \frac{\partial}{\partial t} + u\frac{\partial}{\partial x} + v\frac{\partial}{\partial y} + w\frac{\partial}{\partial z} = \frac{\partial}{\partial t} + \mathbf{u} \cdot \nabla \tag{A.1}$$

This represents the relationship between the two different descriptions. The LHS represents the total time rate of change of a material volume. On the RHS the The first term (temporal) accounts for local changes in fluid properties due to flow unsteadiness and the second term (convective) accounts for changes in fluid properties due to changes in spatial location. In the present study the Eulerian frame of reference is considered.

Finally, the form of the governing equations of fluid mechanics is important to consider. They can be obtained in a number of different forms depending on the quantities of interest, although all forms are equivalent and can be transformed into one another. The different forms are integral and differential. Integral form

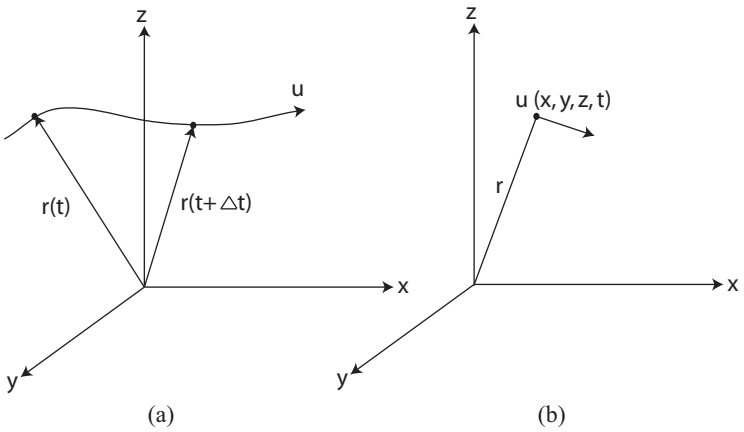

Figure A.1: Different descriptions of fluid motion (a) Lagrangian (b) Eulerian.

is a global approach where the quantities of interest are global properties, such as, flow rates and pressures, whilst differential form is important when quantities such as pressure gradients are under consideration. Furthermore, for the numerical method used to solve the governing equations, the final equations will be given in integral form, as this is required for discretisation in the finite volume method.

A.2 Reynolds Transport Theorem

The method given here follows that given in Kleinstreuer (1997). To begin with, we consider the amount of an extensive property of the system (B), such as mass or momentum, within a control volume (CV) at time (t), see Figure A.2 where the relationship between the extensive (B) and intensive property, ϕ (a per unit mass quantity) is given by

$$\mathrm{B}_{\mathrm{sys}} = \int_{\mathrm{sys}} \rho \phi d\forall \tag{A.2}$$

Now, consider the control volume of Figure A.2.

From a Lagrangian point of view, the time rate of change of the extensive property is given by

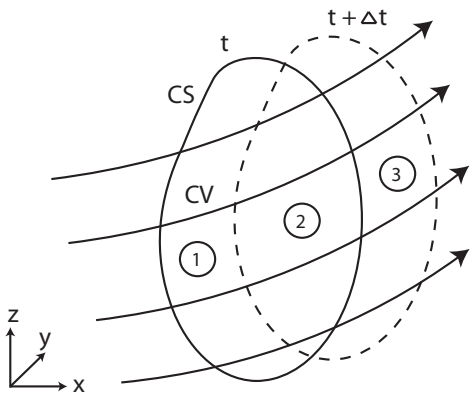

Figure A.2: Moving system in 3D space. At time t, the system occupies the control volume (regions (1) + (2)). At some time Δt later the system has move to a new location occupying regions (2) + (3).

$$\frac{\mathrm{DB_{sys}}}{\mathrm{Dt}} = \lim_{\Delta t \to 0} \frac{B_{\mathrm{sys}}(t + \Delta t) - B_{\mathrm{sys}}(t)}{\Delta t} \tag{A.3}$$

using this and considering Figure A.2, the following is obtained

$$\frac{\mathrm{DB_{sys}}}{\mathrm{Dt}} = \lim_{\Delta t \to 0} \frac{B_2(t + \Delta t) + B_3(t + \Delta t) - (B_1(t) + B_2(t))}{\Delta t} \tag{A.4}$$

where $B_2(t+\Delta t)+B_3(t+\Delta t)$ represents the amount of the extensive property at time $t + \Delta t$, and $B_1(t) + B_2(t)$ at t. To attach physical significance consider the following reformulation

$$\frac{\mathrm{DB_{sys}}}{\mathrm{Dt}} = \lim_{\Delta t \to 0} \frac{B_2(t + \Delta t) - B_2(t)}{\Delta t} + \lim_{\Delta t \to 0} \frac{B_3(t + \Delta t)}{\Delta t} - \lim_{\Delta t \to 0} \frac{B_1(t)}{\Delta t} \tag{A.5}$$

where the first, second and third term of on the RHS respectively represent accumulation, outflow and inflow. Now in the limit as $\Delta t \to 0$ the volume of the system at time $t + \Delta t$ approaches that of the control volume at time t ie. Lagrangian frame coincides with the Eulerian frame, hence the accumulation term becomes

$$\frac{\partial G}{\partial t} = \frac{\partial}{\partial t} \int\limits_{CV} \rho\phi \forall \tag{A.6}$$

For the other terms consider a small elemental area on the control surface, the flux of ϕ across the control surface is given by

$$\lim_{\Delta t \to 0} \frac{B_3(t+\Delta t)}{\Delta t} - \lim_{\Delta t \to 0} \frac{B_1(t+\Delta t)}{\Delta t} = B_{\text{out}} - B_{\text{in}} = \int\limits_{CS} \rho\phi \mathbf{u} \cdot d\mathbf{A} \tag{A.7}$$

On substitution the final form of Reynolds transport theorem is obtained

$$\frac{\mathrm{DB_{sys}}}{\mathrm{DT}} = \frac{\partial}{\partial t} \int\limits_{CV} (\rho\phi) d\forall + \int\limits_{CS} (\rho\phi) \mathbf{u} \cdot d\mathbf{A} \tag{A.8}$$

A.3 Continuity

The continuity condition is a statement of mass balance as it requires that the accumulation within the control volume is balanced by the fluxes across the control surface. Consider equation (C.1), let the extrinsic property ($\mathrm{B_{sys}}$) represent the mass of the system ($\mathrm{m_{sys}}$), hence the intrinsic property is ϕ=1, therefore equation C.1 is written as

$$\frac{\mathrm{Dm_{sys}}}{\mathrm{DT}} = \frac{\partial}{\partial \mathrm{t}} \int\limits_{\mathrm{CV}} \rho \mathrm{d}\forall + \int\limits_{\mathrm{CS}} \rho \mathbf{u} \cdot \mathrm{d}\mathbf{A} = 0 \tag{A.9}$$

Additionally, for a fixed control volume

$$\int\limits_{CV} \frac{\partial \rho}{\partial t} d\forall + \int\limits_{CS} \rho \mathbf{u} \cdot d\mathbf{A} = 0 \tag{A.10}$$

on the assumption of an incompressible fluid ($\rho = c$), this becomes

$$\int_{CS} \rho \mathbf{u} \cdot d\mathbf{A} = 0 \tag{A.11}$$

Applying gauss's divergence theorem

$$\int_{CV} (\nabla \cdot \mathbf{F}) \; d\forall = \int_{CV} \mathbf{F} \cdot d\mathbf{A} \tag{A.12}$$

to equation (A.11),

$$\int_{CV} \nabla \cdot \mathbf{u} d\forall = 0 \tag{A.13}$$

physically, the integrand must be zero leading to the following condition, which is known as the divergence free condition.

$$\nabla \; \cdot \mathbf{u} = 0 \tag{A.14}$$

A.4 Momentum

Reynolds Transport theorem with $\phi = \mathbf{u}$ leads to the the momentum equation (Newton's second law)

$$\sum F_{ext} = \frac{\partial}{\partial t} \int_{CV} \rho \mathbf{u} d\forall + \int_{CS} \rho \mathbf{u}\mathbf{u} \cdot d\mathbf{A} = \rho \frac{D\mathbf{u}}{Dt} \tag{A.15}$$

Here F_{ext} represents two types of forces; body and surface forces. Body forces act throughout the continuum and common examples are gravity and electromagnetic fields. If we denote $\mathbf{f}$ as the force per unit mass, for example, $\mathbf{f}$=$\mathbf{g}$,

the following integral represents the body force acting throughout the volume.

$$\sum F_{\text{body}} = \int_{CV} \rho \mathbf{f} d\forall \tag{A.16}$$

When it comes to surface forces the story is a little different. Body forces are assumed known and are obtained externally, whilst surface forces depend on the motion of the fluid, as they are a result of the surroundings being in direct content with an element of fluid. Surface forces lead to stress acting on the fluid, thus a constitutive relationship (equation) needs to be found to relate the state of stress and state of deformation(or motion). This is purely because equations A.13 and A.15 consist of four equations containing ten unknowns, therefore six constitutive relations are required to make the problem determinant.

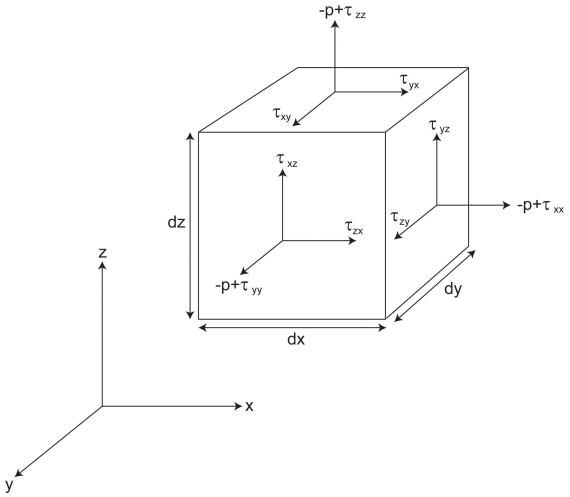

Figure A.3: Fluid element in cartesian coordinates with stress vectors overlain.

The methodology in deriving and evaluating surface forces follows closely that outlined in Schlichting and Gersten (1999). Consider an infinitesimal fluid element, Figure A.4, with associated fluid stresses. When a fluid element is at rest (hydrostatic stress state) the only forces acting on it are due to pressure. This pressure only acts in the normal direction to each planar surface of the element, and is an isotropic quantity given by $-p$ (note this is a negative quantity indicating positive pressure which puts the element in a state of compression). When the element is in motion there are both tangential (shear) and normal forces acting on the element due to viscous forces. It is customary to resolve the total stress tensor into a pressure term and the viscous stress tensor, leading to the following

$$\sum F_{\text{surface}} = \int_{CS} -p\bar{\bar{\mathbf{I}}} \cdot d\mathbf{A} + \int_{CS} \bar{\bar{\tau}} \cdot d\mathbf{A} \tag{A.17}$$

where $\bar{\bar{\tau}}$ described by the following symmetric second order tensor.

$$\bar{\bar{\tau}} = \begin{pmatrix} \tau_{xx} & \tau_{xy} & \tau_{xz} \\ \tau_{xy} & \tau_{yy} & \tau_{yz} \\ \tau_{xz} & \tau_{yz} & \tau_{zz} \end{pmatrix} = \tau_{ij} \tag{A.18}$$

The diagonal terms above correspond with the normal forces described in Figure A.4 without the pressure. For closure of the system defined by equations (A.15, A.16, A.17) it remains to determine the relationship between the viscous stress tensor and the velocity ($\mathbf{u}$) or more precisely ($\nabla\mathbf{u}$).

When fluid is in motion each element undergoes deformation; this motion is completely characterised if the velocity vector ($\mathbf{u}$) is known as a function of spatial and temporal coordinates (x, y, z, t). There is a known kinematic relationship that exists between the rate of deformation and this function. The rate of deformation within a fluid depends on the relative motion of two points within the fluid. Consider Figure A.4, where the velocity field point A is moving to A′ over time dt, with the distance being given by $\mathbf{s}$=$\mathbf{u}$dt. Point B which is a distance d$\mathbf{r}$ from point A moving to point B′ with the distance given by $\mathbf{s}$+d$\mathbf{s}$=($\mathbf{u}$+d$\mathbf{u}$)dt.

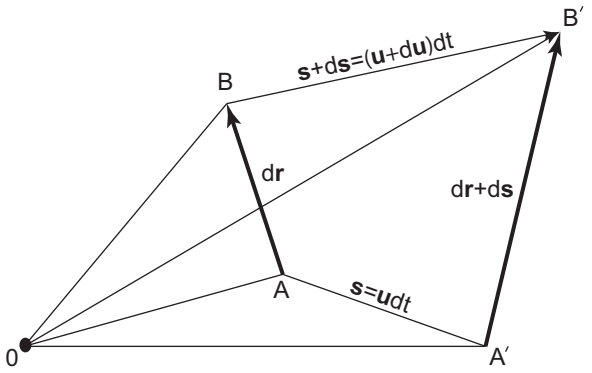

Figure A.4: Relative displacement of two points in a velocity field.

Now, if we consider the velocity in component form following a Taylor series expansion (neglecting higher order terms) the velocity at point A is given by

$$\begin{aligned} u + du &= u + \frac{\partial u}{\partial x}dx + \frac{\partial u}{\partial y}dy + \frac{\partial u}{\partial z}dz \\ v + dv &= v + \frac{\partial v}{\partial x}dx + \frac{\partial v}{\partial y}dy + \frac{\partial v}{\partial z}dz \\ w + dw &= w + \frac{\partial w}{\partial x}dx + \frac{\partial w}{\partial y}dy + \frac{\partial w}{\partial z}dz \end{aligned} \tag{A.19}$$

or in vector notation

$$\mathbf{u} + d\mathbf{u} = \mathbf{u} + \nabla\mathbf{u} \cdot d\mathbf{s} \tag{A.20}$$

where $\nabla\mathbf{u}$ represents the relative motion of the two points in space.

$$\nabla\mathbf{u} = \begin{pmatrix} \frac{\partial u}{\partial x} & \frac{\partial u}{\partial y} & \frac{\partial u}{\partial z} \\ \frac{\partial v}{\partial x} & \frac{\partial v}{\partial y} & \frac{\partial v}{\partial z} \\ \frac{\partial w}{\partial x} & \frac{\partial w}{\partial y} & \frac{\partial w}{\partial z} \end{pmatrix} = \frac{\partial u_i}{\partial x_j} \tag{A.21}$$

The last term on the RHS represents the velocity gradient tensor expressed using Einstein's summation notation. To attach physical significance to the velocity gradient tensor, it is convenient to decompose into its symmetric and anti-symmetric components[1]. The symmetric part represents the *rate of deformation tensor*, this quantity separates fluid motion from rigid body motion, an is given by

[1]Every tensor can be expressed uniquely as the sum of a symmetric and anti-symmetric tensor

$$\bar{\bar{\varepsilon}} = \begin{pmatrix} \dfrac{\partial u}{\partial x} & \dfrac{1}{2}\left(\dfrac{\partial v}{\partial x} + \dfrac{\partial u}{\partial y}\right) & \dfrac{1}{2}\left(\dfrac{\partial w}{\partial x} + \dfrac{\partial u}{\partial y}\right) \\ \dfrac{1}{2}\left(\dfrac{\partial u}{\partial y} + \dfrac{\partial v}{\partial x}\right) & \dfrac{\partial v}{\partial y} & \dfrac{1}{2}\left(\dfrac{\partial w}{\partial y} + \dfrac{\partial v}{\partial z}\right) \\ \dfrac{1}{2}\left(\dfrac{\partial u}{\partial z} + \dfrac{\partial w}{\partial x}\right) & \dfrac{1}{2}\left(\dfrac{\partial v}{\partial z} + \dfrac{\partial w}{\partial y}\right) & \dfrac{\partial w}{\partial z} \end{pmatrix} \tag{A.22}$$

or in summation notation

$$\varepsilon_{ij} = \frac{1}{2}\left(\frac{\partial u_i}{\partial x_j} + \frac{\partial u_j}{\partial x_i}\right) \tag{A.23}$$

The anti-symmetric component is the *vorticity tensor*, and is given by

$$\bar{\bar{\omega}} = \begin{pmatrix} 0 & \dfrac{1}{2}\left(\dfrac{\partial u}{\partial y} - \dfrac{\partial v}{\partial x}\right) & \dfrac{1}{2}\left(\dfrac{\partial u}{\partial z} - \dfrac{\partial w}{\partial x}\right) \\ \dfrac{1}{2}\left(\dfrac{\partial v}{\partial x} - \dfrac{\partial u}{\partial y}\right) & 0 & \dfrac{1}{2}\left(\dfrac{\partial v}{\partial z} - \dfrac{\partial w}{\partial y}\right) \\ \dfrac{1}{2}\left(\dfrac{\partial w}{\partial x} - \dfrac{\partial u}{\partial z}\right) & \dfrac{1}{2}\left(\dfrac{\partial w}{\partial y} - \dfrac{\partial v}{\partial z}\right) & 0 \end{pmatrix} \tag{A.24}$$

or in summation notation

$$\omega_{ij} = \frac{1}{2}\left(\frac{\partial u_i}{\partial x_j} - \frac{\partial u_j}{\partial x_i}\right) \tag{A.25}$$

To fully understand the previous expressions a kinematic interpretation is required. The motion of the two points in the velocity can be considered in four 'modes' making up the components of the previous matrices: translation, rotation, dilation and deformation. An account of each will be considered independently and in 2D for simplicity. Translation of the fluid element, Figure A.5(a), simply refers to the movement of the element in a known velocity field.

Deformation of the fluid element, due to shear, is represented in Figure

A.5(b). This is represented by the off diagonal terms of $\bar{\varepsilon}$ being non zero. For example, in Figure A.5(b), consider the velocity field aligned normal to the x axis; this deforms the element in the positive y direction. The relative velocity at point B, from equation (A.20) is given by

$$dv = \frac{\partial v}{\partial x} \tag{A.26}$$

hence the length of $\overline{BB'}$ is simply given by

$$\overline{BB'} = \frac{\partial v}{\partial x}\delta t \tag{A.27}$$

Let angle between length $\overline{A'B'}$ and $\overline{AB}$ be denoted by $\delta\theta$, providing the deformation is small, we can write

$$\tan\delta\theta \approx \delta\theta = \frac{\partial v}{\partial x}\delta t \tag{A.28}$$

thus shear angular velocity is obtained by dividing both sides of equation A.28 by δt and taking the limit

$$\lim_{\delta t\to 0}\frac{\delta\theta}{\delta t} = \frac{d\theta}{dt} = \dot{\theta} = \frac{\partial v}{\partial x} \tag{A.29}$$

equivalently for the field aligned normal to the y axis, one obtains $\dot{\theta} = \partial u/\partial y$. If both the derivatives are positive, as indicated in Figure A.5(b) the total angle change at the origin ($\overline{AA'}$) is given by the superposition of these two processes, hence the volume conserving deformation on a given plane is defined as averaged of the shear angular velocity,

$$\dot{\varepsilon}_{xy} = \dot{\varepsilon}_{yx} = \frac{1}{2}\left(\frac{\partial v}{\partial x} + \frac{\partial u}{\partial y}\right) \tag{A.30}$$

For Dilatation the element undergoes a volume change. In figure A.5(c),

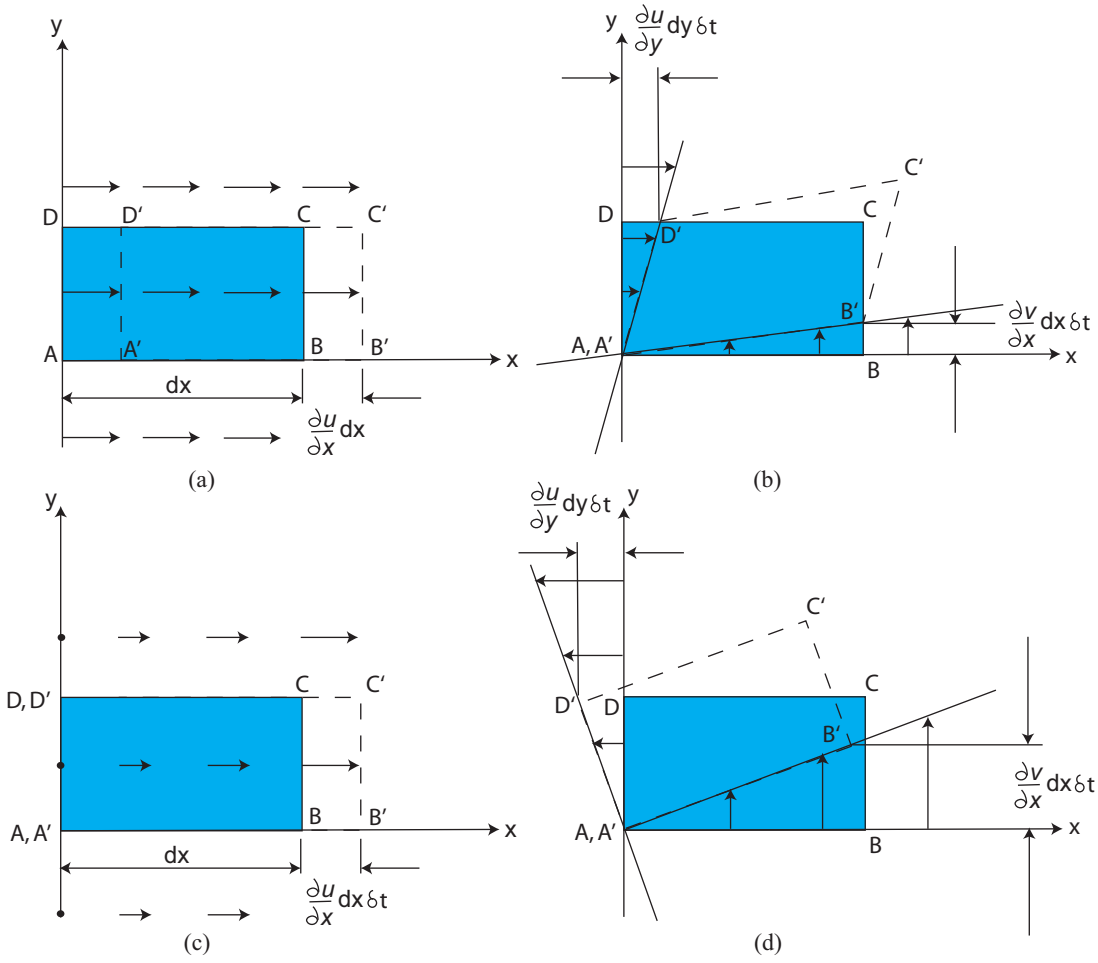

Figure A.5: 2D illustrations of the different types of motion a fluid element undergoes (a) translation (b) deformation (c) dilatation (d) rigid body rotation.

the element is in a velocity field that strengthens in the positive x direction; this implies that all components of the rate of deformation tensor (∇u) are zero except for $\partial u/\partial x$, the relative velocity can therefore be expressed as

$$du = \frac{\partial u}{\partial x} dx \tag{A.31}$$

Now, if this is extended to 3D the deformation is the trace of the normal components of $\nabla \mathbf{u}$, and is the divergence of the velocity field.

Figure A.5(d) represents rigid body rotation. This means all off diagonal components of the vorticity tensor are non zero and no deformation occurs due to the off diagonal terms of $\bar{\varepsilon}$ being equal to zero. For the 2D case, the instantaneous

angular velocity, necessary for rigid body rotation (angle change equal in the same direction) is given by

$$\frac{\partial v}{\partial x} = -\frac{\partial u}{\partial y} \tag{A.32}$$

with the element angular velocity given by the average rotation

$$\omega_{xy} = \frac{1}{2}\left(\frac{\partial v}{\partial x} - \frac{\partial u}{\partial y}\right) \tag{A.33}$$

which is the component of the vorticity tensor. An equivalent extension can be made to other coordinate directions.

From the previous outline it has been established that stress tensor only depends on the components of the rate of deformation tensor and not on translation or rotation, as they do not contribute to relative displacement between two neighbouring points. A well known constitutive relation exists in fluid mechanics (Schlichting and Gersten, 1999) and is given by

$$\bar{\bar{\tau}} = \lambda\bar{\bar{\mathbf{I}}}(\nabla \cdot \mathbf{u}) + 2\mu\bar{\bar{\varepsilon}} \quad \text{or} \quad \tau_{ij} = \lambda\delta_{ij}\varepsilon_{kk} + 2\mu\varepsilon_{ij} \tag{A.34}$$

where λ represents the bulk viscosity. Furthermore, for an incompressible fluid the density is constant (or zero volume dilation) implying that the divergence of the velocity field is zero, hence equation (A.34) reduces to

$$\bar{\bar{\tau}} = 2\mu\bar{\bar{\varepsilon}} \tag{A.35}$$

on substitution into equation (A.17) we obtain

$$\sum F_{\text{surface}} = \int_{CS} -p\bar{\bar{\mathbf{I}}} \cdot d\mathbf{A} + \int_{CS} 2\mu\bar{\bar{\varepsilon}} \cdot d\mathbf{A} \tag{A.36}$$

to get to the final form of the governing equations (convenient for discretisa-

tion) a little bit of algebraic manipulation is required. On substitution of equation (A.36) and (A.16) into equation (A.15) and applying Gauss-Green theorem to the surface integrals we obtain

$$\frac{\partial}{\partial t}\int\limits_{CV}\rho\mathbf{u}d\forall+\int\limits_{CS}\rho\mathbf{u}\mathbf{u}\cdot d\mathbf{A}=\int\limits_{CV}\rho\mathbf{f}d\forall-\int\limits_{CV}\nabla pd\forall+\int\limits_{CV}2\mu\nabla\cdot\bar{\bar{\varepsilon}}d\forall \tag{A.37}$$

It can be shown that the divergence of equation (A.35) is equal to the Laplacian of the velocity field,

$$\nabla\cdot\bar{\bar{\tau}}=\nabla\cdot(2\mu\bar{\bar{\varepsilon}})=\mu\nabla^2\mathbf{u} \tag{A.38}$$

hence the final form of the equations, assuming no body forces, can be written as

$$\frac{\partial}{\partial t}\int\limits_{CV}\rho\mathbf{u}d\forall+\int\limits_{CS}\rho\mathbf{u}\mathbf{u}\cdot d\mathbf{A}=-\int\limits_{CV}\nabla pd\forall+\int\limits_{CS}\mu\nabla\mathbf{u}\cdot d\mathbf{A} \tag{A.39}$$

A.5 Wall Shear stress

A summary of how wall shear stress is obtained from the stress tensor is given below.

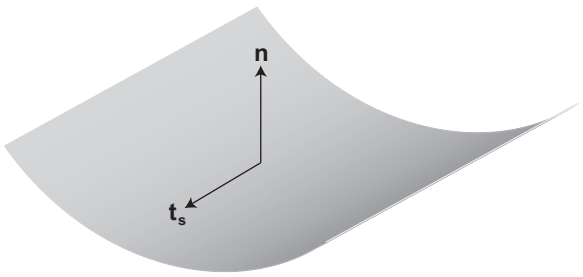

Figure A.6: Surface element with the traction vector ($\mathbf{t_s}$) and the normal ($\mathbf{n}$) defined.

The net traction vector ($\mathbf{T}$) at any point on the surface is given by the inner

product of the cauchy stress tensor ($\bar{\bar{\tau}}$) and the normal vector ($\mathbf{n}$) as defined in Figure A.6.

$$\mathbf{T} = \bar{\bar{\tau}} \cdot \mathbf{n} \tag{A.40}$$

From this, two vectors can be obtained; a normal component and a tangential component. Of interest here is the tangential vector which is derived by taking the projection of the total traction vector onto the surface, also defined in Figure A.6

$$\mathbf{t_s} = \mathbf{T} - (\mathbf{T} \cdot \mathbf{n})\mathbf{n} \tag{A.41}$$

where $\mathbf{T}$ represents the net traction vector and $\mathbf{n}$ the normal direction. The magnitude of this vector is the WSS magnitude, which from here on in will be denoted τ_w.

Appendix B

B.1 Computational fluid mechanics

The governing equations derived in the previous section only have exact analytical solutions for a handful of cases, hence, for complex geometries, as encountered in the human vasculature, numerical methods have to be employed. There are two discretisations to consider, spatial and temporal. Spatial discretisation involves breaking the geometry up into a finite number of nodes/volumes to form a mesh; this allows for a numerical approximation of the governing equations at discrete points throughout the computational domain. Further to spatial discretisation, for transient problems, the temporal discretisation is also important; which involves evaluating flow variables in time. Two different methods exist for this, explicit and implicit; explicit involves variables from the previous time step, whilst implicit is evaluated using variables calculated at the current time step. A number of different schemes exist for transforming governing equations in differential or integral form into a discrete system of algebraic equations. These schemes are: finite difference, finite element and finite volume. The finite difference method discretises the governing differential equations in differential form using Taylor series expansions to approximate derivatives, but is used less and less due to the very structured grids required, which is practically impossible for complex geometries. The next two methods work around a similar approach, using the integral form of the governing equations. The following operator (l), encompassing all expressions in equation (A.39), can be used to represent the governing equations

$$l(\phi) = 0 \tag{B.1}$$

on discretisation equation (B.3), based on an approximate solution ($\bar{\phi}$), becomes

$$l(\bar{\phi}) = R \tag{B.2}$$

where R is the residual. It is required that this is minimised throughout the computational domain (Ω), expressed as

$$\int_{\Omega} W R d\Omega = 0 \tag{B.3}$$

where W represents a weighting function. This form of the governing equations is known as the weak formulation (or method of weighted residuals), where different types of weighting functions lead to different methods. The finite element approach defines interpolation functions at nodal points throughout the domain. A well known method in this field is the Galerkin method, which uses weighting functions that are equal to the interpolation functions and an excellent discussion on this method is given in Hughes (2000). The finite volume approach (also referred to as the control volume approach) can be considered a generalisation of the finite difference approach, but it can also be obtained by considering sub-domains (Ω_s) for equation B.3 in which the following is true

$$W = \begin{cases} 1 & \text{in} \quad \Omega_s \\ 0 & \text{else} \end{cases} \tag{B.4}$$

On each of these control volumes conservation of the variable of interest is enforced. For the present study the finite volume method was used and discretisation and solution procedure for an arbitrary unstructured grid is outlined below.

B.2 Grid definitions

In the finite volume method the domain is broken up into a finite number of non-overlapping control volumes. Typical types of volumes used in this method are demonstrated in Figure B.1.

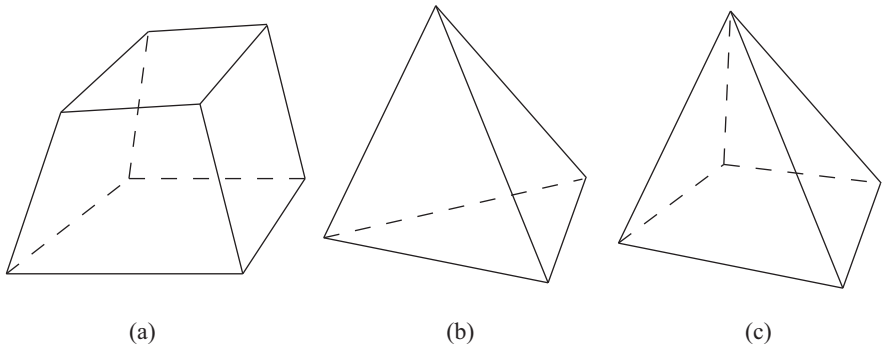

Figure B.1: Different cell types encountered in the finite volume method (a) hexahedral (b) tetrahedral and (c) pyramid.

These types of volumes are then linked together to sub divide the domain into a finite number of volumes leading to a mesh. A typical example of mesh structure and grid definitions are shown in Figure B.2 (2D for clarity). The present scheme uses a cell based solver; this means flow variables are associated with a cell, indicated by the volumes in Figure B.2. The alternative method is using a node based solver, where the solution variables are associated with nodes, but due to the mesh structures used in the present study, predominantly hexahedral, this would yield no increase in accuracy.

B.3 Discretisation

For discretisation we will consider a more general form of transport equation given by

$$\frac{\partial}{\partial t}\int_{CV}\rho\phi d\forall + \int_{CS}\rho\phi\mathbf{u}\cdot d\mathbf{A} = \int_{CS}\Gamma\nabla\phi\cdot d\mathbf{A} + \int_{CV}Sd\forall \tag{B.5}$$

where depending on the choice of ϕ different equations result, such as the

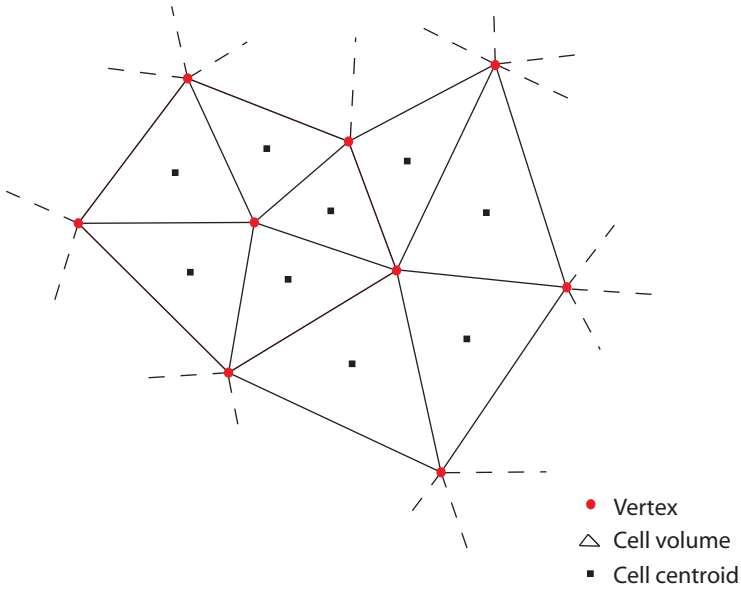

Figure B.2: Cell and vertex definitions on an arbitrary unstructured grid.

momentum equation previously discussed (where the pressure is included in the source term), or the species equation that will be presented in Chapter 4. Hence this approach provides a framework for the discretisation of all transport equations. Consider equation (B.5) following discretisation for arbitrary scalar using the finite volume technique the following equation (in semi-discrete form) is obtained

$$\frac{\partial \phi}{\partial t} + \sum_{f}^{N} (\rho \mathbf{v})_f \phi_f \cdot \mathbf{A}_f = \sum_{f}^{N} \Gamma_f (\nabla \phi)_f \cdot \mathbf{A}_f + S_\phi \forall \tag{B.6}$$

The following subsections each outline the procedure to obtain the final governing equation given in equation (B.6). Once all terms of this equation have been discretised it can then be written for each cell in a linearised form as

$$a_{c0}\phi_{c0} = \sum_{nb} a_{nb}\phi_{nb} + b \tag{B.7}$$

Here a_{c0} incorporates convective and diffusive discretisation terms for the cell $c0$ (see Figure B.3), a_{nb} includes discretisation terms for neigbouring cells and b includes source and secondary terms; these will become clear through the

following sections. The following sections follow closely the procedure outlined by Mathur and Murthy (1997),Kim et al. (1997) and the Fluent user manual (2005).

Convective term

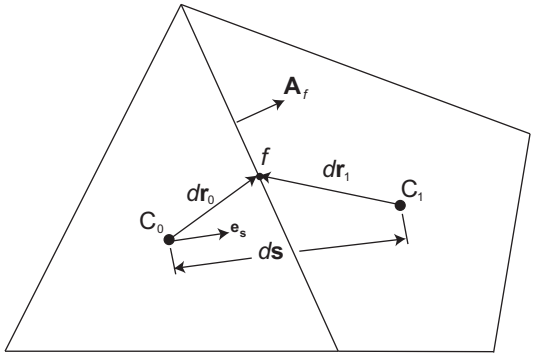

Figure B.3: Control volume with cell notation used to discretise the governing equations. C_0 and C_1 represent adjacent cell centroids, d$\mathbf{r}$ the distance from cell centroid to face centroid, d$\mathbf{s}$ the distance between cell centroids, and $\mathbf{A}_f$ the face area vector.

Discretisation of the convective term has always presented some difficulty in the CFD field. There are a number of different schemes available to deal with the convective term. In the present study second order upwinding was utilised for the velocity field. Before the details of this scheme are discussed some common expressions involved in discretisation for both the convective and diffusive term need to be introduced. Firstly, the gradient operator needs to be defined. This is obtained from Gauss-Greens theorem, and is given by

$$\nabla\phi = \frac{1}{\forall}\sum \phi_f \mathbf{A}_f. \tag{B.8}$$

The above expression requires the determination of the face value of ϕ. In Fluent, the simplest method of determination is used where the arithmetic average of two cells who share a common face is computed.

$$\phi_f = \frac{\phi_{c0} + \phi_{c1}}{2} \tag{B.9}$$

For convection schemes it is convenient to introduce the face mass flow rate

which is defined by

$$J_f = (\rho \mathbf{u})_f \cdot \mathbf{A}_f \tag{B.10}$$

This term is used to assess information about the flow direction, which forms the basis of upwind convection schemes. In order to introduce upwinding a discussion of first order upwinding is warranted, although this is an extremely inaccurate scheme due to the introduction of artificial diffusion. Referring to Figure B.3, illustrated in 2D for clarity, when discretising the convective term of equation (B.6) evaluation of the face value of ϕ is required. First order upwinding simply assumes that the face value is equal to the cell centered value, but an assessment about the flow direction, using equation (B.10) is made, for example

$$J_f \phi_f = \max(J_f, 0)\phi_{c0} + \min(J_f, 0)\phi_{c1} \tag{B.11}$$

Second order upwinding works round the same premise, but makes a multidimensional linear profile assumption about the face value of ϕ. Higher order accuracy is brought about by retaining extra terms in the Taylor series expansion, so

$$\phi_f = \phi_{c0} + \nabla\phi_{c0} \cdot \Delta r + \mathcal{O}(\Delta r)^2 \tag{B.12}$$

and finally the convective flux through the face between c0 and c1 as

$$J_f \phi_f = \max(J_f, 0)\phi_{c0} + \min(J_f, 0)\phi_{c1} + \tag{B.13}$$

$$\max(J_f, 0)(d\mathbf{r} \cdot \nabla\phi)_{c0} + \tag{B.14}$$

$$\min(J_f, 0)(d\mathbf{r} \cdot \nabla\phi)_{c1} \tag{B.15}$$

This is known to be sufficiently accurate when coupled with the appropriate spatial mesh refinement.

Diffusive term

Next we consider the diffusive term in equation (B.6) given by

$$D_f = \mathbf{A}_f \cdot \Gamma_f \nabla(\phi)_f \tag{B.16}$$

This term requires the gradient to be evaluated at the face, due to the non-orthogonality of the mesh. This is evaluated as follows

$$D_f = \Gamma_f \frac{\phi_{c1} - \phi_{c0}}{ds} \frac{\mathbf{A}_f \cdot \mathbf{A}_f}{\mathbf{A}_f \cdot \mathbf{e_s}} + \Gamma_f \left[\mathbf{A}_f \cdot \nabla\phi_f - \mathbf{e_s} \cdot \nabla\phi_f \frac{\mathbf{A}_f \cdot \mathbf{A}_f}{\mathbf{A}_f \cdot \mathbf{e_s}} \right] \tag{B.17}$$

The first term of the RHS is known as the *primary diffusion*, whilst the second term is *secondary diffusion*. The latter term accounts for the difference between the total transport through face (f) and the transport in the $\mathbf{e_s}$ direction. See Mathur and Murthy (1997) for full details. This formulation is extremely important for unstructured 3D meshes as this coordinate direction $\mathbf{e_s}$ (which connects cell centroids of two adjoining cells that share a common face) is the only uniquely defined direction, hence this formulation is most general. The extra diffusion term comes about due to the non-orthogonality of the mesh and it can be observed from equation (B.17) that the secondary diffusion term disappears for orthogonal meshes (d$\mathbf{s}$ is perpendicular to the face f) due to $\mathbf{A}_f \cdot \mathbf{A}_f / \mathbf{A}_f \cdot \mathbf{e_s} = A_f$.

Temporal discretisation

Temporal discretisation requires each term in the equation (B.6) to be integrated over time. For simplicity consider the following form

$$\frac{\partial \phi}{\partial t} \forall = l(\phi) \tag{B.18}$$

where l is an operator that incorporates all non-transient terms and V is included due to the transient term being integrated over the volume. On integra-

tion of the RHS (spatially discretised terms) of equation (B.18) over time using a fully implicit scheme the following is obtained

$$\int_{t}^{t+\Delta t} l(\phi)dt = l(\phi^{t+\Delta t})\Delta t. \tag{B.19}$$

The discretisation of the transient term requires a backwards difference formulation (forward Euler scheme) and is written as follows

$$\frac{\phi^{t+\Delta t} - \phi^{t}}{\Delta t}\forall = l(\phi) \tag{B.20}$$

This leads to the evaluation of ϕ at time $t + \Delta t$ being related to ϕ in its neighbouring cells at the current time $t + \Delta t$, ie.

$$\phi^{t+\Delta t} = \phi^{t} + \frac{l(\phi^{t+\Delta t})\Delta t}{\forall} \tag{B.21}$$

Momentum discretisation

Momentum discretisation takes on the same form as the discretisation for an arbitrary scalar ϕ, but there are some further considerations due to the pressure term. The final discretised momentum equation takes the form

$$a_{c0}\mathbf{u}_{c0} = \sum_{nb} a_{nb}\mathbf{u}_{nb} + \nabla p\forall + b \tag{B.22}$$

The pressure field is not known *a priori*, so this is remedied by using the continuity equation as an equation for pressure. For incompressible flow this does not explicitly appear, but a family of algorithms exist that introduce pressure into the continuity equation.

Consider the continuity equation (A.11) on the assumption of incompressibility

$$\int \rho \mathbf{u} \cdot d\mathbf{A} \tag{B.23}$$

following discretisation this is written

$$\sum_f J_f = 0 \tag{B.24}$$

This equation does not contain pressure and to introduce this Fluent uses the SIMPLE (Semi-Implicit Method for Pressure-Linked Equations) family of pressure velocity coupling algorithms. However, there are still a number of other issues to be dealt with. Equation (B.24) requires the velocity to be evaluated at the face, however Fluent uses a co-located grid where velocity and pressure are stored at the cell centroid. Unfortunately it is widely known in literature that if linear interpolation is used to evaluate the face value, this results in a non-physical solution, where a phenomenon known as pressure 'checkerboarding' results. To rectify this a different interpolation scheme known as momentum interpolation (or added dissipation scheme) is introduced (Rhie and Chow, 1983). Using the interpolation scheme presented by Rhie and Chow (1983), Fluent writes the mass flux at the face as

$$\begin{aligned} J_f &= \rho_f \mathbf{A}_f \frac{\mathbf{u}_{c0} + \mathbf{u}_{c1}}{2} + \rho \frac{\forall_{c0} + \forall_{c1}}{a_{c0} + a_{c1}} \left(\overline{\nabla} p \cdot \mathbf{e_s} - \frac{p_{c0} - p_{c1}}{ds} \right) \frac{\mathbf{A}_f \cdot \mathbf{A}_f}{\mathbf{A}_f \cdot \mathbf{e_s}} \\ &= \hat{J}_f + d_f (p_{c0} - p_{c1}) \end{aligned} \tag{B.25}$$

where $\overline{\nabla} p$ represents the average pressure gradient between two adjacent cells, and the second term on the right hand side is a dissipation term, which is valid providing the pressure variation is smooth. The SIMPLE pressure velocity scheme uses the previous equation (B.25) to derive an expression for pressure in equation (B.24), and is outlined following the methodology in Mathur and Murthy (1997) and the Fluent user manual (2005)

A guess is made for the pressure (p^*) an velocity ($\mathbf{u}^*$) of the flow field. The velocity will satisfy the discrete momentum equation, but not the continuity. As

previously discussed, the face flux is required for the discrete continuity equation (or pressure equation) and this is computed using equation (B.25) with these guessed parameters

$$J_f^* = \hat{J}_f^* + d_f(p_{c0}^* - p_{c1}^*) \tag{B.26}$$

However this will not satisfy the discrete continuity equation so a correction (J_f') must be made

$$J_f = J_f^* + J_f' \tag{B.27}$$

The SIMPLE algorithm proposes that the flux correction is dependent only on the pressure gradient ie. information on how the flux correction responds to variations in pressure gradient. This is written as

$$J_f' = d_f(p_{c0}' - p_{c1}') \tag{B.28}$$

where p' represents cell pressure correction. Additionally, ignoring this term only alters how the solution is approached and also avoids inner iterations that would be required if the term was not ignored. Equation (B.28) yields the following equation for pressure on substitution into equation (B.24) and utilising equation (B.27)

$$a_{c0}p_{c0}' = \sum_{nb} a_{nb}p_{nb}' + b \tag{B.29}$$

where b is the flow rate into and out of the cell given by

$$b = \sum_{f} J_f^* \tag{B.30}$$

On finding a solution to equation (B.29), the cell pressure and velocity are

corrected by

$$\begin{aligned} p &= p^* + \alpha_p p' \\ \mathbf{u} &= \mathbf{u}^* + \mathbf{u}' \end{aligned} \tag{B.31}$$

where α is the underrelaxation parameter that controls the change in pressure of each iteration. The cell centered velocity update is central to the SIMPLE pressure velocity assumption, where the influence of neighbouring cells is neglected for the correction term, hence from equation (B.22), leads to the correction for velocity ($\mathbf{u}'$) being defined as

$$\mathbf{u}' = \frac{\forall}{a_{c0}} \nabla p' \tag{B.32}$$

B.4 Linear solver

Discretisation of the governing equations for each cell leads to a linearised form of the equations (equation B.7). Application of this procedure over the whole domain leads to a linear system of the form

$$\mathbf{A}\phi = \mathbf{b} \tag{B.33}$$

Two different methods exist for solving systems of the form given in equation (B.33): direct and iterative methods. Direct methods seek an exact solution for ϕ, however due to large system of equations these methods are generally of little practical use due to the large memory overheads. Iterative methods, on the other hand, are very useful in CFD application due to the A generally being a sparse coefficient matrix. These methods require an initial guess at the solution.

In order to seek a solution of equation (B.33), the Fluent CFD code uses the point Gauss-Seidel method, of which the algorithm and details are given below. Equation (B.33) can be reformulated into an algebraic operator form for the n^{th}

iteration as

$$(D + L)\phi^{n+1} = U\phi^n + b \tag{B.34}$$

where D represents the main diagonal matrix, L the lower triangular matrix, and U the upper triangular matrix of A. For this scheme to be implemented numerical it is expressed as

$$\phi_i^{n+1} = \frac{1}{a_{ii}} \left(b_i - \sum_{j<i} a_{ij}\phi_j^{n+1} + \sum_{j>i} a_{ij}\phi_j^n \right) \tag{B.35}$$

The term $\sum_{j<i} a_{ij}\phi_j^{n+1}$ represents cells in the computational domain that have already been updated and $\sum_{j>i} a_{ij}\phi_j^n$ those that still require updating. A graphical representation of this process is given in Figure B.4, where the centre cell represents the solution that is being updated.

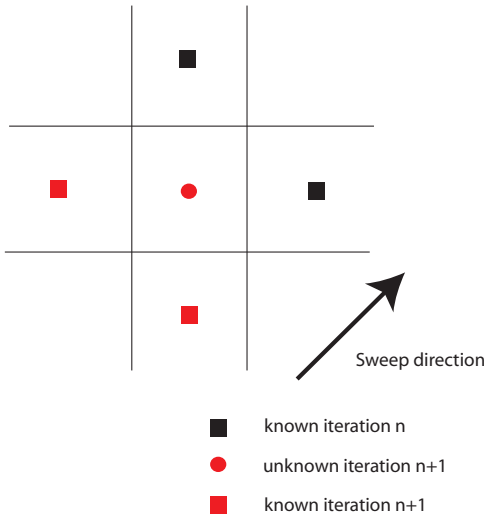

Figure B.4: Solution sweep in the point Gauss-Seidel method.

This Gauss-Seidel iterative method in Fluent is coupled with Algebraic multi-grid to accelerate convergence.

B.5 Convergence

Convergence of the solution is monitored to assess when the iterative solution approaches the exact solution to a predefined level of tolerance. To assess the convergence, scaled residuals are employed, which assess the imbalance of equation (B.7) scaled by the flowrate through the entire domain, and is written as

$$R^{\phi} = \frac{\sum_{\text{cell}} \left| \sum_{nb} a_{nb}\phi_{nb} + b - a_p\phi_p \right|}{\sum_{\text{cell}} a_p\phi_p} \tag{B.36}$$

For continuity the residual assesses mass imbalance over the entire domain defined by

$$R^{c} = \frac{\sum_{\text{cell}} |\text{mass imbalance}|}{\sum_{\text{cell}} |\text{mass imbalance}|_{\text{ref}}} \tag{B.37}$$

where denominator represents the largest mass imbalance recorded over the first five iterations of the numerical solution.

B.6 Solution Procedure

The solution procedure used for solving the governing equations was the segregated implicit solver; this is where the governing equations are solved separately 'segregated'. The alternative procedure is the coupled solver, where all equations are solved simultaneously; this method is widely known to be fairly memory intensive compared with the segregated, albeit convergence is usually obtained more rapidly. The basic algorithm of the segregated solution method is outlined in Figure B.5

In addition, for unsteady problems the same solution procedure is used for the inner iterations, which is the solution of the problem to a specified convergence criteria at a given time step. Following this convergence the solution is advanced by a specified time step size.

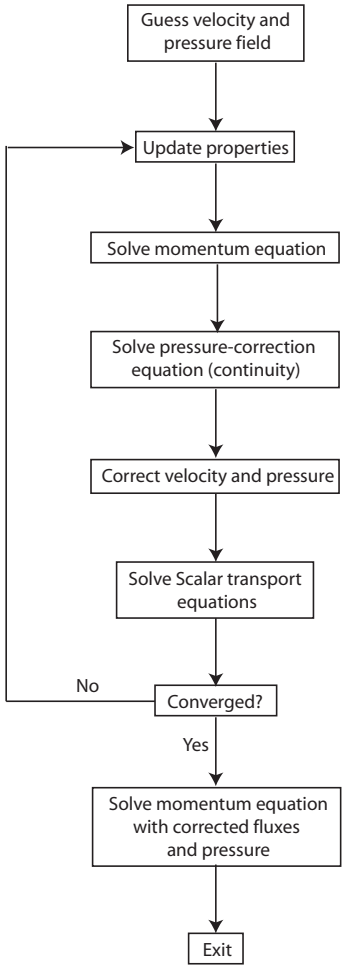

Figure B.5: Algorithm used to solve the governing equations numerically, modified from Fluent user manual (2005).

Appendix C

C.1 Mass transfer equations

The following outlines the derivation of mass transport equations that govern the transport of species in fluid flow that is uncoupled from the momentum equation. This uncoupling is achieved on the assumption of constant density throughout.

Using Reynolds transport theorem:

$$\frac{\mathrm{DB_{sys}}}{\mathrm{Dt}} = \frac{\partial}{\partial t}\int_{CV}(\rho\phi)d\forall + \int_{CS}(\rho\phi)\mathbf{u}\cdot d\mathbf{A} \tag{C.1}$$

If we let the extensive property ($\mathrm{B_{sys}}$) of the system be its mass (m) and define the concentration of species (ϕ) in mass per unit volume, then from equation (C.1) we obtain

$$\frac{\partial}{\partial t}\int_{CV}\phi\ d\forall + \int_{CS}\mathbf{J}\cdot d\mathbf{A} = 0 \tag{C.2}$$

Here $\mathbf{J}$ represents the mass flux vector of the species through the control surface relative to stationary coordinates ie.

$$\underset{\text{(Stationary coordinates)}}{\mathbf{J}} = \underset{\text{(convective flux)}}{\mathbf{J}_C} + \underset{\text{(diffusive flux)}}{\mathbf{J}_D}$$

and it is assumed that there is no volumetric generation/degradation of the

species, hence the LHS of equation (C.1) is zero. Equivalently, using Leibniz's rule, equation (C.2) can be written as

$$\int_{CV} \frac{\partial \phi}{\partial t} d\forall + \int_{CS} \mathbf{J} \cdot d\mathbf{A} = 0 \tag{C.3}$$

Applying Gauss's divergence theorem to equation (C.3) we obtain

$$\int_{CV} \frac{\partial \phi}{\partial t} d\forall + \int_{CV} \nabla \cdot \mathbf{J} d\forall = 0 \tag{C.4}$$

or equivalently

$$\int_{CV} \left[\frac{\partial \phi}{\partial t} + \nabla \cdot \mathbf{J} \right] d\forall = 0 \tag{C.5}$$

Physically, the integrand must be zero, so

$$\frac{\partial \phi}{\partial t} + \nabla \cdot \mathbf{J} = 0 \tag{C.6}$$

Convective transport is given in terms of the flux vector

$$\mathbf{J}_C = \mathbf{u}\phi \tag{C.7}$$

where $\mathbf{u} = [u, v, w]$ represents the velocity vector. From Fick's diffusion law, which simply states that the species diffuses because of a gradient in mass concentration, the diffusive transport is given by

$$\mathbf{J}_D = -D\nabla\phi \tag{C.8}$$

with D representing the diffusion coefficient $[m^2/s]$, and the negative sign

indicating diffusion in the direction of reduced concentration gradient. Now, the total mass flux is due to convection and diffusion, so superimposing these two independent processes then we have that

$$\mathbf{J} = \mathbf{u}\phi - D\nabla\phi. \tag{C.9}$$

On substitution of equation (C.9) into equation (C.6), the following results

$$\frac{\partial\phi}{\partial t} + \nabla \cdot \phi\mathbf{u} = \nabla \cdot D\nabla\phi \tag{C.10}$$

and finally using the relevant vector identity[2], and the continuity of mass condition

$$\frac{\partial\phi}{\partial t} + \mathbf{u} \cdot \nabla\phi = D\nabla^2\phi \tag{C.11}$$

[2]The dot product of a scalar multiplied by a vector: $\nabla \cdot \phi\mathbf{u} = \nabla\phi \cdot \mathbf{u} + \phi\nabla \cdot \mathbf{u}$

Appendix D

D.1 Boundary layer equations

The boundary layer equations treat the fluid domain as two distinct regions: an outer domain in which viscous effects are unimportant due to low velocity gradients; a thin layer close to the surface of the body in which viscous effects are important due to large velocity gradients. These equations were originally proposed by Prandtl (see Schlichting and Gersten (1999) for details) and are an approximate solution of the full equations revealed by order of magnitude analysis. These equations take the form

$$u\frac{\partial u}{\partial x} + v\frac{\partial u}{\partial y} = U\frac{dU}{dx} + v\frac{\partial u^2}{\partial y^2} \tag{D.1}$$

$$\frac{\partial u}{\partial x} + \frac{\partial v}{\partial y} = 0 \tag{D.2}$$

with the following boundary conditions:

$$y = 0 : u = v = 0; \qquad \lim_{y\to\infty} : u = U \tag{D.3}$$

For a full derivation of these equations see Schlichting and Gersten (1999).

D.2 Similarity transformation of the 2D incompressible boundary layer equations to wedge flow

This is an important class of solutions in which the 2D incompressible boundary layer equations are reduced to an ordinary differential equation via a similarity transformation. This is done by beginning with the boundary layer equations for plane flow as outlined in Schlichting and Gersten (1999), and in a similar manner below.

Now, the continuity equation (D.2) can be integrated using the following stream functions ($\psi(x, y)$)

$$u = \frac{\partial \psi}{\partial y}, \quad v = -\frac{\partial \psi}{\partial x} \tag{D.4}$$

and equation (D.1) becomes

$$\frac{\partial \psi}{\partial y}\frac{\partial^2 \psi}{\partial x \partial y} - \frac{\partial \psi}{\partial x}\frac{\partial^2 \psi}{\partial y^2} = U\frac{dU}{dx} + \nu\frac{\partial^3 \psi}{\partial y^3} \tag{D.5}$$

Introducing the following non-dimensional variables

$$\xi = \frac{x}{l} \quad \text{and} \quad \eta = \frac{y}{l}\frac{\sqrt{Re}}{\delta(x)} \tag{D.6}$$

the stream function is made dimensionless by

$$f(\xi, \eta) = \frac{\psi(x, y)\sqrt{Re}}{lU(x)\delta(x)} \tag{D.7}$$

Hence from the above and the stream functions in (D.4), the following expressions are obtained for the boundary layer velocity components

$$u(\xi,\eta) = U\frac{\partial f}{\partial \eta} \tag{D.8}$$

$$-v(\xi,\eta)\sqrt{Re} = \frac{d(U\delta)}{d\xi} + U\left(\delta\frac{\partial f}{\partial \xi} - \frac{\partial \delta}{\partial \xi}\eta f'\right) \tag{D.9}$$

If the trial stream function solution of equation (D.7) is inserted into equation (D.5) the following dimensionless differential equation for the stream function is thus obtained

$$f''' + \alpha f f'' + \beta(1 - f'^2) = \frac{U}{U_\infty}\delta^2\left(f'\frac{\partial f'}{\partial \xi} - f''\frac{\partial f}{\partial \xi}\right) \tag{D.10}$$

where α and β are the following functions of ξ

$$\alpha = \frac{l\delta}{U_\infty}\frac{d(U\delta)}{d\xi}; \quad \beta = \frac{l}{U_\infty}\delta^2\frac{dU}{d\xi} \tag{D.11}$$

Similar solutions exist if the above equation is independent of ξ, which requires the RHS of equation (D.10) be equal to zero. Equivalently, the coefficients α and β must be constant. Hence with the above conditions the following ODE is obtained

$$f''' + \alpha f f'' + \beta(1 - f'^2) = 0 \tag{D.12}$$

with the boundary conditions

$$\eta = 0: \quad f = 0,\ f' = 0; \quad \eta = \infty:\ f' = 1.$$

Without a loss of generality α can be set to 1. This means equation (D.11) has the following solution,

$$\begin{aligned} \frac{U}{U_\infty} &= u_1 \xi^m \\ \delta &= \sqrt{\frac{2}{u_1(m+1)} \xi^{\frac{1-m}{2}}} \end{aligned} \tag{D.13}$$

thus from the previous and equation D.6, the similarity solution in dimensional form is given by

$$\alpha = y \sqrt{\frac{m+1}{2} \frac{u_1}{\nu}} x^{\frac{m-1}{2}} \tag{D.14}$$

Appendix E

E.1 Endothelial cell dynamics code

Code for endothelial cell dynamics (Chapter 5)

```
#include "udf.h"
#include <stdio.h>
#include <string.h>
#include<stdlib.h>
#include <math.h>

static double maxarg1,maxarg2; #define FMAX(a,b)
(maxarg1=(a),maxarg2=(b),(maxarg1) > (maxarg2) ?\
        (maxarg1) : (maxarg2))

static double minarg1,minarg2; #define FMIN(a,b)
(minarg1=(a),minarg2=(b),(minarg1) < (minarg2) ?\
        (minarg1) : (minarg2))

/*Adaptive step parameters*/
#define SAFETY  0.8
#define PGROW   -0.2
#define PSHRNK  -0.25
#define ERRCON  1.89e-4
#define TINY    1e-30

/*Endothelial cell model parameters*/
#define ki      5.46e-3
```

```
#define mu1     0.2
#define krel    6.64
#define kres    5
#define kout    24.7
#define kdis    0.09
#define mu2     0.0167
#define qm      17.6
#define kcce    5.7e-6
#define Cs0     2830
#define Cex     1500
#define Kc      0.026
#define K1      0
#define K2      0.2
#define K3      0.15
#define K4      5
#define K5      0.32
#define K6      0.45
#define Vr      3.5
#define Cc0     0.1
#define Te      310
#define l       3.5e-5
#define s       1e-5
#define N       1e12
#define ep      0.1
#define fe      0.0134
#define k       1.3807e-23
#define alpha   2

/*Other parameters*/
#define Kcicr           0
#define n               4
#define atp_reference   1.80152e-8
#define wss_reference   1

/*Global variables*/
double atp;
double wss;
```

```
double W;
double y[4]        = {0,Cc0,Cs0,(kdis*Cc0)/(mu2*(K6+Cc0))};
double yscal[4]    = {0};
doubledydx[4]      = {0};
double yout[4]     = {0};
double yerr[4]     = {0};
double ytemp[4]    = {0};
double hdid        = 0.001;
double hnext       = 0;
double h           = 0.01;
double x           = 0;
double cytosolic;

/*Function prototype definitions*/
double shear_stress(double);
void derivs(double x, double y[], double dydx[], double);
void rk4(double y[],double h, void (*derivs)(double x,
   double [],double dydx[],double atp));
void rkadap(double y[], double yscal[], double *hdid,
   double *x, double *h, double *hnext, void (*derivs)(
   double, double [],double dydx[],double atp));
void odeprog(void (*derivs)(double, double [], double dydx
   [], double atp), void (*rkadap)(double y[], double
   yscal[], double *hdid, double *x, double *h, double *
   hnext, void (*derivs)(double, double [],double dydx[],
   double atp)));
void ThreadBoundary(int bc);

/*Arterial wall surfaces model is applied to*/
DEFINE_ON_DEMAND(calc_calcium) {
    int wall_left=14;

    ThreadBoundary(wall_left);

}
    /*Wall shear stress function from endothelial cell
       model*/
```

```
double shear_stress(double wss){

W=fe*(pow(ep*wss*l+sqrt(16*pow(s,2)+pow(ep,2)*pow(wss
   ,2)*pow(l,2))-4*s,2))/(8*k*Te*N*(ep*wss*l+sqrt(16*
   pow(s,2)+pow(ep,2)*pow(wss,2)*pow(l,2))));
return W;
}

/*Cell dynamic equations*/
void derivs(double x, double y[], double dydx[],double
    atp)
{
double q;
q=qm/(1+alpha*exp(-W));

dydx[0]=ki*(atp/(Kc+atp))*(y[1]/(K1+y[1]))-mu1*y[0];

dydx[1]= krel*y[2]*pow(y[0]/(K2+y[0]),3)-kres*pow(y
   [1]/(K3+y[1]),2)+(kcce*(Cs0-y[2])*(Cex-y[1]))/(K4+y
   [3])+q-(kout*y[1])/(K5+y[1]);

dydx[2]=-Vr*(krel*y[2]*pow(y[0]/(K2+y[0]),3)-kres*pow(
   y[1]/(K3+y[1]),2));

dydx[3]=(kdis*y[1])/(K6+y[1])-mu2*y[3];
}

/*Runge Kutta routine*/
void rk4(double y[],double h, void (*derivs)(double x,
   double [],double dydx[],double atp)){
int i,j;

double ak2[4], ak3[4], ak4[4], ak5[4], ak6[4];

static double a2=0.2,a3=0.3,a4=0.6,a5=1.0,a6=0.875,b21
   =0.2, b31=3.0/40.0,b32=9.0/40.0,b41=0.3,b42 = -0.9,
   b43=1.2, b51 = -11.0/54.0, b52=2.5,b53 =
```

```
    -70.0/27.0,b54=35.0/27.0, b61=1631.0/55296.0,b62
    =175.0/512.0,b63=575.0/13824.0, b64
    =44275.0/110592.0,b65=253.0/4096.0,c1=37.0/378.0,
    c3=250.0/621.0,c4=125.0/594.0,c6=512.0/1771.0, dc5
    = -277.0/14336.0;

double dc1=c1-2825.0/27648.0,dc3=c3-18575.0/48384.0,
   dc4=c4-13525.0/55296.0,dc6=c6-0.25;

for (i=0;i<=n;i++){
    ytemp[i]=y[i]+b21*h*dydx[i];
derivs(x+a2*h,ytemp,ak2,atp);
}
for (i=0;i<=n;i++){
    ytemp[i]=y[i]+h*(b31*dydx[i]+b32*ak2[i]);
derivs(x+a3*h,ytemp,ak3,atp);
}
for (i=0;i<=n;i++){
    ytemp[i]=y[i]+h*(b41*dydx[i]+b42*ak2[i]+b43*ak3[i
       ]);
derivs(x+a4*h,ytemp,ak4,atp);
}
for (i=0;i<=n;i++){
    ytemp[i]=y[i]+h*(b51*dydx[i]+b52*ak2[i]+b53*ak3[i
       ]+b54*ak4[i]);
derivs(x+a5*h,ytemp,ak5,atp);
}
for (i=0;i<=n;i++){
    ytemp[i]=y[i]+h*(b61*dydx[i]+b62*ak2[i]+b63*ak3[i
       ]+b64*ak4[i]+b65*ak5[i]);
derivs(x+a6*h,ytemp,ak6,atp);
}
for (i=0;i<=n;i++){
    yout[i]=y[i]+h*(c1*dydx[i]+c3*ak3[i]+c4*ak4[i]+c6*
       ak6[i]);
}
for (i=0;i<=n;i++){
```

```
        yerr[i]=h*(dc1*dydx[i]+dc3*ak3[i]+dc4*ak4[i]+dc5*
           ak5[i]+dc6*ak6[i]);
        }
    }

/*Adaptive stepping routine*/
void rkadap(double y[], double yscal[], double *hdid,
   double *x,
double *h, double *hnext, void (*derivs)(double, double
   [],double
dydx[],double atp)) {
    int i,j;
    double errmax,htemp, eps;
    eps=1e-5;
    for (;;) {
    rk4(y,*h,derivs);
    errmax=0.0;
    for (i=0;i<n;i++){ errmax=FMAX(errmax, fabs(yerr[i]/
       yscal[i]));
    }
    errmax=errmax/eps;
    if (errmax <= 1.0) break;
    htemp=SAFETY*(*h)*pow(errmax,PSHRNK);
    *h=(*h >= 0.0 ? FMAX(htemp,0.1*(*h)) : FMIN(htemp
       ,0.1*(*h)));
    }
    if (errmax > ERRCON) *h=SAFETY*(*h)*pow(errmax, PGROW)
       ;
    else *h=5.0*(*h);
    *x += (*h);
    }

    /*Initial conditions, main program (which calls
       subroutines) and steady state finishing criteria*/
    void odeprog(void (*derivs)(double, double [], double
       dydx[], double atp), void (*rkadap)(double y[],
       double yscal[], double *hdid, double *x, double *h,
```

```
        double
    *hnext, void (*derivs)(double, double [],double dydx
       [],double atp))){

    int i,j;
    double y[4] = {0,Cc0,Cs0,(kdis*Cc0)/(mu2*(K6+Cc0))}, x
       =0;
    h           = 0.01;

    for(;;){
    (*derivs)(x,y,dydx,atp);
    for(i=0;i<n;i++){
    yscal[i]=fabs(y[i])+fabs(dydx[i]*(h))+TINY;
    }

    (*rkadap)(y, yscal, &hdid, &x, &h, &hnext, derivs);

    if (fabs(dydx[0]) <0.001 && fabs(dydx[1]) <0.001
        && fabs(dydx[2]) <0.001 && fabs(dydx[3]) <0.001)
           break;
    for (i=0; i<n; i++){
        y[i]=yout[i];
        }
    }
    }

/*Variables obtained from the CFD solver and surface mesh
   loop to obtain spatial distribution of eNOS and Calcium
   */
void ThreadBoundary(int bc) { double wss, A[ND_ND], area;
    Domain *domain;
    face_t f;
    Thread *fthread;
    domain  =   Get_Domain(1);
    fthread = Lookup_Thread(domain,bc);

    begin_f_loop(f, fthread)
```

```
    {
        F_AREA(A,f,fthread);

        area=NV_MAG(A);

        wss=NV_MAG(F_STORAGE_R_N3V(f,fthread,SV_WALL_SHEAR
           ))/(area);

        atp=F_YI(F_C0(f,fthread),THREAD_T0(fthread),0)/
           atp_reference;

        shear_stress(wss);

        odeprog(derivs,rkadap);

        C_UDMI(F_C0(f,fthread),THREAD_T0(fthread),0)=yout
           [0];

        C_UDMI(F_C0(f,fthread),THREAD_T0(fthread),1)=yout
           [1];

        C_UDMI(F_C0(f,fthread),THREAD_T0(fthread),2)=yout
           [2];

        C_UDMI(F_C0(f,fthread),THREAD_T0(fthread),3)=yout
           [3];
    }
end_f_loop(f, fthread) }
```

E.2 Shear stress induced ATP release code

Code for shear stress induce ATP release (Chapter 4) - Note this is also the code for ATP surface reaction without release.

```
#include "udf.h"
#include "math.h"
#include "stdio.h"
#include "string.h"

# define K1 1.68e-6
# define K2 6.45e-7
# define Smax 1e-12
# define wss_ref 3.16

/*Function obtains the wall shear stress from the CFD
   solver. This then provides the WSS to model ATP release
    via a sigmoidal function. The UDF then provides the
   surface reaction rate necessary to model nucleotide
   hydrolysis.*/

DEFINE_SR_RATE(atp_release,f,fthread,r,mw,yi,rr)
{
    double wss, A[ND_ND], area, Satp;

            F_AREA(A,f,fthread);

            area=NV_MAG(A);

            wss=NV_MAG(F_STORAGE_R_N3V(f,fthread,
               SV_WALL_SHEAR))/area;

            Satp    =   Smax*pow((1-exp(-wss/wss_ref)),3);

    if (STREQ(r->name, "reaction-1"))
        {
        *rr=Satp;
```

```
        }


    if (STREQ(r->name, "reaction-2"))
        {
            *rr = K1*C_R(F_C0(f,fthread),F_C0_THREAD(f,
               fthread))*yi[0]/mw[0];
        }

    if (STREQ(r->name, "reaction-3"))
        {
            *rr = K2*C_R(F_C0(f,fthread),F_C0_THREAD(f,
               fthread))*yi[1]/mw[1];
        }
}
```

E.3 Physiological arterial waveform code

Code for physiological inlet waveform (Chapter 3).

```
# include "udf.h"
# include "stdio.h"
# include "string.h"
# include "stdlib.h"
# include "math.h"
# include "para.h"

# define pi      3.14159

double A[41]={0};
double B[41]={0};
double U;
static int last_time = -1;

DEFINE_ON_DEMAND(set_velocity)
{
/*Variables available on host*/
#if !RP_HOST
int p,N,n,j;
double Q, inlet_area=0.0,area[ND_ND],C;
double nue=4e-6,D=3e-3,Re=300;
double *Y;
Domain *domain;
face_t f;
Thread *thread;
domain  =   Get_Domain(1);
thread = Lookup_Thread(domain,6);
#endif

int number_items;

/*Variables available on nodes*/
#if !RP_NODE
```

```
int i;
char * string=NULL;
int size;
int allocation;
double *Y;
FILE *wave_data;

/*Initial memory allocation*/
allocation=10;
Y = malloc(allocation * sizeof(double));
Message0("\nY␣allocated\n");
number_items = 0;


/*File with waveform data*/
if ((wave_data = fopen("waveform.txt", "r"))==NULL)
       Message("\n␣Warning:␣Unable␣to␣open␣%s␣for␣reading\
          n","waveform.txt");
else
       Message("\nReading␣wave␣data␣from␣%s...\n","
          waveform.txt");

/*Files reading and allocation*/
while (getline(&string,&size,wave_data) !=EOF){
    if(number_items >= allocation){
        double *np;
        allocation += 100;
        np = realloc(Y, allocation * sizeof(double));
        if(np == NULL){
            printf("Unable␣to␣allocate␣memory\n");
            free(np);
            exit(1);
            }
        Y = np;
            Message("\nAllocated␣more␣memory\n\n");
    }
```

```
    Y[number_items++] =atof(strtok(string,"\n"));
}

 fclose(wave_data);

/*MPI send routine*/
PRF_CSEND_INT(node_zero, &number_items, 1, myid);
PRF_CSEND_REAL(node_zero, Y, number_items, myid);
free(Y);
#endif

#if !RP_HOST
/*MPI receive routines on node processes*/
PRF_CRECV_INT(node_host, &number_items, 1, node_host);
Y = (double *)malloc(number_items * sizeof(double));
PRF_CRECV_REAL(node_host, Y, number_items, node_host);

if (I_AM_NODE_ZERO_P)
   compute_node_loop_not_zero (j)
   {
     PRF_CSEND_INT(j, &number_items, 1, myid);
     PRF_CSEND_REAL(j, Y, number_items, myid);
     }

if (!I_AM_NODE_ZERO_P){
     PRF_CRECV_INT(node_zero, &number_items, 1, node_zero)
        ;
     Y = (double *)malloc(number_items * sizeof(double));
     PRF_CRECV_REAL(node_zero, Y, number_items, node_zero)
        ;
   }

N = number_items;
C = (double)number_items;

/*Inlet area calculation*/
begin_f_loop(f,thread){
```

```
            F_AREA(area,f,thread);
            inlet_area += NV_MAG(area);
  }
  end_f_loop(f,thread)

  U=Re*nue/D;
  Q=U*inlet_area;

  for (p=0;p<=N-1;p++){
        Y[p]=Y[p]*Q/inlet_area-U;
    }
/*Fourier coefficient calculation */
for (p=0;p<=N/2;p++){
            A[p]=0;
            B[p]=0;

            for (n=0;n<=N-1;n++){
                A[p]=A[p]+2/C*Y[n]*cos(2*pi*p*(n+1)/C);
                B[p]=B[p]+2/C*Y[n]*sin(2*pi*p*(n+1)/C);
            }
            Message("%3d : %f  %f\n", p, A[p], B[p]);
      }

A[N/2]=A[N/2]/2;
B[N/2]=0;

Message0("\nThe size of Y is: %d\n",N);
if (inlet_area !=0){
Message("Artery inlet area: %e\n",inlet_area);
}
Message0("Reynolds number: %.0f\n",Re);
Message0("\nConverting flowrate array to velocity array
   ...\n");
Message0("Calculating fourier coefficients...\n");
free(Y);
#endif
}
```

```
DEFINE_PROFILE(unsteady, thread, index)
{
#if !RPHOST
  int hmax=41, h, current_time;
  double x[ND_ND], z, Ut, T=1;
  double t= RP_Get_Real("flow-time");
  face_t f;
  current_time = N_TIME;

/*Waveform construction from Fourier coefficients*/
Ut=A[0]/2;
for (h=1;h<=hmax;h++){
    Ut=Ut+A[h]*cos(2*pi*h*t/T)+B[h]*sin(2*pi*h*t/T);

}

if (last_time != current_time){
    last_time = current_time;
Message("Unsteady_component:␣%f\n",Ut);
Message("Steady_component:␣%f\n",U);
}
/*Assigning waveform (both spatial and temporal) to inlet
   */
    begin_f_loop(f, thread)
        {
            F_CENTROID(x,f,thread);

            z = sqrt(x[0]*x[0]+x[1]*x[1]);

            F_PROFILE(f, thread, index) = 2*(U+Ut)*(1 - z*
               z/(.0015*.0015));
        }
    end_f_loop(f, thread)
#endif
}
```

E.4 Trifurcation flowrate distribution

This UDF assigns the flowrate distribution used in the trifurcation simulations. The combination of this UDF and the physiological inlet waveform UDF was used for pulsatile simulations in the trifurcation geometry.

```
#include "udf.h"
#include "stdio.h"
#include "string.h"
#include "math.h"

double Qref;

DEFINE_ON_DEMAND(flow)
{
    int inlet=21;
    flowrate(inlet);
}

/*Each DEFINE_PROFILE represents a different outlet of the
trifurcation geometry and applies the associated flow rate
   */

DEFINE_PROFILE(Circumflex_illiac,t,i)
{
  face_t f;
  Message0("Targeted␣mass-flow␣rate␣set␣at:␣%f␣kg/s␣\n",
     0.2*Qref);
      begin_f_loop(f,t)
        {
          F_PROFILE(f,t,i) = 0.2*Qref;
        }
      end_f_loop(f,t)
}

DEFINE_PROFILE(Common_illiac,t,i)
{
```

```
  face_t f;
  Message0("Targeted␣mass-flow␣rate␣set␣at:␣%f␣kg/s␣\n",
     0.7*Qref);
      begin_f_loop(f,t)
        {
          F_PROFILE(f,t,i) = 0.7*Qref;
        }
      end_f_loop(f,t)
}

DEFINE_PROFILE(femoral_artery,t,i)
{
  face_t f;
  Message0("Targeted␣mass-flow␣rate␣set␣at:␣%f␣kg/s␣\n",
     1.1*Qref);
      begin_f_loop(f,t)
        {
          F_PROFILE(f,t,i) = 1.1*Qref;
        }
      end_f_loop(f,t)
}

DEFINE_PROFILE(ref,t,i)
{
  face_t f;
  Message0("Targeted␣mass-flow␣rate␣set␣at:␣%f␣kg/s␣\n",
     Qref);
      begin_f_loop(f,t)
        {
          F_PROFILE(f,t,i) = Qref;
        }
      end_f_loop(f,t)
}

double flowrate(int bc)
{
double area = 0.0, A[ND_ND], Re=885, nue=3.3e-6, u=0.0, d
```

```
   =0.0, Q=0.0;
Domain *domain;
face_t face;
Thread *face_thread;
domain  =   Get_Domain(1);
face_thread = Lookup_Thread(domain,bc);

begin_f_loop(face, face_thread)
    {
        F_AREA(A,face,face_thread);
        area+=NV_MAG(A);
    }
end_f_loop(face, face_thread)


d=sqrt((4*area)/M_PI);
u=(Re*nue)/d;
Q=u*area;

Message0("area of inlet: %f m^2 \n", area);
Message0("inlet velocity: %f m/s \n", u);


Qref=Q/6*1050;

return Qref;

}
```

References

Abbracchio, M. P., Burnstock, G., Boeynaems, J., Barnard, E., Boyer, J., Kennedy, C., Knight, G. E., Fumagalli, M., Gachet, C., Jacobson, K. A., and Weisman, G. A. (2006). International union of pharmacology lviii: Update on the P2Y G protein-coupled nucleotide receptors: From molecular mechanisms and pathophysiology to therapy. *Pharmacol Rev*, 58:281–341.

Abramowitz, M. and Stegun, I. A. (1965). *Handbook of Mathematical Functions with Formulas, Graphs, and Mathematical Tables*. Dover Publications, New York.

Asakura, T. and Karino, T. (1990). Flow patterns and spatial-distribution of atherosclerotic lesions in human coronary-arteries. *Circulation Research*, 66(4):1045–1066.

Barakat, A., Lieu, D., and Gojova, A. (2006). Secrets of the code: Do vascular endothelial cells use ion channels to decipher complex flow signals? *Biomaterials*, 27:671–678.

Barbato, J. E. and Tzeng, E. (2004). Nitric oxide and arterial disease. *Vasclular surgery*, 40:187–193.

Behrendt, D. and Ganz, P. (2002). Endothelial function: From vascular biology to clinical applications. *Am J Cardiol*, 90:40–48.

Berger, S. A., Talbot, L., and Yao, L. (1983). Flow in curved pipes. *Annu. Rev. Fluid Mech.*, 15:461–512.

Berridge, M. J. (1997). Elementary and global aspects of calcium signalling. *The Journal of Experimental Biology*, 200:315319.

Bird, R. B., Stewart, W. E., and Lightfoor, E. N. (1960). *Transport Phenomena*. Joh Wiley and Sons, New York.

Bodin, P. and Burnstock, G. (2001). Evidence that release of adenosine triphosphate from endothelial cells during increased shear stress is vesicular. *J Cardiovasc Pharmacol*, 38:900–908.

Burnstock, G. (2004). Introductionl P2 receptors. *Curr Top Med Chem*, 4:793–803.

Burnstock, G. (2006). Vessel tone and remodelling. *Nature Medicine*, 12:16–17.

Caro, C., Doorly, D., Tarnawski, M., Scott, K., Long, Q., and Dumoulin, C. (1996). Non-planar curvature and branching of arteries and non-planar-type flow. *Proceedings: Mathematical, Physical and Engineering Sciences*, 452:185–197.

Caro, C. G., Fitzgerald, J., and Schroter, R. C. (1971). Atheroma and arterial wall shear - observation, correlation and proposal of a shear dependent mass transfer mechanism for altherogenesis. *Proceedings of the Royal Society of London Series B-Biological Sciences*, 177(1046):109.

Cheng, C., van Haperen, R., de Waard, M., van Damme, L. C. A., Tempel, D., Hanemaaijer, L., van Cappellen, F. W. A., Bos, J., Duncker, C. J., van der Steen, A. F. W., de Crom, R., and krams, R. (2005). Shear stress affects the intracellular distribution of enos: direct demonstration by a novel in vivo technique. *Blood*, 106:3691–3698.

Cho, Y. I. and Kensey, K. R. (1991). Effects of the non-Newtonian viscosity of blood on flows in a diseased arterial vessel. part 1: steady flows. *Biorheology*, 28:241–262.

Cooke, J. (2003). Flow, NO, and atherogenesis. *Proceedings of the National Academy of Science*, 100:768–770.

Crowther, M. (2005). Pathogenesis of atherosclerosis. *Thrombosis I*, pages 436–441.

David, T. (2003). Wall shear stress modulation of ATP/ADP concentration at the endothelium. *Annals of Biomedical Engineering*, 31(10):1231–1237.

David, T., Thomas, S., and Walker, P. (2001). Platelet deposition in stagnation point flow: and analytical and computational solution. *Med. Eng. Phys.*, 23:299–312.

Davies, P., Reidy, M. A., Goode, T. B., and Bowyer, D. E. (1976). Scanning electron microscopy in the evaluation of endothelial integrity of the fatty streak lesion of atherosclerosis. *Atherosclerosis*, 25:125–130.

Davies, P. and Tripathi, S. (1993). Mechanical stress mechanisms and the cell- an endothelial paradigm. *Circulation Research*, 72:239–245.

Davies, P. F. (1995). Flow-mediated endothelial mechanotransduction. *Physiological Reviews*, 75(3):519–560.

Davies, P. F. (2000). Spatial hemodynamics, the endothelium, and focal atherogenesis - a cell cycle link? *Circulation Research*, 86(2):114–116.

Davignon, J. and Ganz, P. (2004). Role of endothelial dysfunction in atherosclerosis. *Circulation*, 109:III–27–III–32.

DeBakey, M. E., Lawrie, G. M., and Glaeser, D. H. (1985). Patterns of atherosclerosis and their surgical significance. *Ann Surg.*, 201:115131.

Deng, D. X., A.Tsalenko, Vailaya, A., Ben-Dor, A., Kundu, R., Estay, I., Tabibiazar, R., Kincaid, R., Yakhini, Z., Bruhn, L., and Quertermous, T. (2004). Differences in vascular bed disease susceptibility reflect differences in gene expression response to atherogenic stimuli. *Circulation Research*, 98:200–208.

Dimmeler, S., Assmus, B., Hermann, C., Haendeler, J., and Zeiher, A. M. (1998). Fluid shear stress stimulates phosphorylation of Akt in human endothelial cells - involvement in suppression of apoptosis. *Circ Res*, 83:334–341.

Dimmeler, S., Fleming, I., Fisslthaler, B., Hermann, C., Busse, R., and Zeiher, A. M. (1999). Activation of nitric oxide synthase in endothelial celss by akt-dependent phosphorylation. *Nature*, 399:601–605.

Drexler, H. and Hornig, B. (1999). Endothelial dysfunction in human disease. *J Mol Cell Cardiol*, 31:5160.

Dudzinski, D., Igarashi, J., Greif, D., and Michel, T. (2006). The regulation and pharmacology of endothelial nitric oxide synthase. *Annu. Rev. Pharmacol. Toxicol.*, 46:235–276.

Dull, R. O. and Davies, P. F. (1991). Flow modulation of agonist ATP-response Ca^{2+} coupling in vascular endothelial-cells. *American Journal of Physiology*, 261(1):H149–H154.

Ethier, C. R. (2002). Computational modeling of mass transfer and links to atherosclerosis. *Annals of Biomedical Engineering*, 30:461–471.

Ethier, C. R., Prakash, S., Steinman, D. A., Leask, R. L., Couch, G. G., and Ojha, M. (2000). Steady flow separation patterns in a 45 degree junction. *Journal of Fluid Mechanics*, 411:1–38.

Evans, H. L. (1968). *Laminar boundary-layer theory.* Addison-Wesley Pub Co., Reading, Mass.

Fluent user manual (2005). *FLUENT 6.2 Documentation.*

Fox, B., James, K., Morgan, B., and Seed, A. (1982). Distribution of fatty and fibrous plaques in young human coronary arteries. *Atherosclerosis.*, 41:337–347.

Friedman, M., Brinkman, A., Qin, J., and Seed, W. (1993). Relation between coronary artery geometry and the distribution of early sudanophilic lesions. *Atherosclerosis*, 98:193–199.

Friedman, M., Deters, O., Mark, F., Bargeron, C., and Hutchins, G. (1983). Arterial geometry affects hemodynamics - a potential risk factor for atherosclerosis. *Atheroslcerosis*, 46:225–231.

Friedman, M. and Ding, Z. (1998). Variability of the planarity of the human aortic bifurcation. *Medical Engineering and Physics*, 20:469–472.

Friedman, M., Hutchins, G., Bargeron, C., Deters, O., and Mark, F. (1981). Correlation between intimal thickness and fluid shear in human arteries. *Atheroslcerosis*, 39:425–436.

Friedman, M. H. and Ehrlich, L. W. (1975). Effect of spatial variations in shear on diffusion at the wall of an arterial branch. *Circ. Res.*, 37:446–454.

Furchgott, R. and Zawadzki, J. (1980). The obligatory role of endothelial cells in the relaxation of arterial smooth muscle by acetylcholine. *Journal of the American Medical Association*, 288:373–379.

Gimbrone, M., Topper, J., Nagel, T., Anderson, K., and Garcia-Cardena, G. (2000). Endothelial dysfunction, hemodynamic forces, and atherogenesis. *Ann N Y Acad Sci.*, 902:230–239.

Gimbrone, M. A. (1999). Vascular endothelium, haemodynamic forces and atherogenesis. *Am. J. Pathol*, 155:1–5.

Goldbeter, A., DuPont, G., and Berridge, M. J. (1990). Minimal model for signal-induced Ca^{2+} oscillations and for their frequency encoding through protein phosphorylation. *Proc. Natl. Acad. Sci.*, 87:1461–1465.

Gordon, J. L. (1986). Extracellular ATP - effects, sources and fate. *Biochemical Journal*, 233(2):309–319.

H.Drexler (1998). Factors involved in the maintenance of endothelial function. *The American Journal of Cardiology*, 82:35–36.

He, X. and Ku, D. N. (1996). Pulsatile flow in the human left coronary artery bifurcation: average conditions. *Journal of Biomechanical Engineering*, 118:74–82.

Hegele, R. (1995). Clinica chimica acta. *Nature*, 246:21–48.

Henderson, J. M., Aukerman, J. A., Clingan, P. A., and Friedman, M. H. (1999). Effect of alterations in femoral artery flow on abdominal vessel hemodynamics in swine. *Biorhelogy*, 36:257–266.

Himburg, H. A., Grzybowski, D. M., Hazel, A. L., LaMack, J. A., Li, X., and Friedman, M. H. (2004). Spatial comparison between wall shear stress measures and porcine arterial endothelial permeability. *Am J Physiol Heart Circ Physiol*, 286:H1916–H1922.

Hughes, T. (2000). *The Finite Element Method: Linear Static and Dynamic Finite Element Analysis*. Dover Pubns. ISBN: 0486411818.

Hyun, S., Kleinstreuer, C., and Archie, J. P. (2000). Hemodynamics analyses of arterial expansions with implications to thrombosis and restenosis. *Medical Engineering and Physics*, 22:13–27.

John, K. and Barakat, A. I. (2001). Modulation of ATP/ADP concentration at the endothelial surface by shear stress: Effect of flow-induced ATP release. *Annals of Biomedical Engineering*, 29(9):740–751.

Kaazempur-Mofrad, M., Wada, S., Myers, J., and Ethier, C. (2005). Mass transport and fluid flow in stenotic arteries: Axisymmetric and asymmetric models. *Heat and Mass Transfer*, 48:4510–4517.

Kaazempur-Mofrad, M. R. and Ethier, C. R. (2001). Mass transport in an anatomically realistic human right coronary artery. *Annals of Biomedical Engineering*, 29:121–127.

Kennedy, C., Delbro, D., and Burnstock, G. (1985). P2-purinoceptors mediate both vasodilation (via the endothelium) and vasoconstriction of the isolated rat femoral artery. *Eur J Pharmacol*, 107:161–8.

Kharbanda, R. and MacAllister, R. J. (2005). The atherosclerosis time-line and the role of the endothelium. *Curr. Med. Chem.*, 5:47–52.

Kim, S., Mathur, S. R., Murthy, J. Y., and Choudhury, D. (1997). A Reynolds-averaged navier-stokes solver using an unstructured mesh based finite-volume scheme. *Fluent Technical Notes*. TN117.

Kleinstreuer, C. (1997). *Engineering fluid dynamics : an interdisciplinary systems approach*. Cambridge University Press, United Kingdom.

Ku, D. (1997). Blood flow in arteries. *Annu. Rev. Fluid Mech.*, 29:399–434.

Ku, D. N., Giddens, D. P., Zarins, C. K., and Glagov, S. (1985). Pulsatile flow and atherosclerosis in the human carotid bifurcation. positive correlation between plaque location and low oscillating shear stress. *Arterioscler. Thromb. Vasc. Biol.*, 5:293–302.

Larzarowski, E., Boucher, R., and Harden, T. (2003). Mechanisms of relese of nucleotides and integration of their action as P2X- and P2Y-receptor activating molecules. *Molecular Pharmacology*, 64:785–795.

Lei, M., Kleinstreuer, C., and Truskey, G. A. (1995). Numerical investigation and prediction of atherogenic sites in branching arteries. *J Biomech Eng.*, 117:350–357.

Libby, P. (2001). *Heart Disease: A Textbook of Cardiovascular Medicine, Chpater 30.* W.B. Saunders Company.

Libby, P. (2002). Inflammation in atherosclerosis. *Nature*, 420:868–874.

Libby, P., Ridker, P. M., and Maseri, A. (2002). Inflammation and atherosclerosis. *Circulation*, 105:1135–1143.

Lin, S., Fagan, K. A., Li, K. X., Shaul, P. W., Cooper, D. M. F., and Rodman, D. M. (2000). Sustained endothelial nitric-oxide synthase activation requires capcitive Ca^{2+} entry. *J. Biol. Chem*, 275:17979–17985.

Lodish, H., Berk, A., Matsudaira, P., Kaiser, C., Krieger, M., Scott, M., Zipursky, S., and Darnell, J. (2004). *Molecular Cell Biology.* W. H. Freeman and Company. ISBN: 0716743663.

Ma, P., Li, X., and Ku, D. N. (1997). Convective mass transfer at the carotid bifurcation. *Journal of Biomechanics*, 30:565–571.

Mahama, P. A. and Linderman, J. J. (1994). Calcium signaling in individual BC3H1 cells: Speed of calcium mobilization and heterogeneity. *Biotechnol. Prog.*, 10:45–54.

Malek, A. M., Alper, S. L., and Izumo, S. (1999). Hemodynamic shear stress and its role in atherosclerosis. *Journal of the American Medical Association*, 21(282):2035.

Mathur, S. R. and Murthy, J. Y. (1997). A reynolds-averaged navier-stokes solver using an unstructured mesh based finite-volume scheme. *Numerical Heat Transfer*, 25:195–216.

Matsuo, S., Tsuruta, M., Hayano, M., Imamura, Y., Eguchi, Y., Tokushima, T., and Tsuji, S. (1988). Phasic coronary artery flow velocity determined by doppler flowmeter catheter in aortic stenosis and aortic regurgitation. *Am J Cardiol*, 62:917–22.

Meyer, T. and Stryer, L. (1988). Molecular model for receptor-stimulated calcium spiking. *Proc. NatI. Acad. Sci. USA*, 85:5051–5055.

Milner, P., Kirkpatrick, K. A., Ralevic, V., Toothill, V., Pearson, J., and Burnstock, G. (1990). Endothelial cells cultured from human umbilical vein release ATP, substance-P and acetylcholine in response to increased flow. *Proceedings of the Royal Society of London Series B-Biological Sciences*, 241(1302):245–248.

Moore, J., Steinman, D., Prakash, S., Johnston, K., and Ethier, C. (1999). A numerical study of blood flow patterns in anatomically realistic and simplified end-to-side anastomoses. *J Biomech Eng.*, 121:265–72.

Moyle, K. R., Antiga, L., and Steinman, D. (2006). Inlet conditions for image-based CFD models of the carotid bifurcation: Is it reasonable to assume fully developed flow? *Annu. Rev. Fluid Mech.*, 128:371379.

Müller, M. and Griesmacher, A. (2000). Markers of endothelial dysfunction. *Clin Chem Lab Med*, 38:77–85.

Myers, J. G., Moore, J. A., Ojha, M., Johnston, K. W., and Ethier, C. R. (2001). Factors influencing blood flow patterns in the human right coronary artery. *Annals of Biomedical Engineering*, 29:109–120.

Naseem, K. M. (2005). The role of nitric oxide in cardiovascular diseases. *Molecular Aspects of Medicine*, 26:33–65.

Nilius, B. and Droogmans, G. (2001). Ion channels and their functional role in vascular endothelium. *Physiological Reviews*, 81:1415–1459.

Nollert, M. U. and Mcintire, L. V. (1992). Convective mass-transfer effects on the intracellular calcium response of endothelial-cells. *Journal of Biomechanical Engineering-Transactions of the Asme*, 114(3):321–326.

OpenCFD (2007). http://www.opencfd.co.uk/openfoam/.

Pearson, J. D. and Gordon, J. L. (1985). Nucleotide metabolism by endothelium. *Annual Review of Physiology*, 47:617–627.

Pedley, T. (1980). *The Fluid Mechanics of Large Blood Vessels*. Cambridge University Press, Cambridge.

Perktold, K. and Hilbert, D. (1986). Numerical simulation of pulsatile flow in a carotid bifurcation model. *J Biomed Eng*, 8:193–199.

Perktold, K., Hofer, M., Rappitsch, G., Loew, M., Kuban, B., and Friedman, M. (1998). Validated computation of physiologic flow in a realistic coronary artery branch. *Journal of Biomechanics*, 31:217–228.

Perktold, K., Peter, R., Resch, M., and Lang, G. (1991a). Pulsatile non-Newtonian blood flow in three-dimensional carotid bifurcation models: a numerical study of flow phenomena under different bifurcation angles. *J. Biomed. Eng*, 285:507–515.

Perktold, K. and Rappitsch, G. (1995). Computer simulation of local blood flow and vessel mechanics in a compliant carotid artery bifurcation model. *J. Biomechanics*, 28:845–856.

Perktold, K. and Resch, M. (1990). Numerical 3D-simulation of pulsatile wall shear stress in an arterial T-bifurcation model. *J Biomed Eng*, 12:2–12.

Perktold, K., Resch, M., and Florian, K. (1991b). Pulsatile non-Newtonain flow characteristics in a three-dimensional human carotid bifurcation model. *Transactions of ASME*, 113:464–475.

Plank, M. J., Comerford, A., David, T., and Wall, D. J. N. (2006a). Concentration of blood-borne agonists at the endothelium. *Proc. R. Soc. A*, 462:671 – 688.

Plank, M. J., Wall, D. J. N., and David, T. (2006b). Atherosclerosis and calcium signalling in endothelial cells. *Prog. Biophys. Mol. Biol.*

Plank, M. J., Wall, D. J. N., and David, T. (2006c). The role of endothelial calcium and nitric oxide in the localisation of atherosclerosis. *Math. Biosci.*

Prakash, S. and Ethier, C. R. (2001). Requirements for mesh resolution in 3D computational hemodynamics. *Transactions of the ASME*, 123:134–144.

Putney, J. W., Broad, L. M., Braun, F., Lievremont, J., and Bird, G. J. (2001). Mechanisms of capacitative calcium entry. *J. Cell Sci.*, 114:2223–2229.

Qiu, Y. and Tarbell, J. M. (1999). Numerical simulation of oxygen mass transfer in a compliant curved tube model of a coronary artery. *Annals of Biomedical Engineering*, 28:26–38.

Quarteroni, A. (2006). Cardiovascular mathematics. *Proceedings of the International Congress of Mathematicians.*

Ralevic, V. and Burnstock, G. (1998). Receptors for purines and pyrimidines. *Pharmacological Reviews*, 50:423–492.

Rappitsch, G. and Perktold, K. (1995). Pulsatile albumin transport in large arteries: A numerical simulation study. *Journal of Biomechanical Engineering*, 118:511–519.

Rappitsch, G. and Perktold, K. (1996). Computer simulation of convective diffusive processes in larger arteries. *J. Biomechanics*, 29:207–215.

Rappitsch, G., Perktold, K., and Pernkopf, E. (1997). Numerical modelling of shear-dependent mass transfer in large arteries. *Int. J. Numer. Meth. Fluids*, 25:847–857.

Ratcliffe, H. and Luginbuhl, H. (1971). The domestic pig: a model for experimental atherosclerosis. *Atherosclerosis*, 29:133–136.

Resnick, N., Yahav, H., Shay-Salit, A., Shushy, M., Schubert, S., Zilberman, L., and Wofovitz, E. (2003). Fluid shear stress and the vascular endothelium: for better and for worse. *Progress in Biophysics and Molecular Biology*, 81:177–199.

Rhie, C. M. and Chow, W. L. (1983). Numerical study of the turbulent flow past an airfoil with trailing edge separation. *AIAA Journal*, 21:1525–1532.

Ross, R. (1999). Atherosclerosis – an inflammatory disease. *The New England Journal of Medicine*, 340:115–127.

Ross, R. and Glomset, J. A. (1976). The pathogensis of atherosclerois. *New Engl J Med*, 295:369–377.

Schlichting, H. and Gersten, K. (1999). *Grenzschicht-Theorie Boundary-layer theory*. Springer, New York, 8th rev and enl. edition.

Seeley, R. R., Stephens, T. D., and Tate, P. (2003). *Anatomy and physiology*. McGraw-Hill, Boston, 6th edition.

Sharc software (2006). http://www.sharc.co.uk.

Sharp, M. K., Kamm, R. D., Shapiro, A. H., Kimmel, E., and Karniadakis, G. E. (1990). Dispersion in a curved tube during oscillatory flow. *Journal of Fluid Mechanics*, 223:537–563.

Sharp, W., Donovan, D., Teague, P., and Mosteller, R. (1982). Arterial occlusive disease: A function of vessel bifurcation angle. *Surgery*, 91:680–685.

Shaul, P. (2002). Regulation of endothelial nitric oxide synthase; location, location, location. *Annual Review of Physiology;*, 64:749–774.

Shaul, P. (2003). Endothelial nitric oxide synthase, caveolae and the development of atherosclerosis. *J Physiol*, 547:21–33.

Shen, J., Gimbrone, M. A., Luscinskas, F. W., and Dewey, C. F. (1993). Regulation of adenine-nucleotide concentration at endothelium fluid interface by viscous shear-flow. *Biophysical Journal*, 64(4):1323–1330.

Shen, J., Luscinskas, F. W., Connolly, A., Dewey, C. F., and Gimbrone, M. A. (1992). Fluid shear-stress modulates cytosolic free calcium in vascular endothelial-cells. *American Journal of Physiology*, 262(2):C384–C390.

Sitzer, M., Puac, D., Buehler, A., Steckel, D. A., von Kegler, S., Markus, H. S., and H.Steinmetz (2003). Internal carotid artery angle of origin: A novel risk factor for early carotid atherosclerosis. *Stroke*, 34:950–955.

Steinburg, D. (1997). Low density lipoprotein oxidation and its pathobiological significance. *The Journal of Biological Chemistry*, 272:20963–20966.

Tarbell, J. (2003). Mass transport in arteries and the localization of atherosclerosis. *Annu. Rev. Biomed. Eng.*, 5:79–118.

Tarbell, J. M. and Pahakis, M. Y. (2006). Mechanotransduction and the glycocalyx. *Journal of Internal Medicine*, 259:339.

Taylor, C. A., Hughes, T. J. R., and Zarins, C. K. (1998). Finite element modeling of three-dimensional pulsatile flow in the abdominal aorta: Relevance to atherosclerosis. *Annals of Biomedical Engineering*, 26:975–987.

Tobak, M. and Peake, D. J. (1982). Topology of three-dimensional separated flows. *Annual Review of Fluid Mechancis*, 14:61–85.

Tran, Q., Ohashi, K., and Watanabe, H. (2000). Calcium signalling in endothelial cells. *Cardiovascular Research*, 48:13–22.

Traub, O. and Berk, B. C. (1998). Laminar shear stress - mechanisms by which endothelial cells transduce an atheroprotective force. *Arteriosclerosis Thrombosis and Vascular Biology*, 18(5):677–685.

Valant, P., Adjei, P., and Haynes, D. (1992). Rapid Ca2+ extrusion via the Na^+/Ca^{2+} exchanger of the human platelet. *J Membr Biol.*, 130:63–82.

Vane, J., Änggard, E., and Botting, R. (1990). Regulatory functions of the vascular endothelium. *The New England Journal of Medicine*, 323:27–36.

Verma, S. and Anderson, T. (2002). Fundamental of endothelial function for the clinical cardiologist. *Circulation*, 105:546–549.

Versteeg, H. K. and Malalasekera, W. (1995). *Computational Fluid Dynamics The Finite Volume Method*. Pearson, London.

Wada, S., , and Karino, T. (2000). Computational study on LDL transfer from flowing blood to artery walls. *Clinical Applications of Computational Mechanics*, pages 157–173.

Wada, S. and Karino, T. (2002). Theoretical prediction of low-density lipoprotiens concentration at the luminal surface of an artery with a multiple bend. *Annals of Biomedical Engineering*, 30:778–791.

Wada, S., Koujiya, M., and Karino, T. (2002). Theoretical study of the effect of local flow disturbances on the concentration of low-density lipoproteins at the luminal surface of end-toend anastomosed vessels. *Med. Biol. Eng. Comput*, 40:576–587.

Wensing, P., Meiss, L., Mali, W., and Hillen, B. (1998). Early atherosclerotic lesions spiraling through the femoral artery. *Arteriosclerosis, Thrombosis, and Vascular Biology*, 18:1554–1558.

White, C. R., Haidekker, M., Bao, X., and Frangos, J. A. (2001). Temporal gradients in shear, but not spatial gradients, stimulate endothelial cell proliferation. *Circ*, 103:2508–2513.

Wiesner, T., Berk, B., and Nerem, R. (1996). A mathmatical model of cytosolic calcium dynamics in human umbilical vein endothelial cells. *Am. J Physiol*, 270:C1556–1569.

Wiesner, T., Berk, B., and Nerem, R. (1997). A mathmatical model of cytosolic-free calcium response in endothelial cells to fluid shear stress. *Proc Natl Acad Sci USA*, 94:3726–3731.

Yamamoto, K., Sokabe, T., Matsumoto, T., Yoshimura, K., Shibata, M., Ohura, N., Fukuda, T., Sato, T., Sekine, K., Kato, S., Isshiki, M., Fujita, T., Kobayashi, M., Kawamura, K., and Masuda, H. (2006). Impaired flow-dependent control of vascular tone and remodeling in P2X4-deficient mice. *Nat. med.*, 12:133.

Yamamoto, K., Sokabe, T., Ohura, N., Nakatsuka, H., Kamiya, A., and Ando, J. (2003). Endogenous released atp mediates shear stress-induced ca^{2+} iflux into pulmonary artery endothelial cells. *Am J Physiol Heart Circ*, 285:H793–H803.

Zamir, M. (2000). *The Physics of Pulsatile Flow*. Springer, New York.

Zand, T., Hoffman, A. H., Savilonis, B. J., Underwood, J. M., Nunnari, J. J., Majno, G., and Joris, I. (1999). Lipid deposition in rat aortas with intraluminal hemispherical plug stenosis. *Am J Pathology*, 55:85 – 92.

Zarins, C. K., Giddens, D. P., Bharadvaj, B. K., Sottiurai, V. S., Mabon, R. F., and Glagov, S. (1983). Carotid bifurcation atherosclerosis. quantitative correlation of plaque localization with flow velocity profiles and wall shear stress. *Circ. Res.*, 53:502–514.